

NORTHWESTERN UNIVERSITY

Numerical Modelling of Cyclic Degradation of Natural Clay

A DISSERTATION

SUBMITTED TO THE GRADUATE SCHOOL
IN PARTIAL FULFILLMENT OF THE REQUIREMENTS

for the degree

DOCTOR OF PHILOSOPHY

Field of Civil Engineering

By

Zhenhao Shi

EVANSTON, ILLINOIS

December 2016

© Copyright by Zhenhao Shi 2016

All Rights Reserved

ABSTRACT

Numerical Modelling of Cyclic Degradation of Natural Clay

Zhenhao Shi

While infrequent, clay slope failures caused by earthquakes result in loss of life and substantial property damage. In strong seismicity areas, it is sometimes assumed that the stability of clay deposits can be evaluated through the residual undrained strength that is applicable at large deformations. A crucial factor missing in this conservative assumption is the understanding and quantification of the loss of natural clay shear strength during the seismic shaking. Consequently, the above assumption can neither address the fundamental issue of the mechanism of the slope failure initiation nor explicitly account for the specific parameters of individual earthquakes (e.g., amplitude and duration). The goal of this work is to study and quantify the strength degradation of natural clay subjected to cyclic loading. The assumption at the core of this thesis is that the strength loss of natural clay is related to the deterioration of its inherent structures (e.g., inter-particle bonds and fabric) caused by plastic deformation that develops during cyclic loading. Furthermore, such a strength reduction also results from the change of effective stress state as a result of the accumulation of excess pore pressure.

A particular case studied in this work is the destructive landslides caused by the 1964 Alaska earthquake, one of the largest earthquakes in history. The strength loss of the Bootlegger Cove Formation (BCF) clay during cyclic loading has been recognized as a critical factor in the initiation of these landslides. The largest slide during this event was located at Turnagain Heights in Anchorage. Based on the in-situ tests at a site adjacent to the scarp of this slide, this work evaluates the BCF's in-situ sensitivity, an index of natural clay's susceptibility to structure degradation. Furthermore, based on the undrained strength of BCF clay interpreted from in-situ tests, a series of stability analysis are conducted, which back-calculates an upper bound on the strength reduction of BCF clay needed to initiate the slope failure. It is found that the computed strength reduction is compatible with the sensitivity of the BCF at the same elevation as the failure zone within the BCF.

The back analysis can estimate the strength loss to initiate slope failure, but to quantify the strength reduction as a function of a specific seismic event, a general and more sophisticated method is needed. In this work, a bounding surface plasticity constitutive model is developed that accounts for the degradation of clay inherent structure as well as the change of effective stress state, i.e., the two major factors affecting material strength degradation. The model is developed in two steps. A basic model is proposed to represent the cyclic behavior of reconstituted clay, i.e., the intrinsic behavior. Compared with existing plasticity models for cyclic clay behavior, three major enhancements are proposed, including the mixed plastic flow rule, a new form of plastic modulus to uniformly reproduce cyclic softening and shakedown, and the adoption of a small strain elasticity model.

The verification of the basic model with experimental observations shows that the aforementioned improvements ensure that the development of plastic deformation and excess pore pressure during cyclic loading is reasonably represented.

To account for the effects of soil structure and its deterioration, the basic model is extended to include a new internal variable S_b that represents the amount of soil structure and a destructuration law that quantifies the monotonic decrease of S_b under irrecoverable deformation. The proposed plastic potential surface in the extended model is a function of fabric anisotropy and inter-particle bonds. The influences of these two aspects of soil structure on material plastic flow are explored based on the stress-dilatancy relation which is derived from the plastic potential surface. The appropriateness of this plastic potential surface to describe natural clay behavior is validated with experimental evidence. The validation of the extended model based on experimental data of seven natural clays shows that the proposed model is capable of reproducing the mechanical behavior of natural clay under monotonic and cyclic loading, and the strength degradation during cyclic loading can be reasonably quantified by this model.

Acknowledgements

I would like to express my thanks from heart to many people who guided, helped and supported me during my study at Northwestern. This thesis could not be finished without them.

First, I would like to thank my advisor, Professor Richard J. Finno, and my co-advisor, Professor Guiseppe Buscarnera, for providing the opportunity to study this exciting project, for their continuous supports and their guidance and inspirations during numerous discussions. What I learn from them are not only knowledge, skills, and experience, but more importantly their attitudes towards exploring unknowns and solving problems for engineering practice. Many thanks also to Professor Charles H. Dowding, my committee member, for his valuable guidance and suggestions.

Also, I want to thank all my colleagues and friends at Northwestern, Charlotte, Chang, Chao, Gabriel, Jose, Luis, Molly, Nathan, Tatiana, Shenjun, Sangrey, Yan, Yida, Yu. Their supports and help make my study a wonderful, warm and unforgettable moment in my all life. Special thanks shall be given to Gabriel for his work day and night in the laboratory to provide valuable data for this thesis.

Then, I want to express my thank to my family, my dad and mom, my dad and mom in law. The long distance between Chicago and China never stops their love and supports and indeed I feel it every day.

Finally, I want to thank my wife, Mulei, for giving up her comfortable job and life at China and choosing to accompany me in an unfamiliar and sometimes lonely place. Her supports for my pursuing dreams, encourages and beliefs on me when I feel frustrated are the most valuable treasures in my heart. I would like to dedicate this thesis to my loved Mulei.

Table of Contents

ABSTRACT	3
Acknowledgements	6
List of Tables	11
List of Figures	14
Chapter 1. INTRODUCTION	34
1.1. Scope and Objectives	37
1.2. Contents of Thesis	38
Chapter 2. TECHNICAL BACKGROUND AND LITERATURE REVIEW	40
2.1. Introduction	41
2.2. Landslides During the 1964 Alaska Earthquake and BCF Soil Failure During Cyclic Loading	42
2.3. Experimental Evidence: Effects of Soil Structure on Mechanical Behavior of Natural Clay	54
2.4. Experimental Evidence: Clay Behavior During Undrained Cyclic Loading and Post Cyclic Shearing	67
2.5. Bounding Surface Plasticity Models For Cyclically Loaded Clay	79
2.6. Modelling strategy for capturing structure effects in natural soils	100

2.7. Summary and Conclusions	105
Chapter 3. BACK ANALYSIS OF THE TURNAGAIN HEIGHTS LANDSLIDE	109
3.1. Introduction	110
3.2. In-Situ Tests at the Lyn Ary Park	113
3.3. The Sensitivity of BCF Clay	117
3.4. Stability Analysis of the Turnagain Heights Slope	129
3.5. Summary and Conclusions	144
Chapter 4. FORMULATION OF A CONSTITUTIVE MODEL FOR CYCLICALLY LOADED RECONSTITUTED CLAY	147
4.1. Introduction	148
4.2. Formulation of the Basic Model	150
4.3. Parametric Analyses of the Primary Constitutive Hypotheses	179
4.4. Calibration of Model Parameters and Initial Conditions	188
4.5. Validation of The Basic Model	201
4.6. Summary and Conclusions	221
Chapter 5. EXTENSION OF THE BASIC CONSTITUTIVE MODEL FOR CYCLICALLY LOADED STRUCTURED CLAY	224
5.1. Introduction	225
5.2. Extension of the Basic Model to Consider the Effects of Soil Structure	226
5.3. The Influence of Natural Clay Structure on Plastic Flow	233
5.4. Calibration of Model Parameters and Initial Conditions for the Extended Model	245

	10
5.5. Validation of the Extended Model	252
5.6. Summary and Conclusions	313
Chapter 6. MODEL GENERALIZATION AND IMPLEMENTATION	316
6.1. Introduction	317
6.2. Model Generalization in Multiaxial Space	318
6.3. Stress Integration Algorithm	327
6.4. Formulation of Triaxial Space Constitutive Driver	338
6.5. Model Implementation into UMAT Subroutine	343
6.6. Summary and Conclusions	346
Chapter 7. SUMMARY AND CONCLUSIONS	349
7.1. Summary	350
7.2. Conclusions	352
References	359

List of Tables

3.1	Soil properties used in the stability analysis of Turnagain Heights slope	116
3.2	Chemical characteristics of six Bootlegger Cove Formation clay samples (Mitchell et al., 1973)	124
3.3	Chemical composition and pH value of pore water extracted from BCF clay samples collected at the Lynn Ary park (Updike and Olsen, 1988)	126
3.4	Comparison between the composition of seawater and the composition of the pore water of BCF clay samples collected at the Lynn Ary park	126
4.1	Parameters in the basic model and their roles	179
4.2	Initial conditions in the basic model	179
4.3	Model parameters in the qualitative evaluations	181
4.4	Initial conditions in the qualitative evaluations	181
4.5	Model parameters for reconstituted Georgia kaolin	203
4.6	Model parameters for insensitive BCF clay	210
4.7	Initial values of internal variables for insensitive BCF clay	212
5.1	Model parameters and their roles in the extended model	246
5.2	Initial conditions in the extended model	246

5.3	Index properties and USGS classification of the investigated natural clays	252
5.4	Model parameters for Norrköping clay	254
5.5	Initial conditions for Norrköping clay simulations	255
5.6	Model parameters for the Vallericca clay	263
5.7	Initial conditions for the Vallericca clay simulations	264
5.8	Model parameters for the Bothkennar clay	270
5.9	Initial conditions for the Bothkennar clay simulations	270
5.10	Model parameters for the Shanghai clay	276
5.11	Initial conditions for the Shanghai clay simulations	277
5.12	Model parameters for the Wenzhou clay	279
5.13	Initial conditions for the Wenzhou clay simulations	280
5.14	Model parameters for the Grande Baleine clay	286
5.15	Initial conditions for Grande Baleine clay simulations	287
5.16	Model parameters for the Cloverdale clay	294
5.17	Initial conditions for the Cloverdale clay simulations	295
5.18	Comparison between model parameters for the insensitive and sensitive BCF clay	305
5.19	Initial conditions for the sensitive BCF clay simulations	305
5.20	Summary of model parameters for different structured clays	312
6.1	Model parameters in the single element test of UMAT	344

6.2	Simulation cases in the single element test of UMAT	345
-----	---	-----

List of Figures

2.1	Alaska earthquakes map (Haeussler and Plafker, 2004)	42
2.2	Slide features and ground movement for the Fourth Avenue landslide and L Street landslide: (a) Fourth Avenue landslide; (b) L Street landslide (Shannon & Wilson Inc., 1964)	44
2.3	Schematic diagram of the formation of a graben in a translatory landslide (Hansen, 1965)	45
2.4	Aerial views after the 1964 earthquake: (a) Fourth Avenue landslide; (b) Turnagain Heights landslide (Shannon & Wilson Inc., 1964)	45
2.5	Failure mechanism observed in model tests (Seed and Wilson, 1967)	46
2.6	Geologic-physiographic units of the Anchorage lowland and adjacent areas. Light-shaded area indicates cohesive facies of the Bootlegger Cove Formation. Dark shade indicates the principal 1964 landslides (Updike and Olsen, 1988)	48
2.7	Relation between sensitivity and liquidity index for BCF specimens collected at Fourth Avenue and Turnagain Heights landslides (Shannon & Wilson Inc., 1964)	50
2.8	Comparison between the sensitivity measured by laboratory vane and field vane(Shannon & Wilson Inc., 1964)	52

2.9	Sensitivity contours for BCF clay determined by triaxial tests (Mitchell et al., 1973)	53
2.10	Oedometer compression curves for undisturbed and reconstituted Shellhaven and Gosport clay (Burland, 1990)	56
2.11	Results of consolidation tests on intact and destructured Saint-Alban clays (Leroueil et al., 1979)	58
2.12	Results of CAU triaxial tests on Troll field clay specimens: (a) stress-strain response; (b) effective stress path (Burland, 1990)	59
2.13	Consolidation paths of Troll field clay specimens (Burland, 1990)	60
2.14	Results of CIU triaxial tests on intact and destructured natural clays (Leroueil et al., 1979)	61
2.15	Results of CID triaxial tests on structured materials (Leroueil and Vaughan, 1990): (a) schematic stress paths; (b) stress-strain curves for Saint Vallier clay (Lefebvre, 1970); (c) stress-strain curves for a soft, high porosity, oolitic limestone (Elliott and Brown, 1985)	62
2.16	Results of CID triaxial tests on artificially bonded soil: (a) stress-strain response; (b) volume change (Maccarini, 1987)	64
2.17	Strength envelopes of Vallericca clay corrected for the dilatancy component	65
2.18	Yield curves for intact and destructured soft clays (Tavenas and Leroueil, 1985): (a) Saint-Alban; (b) Cubzoc-les-Ponts; (c) Atchafalaya; (d) Bäckebol	66

		16
2.19	Stress-strain curves for undrained cyclic tests of high and low shear stresses (Sangrey et al., 1969)	67
2.20	Effective stress paths for undrained cyclic tests of high and low shear stresses (Sangrey et al., 1969)	69
2.21	The equilibrium line and equilibrium excess pore pressure defined from cyclic loading characterized by shakedown (Sangrey et al., 1969)	70
2.22	Experimental observations in an undrained cyclic loading on NC Cloverdale clay: (a) effective stress path; (b) stress-strain response (Zergoun and Vaid, 1994)	71
2.23	Rate of peak strain development and effective stress stability thresholds during undrained cyclic loading on isotropically consolidated NC Cloverdale clay (Zergoun and Vaid, 1994)	72
2.24	Peak strain and effective stress ratio development with cycles during undrained cyclic loading on isotropically consolidated NC Cloverdale clay (Zergoun and Vaid, 1994)	72
2.25	Post-cyclic shear strength and stiffness of San Francisco Bay mud after 200 strain-controlled loading cycles (Thiers and Seed, 1968)	74
2.26	Post-cyclic shear strength and stiffness of BCF clay (Mitchell et al., 1973)	75
2.27	Change in undrained failure shear stress due to previous undrained strain-controlled cyclic loading in simple shear tests (Andersen et al., 1980)	77

		17
2.28	Effective stress paths for monotonic triaxial tests with and without previous undrained cyclic loading (Andersen et al., 1980)	77
2.29	The relation between cyclic strength degradation and excess pore pressure accumulation during cyclic loading on NC clay (Yasuhara, 1994)	78
2.30	Normalized undrained shear strength: (a) with respect to σ'_v ; (b) with respect to p' (Finno and Zapata-Medina, 2013)	80
2.31	Response of NC clay to undrained cyclic loading according to conventional critical state models: (a) effective stress path; (b) stress-strain response; (c) strain-excess pore pressure response (Wood, 1990)	81
2.32	Schematic diagram of bounding surface and related concepts (Dafalias, 1986b)	84
2.33	Definition of plastic flow at a plastic potential surface passing the image stress (Seidalinov and Taiebat, 2014)	87
2.34	Comparison of model prediction with test of two-way, strain controlled, undrained cyclic triaxial test on Kaolin (Zienkiewicz et al., 1985)	89
2.35	Schematic diagram of over-damping caused by the fixed projection center	90
2.36	Computed effective stress path in a test of two-way, strain controlled, undrained cyclic triaxial test on Kaolin (Zienkiewicz et al., 1985)	91

		18
2.37	Schematic diagram of the formation and movement of the bounding surface and loading surface (Li and Meissner, 2002)	93
2.38	Schematic diagram of the issue associated with the relocation of bounding surface upon stress reversal: (a) movement of bounding surface; (b) stress-strain response	94
2.39	Comparison between experimentally observed undrained effective stress path and simulations based on image stress flow rule (Seidalinov and Taiebat, 2014) with experimental data from (Sheu, 1985)	98
2.40	Schematic diagram of structured surface and intrinsic surface	101
2.41	Schematic diagram of flow rule modifications in structured soil models: (a) axial translation; (b) friction deconstruction	103
3.1	Locations of boreholes, CPTs and field vane, vicinity of Lynn Ary Park (modified based on the work of Updike and Olsen (1988))	114
3.2	In-situ tests based soil strength properties and stratigraphy at Turnagain Heights area: (a) undrained shear strength; (b) FV remolded strength and CPT side friction; (c) correlated friction angle from CPT	115
3.3	Soil behavior classification based on the normalized CPT properties (classification chart adopted from Robertson (1990))	118
3.4	BCF clay sensitivity interpreted from in-situ tests at the Lynn Ary Park	120
3.5	Correlation between BCF clay's sensitivity with index properties: (a) sensitivity interpreted from in-situ tests; (b) natural water content; (c) liquidity index	122

- 3.6 Correlation between BCF clay's sensitivity with chemical components concentration: (a) sensitivity interpreted from in-situ tests; (b) total cation concentration; (c) monovalent cation concentration percent 128
- 3.7 Slope stability analysis model: (a) Turnagain Heights slope profile before the 1964 earthquake (adopted from Seed and Wilson (1967)); (b) analysis model geometry; (c) phreatic surface and pore pressure contours based on seepage analysis 131
- 3.8 Slip surface search methods: (a) circular slip with auto grid search; (b) non-circular slip with block search 132
- 3.9 Stability FS of Turnagain Heights slope before the 1964 earthquake: (a) circular slip surface (no lenses); (b) circular slip surface (with lenses); (c) non-circular slip surface (no lenses); (d) non-circular slip surface (with lenses) 134
- 3.10 Required strength reduction for slope failure initiation: (a) reduction in upper stiff clay (no lenses); (b) reduction in upper stiff clay (with lenses); (c) reduction in upper soft clay (no lenses); (d) reduction in upper soft clay (with lenses) 136
- 3.11 Required strength reduction for slope failure initiation: (a) simultaneous reduction in upper stiff clay and upper soft clay (no lenses); (b) simultaneous reduction in upper stiff clay and upper soft clay (with lenses) 137

- 3.12 Required strength reduction for slope failure initiation with and without earthquake-induced excess pore pressure in sand/silt lenses: (a) reduction in upper stiff clay; (b) reduction in upper soft clay 138
- 3.13 Circular slip surface at failure: (a) reduction in upper stiff clay (no lenses); (b) reduction in upper stiff clay (with lenses); (c) reduction in upper soft clay (no lenses); (d) reduction in upper soft clay (with lenses); (e) simultaneous reduction in both layers (no lenses); (f) simultaneous reduction in both layers (with lenses) 140
- 3.14 Non-circular slip surface at failure: (a) reduction in upper stiff clay (no lenses); (b) reduction in upper stiff clay (with lenses); (c) reduction in upper soft clay (no lenses); (d) reduction in upper soft clay (with lenses); (e) simultaneous reduction in both layers (no lenses); (f) simultaneous reduction in both layers (with lenses) 141
- 4.1 Schematic illustrations of important surfaces in the basic model in triaxial stress space: bounding surface and loading surface 151
- 4.2 Schematic illustration of plastic flow direction defined at image stress and current stress 154
- 4.3 Schematic illustration of normalized R_v^c evolution during cyclic loading: (a) s_l varies based on equation 4.14; (b) $s_l = 1$ 158
- 4.4 Plastic flow direction in a undrained cyclic loading tests under different assumptions of plastic flow rules: (a) image stress flow rule; (b) proposed

	flow rule; (c) proposed flow rule with $s_l = 1$; (d) mixed flow rule with deviatoric component	161
4.5	Schematic illustration of projection center update at stress reversal : (a) the detection of stress reversal at current step (step i); (b) forming of new loading surface at next step (step $i + 1$)	164
4.6	Influence of computation step size on computed stress-strain response after the stress reversal	165
4.7	Schematic illustration of projection center location relative to the bounding surface	167
4.8	Modified Hardin-Drnevich elastic shear stiffness degradation curve and definition of the parameter $\gamma_{0.7}$	175
4.9	Simulated effective stress paths during CIU CYC-TX test: (a) $w=0$; (b) $w=1$; (c) $w=5$; (d) $w=10$	182
4.10	Simulated pore pressure build-up during CIU CYC-TX test with different values of parameter w	183
4.11	Simulated peak and residual strains during CIU CYC-TX test with different values of c_d : (a) peak compression and extension strains in each cycle; (b) residual strain at the end of each cycle	185
4.12	Simulated cyclic stress-strain and effective stress paths during CIU CYC-TX test with large cyclic stress amplitude: (a)-(b) consider small strain elasticity; (c)-(d) ignore small strain elasticity	186

4.13	Simulated cyclic stress-strain and effective stress paths during CIU CYC-TX test with small cyclic stress amplitude: (a)-(b) consider small strain elasticity; (c)-(d) ignore small strain elasticity	187
4.14	Calibration of parameters λ and κ	190
4.15	Calibration of parameter ν	191
4.16	Calibration of small strain stiffness parameters: (a) A_g , n_g and e_g ; (b) $\gamma_{0.7}$	192
4.17	Calibration of parameters M_c and M_e	193
4.18	Calibration of parameters h_c and h_e	195
4.19	Calibration of parameter C	196
4.20	Calibration of parameter c_d	197
4.21	Calibration of parameter w : (a) pore pressure build up; (b) experimental data under magnified scale	198
4.22	Comparison between experimental observations and model simulations in a undrained cyclic loading with $q_{cyc} = 140.7\text{kPa}$: (a)-(b) experimental observations; (c)-(d): simulations of the proposed model; (e)-(f): simulations under image stress flow rule	203
4.23	Comparison between experimental observations and model simulations in a undrained cyclic loading with $q_{cyc} = 121.4\text{kPa}$: (a)-(b) experimental observations; (c)-(d): simulations of the proposed model; (e)-(f): simulations under image stress flow rule	204

- 4.24 Comparison between experimental observations and model simulations in a undrained cyclic loading with $q_{cyc} = 136\text{kPa}$: (a)-(b) experimental observations; (c)-(d): simulations of the proposed model; (e)-(f): simulations under image stress flow rule 205
- 4.25 Comparison between experimental observations and model simulations in a undrained cyclic loading with $q_{cyc} = 165.5\text{kPa}$: (a)-(b) experimental observations; (c)-(d): simulations of the proposed model; (e)-(f): simulations under image stress flow rule 206
- 4.26 Comparison between experimental observations and model simulations of pore pressure build-up in cyclic loading: (a) pore pressure accumulation in tests $q_{cyc} = 121.4\text{kPa}$ and $q_{cyc} = 136\text{kPa}$; (b) pore pressure accumulation in tests $q_{cyc} = 140.7\text{kPa}$ and $q_{cyc} = 165.5\text{kPa}$ 207
- 4.27 Comparison between experimental observations and model simulations of strains development in cyclic loading: (a) peak strains development in tests $q_{cyc} = 136\text{kPa}$; (b) peak strains development in tests $q_{cyc} = 140.7\text{kPa}$ 208
- 4.28 Simulated construction-induced stress changes for different samples and their relative positions to the wharf structure 210
- 4.29 Estimation of initial value of internal value α from maximum past pressure 212

4.30	Comparison between experimental observations and model simulations in reconsolidation tests: (a) sample B47-S9-1; (b) sample B47-S7-2; (c) sample B48-S6-2; (d) sample B46-S12-1	214
4.31	Comparison between experimental observations and model simulations of stress-strain response during undrained cyclic loading tests: (a)-(d) experimental data; (e)-(h) simulations by the proposed model; (i)-(l) simulations by the reference model	215
4.32	Schematic illustrations of the effects of pre-cyclic construction paths on the computed strain accumulation directions	216
4.33	Comparison between experimental observations and model simulations of strain-pore pressure response during undrained cyclic loading tests: (a)-(d) experimental data; (e)-(h) simulations by the proposed model; (i)-(l) simulations by the reference model	219
4.34	Comparison between experimental observations and model simulations in post-cyclic undrained shearing: (a): stress-strain response; (b) strain-pore pressure response	221
5.1	Schematic illustration of important surfaces in the extended model: (a) intrinsic surface and structure surface; (b) plastic potential surface	228
5.2	The influences of variable α and p_t/p on stress-dilatancy curve: (a) varying α under $p_t/p = 0$; (b) varying p_t/p under $\alpha = 0$	234
5.3	Experimentally observed stress-dilatancy relations and their comparisons with theoretical predictions: (a) reconstituted clay samples under	

	isotropic and K_0 consolidation history (Lewin, 1973); (b) reconstituted clay samples under constant stress ratio consolidation (Gens, 1982)	236
5.4	Experimentally observed stress-dilatancy relations and their comparisons with theoretical predictions: (a) pyroclastic weak rock (Cecconi and Viggiani, 2001); (b) artificially cemented sand (Schnaid et al., 2001); (c) Bangkok clays (Balasubramaniam and Hwang, 1980); (d) Gravina di Puglia calcarenite (Lagioia et al., 1996)	240
5.5	Calibration of the parameters k_i and A in a 1D compression test on the Bothkennar clay: (a) varying values of k_i ; (b) varying values of A	247
5.6	Calibration of the parameter A in a CK_0U TXC test	247
5.7	Calibration of the parameter r_c : (a) simulated effective stress paths for different r_c ; (b) calibrate r_c for the Bothkennar clay	249
5.8	Estimation of internal variable S_b in 1D compression tests on the Bothkennar clay	250
5.9	Atterberg limits for investigated natural clays on the Casagrande plasticity chart	253
5.10	Comparison between the experimental observation and model simulation for a 1D compression test on the Norrköping clay	256
5.11	Comparison between the experimental observations and model simulations for a CK_0U TXC test and a CK_0U TXE test on the Norrköping clay: (a) stress-strain response; (b) strain-pore pressure response	257

- 5.12 Comparison between the experimental observations and model simulations for a CK_0U TXC test and a CK_0U TXE test on the Norrköping clay: effective stress path 257
- 5.13 Comparison between the experimental observations and model simulations for a CIU TXC test on a Norrköping clay with $OCR=2$: (a) stress-strain response; (b) strain-pore pressure response 258
- 5.14 Comparison between the experimental observations and model predictions for four CAU TXC tests on the Norrköping clay: (a) stress-strain response; (b) strain-pore pressure response 259
- 5.15 Comparison between the experimental observations and model predictions for four CAU TXC tests on the Norrköping clay: effective stress path 260
- 5.16 Comparison between the experimental observations and model predictions for a CIU TXC test on a Norrköping clay of $OCR=5$: (a) stress-strain response; (b) strain-pore pressure response 261
- 5.17 Comparison between experimental observations and model predictions for CID TXC and CAD TXC tests on the Norrköping clay: (a) stress-strain response; (b) volume change 261
- 5.18 Comparison between experimental observations and model simulation for isotropic compression tests on the Vallericca clay 264

- 5.19 Comparison between the experimental observations and model simulations for CAU TXC tests on the Vallericca clay: (a) stress-strain response; (b) strain-pore pressure response 265
- 5.20 Comparison between the experimental observations and model simulations for CAU TXC tests on the Vallericca clay: effective stress path 266
- 5.21 Comparison between the experimental observations and model predictions for CAU TXC tests on the Vallericca clay (MP group): (a) stress-strain response; (b) strain-pore pressure response 267
- 5.22 Comparison between the experimental observations and model predictions for CAU TXC tests on the Vallericca clay (MP group): effective stress path 267
- 5.23 Comparison between experimental observations and model predictions for a CAD TXC test (MP group) on the Vallericca clay: (a) stress-strain response; (b) volume change 268
- 5.24 Comparison between the experimental observations and model predictions in a CAU TXC test (HP group) on the Vallericca clay: (a) stress-strain response; (b) strain-pore pressure response 269
- 5.25 Comparison between the experimental observations and model predictions in a CAU TXC test (HP group) on the Vallericca clay: effective stress path 269

5.26	Comparison between computed initial bounding surface and experimentally observed yield stresses of the Bothkennar clay (Smith et al., 1992)	271
5.27	Comparison between the experimental observation and model simulation for a 1D compression on the Bothkennar clay	272
5.28	Comparison between the experimental observations and model simulations for triaxial shearing tests on the Bothkennar clay: stress path	273
5.29	Comparison between the experimental observations and model simulation for a CAU TXC test on the Bothkennar clay: (a) stress-strain response; (b) strain-pore pressure response	273
5.30	Comparison between the experimental observations and model predictions for triaxial shearing tests on the Bothkennar clay: stress path	275
5.31	Comparison between the experimental observations and model prediction for a CAU TXE test on the Bothkennar clay: (a) stress-strain response; (b) strain-pore pressure response	275
5.32	Comparison between the experimental observation and model simulation in a 1D compression test on the Shanghai clay	277
5.33	Comparison between the experimental observations and model simulations in two CIU TXC tests on the Shanghai clay: (a) stress-strain response; (b) strain-pore pressure response	279

- 5.34 Comparison between the experimental observations and model simulations in two CIU TXC tests on the Shanghai clay: effective stress path 280
- 5.35 Comparison between the experimental observations and model predictions in two CAU TXC tests on the Shanghai clay: (a) stress-strain response; (b) strain-pore pressure response 281
- 5.36 Comparison between the experimental observations and model predictions in two CAU TXC tests on the Shanghai clay: effective stress path 282
- 5.37 Comparison between the experimental observation and model simulation for a 1D compression test on the Wenzhou clay 283
- 5.38 Comparison between the experimental observations and model simulations for a CK_0U TXC test and a CK_0U TXE test on the Wenzhou clay: (a) stress-strain response; (b) strain-pore pressure response 283
- 5.39 Comparison between the experimental observations and model simulations for a CK_0U TXC test and a CK_0U TXE test on the Wenzhou clay: effective stress path 284
- 5.40 Comparison between the experimental observations and model predictions for two CK_0U TXC tests and two CK_0U TXE tests on the Wenzhou clay: (a) stress-strain response; (b) strain-pore pressure response 284

- 5.41 Comparison between the experimental observations and model predictions for two CK_0U TXC tests and two CK_0U TXE tests on the Wenzhou clay: effective stress path 285
- 5.42 Comparison between the effective stress path in a CIU TXC test on a intact sample and the computed bounding surfaces with different values of internal variables 288
- 5.43 Comparison between the experimental observation and model simulation in a 1D compression test on the Grande Baleine clay 288
- 5.44 Comparison between the experimental observations and model simulations in two CIU TXC tests on the Grande Baleine clay: (a) stress-strain response; (b) strain-pore pressure response 289
- 5.45 Comparison between the experimental observations and model simulations in two CIU TXC tests on the Grande Baleine clay: effective stress path 290
- 5.46 Comparison between experimental observations and model simulations in undrained cyclic test and post-cyclic shearing test on the Grande Baleine clay: (a)-(b) stress-strain response ; (c)-(d) strain-pore pressure response 292
- 5.47 Comparison between the experimental observation and model simulation for a 1D compression test on Cloverdale clay 296

- 5.48 Comparison between the experimental observations and model simulations for CIU TXC and CIU TXE tests on NC Cloverdale clay: (a) stress-strain response; (b) strain-pore pressure response 297
- 5.49 Comparison between the experimental observations and model simulations for an undrained cyclic loading test on NC Cloverdale clay: (a)-(b) effective stress path; (c)-(d) stress-strain response 298
- 5.50 Comparison between the experimental observations and model simulations for three CIU TXC and TXE tests on OC Cloverdale clay: (a) effective stress path; (b) stress-strain response 299
- 5.51 Comparison between the experimentally observed and computed effective stress paths for three cyclic loading tests on NC Cloverdale clay: (a)-(b) $q_{cyc} = 75$ kPa; (c)-(d) $q_{cyc} = 88$ kPa; (e)-(f) $q_{cyc} = 100$ kPa 299
- 5.52 Comparison between the experimentally observed and computed stress-strain responses for three cyclic tests on NC Cloverdale clay: (a)-(b) $q_{cyc} = 75$ kPa; (c)-(d) $q_{cyc} = 88$ kPa; (e)-(f) $q_{cyc} = 100$ kPa 300
- 5.53 Comparison between the experimentally observed and computed pore pressure accumulation for three cyclic loading tests on NC Cloverdale clay: (a) $q_{cyc} = 75$ kPa; (b) $q_{cyc} = 85$ kPa; (c) $q_{cyc} = 88$ kPa 301
- 5.54 Comparison between the experimentally observed and computed strains at the peak cyclic shear stress for three cyclic loading tests on NC Cloverdale clay: (a) $q_{cyc} = 75$ kPa; (b) $q_{cyc} = 85$ kPa; (c) $q_{cyc} = 88$ kPa 301

5.55	Comparison between the experimentally observed and computed stress-strain-pore pressure responses for three post-cyclic shearing on Cloverdale clay: (a) stress-strain response ; (b) strain-pore pressure response	302
5.56	Comparison between the experimentally observed and computed effective stress paths for three post-cyclic shearing on Cloverdale clay	303
5.57	Time history of the imposed strain in a strain-controlled cyclic loading test on the BCF clay with $S_t = 5$ to 6	306
5.58	Comparison between the experimental observation and model simulation for the anisotropic consolidation on the BCF clay with $S_t = 5$ to 6: (a) CYC-1 test; (b) CYC-1-Dulp test	307
5.59	Comparison between the experimental observation and model simulation for a strain-controlled cyclic loading test on the BCF clay with $S_t = 5$ to 6: (a) stress-strain response; (b) strain-pore pressure response	308
5.60	Comparison between the experimental observation and model simulation (no destructuration) for a strain-controlled cyclic loading on the BCF clay with $S_t = 5$ to 6: (a) stress-strain response; (b) strain-pore pressure response	309
6.1	Schematic illustration of the dependence of parameters N , M and h on the Lode angle of $\bar{\mathbf{s}} - \bar{p}^* \boldsymbol{\alpha}$	320
6.2	Schematic illustration of variables that define the position of projection center relative to the bounding surface in deviatoric plane	325

6.3	Single element and its boundary conditions for a triaxial sample	345
6.4	The comparison in undrained monotonic loading tests: (a) effective stress path; (b) stress-strain response	346
6.5	The comparison in drained monotonic loading tests: (a) stress-strain response; (b) volume change response	346
6.6	The comparison of small strain responses: (a) undrained compression tests; (b) drained compression tests	347
6.7	The comparison in undrained cyclic loading tests: (a) effective stress path; (b) stress-strain response	347

CHAPTER 1

INTRODUCTION

Clay slopes have failed spectacularly as a result of large earthquakes, one of the most notable being the slope failures in Anchorage, Alaska as a result of the Prince William Sound earthquake in 1964. One critical failure mechanism of these landslides has been referred to natural clay's strength loss during cyclic loading (Shannon & Wilson Inc., 1964; Hansen, 1965; Mitchell et al., 1973; Updike and Olsen, 1988). These disastrous slope failures had a significant impact on the design and seismic evaluation of slopes and earth retaining structures in areas of strong seismicity. The residual undrained shear strength (i.e., the undrained shear strength at large shear strains) is sometimes selected in the post-earthquake stability analysis and the seismic design of slopes (e.g., WSDOT (2006)), because it represents the lower bound of the available strength after the development of large deformations due to the earthquake shakes or the slope sliding. However, a crucial factoring missing in this approach is the strength loss of natural clay subjected to cyclic loading, which prevents the approach addressing the fundamental issue of the initiation mechanism of slope failure. Moreover, the residual strength is considerably lower than the strength that corresponds to the failure initiation (Burland, 1990). Therefore, it is evident that a design based on the peak strength may not be safe, but the one based on the residual strength would be too conservative and results in excessively expensive constructed facilities. A safe and economic slope design in areas susceptible to earthquakes must consider the cyclic strength degradation of natural clay, as suggested by the LRFD seismic analysis and design reference manual (Kavazanjian et al., 2011) . Specifically, the quantification of strength loss as a function of earthquake parameters (e.g., magnitude and duration) is needed. The goal of this work is to study the cyclic strength degradation of natural clay and further quantify it.

To quantify the cyclic strength degradation, one must study the mechanism behind it. There is a distinction between natural and intrinsic properties of clay. The intrinsic properties are those applicable to normally consolidated, reconstituted clay where shear resistance is developed from friction and electro-chemical forces, whereas natural clay also derives strength from its soil structure (e.g., inter-particle bonding and fabric). Monotonic loading tests has shown that structure in natural clay progressively degrades when subjected to external disturbances and this deterioration of the structure leads to a higher compressibility, brittle behavior and loss of strength. A common measure of loss of structure is the sensitivity of a clay, S_t , defined by the ratio of undrained strength of undisturbed samples over that of reconstituted samples. All natural clays are sensitive to a degree, with S_t values from 2 to 4 for low sensitivity (Holtz et al., 2010), even though a significant reduction in undrained strength occurs when such clay is fully remolded. Clay can have S_t values greater than 16, and these are termed quick clay. Studies by Shannon & Wilson Inc. (1964) showed that a portion of the clay of Bootlegger Cove Formation (BCF) that composes the failed slopes at Anchorage can have a sensitivity greater than 40. As a core assumption in this work, it is hypothesized that, similar to monotonic loading, the cyclic loading can cause a progressive degradation of the natural clay's structure and thus results in a loss of strength. Furthermore, such a deterioration of structure is directly related to the development of plastic deformation and excess pore pressure in natural clays.

In addition to the structure deterioration, the change in the effective stress state also significantly affects material strength during cyclic loading, which results from the accumulation of excess pore pressure. An effective stress based elastoplasticity modeling

framework provides an ideal platform to consider the above two factors simultaneously. In elastoplastic constitutive models, soil structure can be idealized as a set of internal variables, whose evolution depends on plastic strains. On the other hand, continuous monitoring in effective stress changes naturally occurs. Moreover, various cyclic loading conditions (e.g., drainage, magnitude, wave shape) can be accounted in a general form.

In this work, to quantify the cyclic strength degradation of natural clay, an effective stress based elastoplasticity constitutive model is developed, which is aimed at reasonably reproducing the irrecoverable deformation and excess pore pressure in cyclically loaded clay, while simultaneously tracking the deterioration of soil structure. The model is developed in two steps. A basic model is proposed to represent the intrinsic behavior of natural clay during cyclic loading, which is of fundamental importance and significantly affects the degradation of soil structure. Compared with existing plasticity models for cyclic clay behavior, three major enhancements are proposed, including the mixed plastic flow rule, a new form of plastic modulus to uniformly reproduce cyclic softening and shakedown, and the adoption of a small strain elasticity model. Then, the basic model is extended to account for the effects of soil structure and its deterioration.

1.1. Scope and Objectives

The scope and objectives of the present research include:

- (1) Evaluate the strength and sensitivity of Bootlegger Cove Formation (BCF) clay based on in-situ tests at a site adjacent to a landslide during the 1964 earthquake, Turnagain Heights landslide;

- (2) Formulate a basic constitutive model to reproduce the intrinsic cyclic behavior of clay;
- (3) Extend the basic model to consider the effects of soil structure and its degradation during cyclic loading;
- (4) Verify both the basic and extended model with respect to experimental observations.

1.2. Contents of Thesis

Chapter 2 presents a literature review of various aspects related to the topic of this thesis, including (a) major landslides caused by the 1964 earthquake; (b) previous research about the BCF and its sensitivity; (c) experimental observations of structure effects on natural clay behavior, clay responses during cyclic loading and post-cyclic shearing; (d) constitutive modeling of cyclically loaded clay and structured soils.

Chapter 3 presents the back analysis of Turnagain Heights landslide. First, the soil strength profile and stratigraphy at the Turnagain Heights area are provided, which is generated based on the results of in-situ tests at a site adjacent to the scarp of the slide. The in-situ sensitivity of BCF clay is presented, which is interpreted based on the same field investigations. Additionally, this chapter discusses the correlation between the interpreted sensitivity and soil index properties and pore fluid chemical compositions. Lastly, Chapter 3 presents the results of the slope stability analysis of Turnagain Heights. In particular, the stability condition before the 1964 earthquake is evaluated, and an upper bound on the strength reduction of BCF clay needed to trigger the slope failure is estimated.

Chapter 4 presents the formulation of the basic model in triaxial space. The results from a series of parametric studies are discussed, which elucidate the roles of the new model components (i.e., the mixed flow rule, the new plastic modulus and the adopted small strain elasticity model.) The steps required to calibrate model parameters and estimate the initial values of the internal variables are presented. Finally, the basic model is validated with respect to experimental observations of reconstituted Georgia kaolin and relatively insensitive BCF clay, two relatively unstructured clays.

Chapter 5 presents the extension of the basic model presented in Chapter 4, to reproduce the effects of soil structure and its deterioration during cyclic loading. The influences of fabric anisotropy and inter-particle bonds on material plastic flow are explored based on the stress-dilatancy relation which is derived from the plastic potential of the extended model. The appropriateness of this plastic potential to describe natural clay behavior is validated with experimental evidence. Finally, this chapter shows the validation of the extended model based on experimental data of seven natural clays.

Chapter 6 presents the generalization of the proposed model from triaxial space to multiaxial space, followed by an introduction of the stress integration algorithm used in the model implementation. Then, a triaxial space constitutive driver that can integrate constitutive relations with elastoplastic modulus being dependent on strain rate, its formulation, and implementation of the proposed model into the driver are presented. Lastly, this chapter presents the implementation of the model into the finite element code Abaqus via its user-defined material subroutine (UMAT).

Chapter 7 presents the summary and conclusions of this thesis.

CHAPTER 2

TECHNICAL BACKGROUND AND LITERATURE REVIEW

2.1. Introduction

Slope failures caused by the 1964 Alaska earthquakes resulted in loss of life and substantial property damage. These landslides were initiated by foundation soil strength loss during cyclic loading and particularly the cyclic degradation of the soft, sensitive strata of the Bootlegger Cove Formation (BCF). This chapter presents a review of major landslides during the 1964 earthquake and relevant studies regarding the Bootlegger Cove Formation and its sensitive strata.

Sensitive clay is characterized by structure, and the loss of strength of sensitive clay is directly related to the deterioration of its structure. During cyclic loading, alterations of soil structure are driven by the accumulation of permanent deformation and excess pore pressure build-up. Accordingly, the experimental evidence regarding the effects of structure on the behavior of natural clay is reviewed, followed by a presentation of experimental observations of clay behavior exposed to cyclic loading and post-cyclic shearing.

The goal of this work is to formulate a constitutive model to quantify the strength degradation of natural clay during cyclic loading. Many constitutive models formulated within the bounding surface plasticity framework have been able to reproduce important characteristics of cyclically loaded clay. While not for cyclic loading, modeling strategies have been developed which can successfully capture the behavior of structured soils during monotonic loading. The review of several bounding surface models and well-proved modeling strategies to incorporate structure effects during monotonic loading is also presented in this chapter.

2.2. Landslides During the 1964 Alaska Earthquake and BCF Soil Failure

During Cyclic Loading

2.2.1. The 1964 Alaska Earthquake

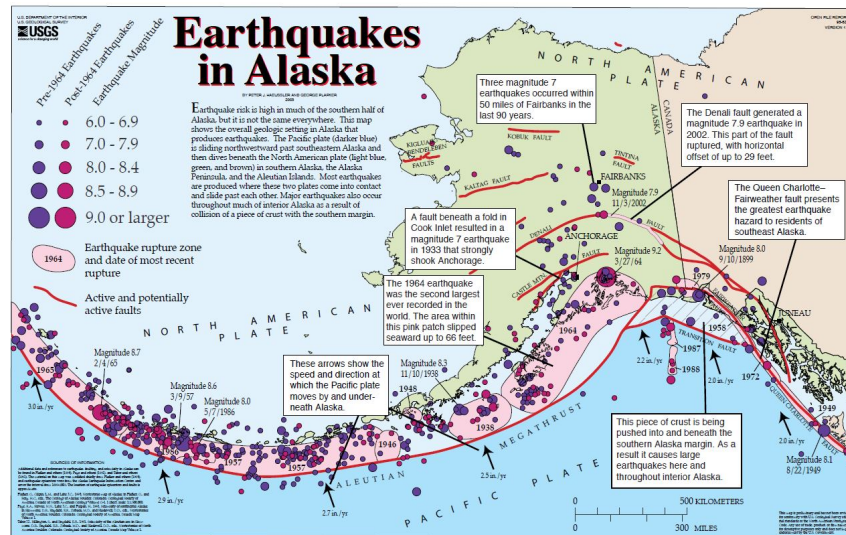


Figure 2.1. Alaska earthquakes map (Haeussler and Plafker, 2004)

South Central Alaska is one of the world's most active seismic regions. As shown in the Figure 2.1, most earthquakes were produced when the Pacific plate and the North American plate came into contact and slid past each other (Haeussler and Plafker, 2004). On March 27, 1964, a powerful earthquake struck the Prince William Sound area, whose unusual severity was characterized by its large magnitude (9.2 on the Richter scale), long duration of the intense ground motions (more than 4 minutes) and extraordinary damage area (50,000 mi²). This great earthquake and ensuing tsunamis took 131 lives and caused about 2.3 billion dollars in property loss. Based on the damages to or displacements of buildings or other structures and data from other earthquakes, the estimated peak acceleration during the 1964 earthquake was 0.18g (g is the gravity acceleration) and

the duration in which the acceleration exceeded 0.02g was estimated to be 3 minutes (Shannon & Wilson Inc., 1964).

2.2.2. Landslides During the 1964 Earthquake

The strong ground motion during the earthquake resulted in many landslides, among which five massive and disastrous landslides took place in the city of Anchorage: Turnagain Heights landslide, L Stress landslide, Four Avenue landslide, Government Hill landslide and First Avenue landslide (Shannon & Wilson Inc., 1964).

Four of these landslides aforementioned are characterized by a translatory sliding movement (Shannon & Wilson Inc., 1964), which means a relatively coherent soil wedge, which was several hundreds of meters long and wide, several tens of meters thick, moved horizontally in the direction of least resistance. Such a horizontal movement resulted in numerous cracks on the ground surface, and a trough-shaped depression zone termed a “Graben”, as shown in Figure 2.2. Since the ground surface within a graben could settle as much as 3 to 4 m, the greatest damage to structures developed within and adjacent to the grabens (Shannon & Wilson Inc., 1964). Figure 2.3 illustrates the formation mechanism of a graben zone in a translatory landslide. When a prismatic soil block starts to move horizontally, tension fractures form at the head of the slide. As the movement progresses, the fractures widen, and consequently the soil mass between fractures loses support and collapse along one or more antithetical fractures to form a graben (Hansen, 1965).

The Turnagain Heights landslide is the largest one during the 1964 earthquake, which was characterized by soil movement over a length of more than 2000 m along the coastal line and inland of 180 m at the east end and 360 m at the west end. Unlike the other

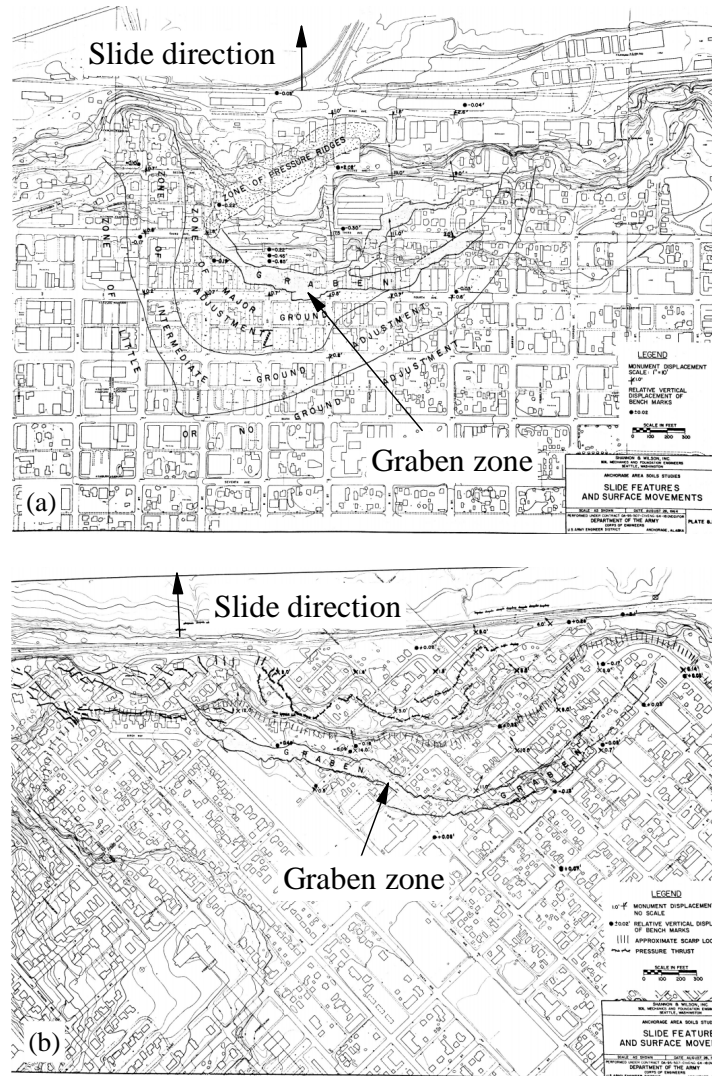


Figure 2.2. Slide features and ground movement for the Fourth Avenue landslide and L Street landslide: (a) Fourth Avenue landslide; (b) L Street landslide (Shannon & Wilson Inc., 1964)

landslides marked by a soil wedge's translatory sliding of several meters, the Turnagain Heights landslide involved a progressive series of slides that retrogressed inland of hundreds of meters. Figure 2.4 compares the aerial view of the Fourth Avenue landslide and the Turnagain Heights landslide. It can be seen that the ground at the Turnagain Heights was

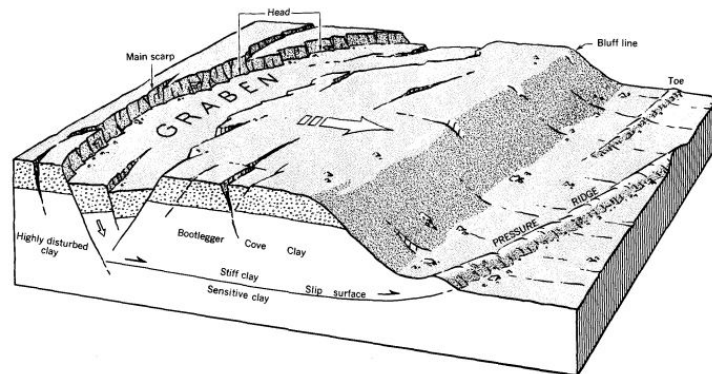


Figure 2.3. Schematic diagram of the formation of a graben in a translatory landslide (Hansen, 1965)

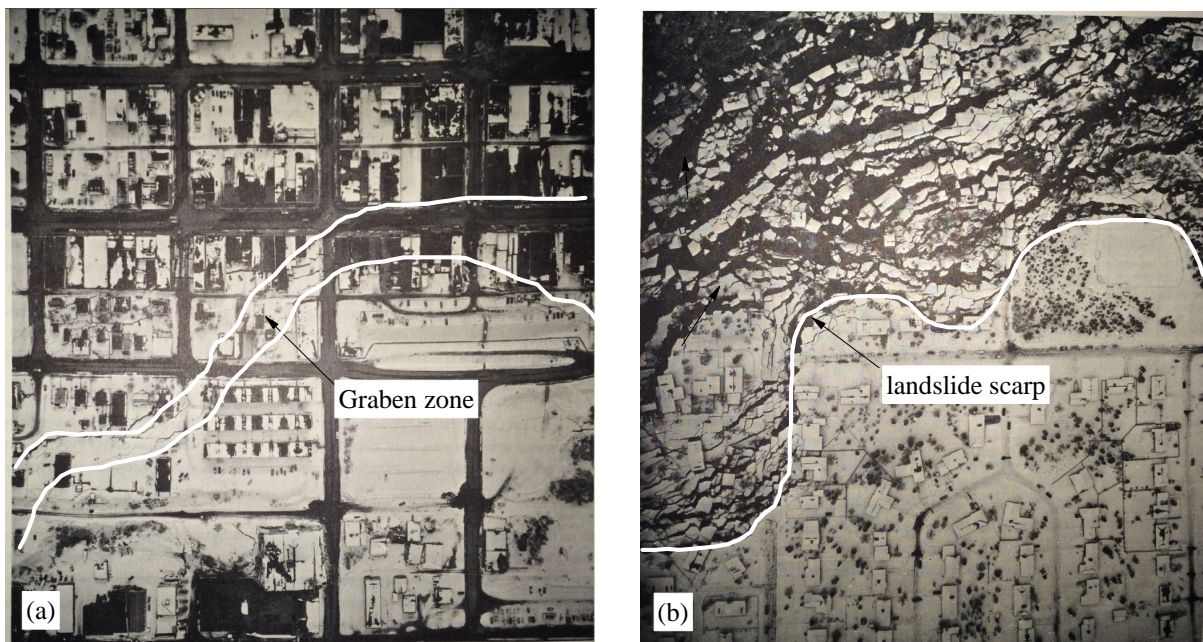


Figure 2.4. Aerial views after the 1964 earthquake: (a) Fourth Avenue landslide; (b) Turnagain Heights landslide (Shannon & Wilson Inc., 1964)

broken up into a complex system of ridges and depressed blocks, producing an extremely irregular and hummocky surface (Seed and Wilson, 1967).

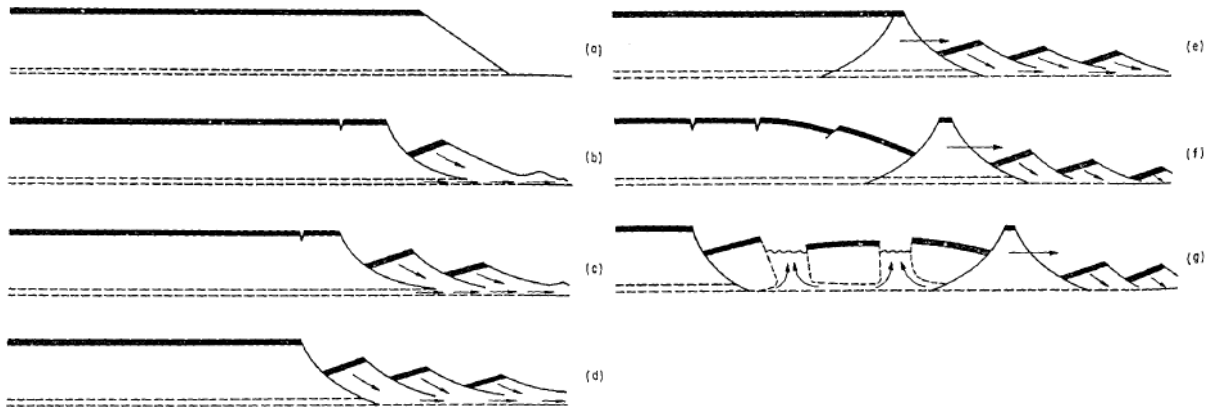


Figure 2.5. Failure mechanism observed in model tests (Seed and Wilson, 1967)

The examination of the ground configuration in the Turnagain Heights slide area revealed that the large scale inland retrogression did not result from repeated slides in the same direction, as trees and poles could be noted inclined in opposite directions (Seed and Wilson, 1967). Another characteristic feature of the Turnagain Heights landslide is that the vertical ridges within the sliding area did not change significantly from their original elevations but experienced large lateral displacement (Shannon & Wilson Inc., 1964). The model tests conducted at the University of California (Figure 2.5) illustrated that the development of the above ridges needed a weak horizontal layer located relatively deep within the slope. Moreover, these tests showed that the Turnagain Heights slide probably started from several rotational slides that initiated from the weak layer at the base of the bluff (Figure 2.5 (b), (c) and (d)). After several such slides, the weak layer was cut off by the upper stronger clay that had rotated downwards and consequently similar rotational slides developed could not continue. Beyond this point, the vertical prismatic ridge started

to move horizontally probably as a result of the dynamic inertia force or the sloping base (Figure 2.5 (e)). Following its horizontal movement, tension fractures developed behind it and a graben-type depressed zone formed in which soil mass was broken into blocks (Figure 2.5 (f) and (g)). Continued sliding of the above graben zone enabled new rotational slides behind it, following which the entire above process was repeated causing a retrogression landslide. In addition to this mechanism, Seed and Wilson (1967) concluded that the exceptional extent of inland penetration of the Turnagain Heights landslide was due to a combination of the following factors: (a) presence of sloping shoreline silt deposits that prevented the accumulation of debris to buttress the slide; (b) loss of strength in soil behind bluff line which created the a significantly weak zone; (c) sensitivity of the soft clay that resulted in a drastic loss of shear strength once the sliding was initiated and facilitated lateral displacement; and (d) long duration of the earthquake.

2.2.3. Bootlegger Cove Formation and Its Failure During the 1964 Earthquake

The Bootlegger Cove Formation (BCF) is a major geologic formation underlying much of metropolitan Anchorage and some adjacent areas. Moreover, it can be seen from Figure 2.6, the major landslides during the 1964 earthquake were located in the zone where the BCF predominantly exists.

The depositional environment of the BCF is complex (Hansen, 1965; Updike and Olsen, 1988). Previous studies showed that the BCF could be glaciolacustrine in origin (Miller and Dobrovolny, 1959), partly marine or estuarine (Schmidt, 1963; Karlstrom, 1964; Schmoll et al., 1972) or of a fresh water origin in some layers (Updike and Olsen, 1988).

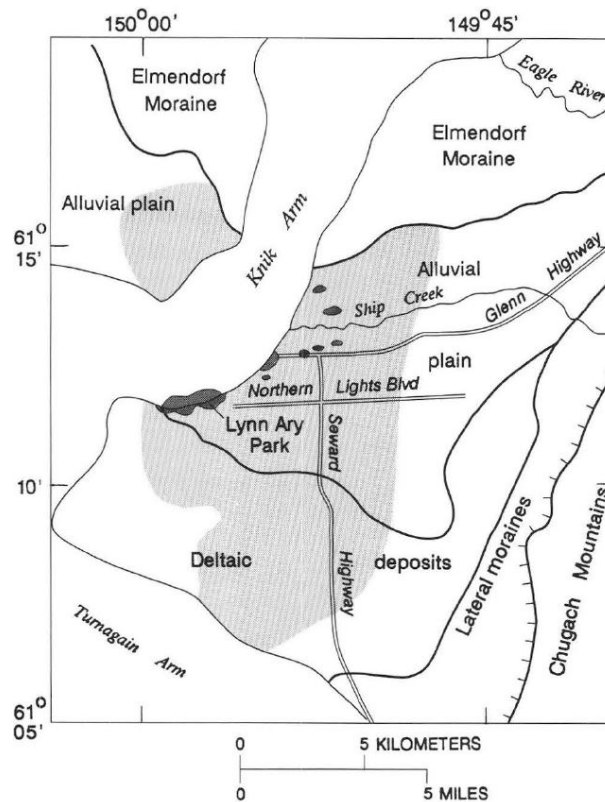


Figure 2.6. Geologic-physiographic units of the Anchorage lowland and adjacent areas. Light-shaded area indicates cohesive facies of the Bootlegger Cove Formation. Dark shade indicates the principal 1964 landslides (Updike and Olsen, 1988)

The work by USGS (Updike, 1982; Updike and Ulery, 1986; Updike and Olsen, 1988) distinguished individual geologic Facies that make up the BCF, based on both geologic and engineering properties. The seven common facies in the Anchorage area are:

Facie I: clay, with minor silt and sand

Facie II: silty clay and (or) clayey silt

Facie III: silty clay and (or) clayey silt, sensitive

Facie IV: silty clay and (or) clayey silt, with thin silt and sand lenses

Facie V: silty clay and (or) clayey silt, with random pebbles, cobbles and boulders

Facie VI: silty fine sand with silt and clay lenses

Facie VII: fine to medium sand with traces of silt and gravel

The post-earthquake investigations concluded that the major landslides at the Anchorage resulted from a drastic loss of strength in the sediments of the BCF, which was due to either the liquefaction of the silt/sand lenses or the disturbance of the sensitive clay strata (i.e., BCF Facie III) (Shannon & Wilson Inc., 1964; Hansen, 1965; Seed and Wilson, 1967). In particular, for the Turnagain Heights landslide, Seed and Wilson (1967) suggested that the liquefaction of sand/silt lenses resulted in a thin extremely weak zone that extended to a considerable distance behind the bluff line and further initiated the landslide. Once the soil started to move, the high sensitivity of the clay would lead to a further loss of strength caused by the remolding in the shear zone, which expedited the long distance movement of the soil mass. Based on a field investigation at the Lynn Ary Park that is adjacent to the Turnagain Heights landslide scarp, Updike and Olsen (1988) found the sand/silt lenses at the elevations near the failure surface of the landslide was denser and therefore less susceptible to liquefaction than that was recognized by Seed and Wilson (1967). Consequently, Updike and Olsen (1988) suggested that the sensitive strata was more critical in governing the earthquake-induced ground failure in the BCF.

2.2.4. Sensitivity of BCF Clay

The clay strength during cyclic loading and its quantification are central to the main thrust of this dissertation. Presumably such a degradation is strongly related to the sensitive nature of clay. Therefore, the measure and quantification of BCF clay sensitivity in previous studies deserve a review.

Throughout this thesis, the sensitivity, S_t is defined as the ratio of the undisturbed strength over the remolded strength (Holtz et al., 2010):

$$S_t = S_u/S_{ur} \quad (2.1)$$

where S_u and S_{ur} are the undrained shear strength measured from undisturbed and remolded clay, respectively.

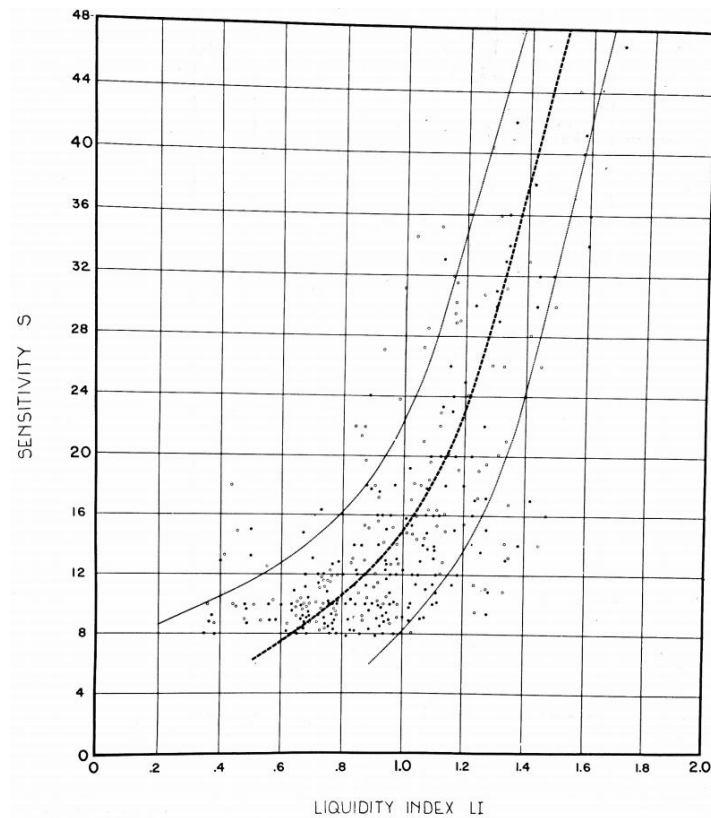


Figure 2.7. Relation between sensitivity and liquidity index for BCF specimens collected at Fourth Avenue and Turnagain Heights landslides (Shannon & Wilson Inc., 1964)

Figure 2.7 shows the relation between the sensitivity of BCF clay and the liquidity index reported by Shannon & Wilson Inc. (1964). The sensitivity was measured by the

laboratory torsional vane shear devices on undisturbed specimens collected from Fourth Avenue and Turnagain Heights landslides areas. It is worth mentioning that only data of specimens having a sensitivity greater than 8 were included in the figure. It can be seen that the maximum sensitivity of BCF clay is greater than 40, and the majority of tested samples has a sensitivity less than 20. Figure 2.7 also shows that the sensitivity correlates relatively well with the liquidity index, which is typical of sensitive clay (e.g., the Norwegian clay (Bjerrum, 1954)). Complimentary to the above figure, Shannon & Wilson Inc. (1964) reported that out of approximately 2100 tested specimens, about 14% specimens showed a sensitivity greater than 10; about 6% specimens showed a sensitivity greater than 20; about 1.9% specimens showed a sensitivity greater than 30 and 0.5% specimens showed a sensitivity greater than 40. This fact indicates that the very sensitive clay does not predominate the BCF.

In addition to the laboratory vane shear tests, field vane shear tests were performed during the post-earthquake investigation (Shannon & Wilson Inc., 1964). Among nine tested boring holes, the maximum sensitivity varied between 5 and 14. It can be noted that the sensitivity measured in the field was considerably lower than that obtained in the laboratory. Figure 2.8 shows the boring log of the borehole A121 drilled at the Fourth Avenue landslide area (Shannon & Wilson Inc., 1964). It can be seen that for clay at the same borehole, sensitivity measured by the laboratory vane (circle in Figure 2.8) is considerably higher than that measured by the field vane (square in Figure 2.8). This discrepancy may suggest that the sensitivity measured by the laboratory vane is less representative of the conditions in the field, due to inevitable sampling disturbance and stress release. On the other hand, this difference may result from the different remolding

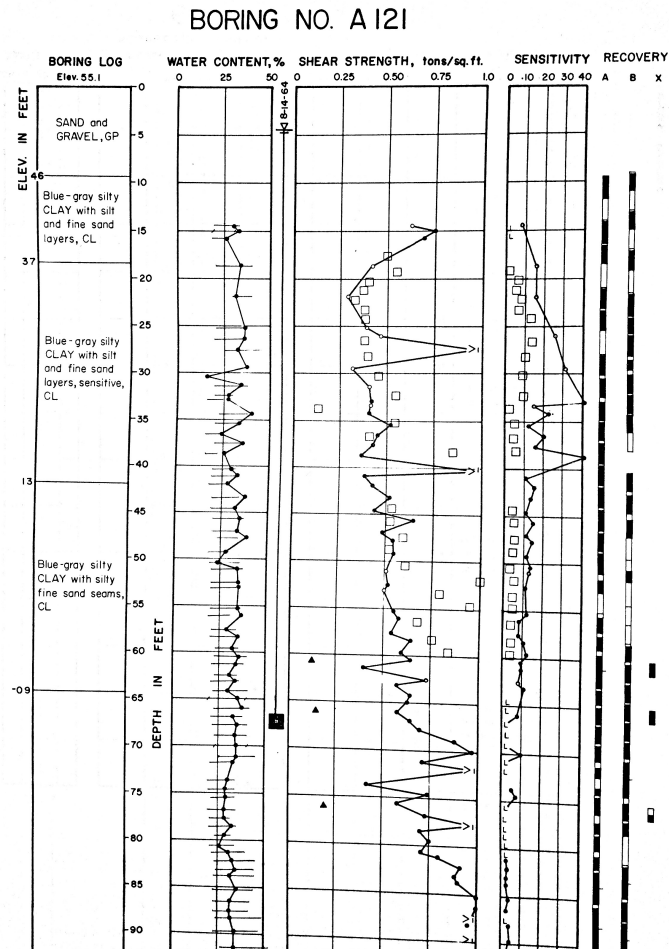


Figure 2.8. Comparison between the sensitivity measured by laboratory vane and field vane(Shannon & Wilson Inc., 1964)

degree associated with the two methods. In other words, the laboratory vane may lead to a more thoroughly remolded clay and consequently a lower remolded strength and higher sensitivity.

Figure 2.9 shows the sensitivity contours for the BCF clay reported by Mitchell et al. (1973). To determine the sensitivity, the undisturbed strength was measured by triaxial tests performed on undisturbed specimens and the remolded strength was estimated based

its correlation with the liquidity index. It can be seen that the sensitivity of tested samples varied from 1 to 12 and most of the data falls within the range between 2 to 5. Moreover, Figure 2.9 shows that in addition to the liquidity index, the sensitivity of BCF clay depends on the effective confining stress as well, i.e., the sensitivity increases under an increasing confining stress given that the liquidity index is constant.

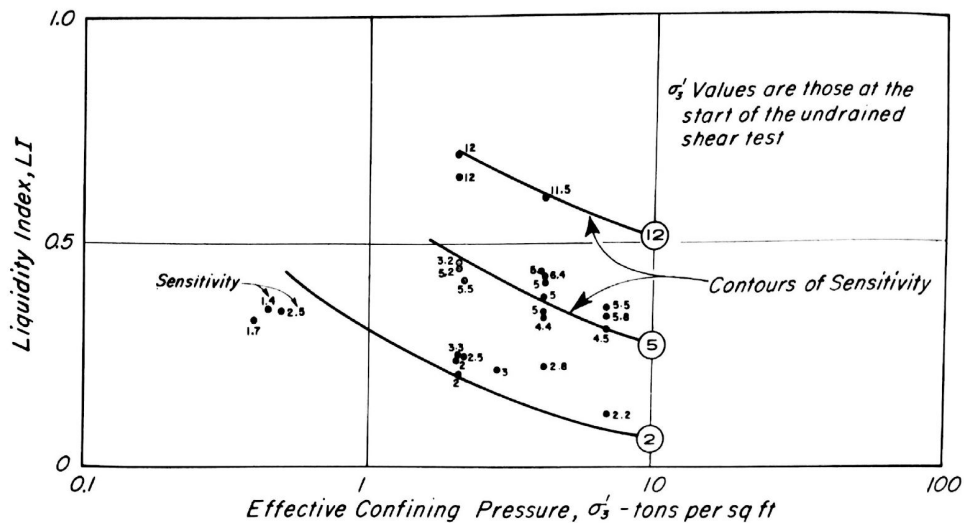


Figure 2.9. Sensitivity contours for BCF clay determined by triaxial tests (Mitchell et al., 1973)

By performing torsional vane shear tests in the laboratory, Urdike and Olsen (1988) found that the undisturbed BCF samples collected at the Lynn Ary Park showed a sensitivity varying between 2 and 7. The above facts show that there is a relatively large variation of the sensitivity of BCF clay.

2.3. Experimental Evidence: Effects of Soil Structure on Mechanical Behavior of Natural Clay

Compared with the behavior of reconstituted clay, natural clay exhibits remarkably different compressibility and shear strength characteristics, e.g., higher strength, enlarged elastic domain, the abruptness of yield, high post-yield compressibility and strain-softening and so on. These differences primarily originate from soil structure (Burland, 1990; Leroueil and Vaughan, 1990). Leroueil and Vaughan (1990) suggested that in addition to the stress history and void ratio, the structure is also a fundamental property that governs the mechanical behavior of natural soils. Following Mitchell (1993), the main components of soil structure include fabric (arrangement of soil particles) and inter-particle bonds. For natural clay, its structure can arise from various causes including aging, cementation, and salt leaching.

For most of the previous studies on natural clay, its behavior was hypothesized as a superposition of the effects of soil structure on the behavior of reconstituted clays, about which comprehensive and consistent experimental evidence have been accumulated and successful numerical modeling frameworks established (e.g., the family of Cam-Clay models.) For example, Burland (1990) introduced the concept of ‘intrinsic properties’ to describe the behavior of clay reconstituted at 1 to 1.5 times the liquid limit and used it as a reference to interpret the corresponding characteristics of natural clay. Follow the same logic, the experimental observations regarding compressibility and shearing characteristics of natural clay will be presented in this section accompanied by responses of reconstituted clays to highlight the influences of soil structure.

2.3.1. Compression Characteristics

Figure 2.10 presents the results of oedometer tests conducted on undisturbed and reconstituted Shellhaven and Gosport clay specimens in the plane of void index I_v and vertical effective stress σ'_{vc} . Following Burland (1990), the void index I_v is defined as:

$$I_v = \frac{e - e_{100}^*}{e_{100}^* - e_{1000}^*} \quad (2.2)$$

where e_{100}^* and e_{1000}^* are the void ratios corresponding to $\sigma'_{vc} = 100$ kPa and $\sigma'_{vc} = 1000$ kPa, respectively.

It can be seen that the compression curves of intact Shellhaven clay specimens lay above those of the corresponding reconstituted samples defined as the intrinsic compression line (ICL) by Burland (1990). This fact implies that natural clay can sustain a structure featuring higher void ratio than the corresponding reconstituted soil under the same stress level. Leroueil and Vaughan (1990) suggested that the difference in void ratio between natural and reconstituted clay under the same stress can be seen as an indication of the extent to which the natural soil is structured. Figure 2.10 also shows that the undisturbed Shellhaven clay samples exhibit a greater post-yield compressibility than that of the reconstituted samples, i.e., the slope of the compression curve is steeper, and this compressibility decreases at higher vertical effective stress, which results in a progressive flattening curve and its gradual convergence to the ICL.

In contrast, the compression curves of natural Gosport clay do not exhibit a high post-yield compressibility and the curves more or less coincide with those of the reconstituted clay, except the initial flatter portion due to the overconsolidated stress history.

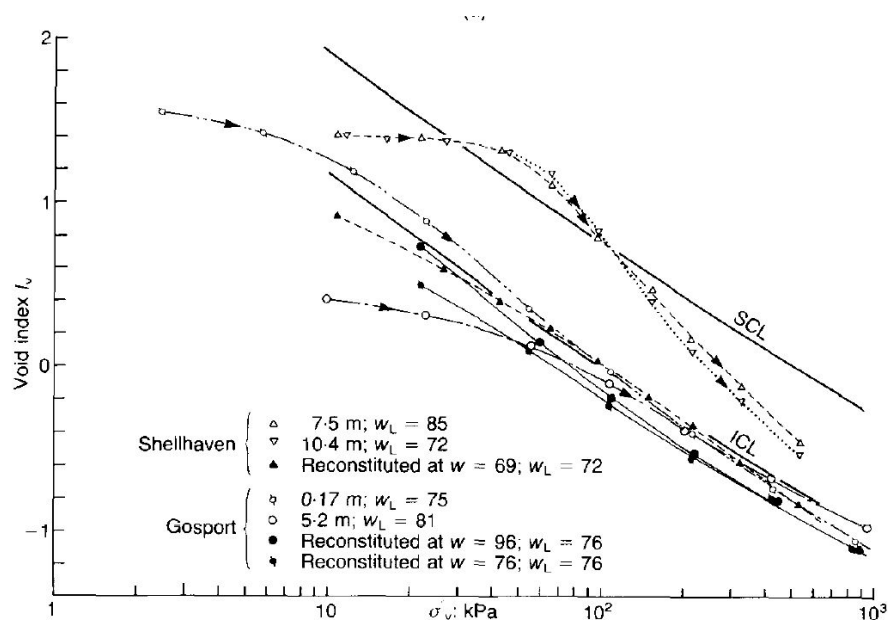


Figure 2.10. Oedometer compression curves for undisturbed and reconstituted Shellhaven and Gosport clay (Burland, 1990)

Burland (1990) suggested the above difference in compression behavior between the two natural clays mainly arises from soil deposition conditions. Slow deposition in still water can induce an open random fabric accompanied by inter-particle bonds, which can create a soil structure characterized by a high void ratio, like the Shellhaven clay. For such a material, sufficiently high external loading (e.g., incremental loads in the oedometer test) can break the bonds between soil particles and alter the fabric, which consequently creates a high post-yield compressibility and makes the soil structure progressively converge to that of reconstituted clay. Following Leroueil et al. (1979), this disruption of soil structure is termed as “destruction” in this thesis.

In contrast, rapidly deposited clays within the water of a low stillness tends to have a more oriented fabric with less inter-particle bonds, and thus a more compact soil structure with a lower void, like the Gosport clay. For such a clay, soil structure cannot be changed

significantly by external loads, since the in-situ soil fabric has already been oriented and compact. Therefore, the compression curve of undisturbed samples is close to the ICL.

The natural clays characterized by soil structure similar to the Shellhaven clay tend to exhibit brittle response and pronounced strain-softening when subjected to shearing deformation (Burland, 1990; Leroueil and Vaughan, 1990; Smith et al., 1992). Consequently, they are more vulnerable to strength loss during cyclic loading. This work has been focused on this type of natural clay.

Figure 2.11 shows the results of oedometer tests on intact and destructured natural Saint-Alban clays (Leroueil et al., 1979). To produce the destructuration, undisturbed specimens were consolidated to vertical effective stresses that are 3 to 30 kPa higher than the maximum past pressure resulting in 8% to 20% volumetric strain. It can be seen from Figure 2.11 that the preceding destructuration makes the yield stress in compression tests smaller and less well defined. Also, the pre-yield compressive stiffness of destructured samples is noticeably lower than that of the intact samples. These facts indicate that the existence of structure increases the yield stress and probably enlarges the whole elastic domain in stress space. Moreover, the degradation of soil structure can lead to a smaller pre-yield stiffness, i.e., a deterioration of soil elastic properties.

2.3.2. Shearing Characteristics

Figure 2.12 shows the results of CAU triaxial tests on clay specimens collected from Troll field, which is located in the Norwegian sector of the northern North Sea (Burland, 1990). Two consolidation strategies were employed in these tests: Recompression and SHANSEP. In the recompression, specimens were directly recompressed to their estimated in situ

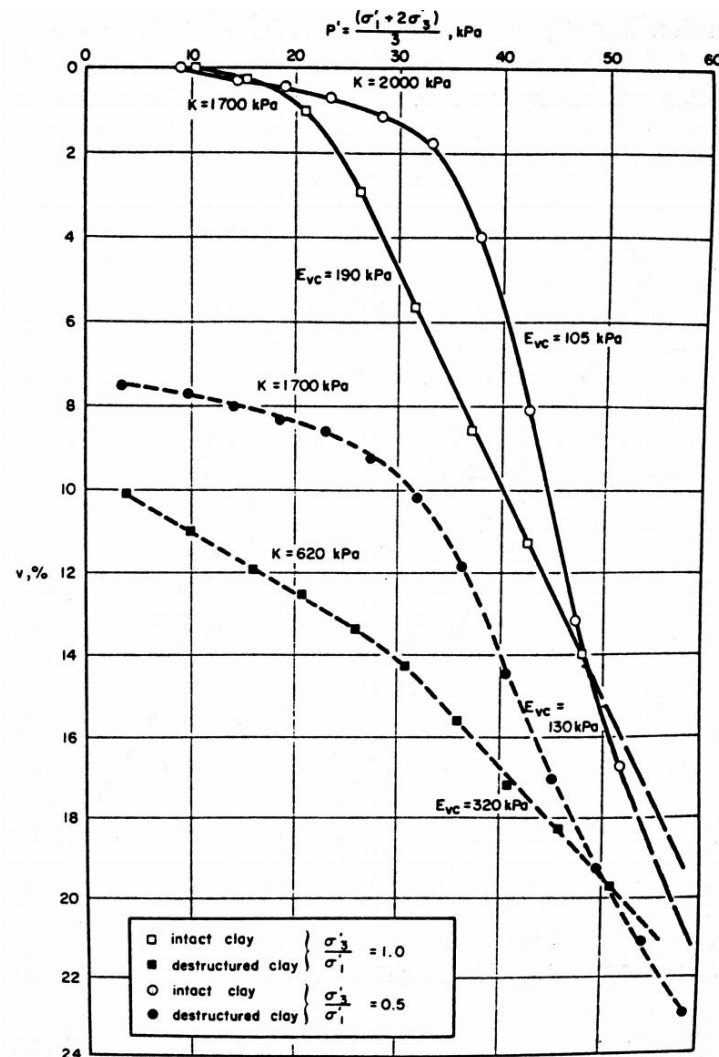


Figure 2.11. Results of consolidation tests on intact and destructured Saint-Alban clays (Leroueil et al., 1979)

effective stress state prior to undrained shearing, whereas in SHANSEP method, samples were compressed anisotropically to well beyond their in situ stress state and then unloaded a little to reproduce a lightly overconsolidated stress history.

Figure 2.13 shows the void changes associated with the above two consolidation techniques. Tests 22C used the recompression technique and a small void change was observed

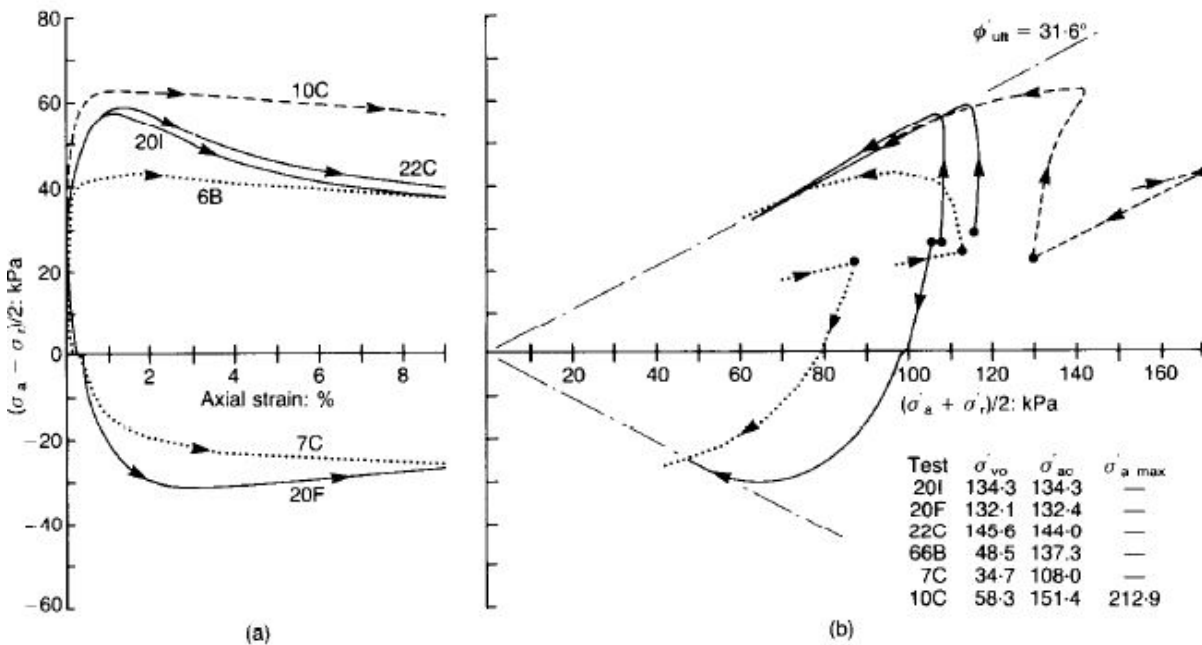


Figure 2.12. Results of CAU triaxial tests on Troll field clay specimens: (a) stress-strain response; (b) effective stress path (Burland, 1990)

when the in-situ stress was restored, which implies the soil structure is more or less intact. The SHANSEP method was used in the test 10C, and remarkable volume decreases took place during the consolidation indicating a considerable destructuration.

It can be seen from Figure 2.12(a) that the specimen in test 22C exhibits brittle behavior and strong strain-softening. The corresponding effective stress path in Figure 2.12(b) shows that the peak strength and peak stress ratio (i.e., peak mobilized friction) were reached simultaneously, after which the strain-softening and increases in excess pore pressure led the stress path to migrate towards the origin of the stress space. On the other hand, test 10C shows much less brittle stress-strain response and its effective stress path did not rise all the way to the peak stress ratio but sharply migrated to the left before reaching it, as a reconstituted soil would do (Gens, 1982; Sheahan, 1991). The above

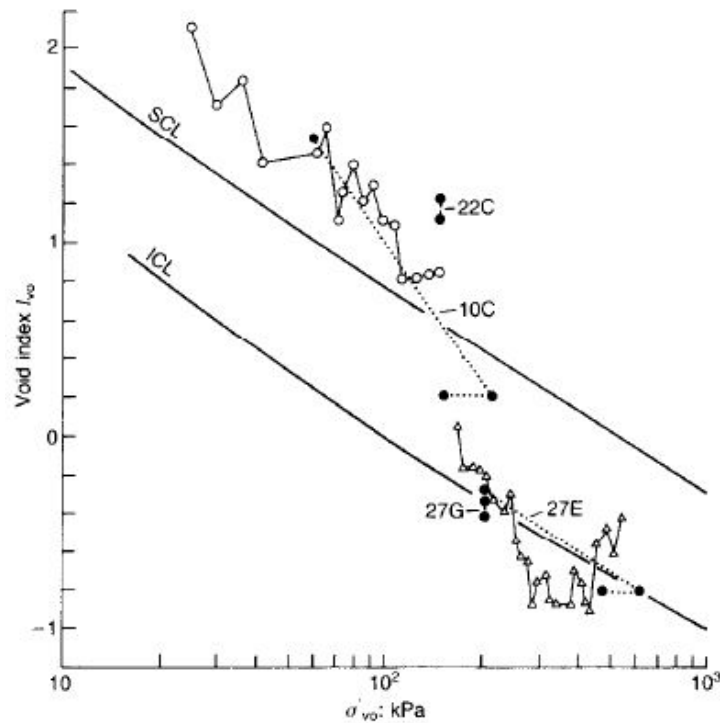


Figure 2.13. Consolidation paths of Troll field clay specimens (Burland, 1990)

distinctive behavior suggests that the existence of soil structure tends to increase material brittleness during undrained shearing. Similar to the yield stress in oedometer tests, the peak strength in undrained shearing is likely to mark the breakage of inter-particle bonds and the initiation of the destructuration. The strain-softening after the peak strength reflects the progressive loss of soil structure, as does the decreasing compressibility in compression tests. Moreover, the comparison of effective stress paths indicates that the peak mobilized friction of natural clay is governed by soil structure, as opposed to that observed in reconstituted clay or destructured clay, which is mobilized by generating a relatively large amount of strain and positive pore pressure (i.e., by mobilizing the soil's tendency to contract).

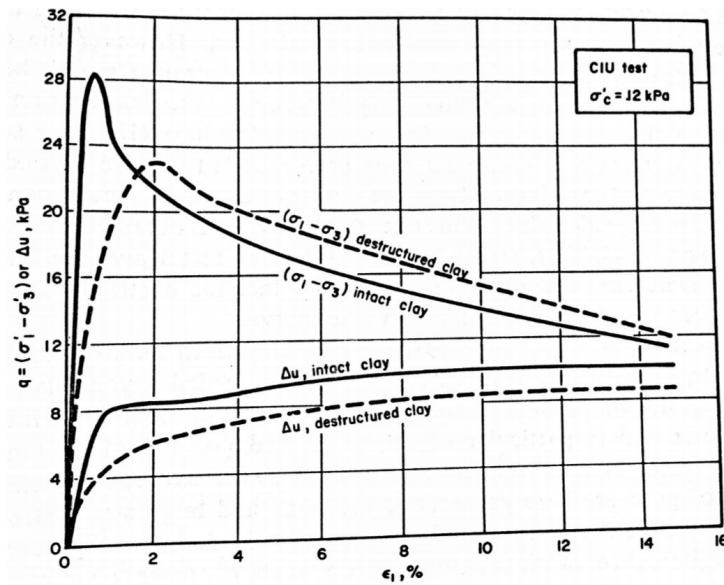


Figure 2.14. Results of CIU triaxial tests on intact and destructured natural clays (Leroueil et al., 1979)

In addition to the comparison shown in Figure 2.11, Leroueil et al. (1979) compared the behavior of intact and destructured Saint-Alban clay samples in CIU triaxial tests wherein both samples were consolidated to the same effective stress $\sigma'_v = 12$ kPa prior to shearing. It can be seen from Figure 2.14 that a higher amount of soil structure leads to higher peak strength, more brittle response and greater positive excess pore pressure. Additionally, the destructured clay reached its peak strength at a larger strain level, which implies the preceding destructuration reduced soil shear stiffness.

To illustrate the congruent effects of structure in natural soils and weak rocks, Leroueil and Vaughan (1990) compared the CID triaxial tests on Saint Vallier clays and a soft, high-porosity rock (Figure 2.15). It can be seen that as the confining stress increases, the brittle stress-strain curve becomes more ductile, which is typical of a cemented material (e.g., concrete). As shown in Figure 2.15 (a), the above distinctive behavior results from the

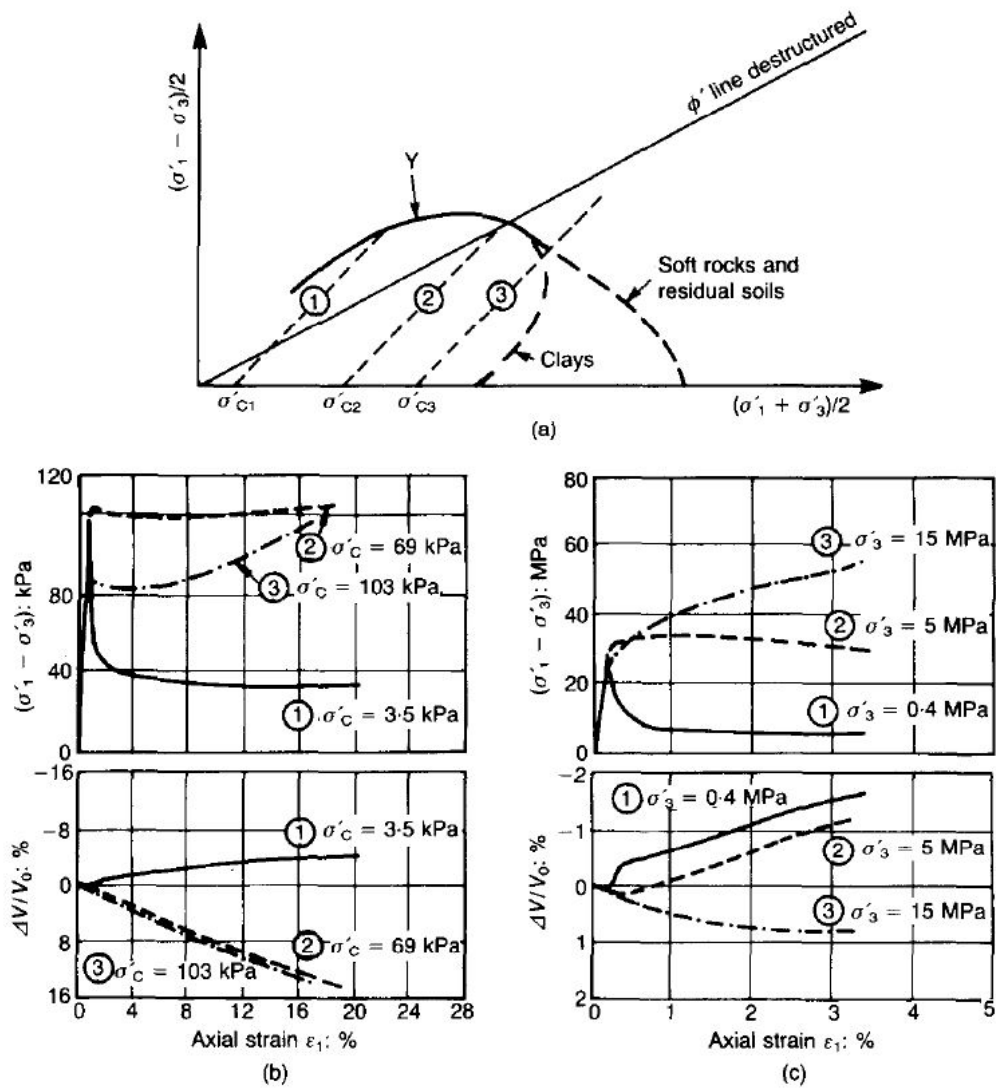


Figure 2.15. Results of CID triaxial tests on structured materials (Leroueil and Vaughan, 1990): (a) schematic stress paths; (b) stress-strain curves for Saint Vallier clay (Lefebvre, 1970); (c) stress-strain curves for a soft, high porosity, oolitic limestone (Elliott and Brown, 1985)

different locations where the stress path touched the yield envelope. When the stress path reaches the dry size of the yield surface (i.e., test ①), the material tends to dilate after yielding, which combined with the deconstruction leads to an abrupt strain-softening

after the peak strength. When the yield stress lies on the wet side (i.e., test ③), the material tends to contract and thus the consequent hardening caused by density increase compensates the destructuration-induced softening, and thereby producing a more ductile behavior. The intermediate state between the above two cases, test ② on Saint Vallier clay, reached a plateau (i.e., axial strain steadily increases at a constant deviatoric stress) followed by a considerable strain-hardening. Similar response was observed in Norrköping clay (Westerberg, 1995) and a calcarenite (Lagioia and Nova, 1995). The plateau is likely to reflect a balanced state between softening and hardening caused by destructuration and density increase, respectively.

The existence of structure can also affect the stress-dilatancy relation, i.e., the plastic flow of soil. Figure 2.16 presents CID triaxial tests on artificially bonded soils performed by Maccarini (1987). The same brittle-ductile transition can be observed as the confining stresses increase. The significant point made in this example is that for tests under relative low confining stresses, the maximum rate of dilatancy does not occur at the peak strength, which is contrary to the response of a dense sand or a heavily over-consolidated reconstituted clay. Cecconi and Viggiani (2001) observed a similar delay of maximum dilatancy rate with respect to peak strength in a weak pyroclastic rock. Leroueil and Vaughan (1990) suggested that the above observation indicates that the peak strength of structured soils is controlled by soil structure rather than its dilatancy. This conclusion is compatible with the observation shown in Figure 2.12, in which the peak mobilized friction of natural clay is also governed by the soil structure under the undrained condition.

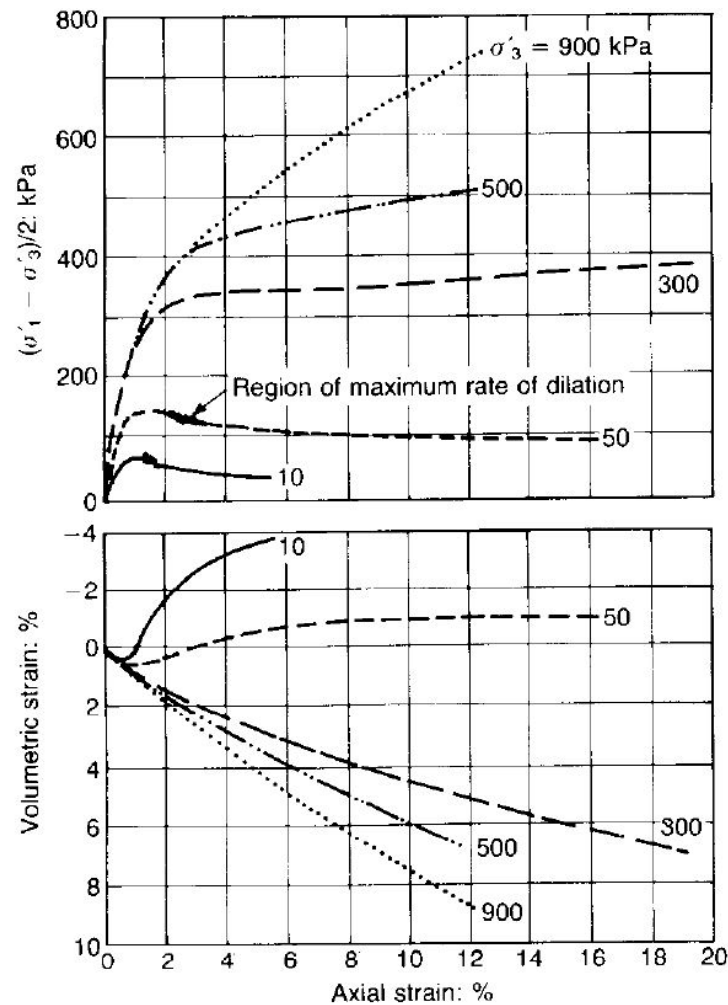


Figure 2.16. Results of CID triaxial tests on artificially bonded soil: (a) stress-strain response; (b) volume change (Maccarini, 1987)

The influence of soil structure on the strength of natural clay can be further illustrated by Figure 2.17, which shows the strength envelopes of undisturbed and reconstituted Val-lericca clay, which were determined through CIU and CID triaxial tests (Rampello et al., 1993). Note that the stress invariant data shown in this figure was after a dilatancy correction proposed by (Rowe, 1963) was applied; this correction subtracts the contribution of soil dilatancy in the shear strength to underline the strength mechanism regarding

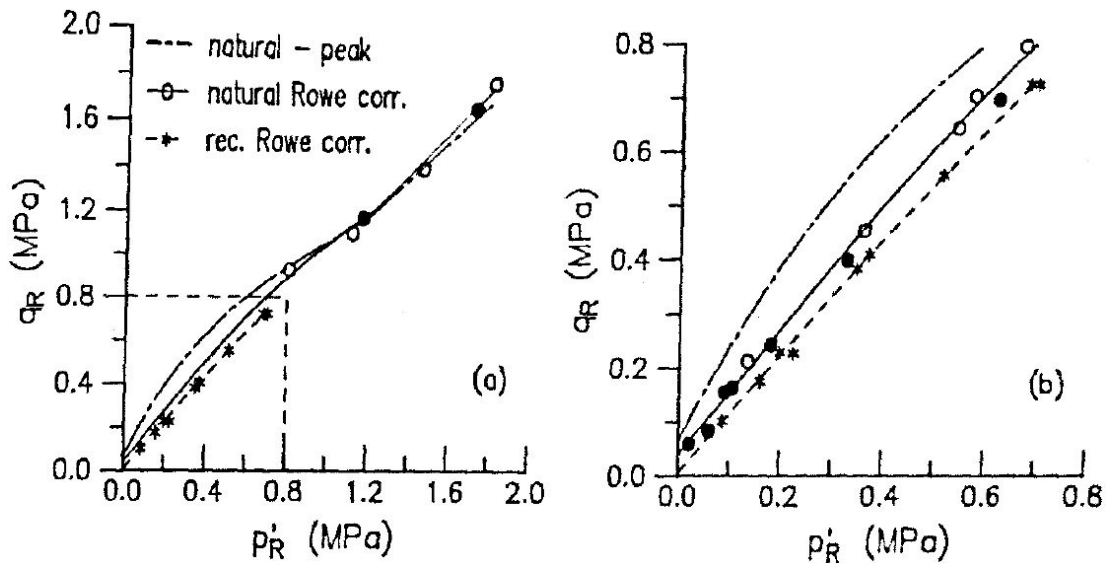


Figure 2.17. Strength envelopes of Vallericca clay corrected for the dilatancy component

friction and cohesion. It can be seen that the corrected strength data of reconstituted clays form a straight line without the intercept, which implies for reconstituted clays shear strength is primarily derived from particle friction. On the other hand, the strength envelope of natural clays is curved and has an intercept. This comparison shows that the cohesion, which possibly results from inter-particle bonds, is an important component of peak strength of natural clays. Figure 2.17 also shows that natural clays can mobilize higher stress ratio (i.e., the ratio q_R/p'_R) and thus higher friction angle than that of reconstituted clays, which confirms the previous conclusion that the peak mobilized friction of natural clay is a function of soil structure.

The aforementioned effects of structure during undrained and drained shearing partially reflect the effects of structure on the yield surface of natural clays. Figure 2.18 compares the yield envelope of intact and destructured natural clays. It can be seen that

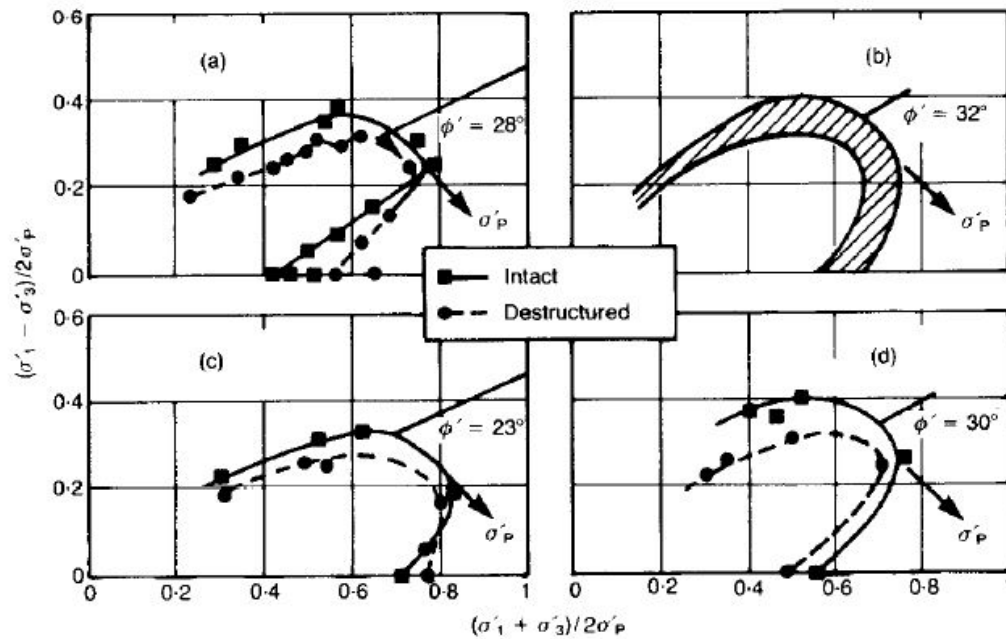


Figure 2.18. Yield curves for intact and destructured soft clays (Tavenas and Leroueil, 1985): (a) Saint-Alban; (b) Cubzac-les-Ponts; (c) Atchafalaya; (d) Bäckebo

the existence of structure induces a homologous increase of the yield curves and the yield surface of natural clay are more or less centered on the $K_{0,NC}$ line, as does the yield surface of reconstituted clay that has experienced K_0 consolidation (Parry and Nadarajah, 1973; Hight et al., 1985). These observations indicate that the plasticity anisotropy of natural clay primarily results from the anisotropic consolidation history during the initial deposition, and this anisotropy is retained when clay becomes structured, which mainly enlarges the size of the yield surface. In other words, the plasticity anisotropy is an intrinsic property of natural clay.

2.4. Experimental Evidence: Clay Behavior During Undrained Cyclic Loading and Post Cyclic Shearing

2.4.1. Cyclic Loading Characteristics

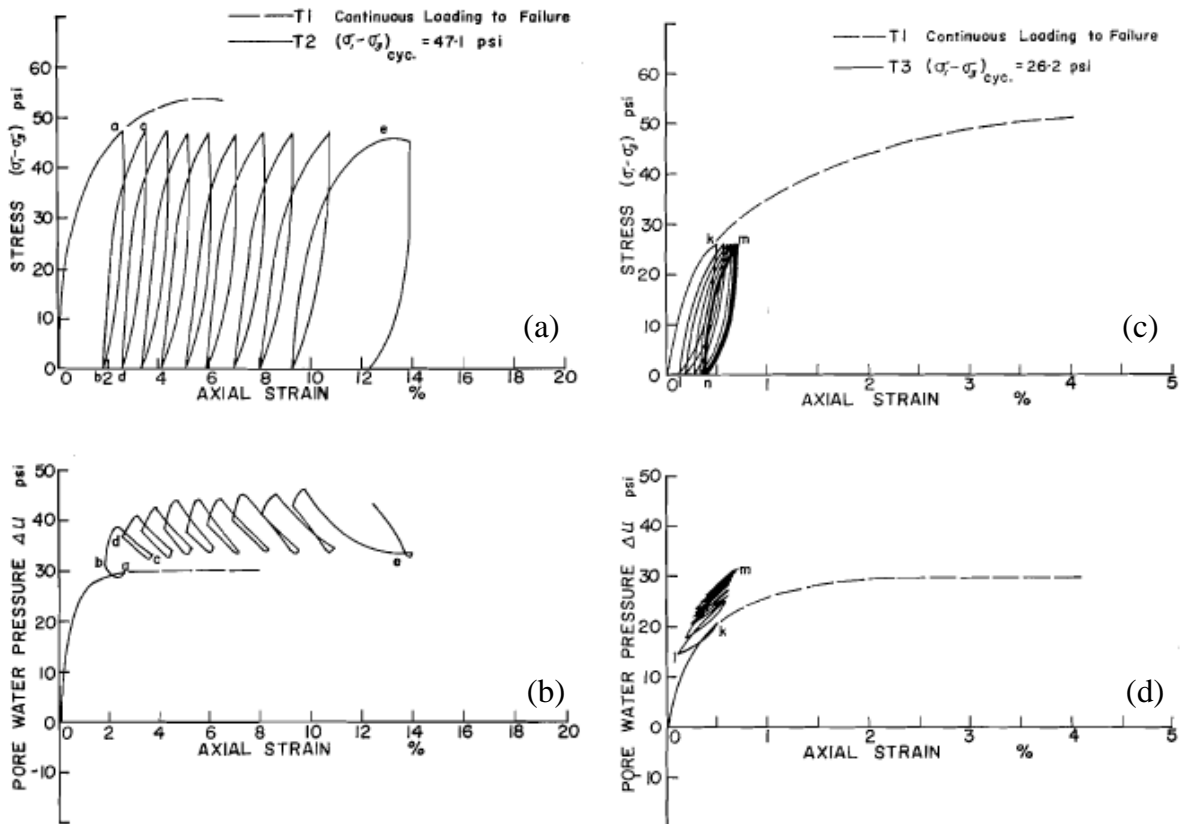


Figure 2.19. Stress-strain curves for undrained cyclic tests of high and low shear stresses (Sangrey et al., 1969)

Clay's behavior regarding strain accumulation during undrained cyclic loading can be illustrated by the "slow" cyclic triaxial tests on undisturbed Newfield clay in Figure 2.19. The term "slow" means that the tests were conducted sufficiently slow to ensure pore pressure equilibrium within soil specimen and consequently reliable measurements of pore pressure, as opposed to the more common seismic loading rates of 1Hz at which

pore pressure measurements are unreliable for clay samples (Boulanger and Idriss, 2004). For tests of the Newfield clay, an axial strain rate of about 0.0002%/min was employed. Figure 2.19 exemplifies the different soil responses during cyclic loading characterized by large and small cyclic shear stresses. It is worth mentioning that specimens in both tests had been isotropically consolidated to the same stress before shearing. It can be seen that with a large cyclic shear stress, irrecoverable axial strain kept increasing until failure was observed (point “e” in Figure 2.19(a)) and the strain accumulation rate started to increase in the last several cycles. This type of strain development is called *cyclic softening*. Figure 2.19(b) shows that the majority of excess pore pressure was generated during the first cycle. In the subsequent cycles, excess pore pressure decreased during loading and increased during unloading, which prevented a further build-up of excess pore pressure. In contrast, Figure 2.19(c) and (d) show soil can exhibit a very different behavior under a small cyclic shear stress. It can be seen that after six cycles, an equilibrium state was reached, after which additional cycles produced no further changes in either the excess pore pressure or irrecoverable strains. This type of strain accumulation is termed as *cyclic shakedown*, which is referred to the case when the generation of plastic deformation decreases with increasing loading cycles until a purely elastic response is reached.

Figure 2.20 compares the effective stress paths of the above two tests, in which the most noticeable difference is their positions relative to the failure line defined from monotonic undrained tests. It can be seen from Figure 2.20(a) that the excess pore pressure generated during the first two cycles was large enough to bring the stress state to the failure envelope, which probably resulted in the subsequent continuous accumulation of strains and cyclic failure. On the other hand, the stress path shown in Figure 2.20(b) is relatively far from

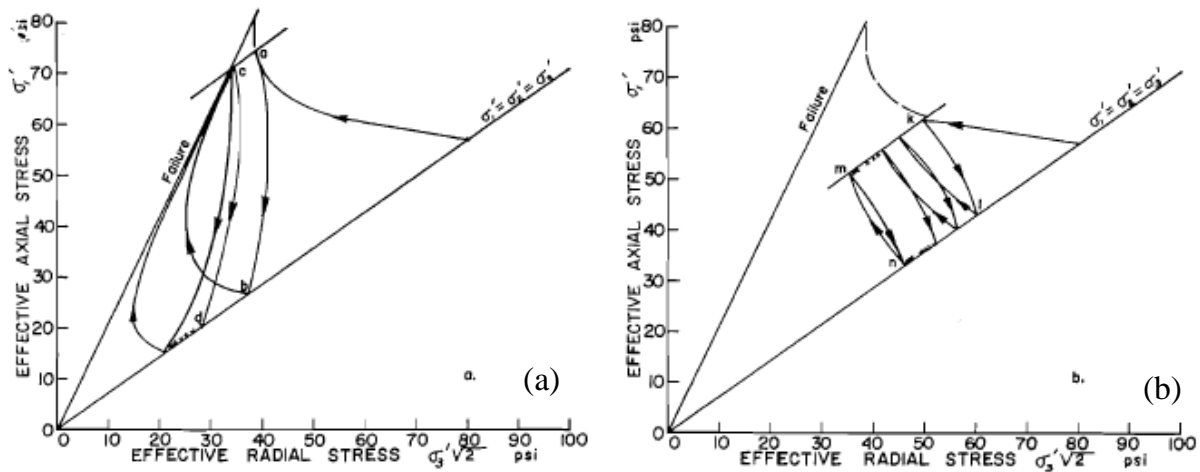


Figure 2.20. Effective stress paths for undrained cyclic tests of high and low shear stresses (Sangrey et al., 1969)

the failure line and the continuous pore pressure accumulation led to a migration of the stress state towards the origin of stress space until the equilibrium state characterized by a closed loop (i.e., loop m-n).

This equilibrium state was termed “non-failure equilibrium” by Sangrey et al. (1969) and he collected the stress points that correspond to the peak in the closed loop formed at the non-failure equilibrium state (e.g., point “m” in Figure 2.20(b)), as shown in Figure 2.21(a). It can be noted that these stress points form a straight line in stress space passing through the point representing the end of consolidation. This line was named equilibrium line by Sangrey et al. (1969). This straight line implies a linear relation between the maximum excess pore pressure and the corresponding applied cyclic shear stress, as shown in Figure 2.21(b). Moreover, Sangrey et al. (1969) suggested that the cyclic shear stress corresponding to the intercept between the failure line and the equilibrium line (i.e., point

“P” in Figure 2.21(a)) defined an upper bound for the applied cyclic stress that can result in a shakedown type of strain accumulation. In other words, any cyclic loading with cyclic shear stress above the limit will eventually lead to a cyclic failure due to excessive deformation.

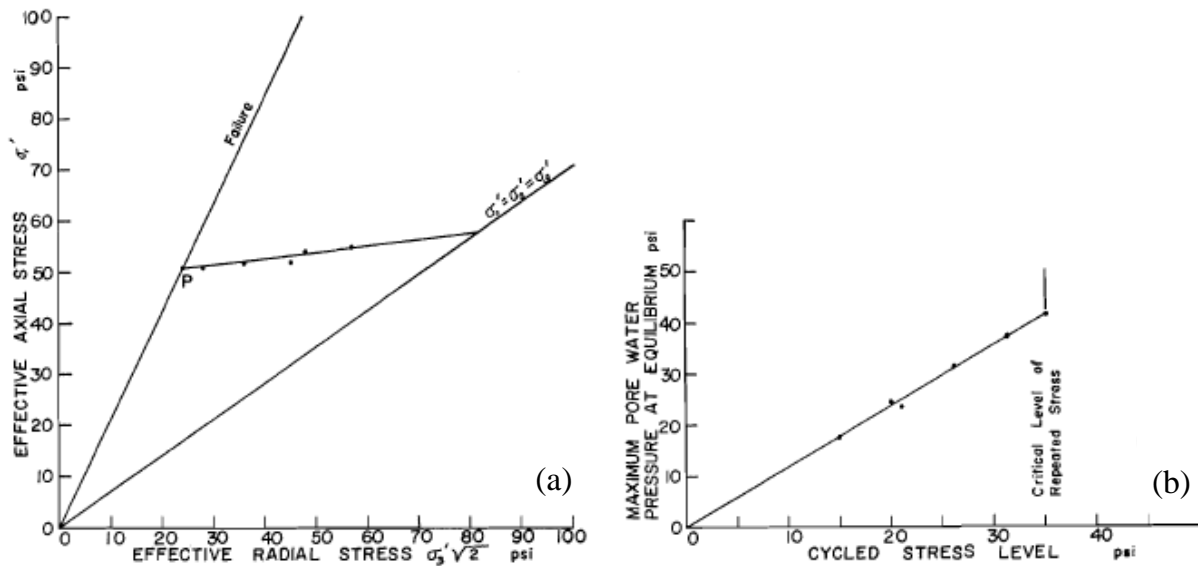


Figure 2.21. The equilibrium line and equilibrium excess pore pressure defined from cyclic loading characterized by shakedown (Sangrey et al., 1969)

The clay's cyclic shakedown and softening were also observed by Zergoun and Vaid (1994), in a series of slow undrained triaxial cyclic tests on normally consolidated Cloverdale clay. Figure 2.22 shows the observed typical stress-strain responses and effective stress path during cyclic loading. It can be seen that the undrained cyclic loading resulted in a progressive build-up of excess pore water pressure (i.e., migration of the effective stress path to the left) to some limiting level. For this particular test, the ultimate excess pore pressure ratio r_u reached 80% indicating that the sample never attained an “initial liquefaction”. Moreover, one can find the “butterfly” shape effective stress loop formed when

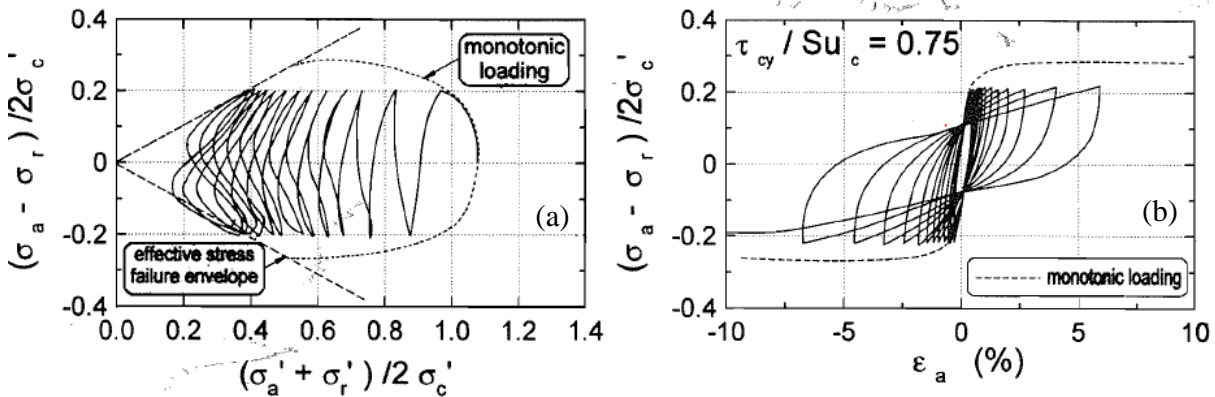


Figure 2.22. Experimental observations in an undrained cyclic loading on NC Cloverdale clay: (a) effective stress path; (b) stress-strain response (Zergoun and Vaid, 1994)

the effective stress path was close to the failure line defined from undrained monotonic loading. In Figure 2.22(b), one can see that at some time the sample developed rapidly increasing strains with each subsequent cycle and the corresponding stress-strain hysteresis loops were broader (i.e., more energy could be dissipated). This acceleration of strain development indicates the sample would fail due to excessive deformation if more loading cycles would be applied.

As shown in Figure 2.23, Zergoun and Vaid (1994) found that the rate of peak strain increase per cycle (i.e., the difference between peak strains of current and previous cycles) is directly related to the peak mobilized effective stress ratio (i.e., σ'_1/σ'_3). They also found there is an effective stress ratio threshold, beyond which the development of peak strain begins to accelerate.

Figure 2.24 shows the development of peak strain and stress ratio during cyclic loading with various cyclic shear stresses, in which τ_{cy}/Su_c is the ratio of applied cyclic shear stress

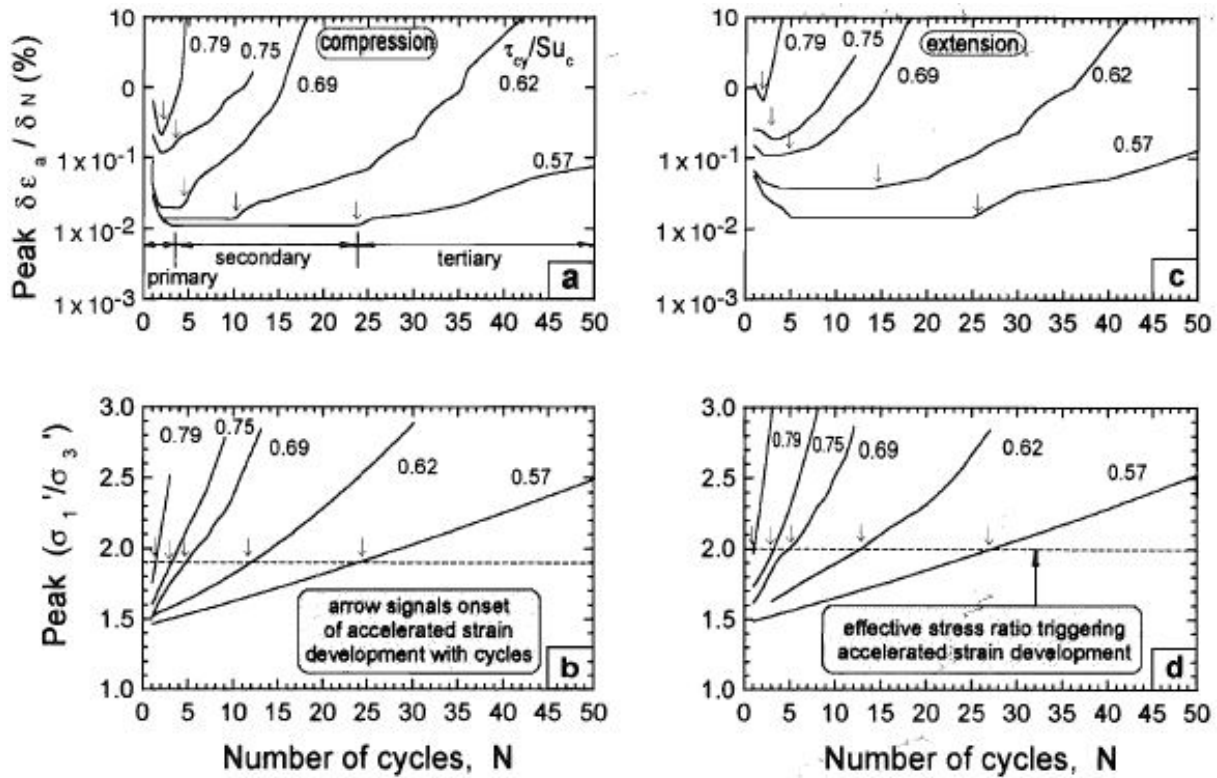


Figure 2.23. Rate of peak strain development and effective stress stability thresholds during undrained cyclic loading on isotropically consolidated NC Cloverdale clay (Zergoun and Vaid, 1994)

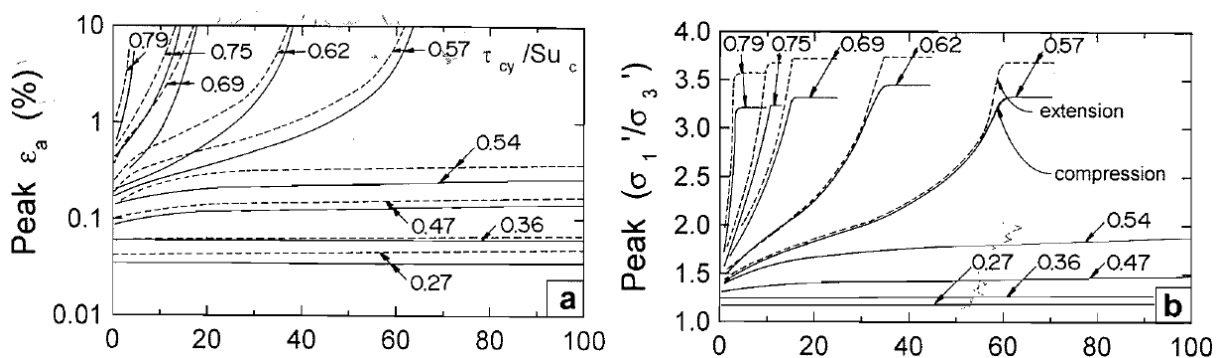


Figure 2.24. Peak strain and effective stress ratio development with cycles during undrained cyclic loading on isotropically consolidated NC Cloverdale clay (Zergoun and Vaid, 1994)

over the undrained strength defined in monotonic loading. The significant point made in this figure is that Cloverdale clay exhibits cyclic softening and shakedown under large and small cyclic stresses, respectively, as does Newfield clay. Moreover, for tests characterized by cyclic shakedown, the mobilized effective stress ratio tends to stabilize at relatively low values, whereas for tests wherein cyclic softening was observed, the mobilized effective stress ratio keeps increasing until failure.

In summary, the experimental evidence reported by Sangrey et al. (1969) and Zergoun and Vaid (1994) supports the idea that the clay behavior during cyclic loading can be interpreted from the corresponding effective stress states. Furthermore, the evidence suggests that whether clay exhibits cyclic softening or shakedown is a function of effective stress state and particularly the effective stress ratio.

2.4.2. Post-Cyclic Shearing Characteristics

In addition to the progressive accumulation of excess pore pressure and deformation, cyclic loading may result in a degradation of the static strength of clay samples from their initial values. Thiers and Seed (1968) reported the results of a series of cyclic direct simple shear (DSS) tests on San Francisco Bay mud, in which they compared the undrained shearing responses after 200 strain-controlled loading cycles to that before cyclic loading. It is worth mentioning that no drainage was allowed between cyclic loading and post-cyclic shearing. Figure 2.25 (a) and (b) show the undrained shear strength and stiffness (expressed as the ratio of the original value before cyclic loading) after cyclic loading with various strain amplitudes, respectively. It can be seen that after 200 cycles of appreciable strain amplitudes, the tested samples exhibited a relatively small amount

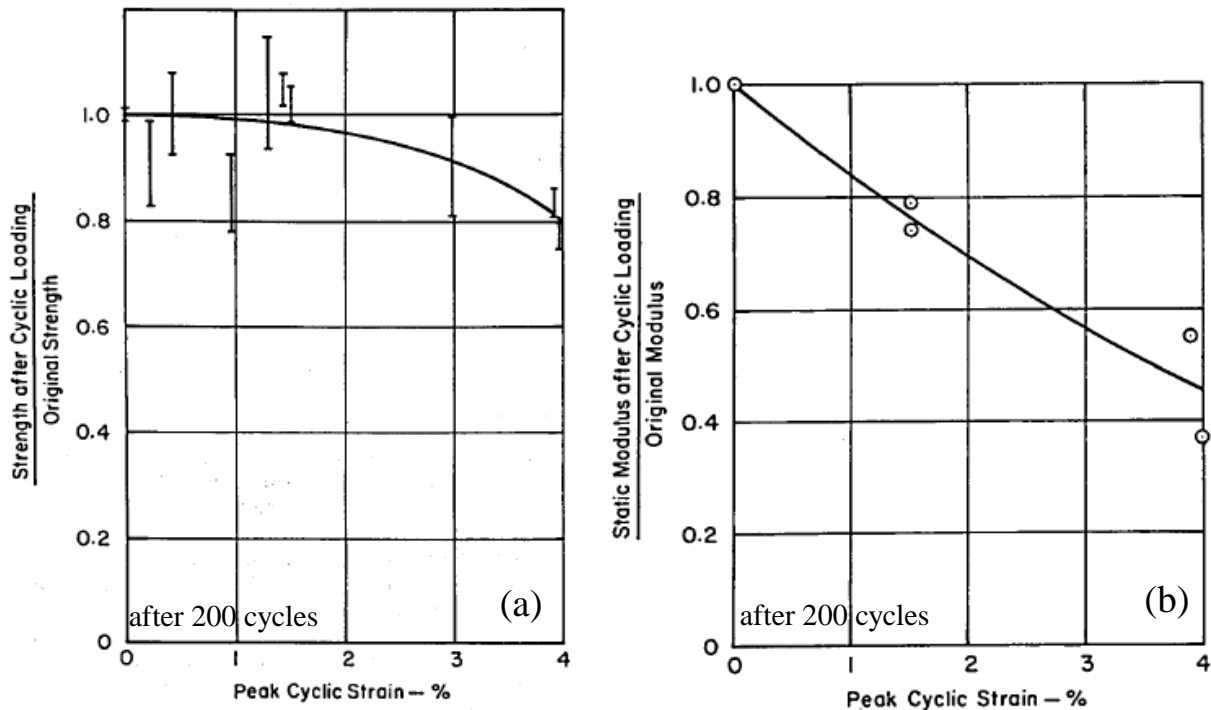


Figure 2.25. Post-cyclic shear strength and stiffness of San Francisco Bay mud after 200 strain-controlled loading cycles (Thiers and Seed, 1968)

of strength reduction. 200 cycles of 2% and 3% shear strain caused a strength reduction of only about 10%, and cyclic strains less than 1.5% had almost no effect on the peak material strength. Figure 2.25 (a) also shows the clay strength degradation is dependent on the strain levels developed during cyclic loading. In contrast to the peak strength, Figure 2.25(b) shows that cyclic loading could considerably reduce material stiffness. It can be seen that 200 cycles of 2% to 3% cyclic strain caused a reduction of 40% to 50% in the shear stiffness. Castro and Christian (1976) observed similar behavior as those reported by Thiers and Seed (1968) in a laboratory testing program on undisturbed silty clay. They found that the monotonic undrained strength after cyclic loading was close to those observed in tests without cyclic loading. Moreover, the observed limited strength

reduction is proportional to the strain levels during cyclic loading. They also found the modulus of deformation can be greatly reduced by cyclic loading. It is noteworthy that the above tested San Francisco Bay mud and silty clay have a sensitivity of 8 to 10 indicating they are not very sensitive or at least not quick clay. Castro and Christian (1976) suggested more pronounced strength degradation during cyclic loading would be observed on very sensitive clay, as the soil structure will be more susceptible to the cyclic disturbance.

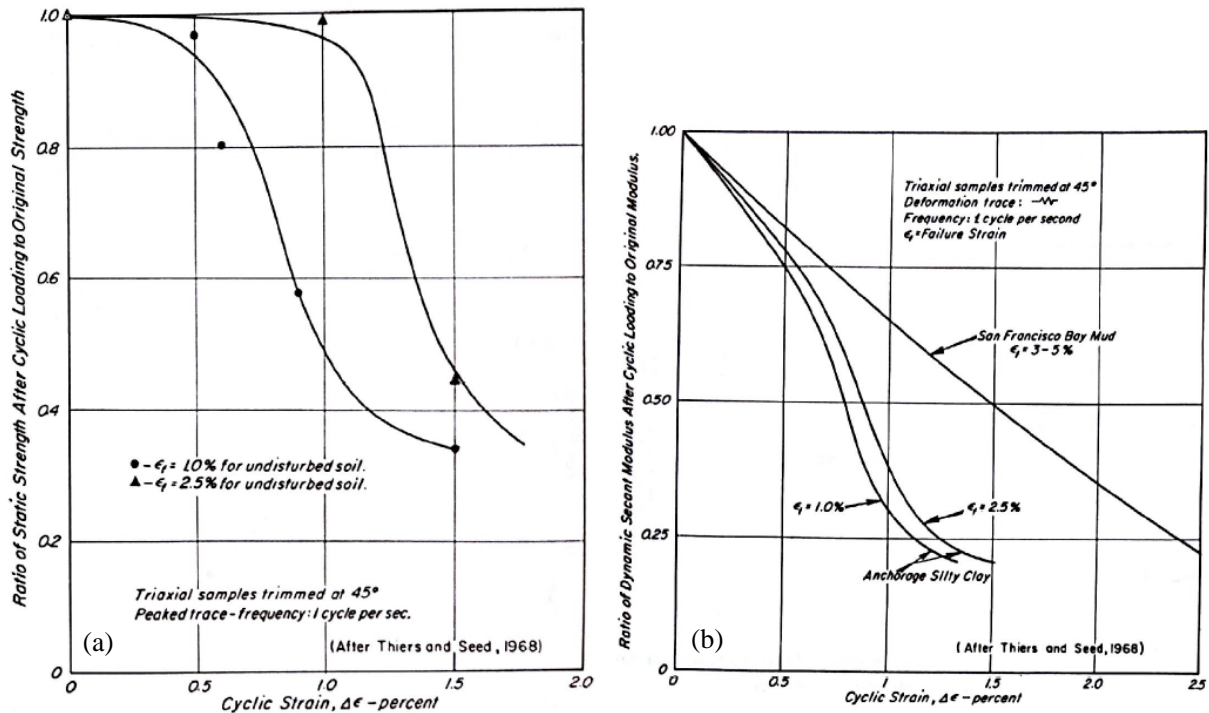


Figure 2.26. Post-cyclic shear strength and stiffness of BCF clay (Mitchell et al., 1973)

Figure 2.26 shows the post-cyclic strength and stiffness of BCF clay after subjected to strain-controlled cyclic loading. The ϵ_f in the figure is the strain at failure defined from monotonic tests. Note that BCF clay exhibits higher strength degradation than the San

Francisco Bay mud under cyclic loading of the same strain level. Such a different resistance to cyclic strength degradation presumably results from their different soil structure and sensitivity. Moreover, it can be noted that the lower the failure strain in monotonic tests, the greater is the degradation in shear strength and stiffness. As previously discussed, the more structured clay develops more brittle stress-strain during shearing, and thus the strain at failure is smaller. Therefore, the trend shown in Figure 2.26 implies that the more structured and presumably more sensitive the soil is, the more significant the cyclic strength degradation will be.

Andersen et al. (1980) reported the results of a series of cyclic DSS and cyclic triaxial tests on undisturbed Drammen clay and post-cyclic undrained shearing tests. Figure 2.27 shows the change of monotonic shear strength after strain-controlled cyclic DSS wherein the numbers indicate the number of loading cycles. It can be noted that in general shear strength decreases during cyclic loading and the reduction amount tends to increase with the increase in the applied cyclic strain levels. Moreover, the experimental data suggest that the Drammen clay's strength degradation during cyclic loading is not significant, i.e., the maximum reduction is 20% of the original value. Figure 2.28 shows the effective stress path for monotonic triaxial tests with and without previous undrained cyclic loading. It can be seen that with the increase in the residual excess pore pressure after cyclic loading, the corresponding post-cyclic effective stress path becomes close to those from monotonic tests on OC samples without cyclic loading. For instance, the upper diagram in Figure 2.28 shows that an NC sample after cyclic loading had a stress path very similar to that of a monotonic test on a sample with $OCR = 4$. Andersen et al. (1980) suggested that the cyclic pore pressure build-up and the consequent reduction of the effective stress create an

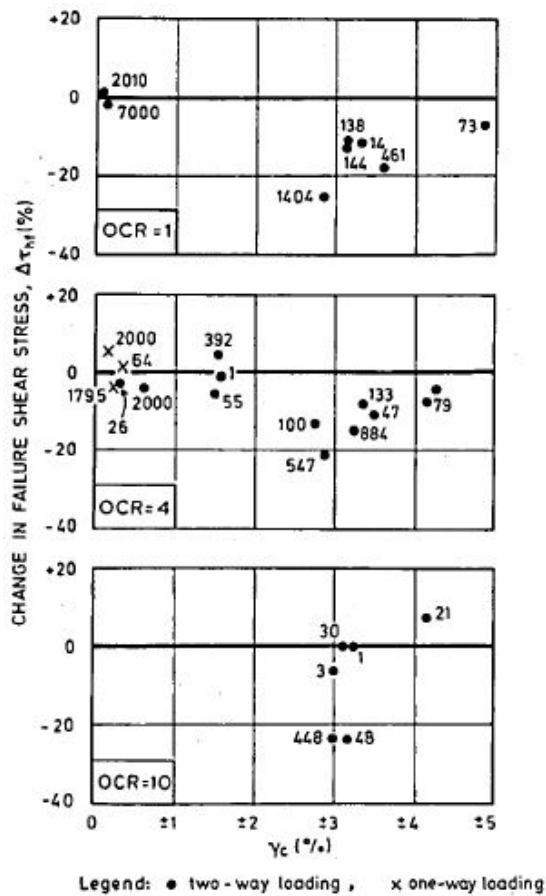


Figure 2.27. Change in undrained failure shear stress due to previous undrained strain-controlled cyclic loading in simple shear tests (Andersen et al., 1980)

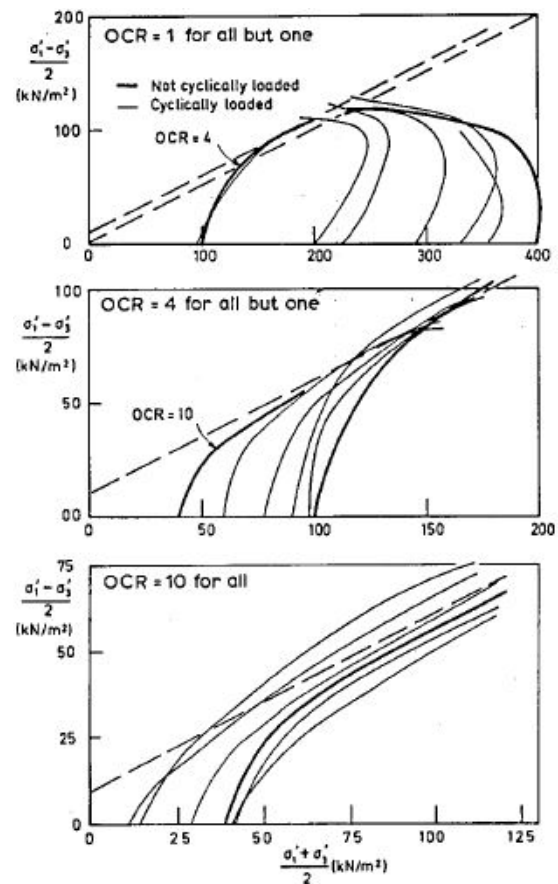


Figure 2.28. Effective stress paths for monotonic triaxial tests with and without previous undrained cyclic loading (Andersen et al., 1980)

apparent over-consolidated state, which is equivalent to that resulted from a mechanical unloading. This apparent over-consolidation caused by undrained cyclic loading were also observed in Boston blue clay (Azzouz et al., 1989) and reconstituted Ariake clay (Yasuhara et al., 1992).

The observation in Figure 2.28 also implies that in addition to the strain levels developed during the cyclic loading, the post-cyclic strength is also related to the change

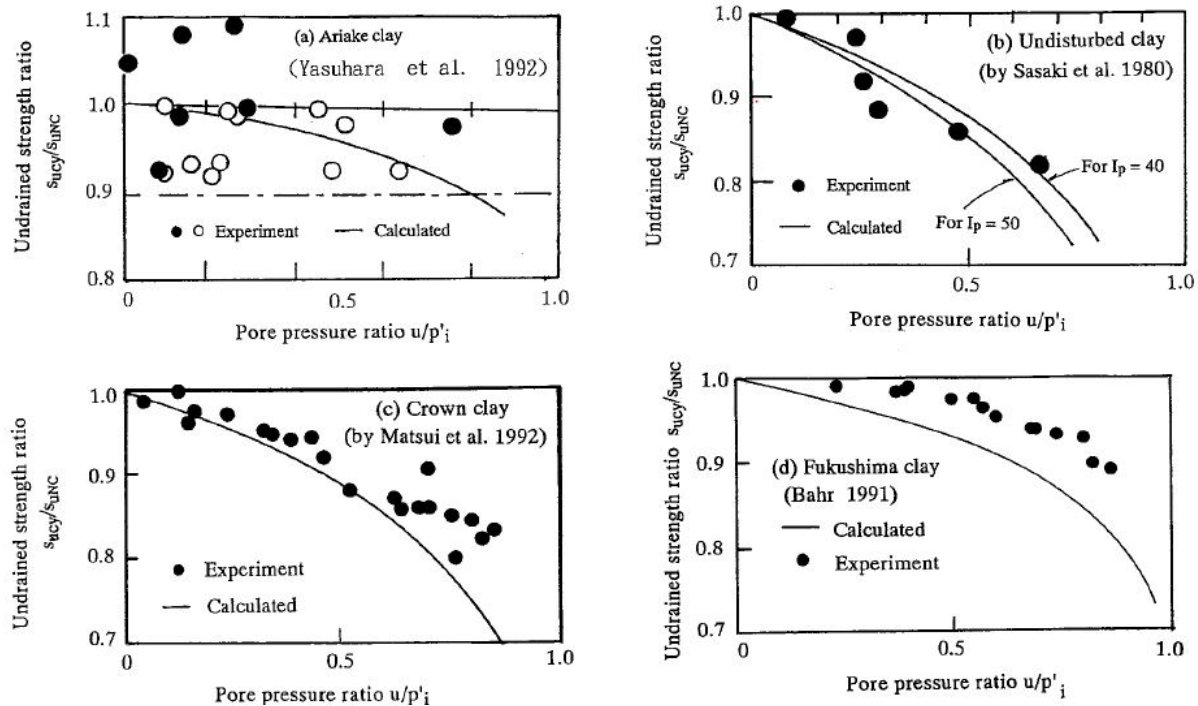


Figure 2.29. The relation between cyclic strength degradation and excess pore pressure accumulation during cyclic loading on NC clay (Yasuhara, 1994)

of soil effective stress states due to excess pore pressure build-up, which can be further illustrated in Figure 2.29. In the figure, $S_{u_{cy}}$ and $S_{u_{NC}}$ are the post-cyclic strength and strength defined from monotonic triaxial tests on NC samples. It is worth mentioning that all the tested samples had been isotropically consolidated to NC state before the cyclic loading and the variable p'_i denotes the consolidation stress. The data in Figure 2.29 show that the cyclic strength degradation increases with the accumulation of excess pore pressure during the cyclic loading that starts from NC state.

Finno and Zapata-Medina (2013) evaluated the effects of construction-induced stress changes on the dynamic properties of the BCF clay at the site of Port of Anchorage expansion projection. 3-D numerical simulations of the construction of an open-cell wharf

structure were made to compute the stress changes at various locations in the BCF soils which comprised its foundation. Laboratory procedures were developed to replicate the construction-induced stresses on natural specimens of BCF, after which specimens were subjected to 40 stress-controlled loading cycles with a cyclic stress ratio (CSR) equal to 0.2. Immediately after the cyclic loading, undrained triaxial compression and extension loadings to failure were applied to the specimens to determine the post-cyclic shear strength. As shown in Figure 2.30, Finno and Zapata-Medina (2013) compared the post-cyclic strength with free-field in situ values (i.e., neither construction-induced stress change nor cyclic loading). The peak strength was normalized by both the vertical effective stress in (a) and mean normal effective stress in (b). Both normalizations suggest that the tested BCF clay exhibits negligible strength reduction after cyclic loading, which is probably related to the relatively small amount of strain and pore pressure accumulation during cyclic loading, and the fact that the tested samples are not from the sensitive Facie III of the BCF (Finno and Zapata-Medina, 2013).

2.5. Bounding Surface Plasticity Models For Cyclically Loaded Clay

The experimental evidence presented above shows that the cyclic strength degradation of natural clay is related to the accumulation of strains and excess pore pressure during cyclic loading. Therefore, to quantify such a cyclic strength reduction through a constitutive model, it is fundamentally required that the model can provide a reliable representation of the continuing build-up of pore pressure and deformation during cyclic loading.

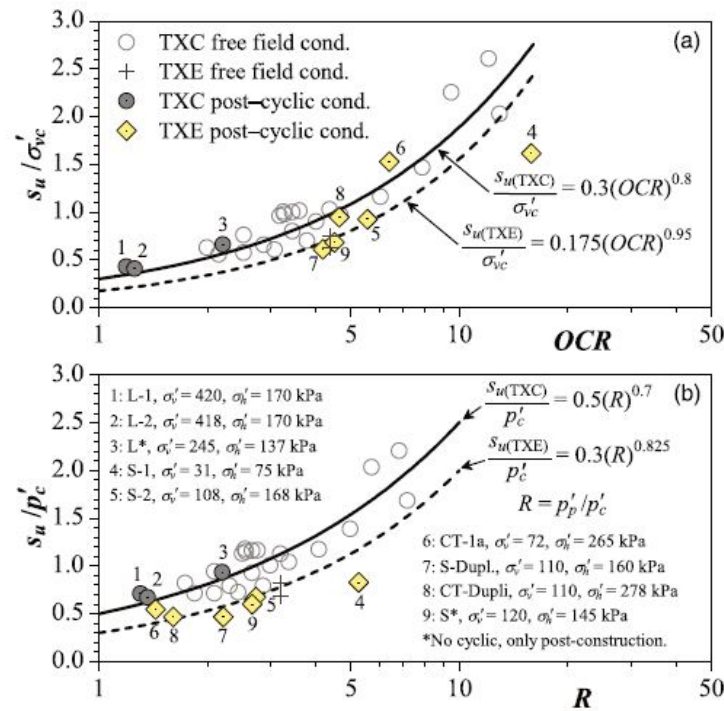


Figure 2.30. Normalized undrained shear strength: (a) with respect to σ'_{vc} ; (b) with respect to p' (Finno and Zapata-Medina, 2013)

The essential features of classical elastoplasticity models (e.g., Modified Cam-Clay model) are that the yield surface encloses an elastic domain in stress space, and any effective stress path that lies entirely within this domain cannot mobilize plastic deformation. It is clear that this type of models is deficient in modeling the cyclic behavior of clay. As an illustration, Figure 2.31 presents the response of NC clay to undrained cyclic loading according to the MCC model. It can be seen that except for the first loading branch (AB), all subsequent loading and unloading are within the yield surface and consequently neither deformation nor excess pore pressure accumulates with the increase of loading cycles (i.e., stress-strain and strain-pore pressure response retrace the path CBC in Figure 2.31(b) and (c), respectively.)

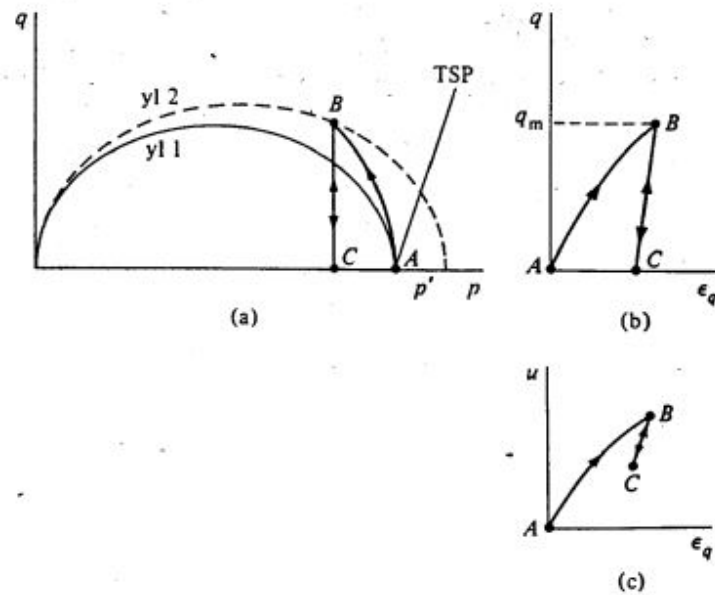


Figure 2.31. Response of NC clay to undrained cyclic loading according to conventional critical state models: (a) effective stress path; (b) stress-strain response; (c) strain-excess pore pressure response (Wood, 1990)

Motivated by the need to consider soil's inelastic behavior when the stress state is within the yield surface, the bounding surface plasticity framework was proposed (Dafalias, 1979; Dafalias and Herrmann, 1982; Dafalias, 1986b). Many constitutive models formulated within this framework have achieved encouraging success in terms of reproducing clay's accumulation of strain and pore pressure during cyclic loading (Banerjee and Yousif, 1986; Liang and Ma, 1992; Li and Meissner, 2002; Yu et al., 2007a; Seidalinov and Taiebat, 2014). In this section, the basic concepts of the bounding surface plasticity are briefly described, followed by a selective review of bounding surface constitutive models for cyclically loaded clay.

2.5.1. General Formulation of Elastoplasticity Models

To facilitate the understanding of the bounding surface plasticity, it is necessary to introduce the general elastoplasticity formulation.

In an elastoplasticity model, the material state is defined in terms of stress $\boldsymbol{\sigma}$ (bold symbol indicates tensor or vector) and a set of internal variables $\boldsymbol{\rho}$, which are the macroscopic manifestation of the material microstructure (Dafalias, 1986b). One of the most important assumptions is that strain rate can be decomposed additively into elastic and plastic parts:

$$\dot{\boldsymbol{\epsilon}} = \dot{\boldsymbol{\epsilon}}^e + \dot{\boldsymbol{\epsilon}}^p \quad (2.3)$$

where a superposed dot denotes the rate and the superscript e and p indicate the elastic and plastic parts, respectively. The stress rate is related to the elastic strain rate via:

$$\dot{\boldsymbol{\sigma}} = \mathbf{E}\dot{\boldsymbol{\epsilon}}^e \quad (2.4)$$

with elastic tangent stiffness moduli \mathbf{E} being a fourth order tensor, which can be assumed as a function of stress, and/or internal variables $\boldsymbol{\rho}$ if the elastoplastic coupling is considered (Maier and Hueckel, 1979). If a hyperelastic law is used, \mathbf{E} can be derived from an energy density function (Wood, 2003).

Suppose \mathbf{L} is the loading direction, \mathbf{R} is plastic flow direction, and \mathbf{r} is a vector indicating the direction of $\dot{\boldsymbol{\rho}}$, then the plastic strain rate, the evolution of internal variables, and the total strain rate-stress rate relation for an elastoplasticity model can be expressed

as:

$$\begin{aligned}
\dot{\boldsymbol{\varepsilon}}^p &= \langle \Lambda \rangle \mathbf{R} \\
\dot{\boldsymbol{\rho}} &= \langle \Lambda \rangle \mathbf{r} \\
\dot{\boldsymbol{\sigma}} &= \mathbf{D}^{ep} \dot{\boldsymbol{\varepsilon}} \\
\mathbf{D}^{ep} &= \mathbf{E} - \bar{h}(\Lambda) B^{-1} \mathbf{P} \otimes \mathbf{Q} \\
\mathbf{Q} &= \mathbf{E} \mathbf{L}; \quad \mathbf{P} = \mathbf{E} \mathbf{R} \\
B &= K_p + \mathbf{L} \mathbf{E} \mathbf{R} \\
\Lambda &= B^{-1} \mathbf{Q} \dot{\boldsymbol{\varepsilon}} = B^{-1} \mathbf{L} \dot{\boldsymbol{\sigma}}^{trial}
\end{aligned} \tag{2.5}$$

where \mathbf{D}^{ep} is the tangent elastoplastic stiffness tensor; symbol \otimes denotes the outer product between two tensors, i.e., $\mathbf{C} = \mathbf{A} \otimes \mathbf{B}$ leads to $C_{ijkl} = A_{ij} B_{kl}$; scalar K_p is the plastic modulus; Λ is the plastic multiplier; $\dot{\boldsymbol{\sigma}}^{trial}$ is the trial stress rate, which is obtained by freezing evolution of internal variables and assuming all strain rates are elastic (i.e., $\dot{\boldsymbol{\sigma}}^{trial} = \mathbf{E} \dot{\boldsymbol{\varepsilon}}$); Heaviside step function $\bar{h}(\Lambda) = 0$ when $\Lambda \leq 0$ and $\bar{h}(\Lambda) = 1$ when $\Lambda > 0$; and $\langle \cdot \rangle$ indicates the Macaulay Brackets, defined as $\langle \Lambda \rangle = \bar{h}(\Lambda) \Lambda$.

In summary, to obtain a stress and strain relation within the elastoplasticity framework, one needs to specify several key model components, including loading direction, plastic flow direction, plastic modulus and elasticity model.

2.5.2. Basic Concepts of Bounding Surface Plasticity

The basic concept of the bounding surface plasticity is that for a stress state within or on the bounding surface, a mapping rule uniquely relates an “image” stress on the bounding surface, and a measure of the distance between the actual and image stresses is used to

quantify the plastic modulus at the actual stress state as a function of a plastic modulus defined at the “image” stress (Dafalias, 1986b). As illustrated in Figure 2.32, symbols σ_{ij}

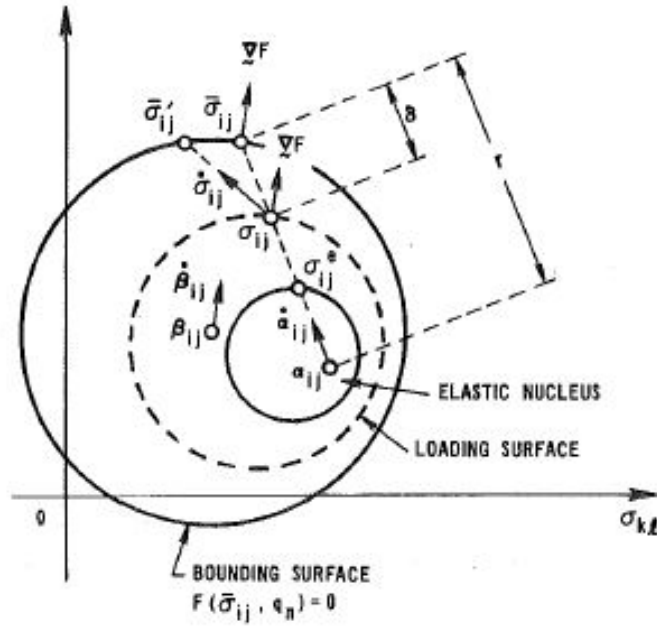


Figure 2.32. Schematic diagram of bounding surface and related concepts (Dafalias, 1986b)

and $\bar{\sigma}_{ij}$ denote the actual stress (or current stress) and the image stress, respectively. To define the image stress on the bounding surface, a proper, noninvertible mapping rule is needed, which must satisfy in a continuous way the identity condition, i.e., $\bar{\sigma}_{ij} = \sigma_{ij}$ when the current stress lies on the bounding surface (Dafalias, 1986b). The radial mapping rule proposed by Dafalias (1981) is most commonly used (Banerjee and Yousif, 1986; Liang and Ma, 1992; Li and Meissner, 2002; Yu et al., 2007a; Seidalinov and Taiebat, 2014). As shown in Figure 2.32, a projection center, α_{ij} is introduced to radially project the current stress, σ_{ij} onto the image stress, $\bar{\sigma}_{ij}$. Mathematically, $\bar{\sigma}_{ij}$ is related to σ_{ij} through:

$$\bar{\sigma}_{ij} = b(\sigma_{ij} - \alpha_{ij}) + \alpha_{ij} \quad (2.6)$$

It is commonly assumed that the loading direction \mathbf{L} at the current stress is defined as the gradient of the bounding surface, $F = 0$ passing the image stress such as:

$$\mathbf{L} = \frac{\partial F}{\partial \boldsymbol{\sigma}}; \quad L_{ij} = \frac{\partial F}{\partial \bar{\sigma}_{ij}} \quad (2.7)$$

Based on the Caratheodory's theorem, Lubliner (1975) have shown that to mobilize plasticity, the loading direction \mathbf{L} must be along the gradient of a loading surface passing the current stress, which is the surface $f = 0$ in Figure 2.32. Note that the assumption in equation 2.7 ensures that the bounding surface and loading surface cannot intersect. It is noteworthy that in classical elastoplasticity framework, the loading surface coincides with the yield surface.

The radial mapping rule together with the assumption in equation 2.7 implies that the loading surface is homologous to the bounding surface with the projection center as the center of homology. The variable b in equation 2.6 can also be interpreted as the similarity ratio of the bounding surface over the loading surface. Note that $b \geq 1$ and when $\bar{\sigma}_{ij}$ equals σ_{ij} , b equals 1, while when σ_{ij} equals α_{ij} , b equals ∞ .

The plastic modulus, K_p is related to the plastic modulus defined at the image stress, \bar{K}_p and the distance between the image stress and current stress. Dafalias (1986b) suggested that when the radial mapping rule is employed, the plastic modulus K_p can take the general form:

$$K_p = \bar{K}_p + \hat{H} \left\langle \frac{b}{b-1} - s \right\rangle^{-1} \quad (2.8)$$

which implies that as the current stress moves towards the bounding surface and consequently the variable b decreases, the K_p will monotonically decrease, and K_p equals \bar{K}_p when current stress lies on the bounding surface, i.e., $b = 1$. The modulus \bar{K}_p can be derived by enforcing $\bar{\sigma}_{ij}$ must remain on $F = 0$, i.e., the consistency condition of the bounding surface. \hat{H} is a positive shape hardening scalar function that defines the dependence of K_p on stress and other state-dependent variables in addition to the distance between the current stress and the image stress. The constant s indirectly defines an “elastic nucleus” as shown in Figure 2.32, which is also homologous to the $F = 0$ in reference to α_{ij} (Dafalias, 1986b). When σ_{ij} is inside the above nucleus, $K_p = \infty$ since the term inside the Macauley brackets (i.e., $b/(b-1) - s$) is less than zero. Consequently, a purely elastic response is computed. Note that the value of s is equal or greater than 1. When s equals 1, the elastic nucleus shrinks to the projection center (i.e., a vanishing elastic range), and as s increases, the elastic range grows towards the bounding surface. Note that the above form of plastic modulus provides a smooth transition from elastic to elastoplastic behavior.

Similar to the loading direction L_{ij} , the plastic flow direction R_{ij} is commonly defined at the image stress. Depending whether a separate plastic potential is assumed, R_{ij} either is the same as L_{ij} (i.e., the associated flow) (Liang and Ma, 1992; Li and Meissner, 2002) or is defined as the gradient of a plastic potential passing the image stress, as illustrated in Figure 2.33. The above way to define plastic flow direction will be referred as image stress flow rule in the rest of this thesis.

From the above definitions of the loading direction, plastic modulus and plastic flow direction, one can see that the plastic deformation can occur within the bounding surface

these models define the plastic modulus as a function of the plastic modulus at the image stress and the distance between the current and image stress, different interpolation rules are employed, which may significantly impact the behavior produced by the model. In the following review, particular attention is given to these specific forms of interpolation rules.

Bounding surface model proposed by Zienkiewicz et al. (1985)

Zienkiewicz et al. (1985) assumed an elliptic shape MCC yield surface as the bounding surface and the projection center was fixed at the origin of stress space. Similar to the MCC model, the bounding surface is solely controlled by an isotropic hardening internal variable. The loading direction was defined at the image stress and an associative flow rule was employed. In this model, the plastic modulus at the current stress is defined as:

$$K_p = \bar{K}_p b^\gamma \quad (2.9)$$

It can be seen that when the current stress moves towards the bounding surface, the variable K_p monotonically decreases with a power law relation of the similarity ratio b , and when the current stress reaches the bounding surface, K_p equals \bar{K}_p , because the b equals 1. To reproduce the cyclic softening, a degradation damage was introduced into the variable γ as:

$$\gamma = \gamma_0 \exp(-D\bar{\varepsilon}^p) \quad (2.10)$$

where γ_0 and D are model parameters, and $\bar{\varepsilon}^p$ is the accumulated plastic deviatoric strain defined as

$$\bar{\varepsilon}^p = \int \left(\frac{2}{3} d\varepsilon_{ij}^p d\varepsilon_{ij}^p \right)^{1/2} \quad (2.11)$$

and

$$d\bar{\varepsilon}_{ij}^p = d\varepsilon_{ij}^p - \delta_{ij}d\varepsilon_v^p \quad (2.12)$$

where $\bar{\varepsilon}_{ij}^p$ and ε_v^p are the plastic deviatoric and volumetric strains, respectively and δ_{ij} is the Kronecker delta. It can be seen that with the accumulation of plastic deviatoric strains, the plastic modulus will decrease as a result of a decreasing γ . Therefore, the soil stiffness will gradually reduce and the cyclic softening can be reproduced.

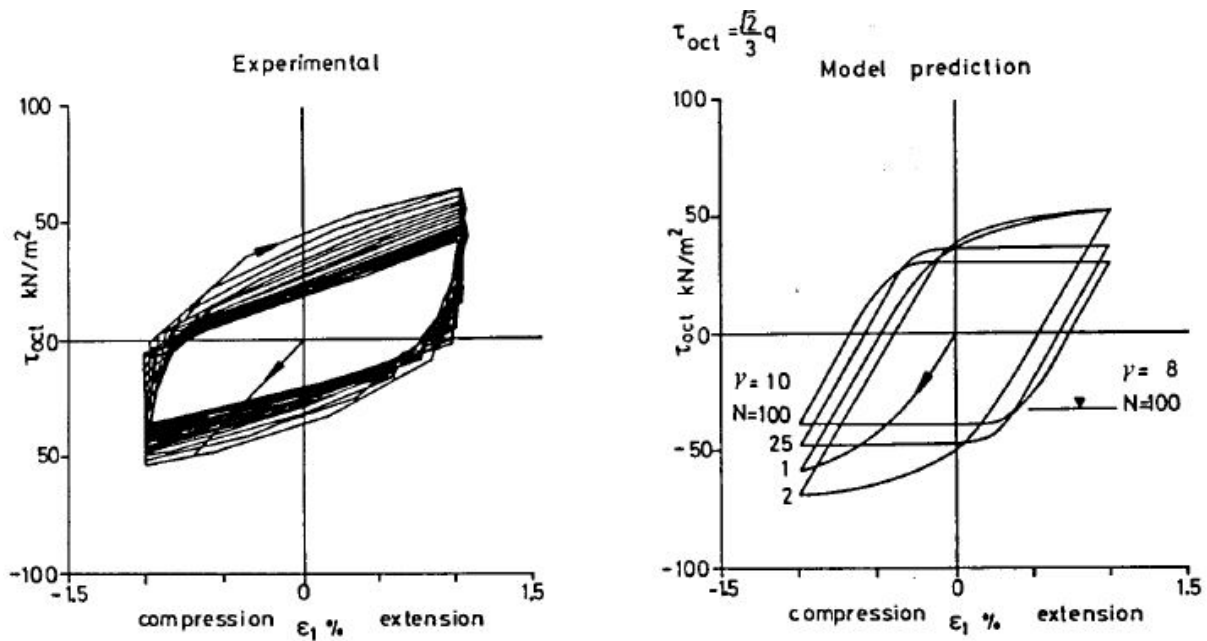


Figure 2.34. Comparison of model prediction with test of two-way, strain controlled, undrained cyclic triaxial test on Kaolin (Zienkiewicz et al., 1985)

Figure 2.34 presents a comparison between experimentally observed stress-strain responses and the corresponding model simulation. It can be seen that the model successfully reproduces the general trend observed from the experiment. However, the simulated stress-strain hysteresis loop is broader than that observed, and consequently, the energy dissipated during each cycle is overestimated (i.e., over-damping). As shown in Figure

2.34, the above over-damping results from the difference between the observed and computed stiffness degradation rate during unloading and reloading. In the experiment, the shear stiffness started to decrease at a very early stage of the unloading/reloading, whereas the simulated shear stiffness reduction occurred considerably later and was more abrupt.

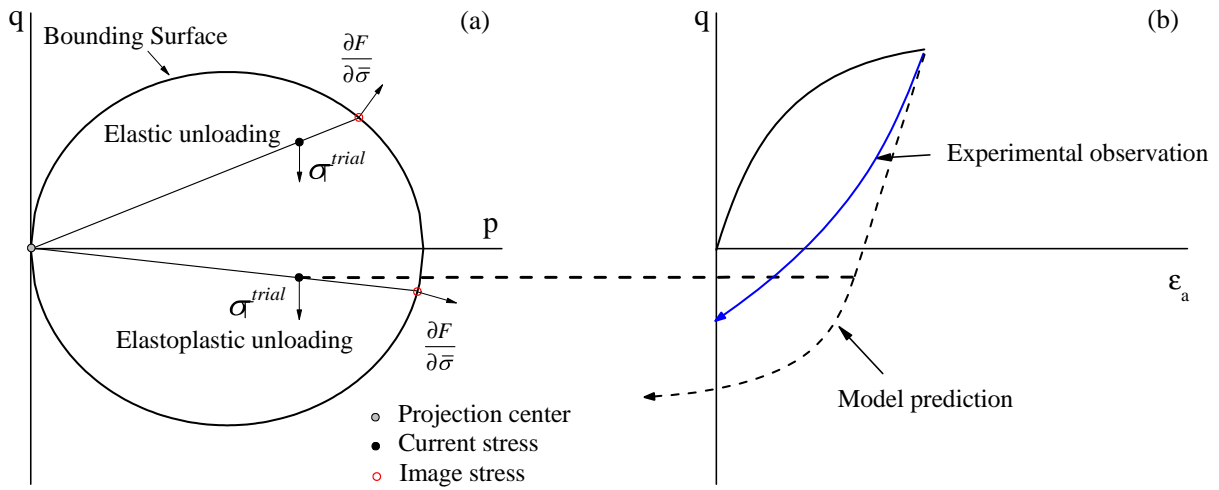


Figure 2.35. Schematic diagram of over-damping caused by the fixed projection center

As illustrated in Figure 2.35, the aforementioned discrepancy is caused by the employment of a fixed projection center. During the initial stage of the unloading, the inner product between the trial stress rate and the loading direction is non-positive (i.e., $L_{ij}\dot{\sigma}_{ij}^{trial} \leq 0$), which, by definition, only generates elastic deformation (i.e., the elastic unloading in Figure 2.35(a)) until the above product regains a positive value. The same situation will repeat in the reloading as well. Such a delay of generating plastic deformation leads to a slower stiffness deterioration and consequently the over-damping. Figure 2.36 shows the computed effective stress path corresponding to the simulation in Figure

2.36, wherein one can find that during unloading and reloading, the effective stress path is vertical until the stress state is close to the bounding surface indicating the computed predominance of the elastic behavior during the unloading and reloading. It is worth mentioning that the above over-damping is a common issue when the projection center is either fixed at the origin of the stress space or the rotation axis of the bounding surface with a constant ratio defining its position relative to the bounding surface (e.g., models proposed by Liang and Ma (1992) and Jiang et al. (2012))

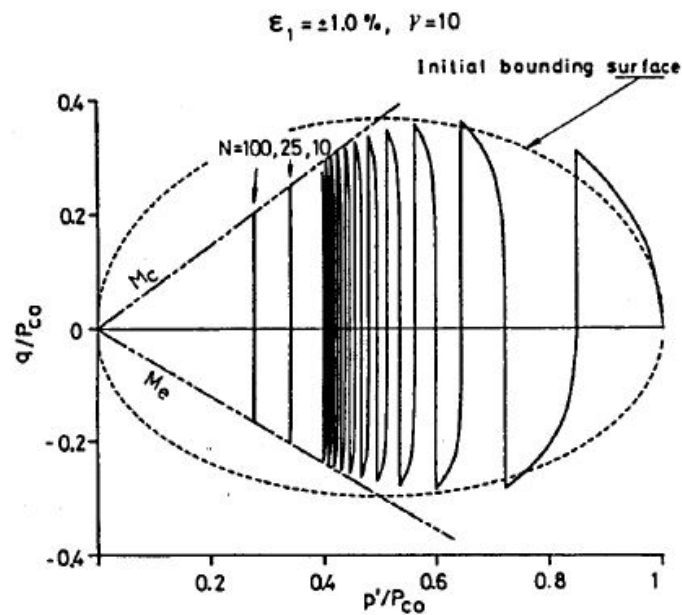


Figure 2.36. Computed effective stress path in a test of two-way, strain controlled, undrained cyclic triaxial test on Kaolin (Zienkiewicz et al., 1985)

Anisotropic bounding surface model proposed by Liang and Ma (1992)

Liang and Ma (1992) employed a bounding surface consisting of two ellipsoids and one sinusoid segments, similar to the model proposed by Anandarajah and Dafalias (1986). A rotation hardening law, a distortional hardening law and an isotropic hardening law were introduced to govern the change of inclination, slenderness and size of the bounding surface upon plastic loading, respectively. The projection center is fixed on the rotation axis with a constant distance ratio. An associative flow rule was employed to define the plastic flow direction. The plastic modulus K_p takes the following form:

$$K_p = \bar{K}_p + \hat{H}[(b)^\mu - 1] \quad (2.13)$$

where the power law variable μ is related to the accumulated plastic deviatoric strain through a constant D :

$$\mu = \mu_0 \exp(-DE) \quad (2.14)$$

where

$$E = \int (\bar{\varepsilon}_{ij}^p \bar{\varepsilon}_{ij}^p)^{1/2} \quad (2.15)$$

Similar to Zienkiewicz et al. (1985)'s model, as the accumulation of plastic deviatoric strain, the cyclic softening is simulated.

Two surface model proposed by Li and Meissner (2002)

Li and Meissner (2002) proposed a two surface model to reproduce the cyclic behavior of clay. As illustrated in Figure 2.37, the outer surface is the bounding surface, and the inner surface is the loading surface that has the same shape as the bounding surface and always passes through the current stress. Both the loading direction and the plastic flow

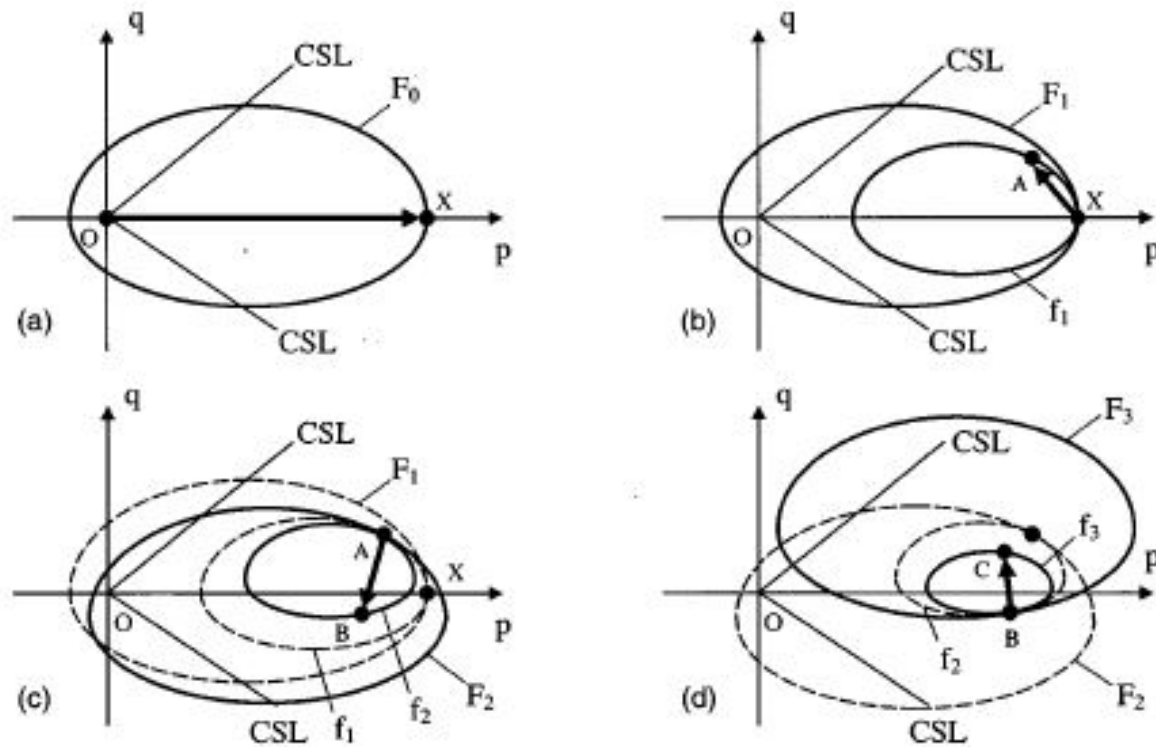


Figure 2.37. Schematic diagram of the formation and movement of the bounding surface and loading surface (Li and Meissner, 2002)

direction are defined as the gradient of the loading surface at the current stress. As a novelty of this model, a memory center (e.g., point A and point B in the Figure 2.37 (c) and (d), respectively) is employed to remember the most recent stress history. It is postulated that upon stress reversal, the current stress is defined as the memory center, the old bounding surface and loading surface developed in the previous loading event are erased, and the new bounding and loading surface are defined and are assumed to pass the new memory center. Between two subsequent stress reversals, the current stress remains on the loading surface, and the loading surface and the bounding surface are tangent to each other at the memory center. By drawing an analogy to the aforementioned radial mapping rule, it can be seen that the memory center serves as the projection center,

and the loading and bounding surfaces are homologous to each other with the memory center being the center of homology. Compared with the previously discussed models that have a fixed projection center, the employment of such a memory center enables plastic deformation to occur at the early stage of unloading and reloading and thus addresses the over-damping issue.

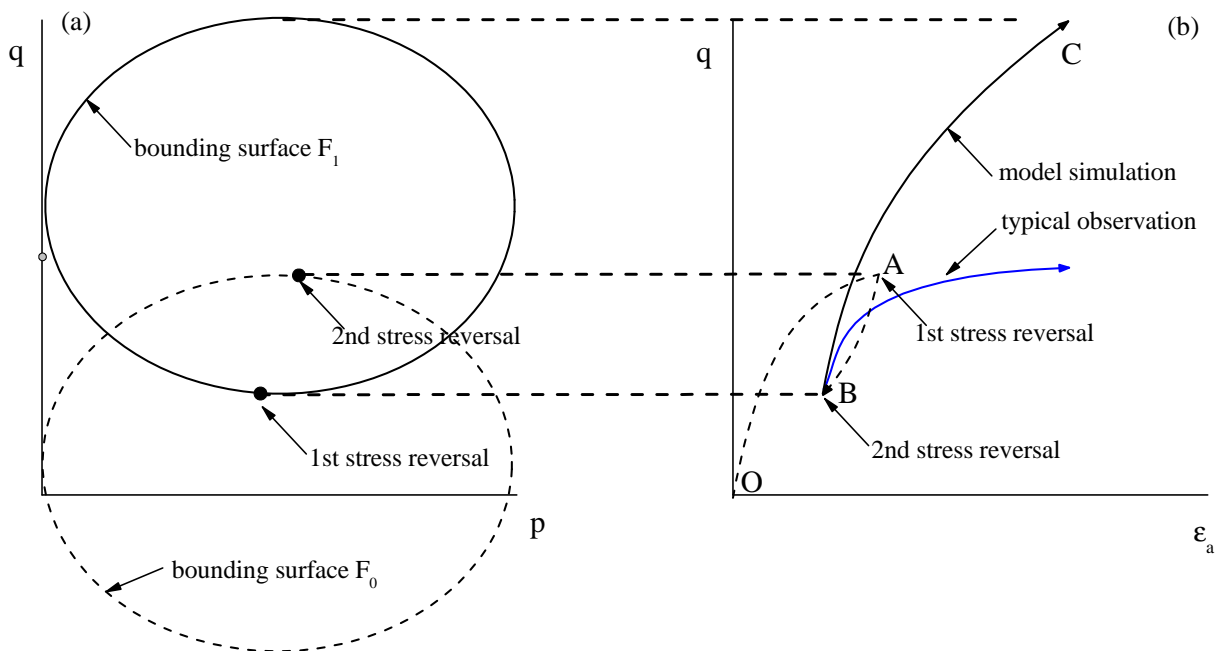


Figure 2.38. Schematic diagram of the issue associated with the relocation of bounding surface upon stress reversal: (a) movement of bounding surface; (b) stress-strain response

The aforementioned relocation of the bounding surface upon stress reversal may result in unrealistically high material strength during irregular cyclic loadings. To illustrate this point, assume that there is a clay sample that has been unloaded (AB path in Figure 2.38(b)) following a primary loading (path OA in Figure 2.38(b)) from an isotropic NC state. If the above sample is reloaded in compression (i.e., the path BC in Figure 2.38

(b)), a memory center forms at the second stress reversal point in Figure 2.38 (a) and the bounding surface is relocated so that it passes the memory center, i.e., the surface F_1 in Figure 2.38 (a). Consequently, the reloading can achieve a considerably higher strength than the primary loading. This response is in contrast to that typically observed in experiments, in which the reloading strength is governed by the hardening and strength in the primary loading. The above discrepancy is attributed to the fact only the most recent stress history, which is the unloading in the above example, is memorized by the model. To address this issue, one could formulate the model to record all the loading history, like the nesting surface models (Mróz et al., 1981, 1978) or employ a bounding surface that will not relocate upon stress reversal.

The plastic modulus in this model takes the form as:

$$K_p = \bar{K}_p + (H_m - \bar{K}_p) \left(1 - \frac{1}{b}\right)^\gamma \quad (2.16)$$

To capture the cyclic softening, the variable γ is assumed to increase hyperbolically with the accumulated plastic deviatoric strains:

$$\gamma = \frac{b\gamma_b\varepsilon_{QL}}{\gamma_b + b\varepsilon_{QL}} \quad (2.17)$$

where the parameters γ_b and b are the slope of the hyperbola at $\varepsilon_{QL} = 0$ and the asymptotic value of γ , respectively. The accumulated plastic deviatoric strain is defined as $\varepsilon_{QL} = \int |d\varepsilon_d^p|$.

The variable H_m in equation 2.16 is the reference plastic modulus at the memory center and takes different forms for loading, unloading and reloading (Li and Meissner, 2002). While such a division between different loading branches allows more freedom in

controlling the plastic behavior during cyclic loading, it inevitably increases the model complexity and the number of parameters. Moreover, the plastic modulus H_m are functions of applied cyclic shear stress amplitude and undrained strength during monotonic loading, which must be known before the simulation. This makes the model not suitable for simulation of soil responses during irregular or strain-controlled cyclic loading, in which the applied cyclic stress is not constant or is a response rather than an input.

CASM-c model proposed by Yu et al. (2007a)

Based on the bounding surface framework, the unified critical state CASM model proposed by Yu (1998) is extended to reproduce the cyclic behavior of sand and clay. The radial mapping rule is employed with the projection center being fixed at the origin of the stress space. The plastic flow direction is based on the stress-dilatancy relation proposed by Rowe (1962) and thus a non-associative flow is used. The plastic modulus takes different forms for loading, unloading, and reloading:

$$K_p = \begin{cases} \bar{K}_p + \frac{h}{p}b(1 - 1/b)^m & \text{loading} \\ H_u \left(\frac{b}{b-1}\right) & \text{unloading} \\ \bar{K}_p + H_r b(1 - 1/b)(1 + \varepsilon_d^p)^k & \text{reloading} \end{cases} \quad (2.18)$$

where H_u , H_r , h , m and k are model parameters. In particular, the parameter k is introduced to reproduce the cyclic shakedown. With an increase of the plastic deviatoric strain ε_d^p , the plastic modulus during reloading gradually increases and thus the model generates less plastic deformation. When the value of K_p during reloading is sufficiently large, the plastic deformation occurred in each loading cycle is negligible, and the cyclic shakedown is reproduced.

SANICLAY-B model proposed by Seidalinov and Taiebat (2014)

As an extension of the SANICLAY model (Dafalias et al., 2006), Seidalinov and Taiebat (2014) proposed a bounding surface model to simulate the clay response during cyclic loading. As shown in Figure 2.33, the yield surface in the SANICLAY model is adopted as the bounding surface, which is a rotated and distorted ellipse representing the plastic anisotropy. An image stress flow rule is employed to define the plastic flow, i.e., the plastic flow direction is defined as the gradient of the plastic potential at the image stress. Since the plastic potential surface is different than the bounding surface, a non-associative flow is yielded. A specific feature of this model is that a moving projection center is employed, which will be relocated to the current stress upon stress reversal. As a result, the over-damping caused by the fixed projection center is minimized.

However, As illustrated in Figure 2.39, the image stress flow rule together with the discrete projection center leads to an undesired early stabilization of the effective stress path in simulations of undrained cyclic loading, and thereby to a severe underestimation of pore pressure build-up compared to experimental observations. The influence of this discrepancy can be significant, as the very low confining stress that arises if large pore pressure accumulates and the corresponding reduction in stiffness and strength are major reasons for catastrophic failures of clay and large permanent deformations of geotechnical facilities. In addition, the post-cyclic shearing response of clays, i.e., one of the central topics of this study, is also a function of soil's effective stress and thus the accumulation of excess pore pressure during cyclic loading.

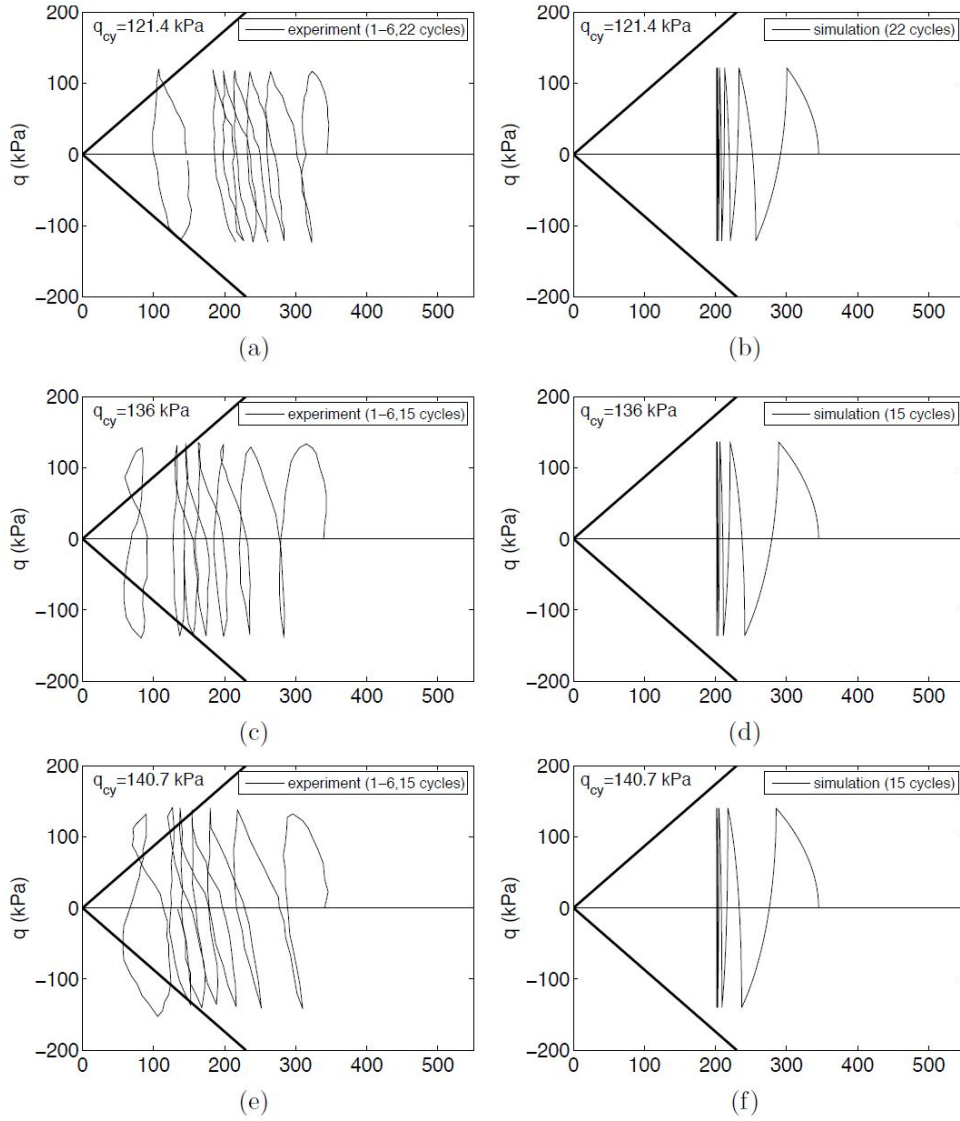


Figure 2.39. Comparison between experimentally observed undrained effective stress path and simulations based on image stress flow rule (Seidalinov and Taiebat, 2014) with experimental data from (Sheu, 1985)

The plastic modulus of SANCLAY-B model takes the form:

$$K_p = \bar{K}_p + \frac{hp_0^3}{< b/(b-1) - s >} \quad (2.19)$$

where p_0 is the internal variable that controls the size of the bounding surface. To consider cyclic softening, the shape factor h decreases with the accumulation of plastic deviatoric strain ε_d^p :

$$h = \frac{h_0}{1 + d} \quad \text{and} \quad \dot{d} = a_d |\dot{\varepsilon}_d^p| \quad (2.20)$$

where the parameters h_0 and a_d define the initial value of h and rate of the cyclic softening.

2.5.4. Comments about bounding surface models for cyclically loaded clay

Many constitutive models developed within the framework of bounding surface plasticity can reproduce important features of clay behavior under cyclic loading, i.e., the accumulation of deformation and excess pore pressure. The radial mapping rule is the most common mapping rule employed by these models, and when the projection center is appropriately relocated upon stress reversal, the over-damping caused by the fixed projection center can be minimized. The image stress flow rule is commonly used by these models and depending on whether a separate plastic potential is assumed, associative and non-associative flow rule can be rendered. However, this image flow rule may underestimate the magnitude of cyclic pore pressure build-up during cyclic loading. Moreover, cyclically loaded clay can exhibit a complex plastic behavior, which has been referred to either cyclic softening or cyclic shakedown. Each behavior has been successfully captured by different constitutive models through modifications of the plastic modulus formulation. Nevertheless, to the author's knowledge, no model currently can reproduce both the cyclic shakedown and softening. Furthermore, the clay's small strain stiffness responses are usually ignored in the models. Even though, these model performs well for cyclic

loading that is characterized by large plastic deformation, a soil's nonlinearity and corresponding stress-strain hysteresis may not be satisfactorily reproduced when elastic strain is the dominant component during cyclic loading, as illustrated by Papadimitriou and Bouckovalas (2002). Lastly, while various models have clearly shown the capacity of the bounding surface framework in terms of reproducing cyclic soil behavior, most of them does not consider the effects of soil structure and the coupling between destructuration, permanent strain, and excess pore pressure. These factors are crucial if one wants to quantify the cyclic degradation of natural clay.

2.6. Modelling strategy for capturing structure effects in natural soils

Two basic ideas for modeling the behavior of structured soil are: (1) the fundamental role played by the yield phenomenon and (2) the need to consider the observed behavior of the structured material in relation with that of equivalent structureless material (Leroueil and Vaughan, 1990; Burland, 1990; Gens and Nova, 1993). For the former, the progressive loss of structure is related to the generation of plastic strains. For the latter, the constitutive models proposed for structureless soils are enhanced with additional internal variables that are assumed to deteriorate monotonically with loading and deformation. This assumption is consistent with the observation that the behavior of structured clay converges to that of reconstituted clay as a result of destructuration (Burland, 1990).

The main features of these strategies are illustrated in Figure 2.40. The intrinsic surface is the governing surface for the reconstituted clay and can take the form of any yield surface proposed for the reconstituted clay, e.g., the MCC model (Wood, 1990) or SAN-ICLAY model (Dafalias et al., 2006). Additional structure-associated internal variables

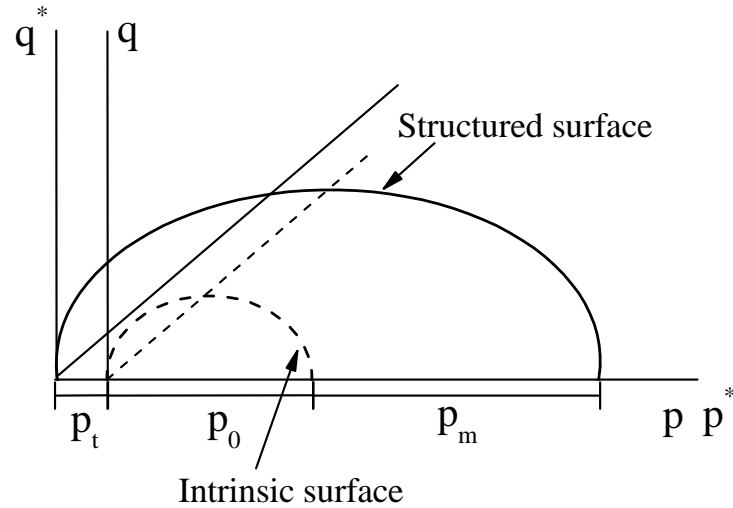


Figure 2.40. Schematic diagram of structured surface and intrinsic surface

p_m and p_t enlarge the intrinsic surface to the structured surface (i.e. the yield surface for structured clay), expanding the elasticity regime, postponing the onset of yielding and increasing the material strength, as shown in the aforementioned experimental evidence. The variable p_t represents the true cohesion of the structured soil, and can be linearly related to p_m with a constant coefficient (Gens and Nova, 1993) or be assumed as an independent internal variable (Horpibulsuk et al., 2010; Suebsuk et al., 2011), or be ignored (Liu and Carter, 2003; Yu et al., 2007b; Taiebat et al., 2010).

Regardless of the assumption of p_t , it and p_m will monotonically decrease when plastic deformation is generated, which is the key for reproducing the high post-yield compressibility and strain-softening in compression and shearing tests, respectively. The deterioration of these structure internal variables can be solely driven by plastic volumetric strain

(Liu and Carter, 2003) or a combination of plastic volumetric and deviatoric strain (Gens and Nova, 1993; Taiebat et al., 2010).

On the wet side of the yield surface, the post-yield behavior is governed by the competition between the volumetric hardening, encapsulated by the internal variable p_0 , similar to the classical critical state models, and the destructuration softening, represented by the deterioration of p_m . Such competition can result in overall strain-hardening, strain-softening or very complex response (e.g., the unstable plateau of deviatoric stress shown in Figure 2.15). On the dry side of the yield surface, both dilation and destructuration result in a shrinkage of the yield surface, which further create a severe post-yield softening as also shown in Figure 2.15.

To cope with the plastic anisotropy of natural soils, the structured surface can be assumed to be translated or rotated in stress space. Rouainia and Wood (2000) assumes a translated structured surface that deviates from the hydrostatic axis. This anisotropy is related to the amount of structure and evolves according to a kinematic hardening that associated with the destructuration. This assumption implies that the anisotropy only exists for the structured surface and not for the intrinsic surface. It also implies that when all the structure has been removed, the plastic anisotropy will be completely eliminated. In contrast, the experimental evidence presented in the section 2.3 shows that similar anisotropy exists in both natural and reconstituted clay samples, given both have experienced the same stress history. Being more compatible with the above experimental observation, Belokas and Kavvadas (2010); Taiebat et al. (2010); Sivasithamparam and Karstunen (2012) assumed that both the intrinsic and structured surfaces are rotated in

stress space and are characterized by the same rotation hardening variable that evolves according to the applied stress path.

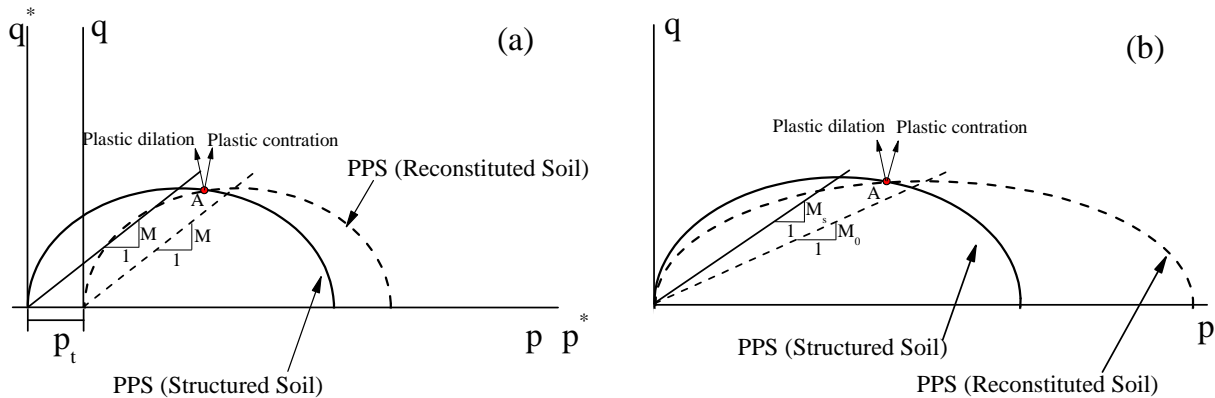


Figure 2.41. Schematic diagram of flow rule modifications in structured soil models: (a) axial translation; (b) friction destructure

Experimental work has shown that the existence of structure can alter soil's stress-dilatancy relation. For instance, Leroueil and Vaughan (1990) and Maccarini (1987) reported that in CIU TXC tests on an artificial soil, the maximum rate of dilation does not occur at peak strength, but at significantly larger strains. The work of Schnaid et al. (2001) and Yu et al. (2007b) show that the dilation of artificially cemented sand is inhibited by inter-particle bonds. Accordingly, the plastic flow rule in some structured soil models is formulated to explicitly consider the effect of soil structure (Gens and Nova, 1993; Yu et al., 2007b; Taiebat et al., 2010; Belokas and Kavvas, 2010). Gens and Nova (1993) applied the axial translation technique to the plastic potential surface such that it is shifted to the left with an amount of p_t , as shown in Figure 2.41(a). In addition, the

slope of critical state line (i.e., M value) is assumed to be independent of soil structure. Considering the stress state A in Figure 2.41(a), which falls between the critical state lines for reconstituted and structured soil. As indicated by the plastic flow direction vector, at stress A the dilatant volumetric response would be predicted by the reconstituted soil model changes to contractive behavior after the translation of the plastic potential surface, thereby predicting the delay of dilation observed in experiments. Taiebat et al. (2010) introduced the concept of friction destructuration, which assumed that the degradation of structure results in a reduction in friction angle. As illustrated in Figure 2.41(b), the slope of failure line for the structured soil (i.e., M_s) is higher than that for the reconstituted soil (i.e., M_0). The plastic flow vectors plotted at the stress point A indicate that the delay of dilation also can be reproduced through this strategy.

In summary, the aforementioned modeling strategies have been proven successful in reproducing essential characteristics of the structured soils, including the enlarged elastic regime, higher post-yield compressibility, compression line converging to that of reconstituted soil, strain-softening and so on. However, most of the structured soil models focus on the analysis of monotonic loading. And only very few models look at the case of cyclic loading (Liu and Carter, 2003; Seidalinov and Taiebat, 2014). Moreover, based on the author's knowledge, none of these models has been evaluated regarding their capacity to quantify the soil strength degradation during cyclic loading.

2.7. Summary and Conclusions

This chapter presents a review of the major landslides caused by the 1964 earthquake and the Bootlegger Cove Formation (BCF) that composes the failed slopes. Then observations from experimental tests on natural clays are summarized to illustrate the effects of soil structure on the mechanical behavior of natural clays, followed by a review of clays behavior during undrained cyclic loading and post-cyclic shearing to show the factors that affect the strain accumulation during cyclic loading and post-cyclic shear strength. Lastly, Chapter 2 presents a review of bounding surface models aimed at simulating cyclically loaded clay and constitutive modeling strategies used to reproduce the effects of soil structure. The following main conclusions can be drawn from this chapter:

- (1) Different failure modes were observed in the landslides in Anchorage during the 1964 earthquake, among which the Turnagain Heights landslide is characterized by a series of retrogression slope failures and others are characterized by a translatory sliding of a soil block. Regardless of the failure mode, these landslides were all caused by the strength loss of the BCF soil during cyclic loading, which is more likely related to the cyclic structure degradation of the soft, sensitive BCF clay, as the silt and sand lenses within the BCF is relatively dense and less susceptible to a liquefaction.
- (2) Regarding the sensitivity of the BCF clay, there is a relatively large variation of it among different studies and different measurement methods. In particular, the sensitivity measured by the laboratory vane tests is considerably higher than those measured by the field vane tests. Moreover, the results of laboratory vane

tests indicate that the very sensitive clay only occurs in Facies III of the BCF and not all Facies III is very sensitive.

- (3) The soil structure can significantly impact the compression and shearing characteristics of natural clay. In compression tests, the existence of structure leads to a larger and readily identified yield stress and a considerably higher post-yield compressibility. As the soil structure progressively deteriorates, the compression curve of natural clay gradually converges to that of the corresponding reconstituted clay.

During undrained shearing, more soil structure leads to a higher peak strength, more brittle response and higher positive excess pore pressures. In drained shearing, stress-strain behavior changes from brittle to ductile as the confining stress increases. When a soil dilates during drained shearing, the maximum rate of dilatancy is governed by the structure. The cohesion, which results from inter-particle bonds, is an important component of peak strength of natural clays. In both undrained and drained shearing, the existence of soil structure results in a higher peak mobilized friction.

The plasticity anisotropy is an intrinsic property of natural clay, which primarily results from the anisotropic consolidation history during the initial deposition, and this anisotropy is retained when clay becomes structured, which mainly enlarges the size of the yield surface.

- (4) Clay exhibits two distinctive types of strain accumulation during undrained cyclic loading: cyclic softening and cyclic shakedown. The former refers to the condition for which the strain accumulation rate increases as more loading cycles are applied

until the soil failure result, due to the excessive deformation, whereas the latter refers to the condition for which the generation of plastic deformation decreases with increasing loading cycles until a purely elastic response is reached. Moreover, the above behavior can be interpreted from the corresponding effective stress states during undrained cyclic loading and whether clay exhibits cyclic softening or shakedown is a function of effective stress state, and particularly the effective stress ratio.

- (5) Clay cyclic strength degradation is proportional to the strain levels and excess pore pressure developed during cyclic loading. Given the same cyclic strain level, the lower the failure strain in monotonic tests, the greater is the degradation in shear strength and stiffness during cyclic loading. The pore pressure build-up during undrained cyclic loading of a NC clay creates an apparent over-consolidated state and thus the post-cyclic shearing is similar to the monotonic test on clay experienced a mechanical unloading.
- (6) Constitutive models developed within the framework of bounding surface plasticity can reasonably reproduce the accumulation of deformation and excess pore pressure in a cyclically loaded clay. The radial mapping rule is the most commonly used by these models, and when the projection center is appropriately relocated upon stress reversal, the over-damping caused by the fixed projection center can be minimized. The image stress flow rule may underestimate the magnitude of cyclic pore pressure build-up during cyclic loading. Moreover, cyclic softening and shakedown have been successfully captured by different models.

Nevertheless, none of them currently can reproduce both cyclic shakedown and softening.

- (7) Two strategies have been proven successful in modeling the behavior of structured soil during monotonic loading: (a) the progressive loss of structure is related to the generation of plastic strains; (b) the constitutive models proposed for structureless soils are enhanced with additional internal variables that are assumed to deteriorate monotonically with loading and permanent deformation.

CHAPTER 3

**BACK ANALYSIS OF THE TURNAGAIN HEIGHTS
LANDSLIDE**

3.1. Introduction

During the 1964 Alaska earthquake, several major landslides occurred in the city of Anchorage. The largest one was the Turnagain Heights landslide, which extended more than 2400 m along the coastline (Shannon & Wilson Inc., 1964; Seed and Wilson, 1967).

Extensive subsurface investigations revealed that the Bootlegger Cove Formation (BCF) is ubiquitous in the vicinity of Turnagain Heights. The Bootlegger Cove Formation is at least 30 m thick and consists of a sequence of silty clays and clayey silts with interbedded silt, silty fine sand, and fine to medium sand and with scattered pebbles and cobbles (Shannon & Wilson Inc., 1964; Updike and Ulery, 1986; Updike and Olsen, 1988).

Regarding the initiation of the Turnagain Heights landslide, Seed and Wilson (1967)'s study concluded that the slope failure was triggered by liquefaction of thin sand lenses located within the BCF, which generated a severely weakened zone extending backward from coastline to some considerable inland distance. However, in-situ cone penetration tests (CPT) conducted by USGS (Updike and Olsen, 1988; Olsen, 1989) at a site adjacent to the scarp of the Turnagain Heights landslide shown that the sandy strata closest to the landslide slip surface were too dense to liquefy. Also, their work concluded that it was more likely that the sensitive clay layer of BCF and its loss of strength during the 1964 earthquake were responsible for the landslide initiation.

To evaluate the role of sensitivity in the initiation of the Turnagain Heights landslide, one must first evaluate the stability of the slope prior to the 1964 earthquake based on the best estimation of the undrained shear strength within BCF at Turnagain Heights. Presumably, the pre-earthquake conditions are stable. The cyclic strength of the BCF must be determined and compared to the cyclic loading imposed by the 1964 event to

evaluate if a failure would be *initiated*. Presumably, the cyclic loading will cause degradation of the BCF so that the cyclic strength would be less than that determined based on monotonic loadings. Quantifying this degradation is central to the main thrust of this thesis. Once the cyclic strength is exceeded, and movements begin to develop along a failure surface, then the sensitivity would define a lower bound on the post-peak shearing resistance and have a significant impact on the deformations of the failure mass.

One can approach the cyclic strength degradation both experimentally and analytically. Experimentally, one can define monotonic, and cyclic strength of the BCF at Turnagain Heights and the difference between monotonic and cyclic strength applicable to the 1964 earthquake will define the amount of degradation that occurred to initiate failure for that level of earthquake. Analytically, one can compute the stability of the natural slope before the earthquake and then reduce the strength until the results of stability analysis indicates that a failure would occur, i.e., the slope would have a factor of safety (FS) equal to one. The strength reduction would correspond to the amount of BCF degradation caused by the earthquake. The latter approach will be discussed in the present chapter. The Turnagain Height slope failed during the earthquake, so the dynamic effect (e.g., inertial actions) is an important factor affecting the stability. Pseudo-static method and Newmark method have often been used to estimate the yield acceleration and consequently permanent displacement of a slope subjected to dynamic loading (Abramson et al., 2002; Jibson, 2011). Nevertheless, these methods cannot account for the soil's stress-strain responses during cyclic loading and thereby yields less realistic slope responses. Therefore, the stability analysis in this work only consider the

static loads, which consequently provides an upper bound on the strength reduction of BCF clay needed to initiate the slope failure.

The sensitive BCF clay has been shown to be quite variable (Shannon & Wilson Inc., 1964; Mitchell et al., 1973). It is generally thought to be highest in Facies III (Updike and Olsen, 1988). Work has been done regarding the interpretation of BCF clay sensitivity (Mitchell et al., 1973; Olsen, 1989; Shannon & Wilson Inc., 1964; Updike and Olsen, 1988). However, as discussed in Chapter 2, a relatively large variation exists within the results from different studies. Furthermore, most measurements in the above work were conducted on cores in sampling tubes or trimmed samples (e.g., tube vane test and torsional vane test), for which the inevitable sampling disturbance and stress release may render results that are less representative of the conditions in the field.

Accordingly, the sensitivity of BCF clay has been evaluated herein based on in-situ tests results obtained at Turnagain Heights, and by a correlation between the obtained sensitivity with soil index properties and chemical composition of pore fluid. This work is aimed at quantifying the in-situ sensitivity of BCF clay and studying the causes of such sensitivity.

This chapter is organized in the following manner: the in-situ tests at Lynn Ary Park and its interpretation are presented; then, the evaluation of the sensitivity of BCF clay based on in-situ tests and the correlation between the sensitivity, index properties and pore fluid chemical features are presented. Methods of analysis, model geometry, material parameters as well as the assumptions used in the slope stability analysis are discussed; the results of the analysis and its implications are shown at the end.

3.2. In-Situ Tests at the Lyn Ary Park

The site investigation took place in 2015 at the Lyn Ary Park in Anchorage, Alaska, which is located at the top of the scarp of the Turnagain Heights landslide, an area where Shannon & Wilson Inc. (1964) and the USGS (Updike and Olsen, 1988) conducted field investigations and performed laboratory tests on specimens of BCF soils (Figure 3.1). Three, approximately 20 m deep boreholes were drilled by GeoTek Alaska (GTA) using water filled-hollow stem augers. Two boreholes (NWU-1 and NWU-3 in Figure 3.1) were used to collect 3-inch diameter, Shelby Tubes samples from 6 m below ground surface to 20 m below ground surface. In the third borehole (FV-1 in Figure 3.1), GTA conducted a field vane shear test (FV) in the clays at 0.76 m (2.5 ft.) interval starting from 6 m to 20 m below ground surface. As shown in Figure 3.1, USGS had drilled and sampled two boreholes (B-3 and B-5) and conducted three CPT probes, in close proximity to the three boreholes. These data were reported in their report USGS 1817 (Updike and Olsen, 1988).

3.2.1. In-Situ Tests Results and Interpretations

Figure 3.2(a) presents the undrained shear strength S_u measured by several ways, including FV, unconsolidated-undrained (UU) (Shannon & Wilson Inc., 1964) and USGS CPT probes. To interpret undrained strength from CPT, the following correlation is used:

$$S_u = \frac{q_t - \sigma_v}{N_k} \quad (3.1)$$

where σ_v is the vertical total stress; q_t is the cone tip resistance and N_k is a cone factor that varies from 10 to 20 (Robertson, 2009). In this work, $N_k = 15$ is used, which

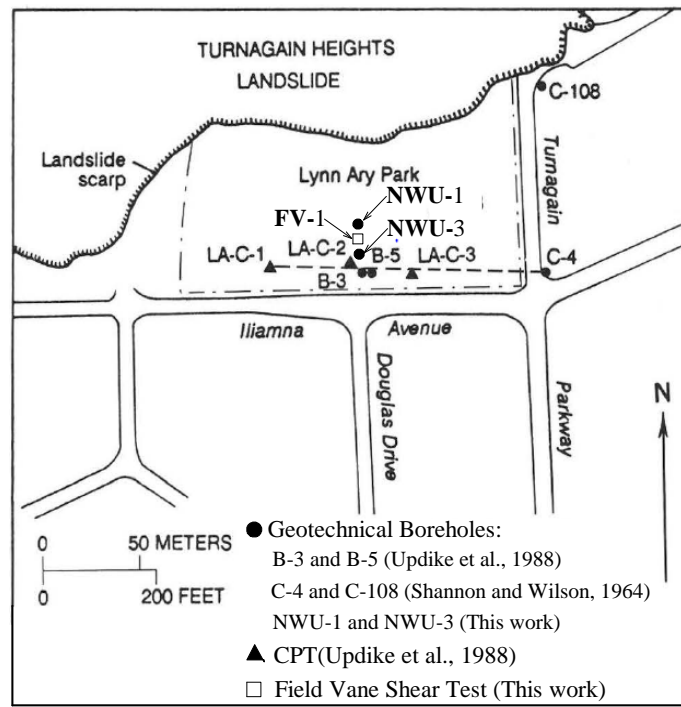


Figure 3.1. Locations of boreholes, CPTs and field vane, vicinity of Lynn Ary Park (modified based on the work of Updike and Olsen (1988))

corresponds to a simple shear mode of shearing. Except the UU results and several FV results collected between elevation 0 m to 3m, good agreement is seen between the two field results. Moreover, it can be seen that the normalized undrained strength S_u/σ'_v , is about 0.25 below elevation 5 m. This strength data trend suggests that BCF soil at the tested site is overconsolidated at the top of the layer, and gradually becomes normally consolidated with depth. This interpretation is supported by the consolidation tests conducted by Shannon & Wilson Inc. (1964), which concluded that the upper clay is over-consolidated as a result of desiccation.

To facilitate the stability analysis discussed later, an idealized stratigraphy for Turnagain Heights is suggested (Figure 3.2 (a)), in which the BCF clay is divided into four

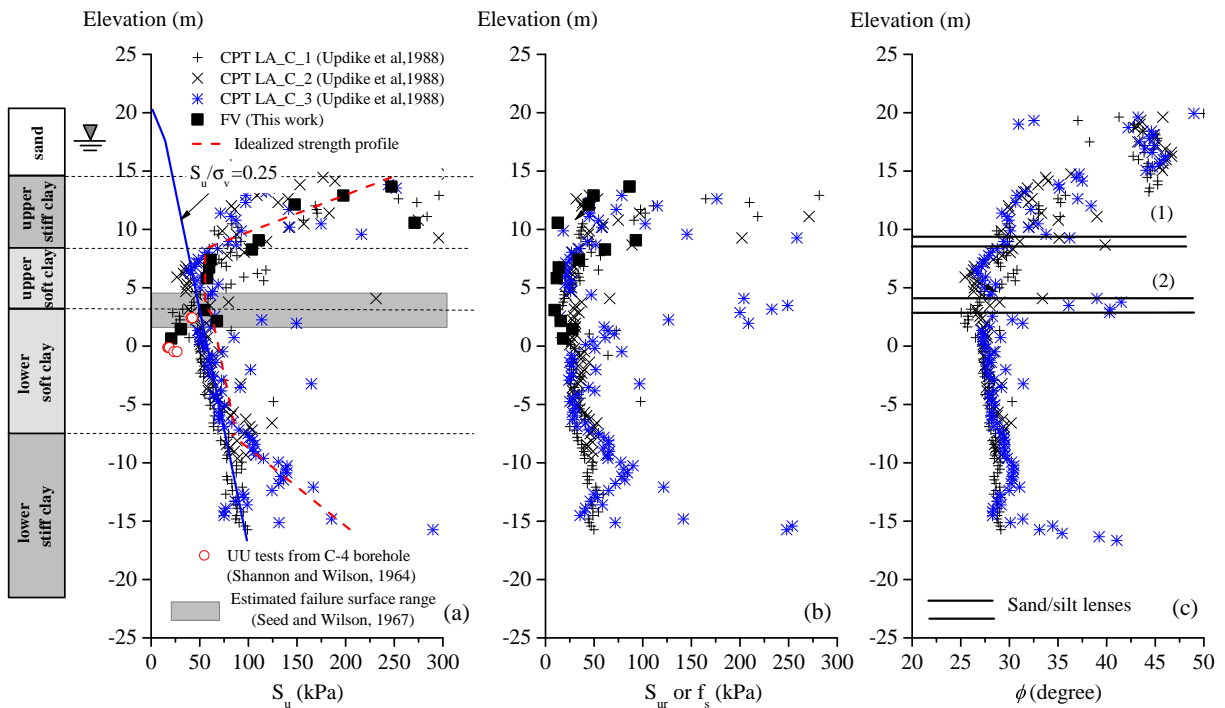


Figure 3.2. In-situ tests based soil strength properties and stratigraphy at Turnagain Heights area: (a) undrained shear strength; (b) FV remolded strength and CPT side friction; (c) correlated friction angle from CPT

sublayers based on its undrained shear strength variation. In the upper stiff clay layer, the undrained strength decreases with depth, while the strength in the upper soft clay layer is relatively constant. In both the lower soft clay and lower stiff clay layer, the undrained strength increases with depth. Additionally, the dashed line in Figure 3.2 (a) is the idealized strength profile used in stability analysis, and the corresponding values are summarized in Table 3.1.

Also, Figure 3.2(a) shows that the in-situ water table at Turnagain Height is assumed to be at the elevation of 17.5 m, which is suggested by the USGS report (Updike and Olsen, 1988) and is confirmed by the borehole logs of the Northwestern field investigation. By studying the strength of samples obtained in Turnagain Heights slide area, Seed and

Wilson (1967) estimated that the position of the slide surface varied between 1.5 and 4.6 m in elevation (shaded band in Figure 3.2 (a)), which is consistent with the location of the weakest material found at the Lynn Ary Park.

Table 3.1. Soil properties used in the stability analysis of Turnagain Heights slope

Layer/ Sublayer	Thickness (m)	Drainage condition	Unit weight (kN/m ³)	S_u (kPa) ^a	Friction angle (°)	Perme- ability (cm/s)
Sand	6.1	Drained	19.5	-	43	1E-3
Upper stiff clay	6.1	Undrained	19.5	440.4 -31.5z	-	1E-7
Upper soft clay	5.2	Undrained	19.5	55.8	-	1E-7
Lower soft clay	10.7	Undrained	19.5	18.5 +2.5z	-	1E-7
Lower stiff clay	8.5	Undrained	19.5	-338.0 +15.0z	-	1E-7
Lenses (1)	0.7	Drained	19.5	-	36	1E-3
Lenses (2)	1.2	Drained	19.5	-	36	1E-3

Note: ^a z is the depth below the ground surface

Figure 3.2 (b) compares the remolded undrained strengths from the FV and the side friction f_s from the cone probes. Given the large shear strains that occur during penetration testing as the probe moves past at point, the f_s values should reflect some sample disturbance. The FV values tend to be near the lower bound of the CPT values, and are closer to the CPT values when the shear strength is lower. The significant point made in this figure is that the USGS reported that the BCF clay from 6.8 to 5.3 m and 3.8 to 2.3 m in elevation had zero remolded strength at this location, which is based on tests made on the tube samples they recovered (Updike and Olsen, 1988). This clearly is not the case based on the data in Figure 3.2 (b).

Figure 3.2 (c) shows the profile of soil friction angle ϕ based on its correlation with the CPT results (Kulhawy and Mayne, 1990):

$$\phi = 17.6 + 11.0 \log[(q_t/p_a)(\sigma'_v/p_a)^{0.5}] \quad (3.2)$$

where p_a is the atmosphere pressure and σ'_v is the vertical effective stress. It is found that the friction angle for the top sand layer is around 43° , which suggests the material is dense to very dense. Furthermore, Figure 3.2 (c) identifies the location of two sand/silt lenses, whose correlated friction angle is remarkably higher than its neighboring zones consisting of cohesive BCF. These locations of the lenses are consistent with the visual interpretation of collected samples of USGS (Updike and Olsen, 1988) and the Northwestern field investigation. In general, the friction angles for these lenses vary from 33° to 40° .

3.3. The Sensitivity of BCF Clay

3.3.1. The Sensitivity Interpreted from In-situ Tests

Figure 3.3 presents normalized USGS CPT data in the soil classification chart proposed by Robertson (1990), which categorizes soil based on their in-situ behavior instead of their grain-size distribution and Atterberg limits. Two parameters are used: normalized tip resistance Q_t and normalized side friction F_r :

$$Q_t = \frac{q_t - \sigma_v}{\sigma'_v}; \quad F_r = \frac{f_s}{q_t - \sigma_v} \times 100\% \quad (3.3)$$

In Figure 3.3, the CPT data measured at different sublayers are presented as different symbols. Given the location of the slide surface, the lower stiff clay is not considered here

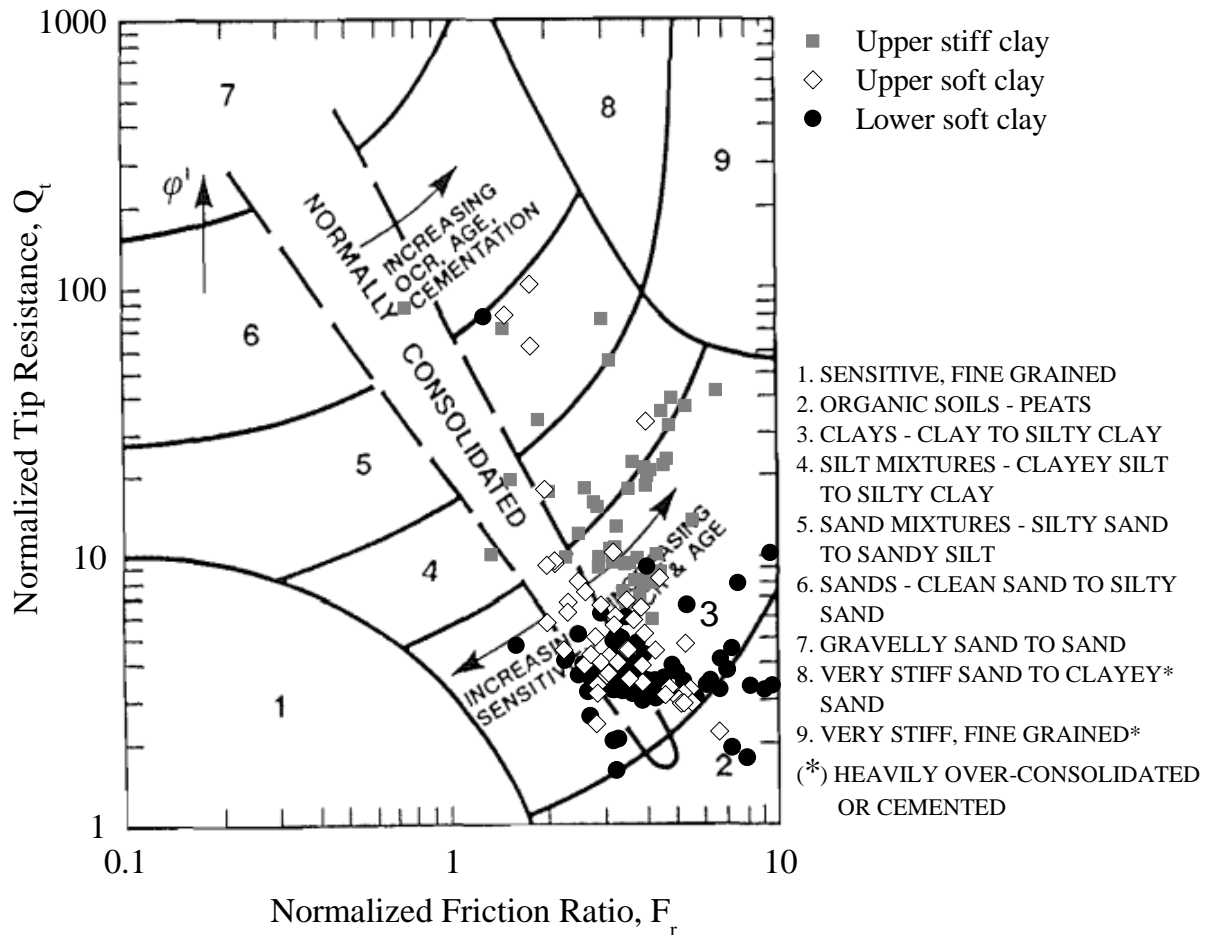


Figure 3.3. Soil behavior classification based on the normalized CPT properties (classification chart adopted from Robertson (1990))

for the purpose of clarity. It can be seen that most of the data fall into the soil category 3 and 4, which are labeled as clay, silty clay or clayey silt. This result is consistent with the visual classification of the collected samples from the same site as well as previous findings (e.g., Shannon & Wilson Inc. (1964); Hansen (1965); Updike and Olsen (1988)). The data points for the upper stiff clay mostly fall into the zone representing over-consolidated soil. Also, data from soft clay layers (i.e., upper soft and lower soft layer) mostly fall into the zone that represents the normally consolidated soil. This information of stress

history matches the interpretation of strength mentioned above and consolidation tests results (Shannon & Wilson Inc., 1964). The most significant finding from Figure 3.3 is the fact that most of the data points fall within the category representing soil with small or negligible sensitivity, and none of the points falls in the zone of soil category 1, which is denoted as sensitive, fine-grained soil. While both CPT measurement and the generalization of the chart in Figure 3.3 involve some uncertainties, the observation above provides a strong indication that BCF clay at this location may not be as sensitive as that has been previously concluded by other research (Shannon & Wilson Inc., 1964; Seed and Wilson, 1967; Mitchell et al., 1973). Besides, several data points lie in the zone 5, which agrees with the existence of silt or sand lenses within BCF clays.

Results shown in Figure 3.3 qualitatively evaluates the sensitivity of BCF clay, while the quantification of sensitivity based on FV and CPT tests is presented in Figure 3.4. It is worth mentioning that the sensitivity from CPT is interpreted based on the assumption that the remolded strength is equal to the side friction, which has been proved to be reasonable by Lunne et al. (1997) and Farrar et al. (2008). Besides the in-situ tests at the Lynn Ary Park, Figure 3.4 also includes FV results reported by Shannon & Wilson Inc. (1964), obtained from a bore hole near Turnagain Heights and outside the zone of the 1964 landslide, i.e., to avoid the influence of soil disturbance caused by the landslide.

FV results in Figure 3.4 shows that the sensitivity of BCF clay generally increases with depth in the upper stiff and upper soft clay layers. Moreover, the BCF stratum that has the lowest strength value (i.e., the upper soft clay), tends to have the highest sensitivity, which was also reported by previous research (Hansen, 1965; Olsen, 1989). Quantitatively, FV results suggest that the sensitivity of the upper stiff clay layer varies

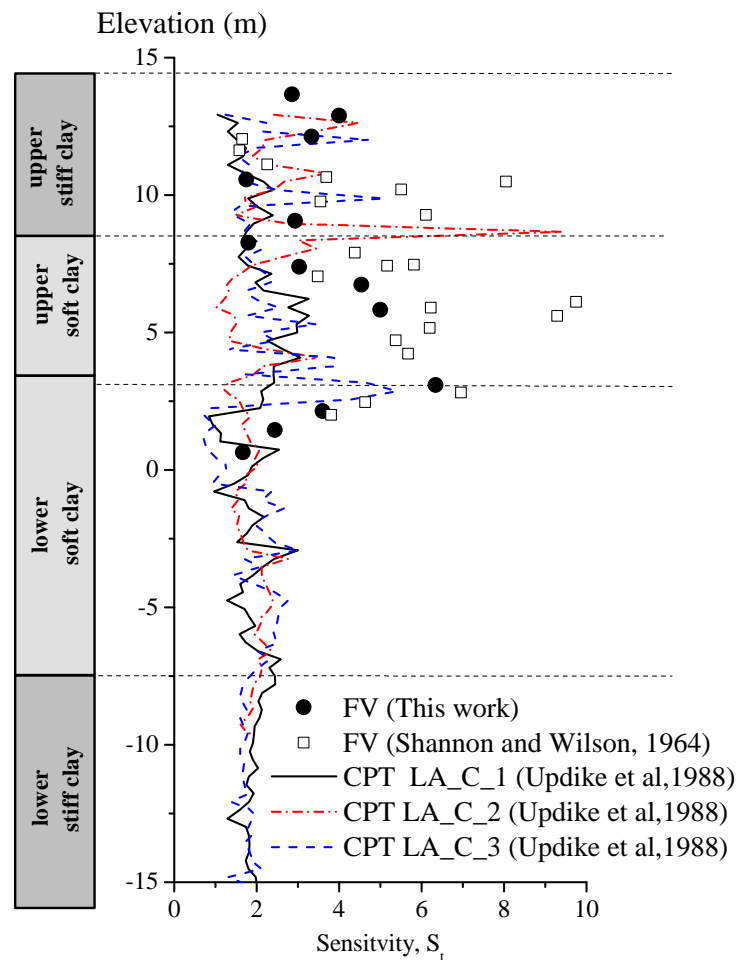


Figure 3.4. BCF clay sensitivity interpreted from in-situ tests at the Lynn Ary Park

from 1.6 to 8.1 with the averaged value being 3.6, and for the upper soft clay, its sensitivity ranges from 1.7 to 9.8, with averaged value being 5.0. Concerning the lower soft clay and lower stiff clay layers, no decisive trend is seen due to the lack of data at deeper locations. Nevertheless, available data indicate a trend of decreasing sensitivity with depth and this tendency is consistent with the previous study which showed that the sensitivity of BCF clay is lower at lower elevations (Shannon & Wilson Inc., 1964).

Compared with the FV, the sensitivity interpreted from the CPT exhibits much larger scattering, which prevents a general trend observed regarding the variation of sensitivity. Nevertheless, similar to the FV tests, the CPT results indicate that the sensitivity of the upper stiff and soft clay layers is higher than that of the two lower clay layers. Furthermore, it can be seen that FV and CPT give a similar range of sensitivity for the upper stiff clay, but for the upper soft clay layer, the CPT interpretation is considerably lower. This discrepancy may reflect the different degree of sample disturbance associated with each test method. The above difference may also be attributed to the CPT's inherent loss of accuracy on side friction measurement when the CPT is used in clay with high sensitivity (Robertson, 2009).

Most importantly, the interpretation of the in-situ tests shows that the maximum sensitivity of BCF clays at the Lynn Ary Park is less than 10 and the majority of data fall within the range from 2 to 6, which suggests the measured BCF clay is not very sensitive.

3.3.2. Correlation Between Sensitivity and Index Properties

The sensitivity of clay is closely related to its index properties and in particular, a high liquidity index is one of the characteristics of very sensitive clay (Bjerrum, 1954; Mitchell, 1993). Therefore, the above distribution of sensitivity is compared with the distribution of index properties of the BCF soil specimens collected at Lynn Ary Park (Updike and Olsen, 1988) and other Turnagain Heights areas (Shannon & Wilson Inc., 1964), as shown in Figure 3.5. The selected index properties are natural water content and liquidity index. Figure 3.5 shows that most of the tested specimens has a liquidity index that

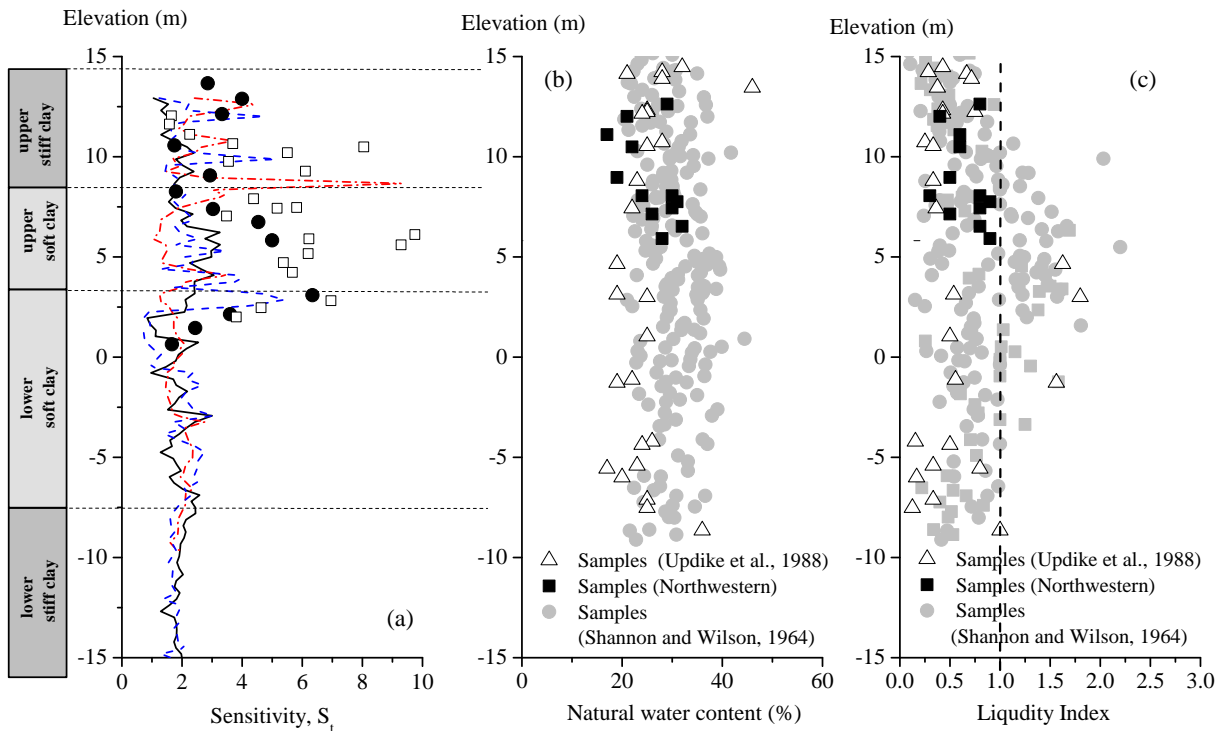


Figure 3.5. Correlation between BCF clay's sensitivity with index properties: (a) sensitivity interpreted from in-situ tests; (b) natural water content; (c) liquidity index

is less than one. Given the high correlation between sensitivity and liquidity index, this fact suggests that the proportion of BCF clay that has a high sensitivity is low, which is also supported by the results of laboratory vane shear tests conducted during the post-earthquake investigation (Shannon & Wilson Inc., 1964). In particular, except three outliers, the tested specimens collected from Lynn Ary Park (both by USGS and Northwestern) all have a liquidity index lower than one. This observation is consistent with the fact that the sensitivity interpreted from the in-situ tests at the same site is relatively low. Additionally, the variation of the liquidity index increases with depth in the upper stiff and upper soft clay layers and decreases with depth in the two lower

layers, as does the sensitivity. Since Figure 3.5 includes specimens collected from locations other than Lynn Ary Park, it is reasonable to assume that the sensitivity variation trend obtained from the in-situ tests at Lynn Ary Park can be applied to other locations of Turnagain Heights. Regarding the natural water content, no clear and consistent trend is observed.

3.3.3. Correlation Between Sensitivity and Pore Fluid Chemical Composition

The chemical composition of pore fluid contains important information regarding the causes of sensitivity, as the differences between the composition that may develop at the time of formation of clay deposit and the present is a major factor that contributes to the sensitivity of natural clays (Mitchell, 1993). The results of pore fluid chemical analysis of BCF clay conducted by the University of California, Berkeley (Mitchell et al., 1973) and USGS (Updike and Olsen, 1988) are summarized in this work. The specimens used in chemical analysis by USGS are from the same site as the Northwestern in-situ tests. Accordingly, a direct comparison is made between the sensitivity distribution in section 3.3.1 and the chemical composition concentration profile at the same site, which is aimed at providing more insights regarding the causes of the sensitive nature of BCF clays.

Physicochemical analyses conducted at the University of California, Berkeley

As part of the post-investigation of the 1964 Alaska earthquake, Mitchell et al. (1973) conducted a series of chemical analysis on six BCF clay samples collected from the areas, where the 1964 earthquake triggered landslides. The results of the analyses are summarized in Table 3.2. Based on these results, Mitchell et al. (1973) suggested that the

leaching of salt from the pore water and the introduction of dispersing agents were the two major reasons for the high sensitivity of BCF clays.

Table 3.2. Chemical characteristics of six Bootlegger Cove Formation clay samples (Mitchell et al., 1973)

Area	Depth (m)	Consistency	Water content (%)	Sensitivity	pH	Pore water salt content g/liter	Cations in solution		
							$C_i/\Sigma C_i =\%$		
							Na ⁺	Ca ²⁺	Mg ²⁺
Fourth Avenue	23.8	Sensitive	35	14	10.2	5.8	29	66	5
Fourth Avenue	38.1	Stiff	29	low	10.2	2.8	36	61	3
L Street	7.3	Sensitive	38	>20	9.1	2.7	26	40	34
L Street	10.1	Stiff	29	11	8.3	4.2	29	67	4
Turnagain	22.4	Sensitive	36	16	10.3	3.3	30	45	25
Turnagain	35.7	Stiff	21	Low	9.9	2.8	31	58	11

Salt content and composition of pore fluid were seen as evidence to support that considerable leaching of salt had taken place within BCF clays. Specifically, Table 3.2 shows that the salt content in BCF clays pore fluid ranged from 2.7 to 5.8 g/liter and this value is remarkably lower than 36g/liter, the typical value of seawater (Sverdrup et al., 1942). This evidence may indicate that extensive leaching has occurred within BCF clay, if the BCF clay was initially deposited in a marine environment. Nevertheless, the depositional environment of the BCF is in serious doubt, if not dispute (Hansen, 1965). The environment has been considered to be glaciolacustrine, marine or estuarine by different research (Miller and Dobrovlny, 1959; Schmidt, 1963; Karlstrom, 1964; Smith, 1964; Schmoll et al., 1972). Moreover, composition analyses showed that calcium is the most abundant cation, which is followed in order by sodium and magnesium. Groundwater studies in the Anchorage area showed that the principal source of groundwater is an aquifer

that contains calcium-magnesium bicarbonate. Considering the possible interconnection between the above aquifer and sand/silt lenses within BCF clays, Mitchell et al. (1973) suggested that calcium and magnesium have replaced the initially predominant sodium in the pore fluid of BCF clay via groundwater leaching.

The abnormally high pH values (8.3 to 10.2) was seen as an indication of the existence of dispersing agents. The dispersing agents can create a favorable condition for clay particle flocculation and thereby high sensitivity. Regarding the origin of this dispersing agent, Mitchell et al. (1973) suggested that it was created by organic deposits and transferred via groundwater within sand/silt lenses.

Another important observation from Table 3.2 is that no significant difference concerning the salt content and the pH value was observed between those insensitive and sensitive specimens. Since low sensitivity was observed in specimens that were recovered from lower elevations, Mitchell et al. (1973) suggested that their low sensitivity can be partially attributed to the low water content induced by high effective stress. However, the significantly different sensitivity between specimens is not likely to be explained by the variation of water content presented in Figure 3.5. Therefore, besides leaching of salt and dispersing agents, there are probably other reasons that account for the sensitivity of BCF clays.

Chemical analysis conducted by USGS

USGS conducted chemical analysis on the pore fluid obtained from samples from their two borings at the Lynn Ary park. The chemical composition and pH values for pore water reported by Updike and Olsen (1988) are summarized in Table 3.3.

Table 3.3. Chemical composition and pH value of pore water extracted from BCF clay samples collected at the Lynn Ary park (Updike and Olsen, 1988)

Elevation (m)	pH	Concentration (mg/liter)							
		Na ⁺	K ⁺	Ca ²⁺	Mg ²⁺	Cl ⁻	SO ₄ ²⁻	HCO ₃ ⁻	organic carbon
-9.82	7.99	726	20	16	27	23	240	1685	34
-5.82	8.11	741	22	16	24	20	60	1928	69
-1.21	7.91	647	16	15	16	14	546	1116	49
2.04	8.25	535	15	14	18	18	250	1052	54
5.32	8.19	510	13	10	15	25	456	723	20
5.63	8.16	496	13	12	15	14	596	630	0
6.08	8.18	496	12	14	18	10	456	694	0
6.84	8.21	546	19	15	22	12	116	1290	39
7.31	8.17	550	17	18	25	15	113	1291	69
8.84	8.11	493	18	31	26	21	216	1045	107
10.14	8.24	358	33	70	42	23	413	722	118
12.28	8.02	258	34	110	126	85	920	400	8

Table 3.4. Comparison between the composition of seawater and the composition of the pore water of BCF clay samples collected at the Lynn Ary park

Ion	Seawater *	Pore water	Ratio seawater/ pore water
	meq/L	meq/L	
Na	459	11 ~ 32	14 ~ 42
K	10	0.3 ~ 0.9	11 ~ 33
Mg	106	1.2 ~ 10.3	10 ~ 88
Ca	20	0.5 ~ 5.5	4 ~ 40
Cl	535	0.3 ~ 2.4	223 ~ 1911
SO ₄	55	1.2 ~ 19.2	3 ~ 46
HCO ₃	2.3	6.5 ~ 31.6	0.07 ~ 0.35

Note: * values taken from Sverdrup et al. (1942)

Table 3.4 compares the concentration of chemical composition in pore fluid of BCF specimens collected at the Lynn Ary Park and the seawater. Except bicarbonate, the concentration of all ions in pore fluid is significantly lower than the averaged level of

seawater. Again, this fact may support the existence of previous salt leaching, but only when the BCF clay at the Lynn Ary Park can be confirmed to deposit in marine or at least estuarine. Two significant differences in chemical analysis results reported by USGS and UC Berkely are the pH value and dominant cation of concentration. pH value of BCF specimens collected at the Lynn Ary Park is noticeably lower than that reported by Mitchell et al. (1973). Also, sodium's predominance in pore fluid that is found by USGS is in contrast with the analysis results of Mitchell et al. (1973), which shows calcium is the most abundant cation. These differences may be attributed to the spatial variation, or possible physiochemical reactions that happened between the above two investigations, i.e., from the 1960s to 1980s.

To provide more insights regarding the cause of the BCF sensitivity, the variation of the sensitivity interpreted from the above in-situ tests is compared with the concentration profile of pore water chemical composition reported by USGS.

Figure 3.6 shows the sensitivity variation, the concentration profile of total cation (i.e., $C_{Na} + C_K + C_{Ca} + C_{Mg}$) and associated percent monovalent cations. Note that all concentrations C_i are in the unit of milliequivalents per liter, as suggested by Mitchell (1993). Following Mitchell (1993), the percent monovalent cations is defined as:

$$\frac{C_{Na} + C_K}{C_{Na} + C_K + C_{Ca} + C_{Mg}} \times 100\% \quad (3.4)$$

It can be seen that the total cation concentration in the upper stiff clay and upper soft clay layer is relatively small, and this concentration begins to increase with depth in the lower soft clay and lower stiff clay layers. Such a profile correlates well with the variation of BCF sensitivity that is interpreted from the in-situ tests at the Lynn Ary Park, in

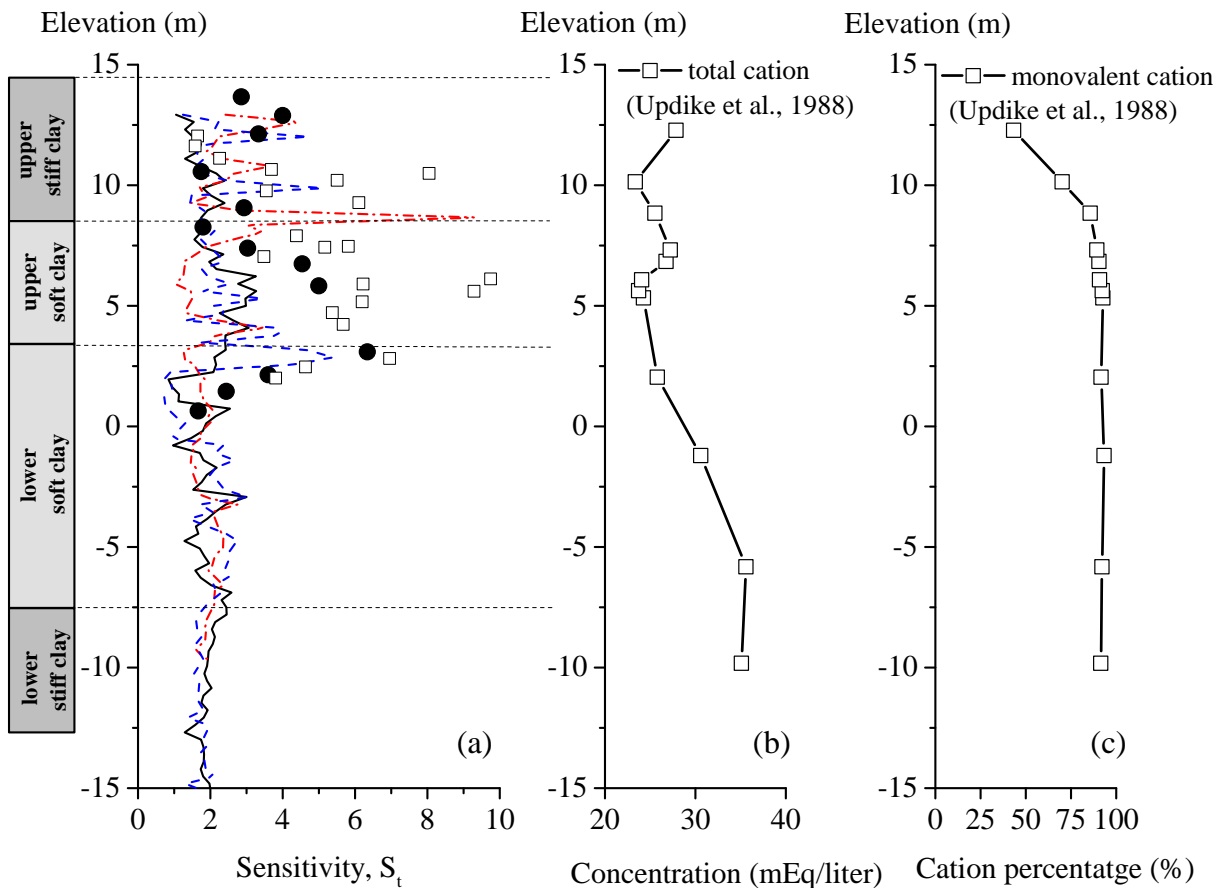


Figure 3.6. Correlation between BCF clay's sensitivity with chemical components concentration: (a) sensitivity interpreted from in-situ tests; (b) total cation concentration; (c) monovalent cation concentration percent

which clays in the upper stiff clay and upper soft clay layer has a higher sensitivity, while the sensitivity of the lower soft clay and lower stiff layer is lower and tends to decrease with depth. Moreover, in Figure 3.6 (b), one can observe two local minimum concentrations of total cation at the elevation around 10 m and 5 m. These two elevations correlate well with the elevations where the interpreted sensitivity is higher than that at the adjacent elevations. The correlation in Figure 3.6 suggests that the sensitivity of BCF clay is partially caused by the loss of cations in pore fluid, which accordingly increases the

interparticle repulsion. The stronger interparticle repulsion can lead to deflocculation of clay on mechanical remolding and thereby the reduction of remolded strength (Mitchell, 1993; Lessard and Mitchell, 1985). Figure 3.6(c) shows that the increasing sensitivity with depth in the upper stiff and soft clay layers is also correlated well with a gradual increase of percent monovalent cation with depth. This correlation suggests that in addition to the lower cation concentration, the sensitivity of BCF clay is also likely to be caused by the selective removal of divalent cations (e.g., Mg^{2+} and Ca^{2+}) from pore fluid, which can increase the repulsion force between clay particles (Moum et al., 1971; Mitchell, 1993). It is worth mentioning that the percent monovalent cation remains relatively high within the relatively insensitive layers (i.e., the lower soft clay and lower stiff clay layers). This fact suggests that the relative amount of monovalent and divalent cations may significantly affect the sensitivity of clay only when the pore fluid cation concentration is relatively small. This explanation is supported by the fact that good correlation between sensitivity and the percent of monovalent cations was found for clay with low salinity pore fluid (Moum et al., 1971; Lessard and Mitchell, 1985).

In summary, the interpretation of in-situ tests and index properties shows that the BCF clay at the Lynn Ary Park is not very sensitive, i.e., the maximum sensitivity is 10 and majority of data fall between 2 and 6.

3.4. Stability Analysis of the Turnagain Heights Slope

3.4.1. Analysis Model, Method, and Soil Parameters

The stability analysis is conducted by slice methods in a 2D stability analysis software, i.e., Slide (Rocscience Inc., 2015). The geometric model is based on a typical profile at

the east section (the same as Lynn Ary Park) of the Turnagain Heights slope before the 1964 earthquake (Figure 3.7 (a)), which was reconstructed by Seed and Wilson (1967). In this profile, the slope of the upper part of the clay layer is steeper than that of the lower part, which confirms the higher strength of the top BCF clay shown in Figure 3.2. Figure 3.7 (b) shows the geometric model used in the analysis, in which the BCF clays have been further partitioned based on the idealized stratigraphy shown in Figure 3.2. Different slopings are assigned to different portions of the slope to reproduce Turnagain Heights as realistically as possible. Also, the effects of interbedded sand/silt lenses on the slope stability are studied in this work. Given the fact that the lenses found at Turnagain Heights are not continuous throughout the BCF clay deposit (Shannon & Wilson Inc., 1964; Updike and Olsen, 1988), two extreme scenarios are modeled, i.e., no lenses and continuous lenses. The real situations shall fall between the above two limits. Figure 3.7 (b) depicts the locations and thickness of lenses in the analysis model, which is based on the interpretation shown in Figure 3.2 (b). The silt layer (i.e., mud) shown in Figure 3.7 (a) is relatively thin and has a low strength due to low confinement (i.e., submerged under the water). As a result, its effect on the stability of the Turnagain Heights is expected to be minor. Moreover, a reliable measurement of its properties is not available. Therefore, this silt layer is not modeled in the analysis. The phreatic surface (i.e., groundwater table) and pore pressure distribution used in calculating factor of safety are obtained by the seepage analyses in Slide. A fixed total head condition is assigned to the left model boundary, which is equivalent to the water table shown in Figure 3.2, i.e., elevation 17.5 m. Meanwhile, boundary a-b-c shown in Figure 3.7 (b) is also assigned a fixed total head, which is based on the water table of the pond in the model, i.e., elevation 3 m. The values

of permeability used for various soils layers are summarized in Table 3.1. An example of computed phreatic surface and pore pressure distribution is given in Figure 3.7 (c), in which pore pressure contours range between 50 kPa and 350 kPa with the interval being 50 kPa.

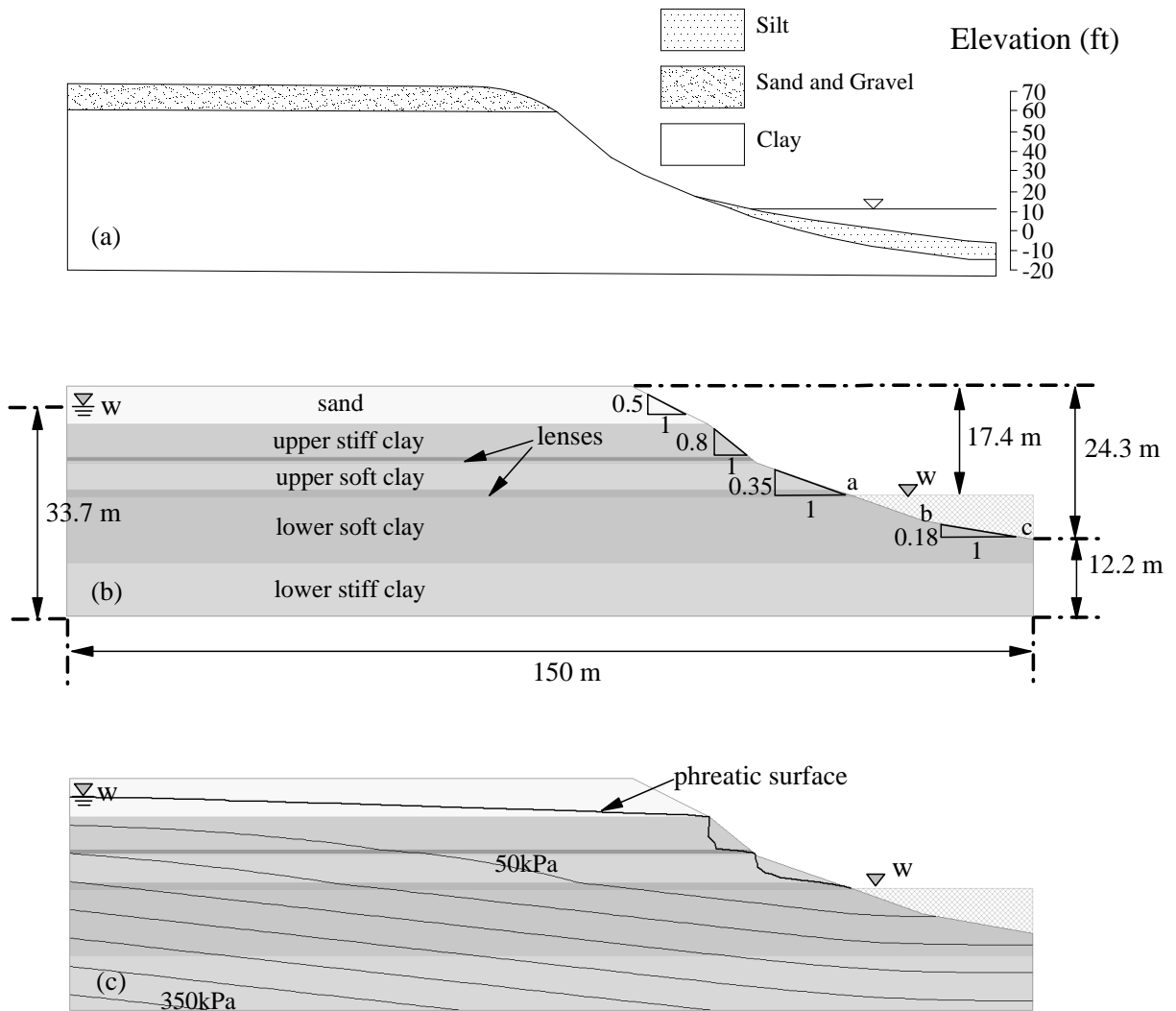


Figure 3.7. Slope stability analysis model: (a) Turnagain Heights slope profile before the 1964 earthquake (adopted from Seed and Wilson (1967)); (b) analysis model geometry; (c) phreatic surface and pore pressure contours based on seepage analysis

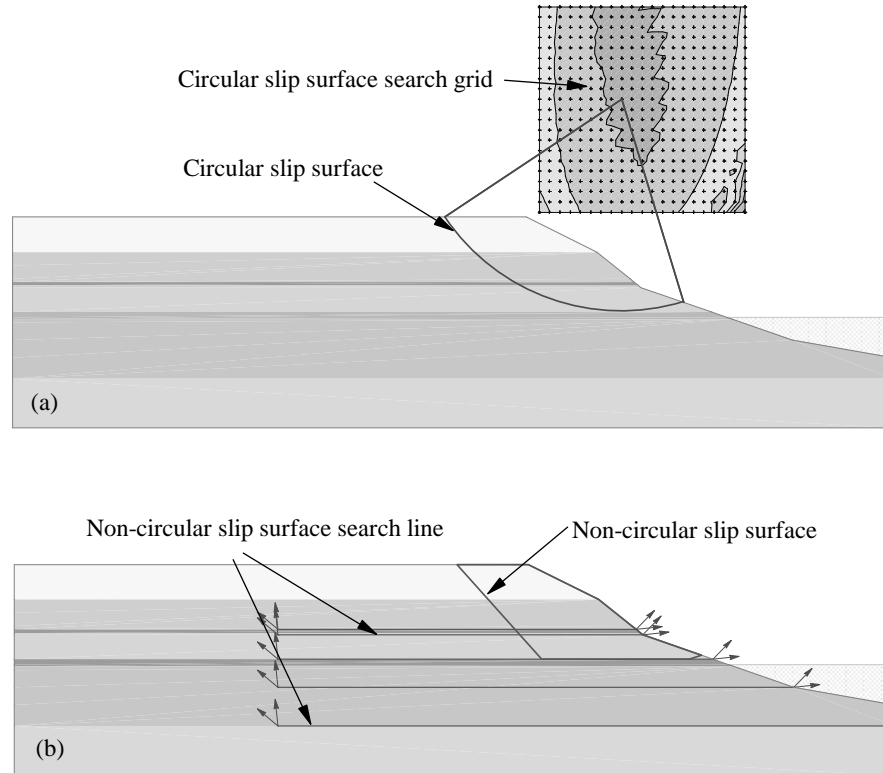


Figure 3.8. Slip surface search methods: (a) circular slip with auto grid search; (b) non-circular slip with block search

Spencer's method and Morgenstern-Price (M-P) method are used in the stability analysis to account the effects of interslice shear force. For M-P method, the interslice force function is assumed to be half sine. An extensive review of both methods, their assumptions and limitations are given by Abramson et al. (2002). Both circular slip and non-circular slip surface are checked in this work, as no decisive evidence is present regarding the shape of the very beginning slope failure in the regression landslide at Turnagain Heights. As shown in Figure 3.8, grid search and block search are used to find the global

minimum factor of safety (FS) for circular and non-circular slip surfaces, respectively. In the block search, line search objects are assigned to the elevations where the failure surface will be most likely to occur. Regarding the applying loads, only static one is considered in the current analysis. In other words, no inertial effects induced by the 1964 earthquake is taken into account, whose implications will be discussed later.

As Turnagain Heights slope failed within a relatively short period (Shannon & Wilson Inc., 1964), BCF clay layers are assumed to be undrained in the analysis while sand layer and lenses are assumed to be drained due to their permeability. The corresponding undrained shear strength and effective friction angle are given in Table 3.1. These parameters are considered to represent the in-situ soil strengths before the 1964 earthquake.

After evaluating the stability of the Turnagain Heights slope before the 1964 earthquake, the strength of BCF clay is progressively reduced in the analysis. The strength reduction needed to initiate the slide is obtained when the computed FS equals to one or is close enough to one. Considering the estimated location of slip surface in Figure 3.2, the strength reduction is only conducted in the upper stiff clay and upper soft clay layer. Three cases regarding BCF strength reduction are analyzed: (a) strength reduction in the upper stiff clay layer; (b) strength reduction in the upper soft clay layer; (c) simultaneous strength reduction in the upper stiff and soft clay layers. It is noteworthy that for the last case, the reduction amount in both layers is the same.

3.4.2. Slope Stability Before The 1964 Earthquake

Figure 3.9 presents the stability analysis results of the Turnagain Heights slope without any strength reduction, which provides an assessment of the slope stability condition

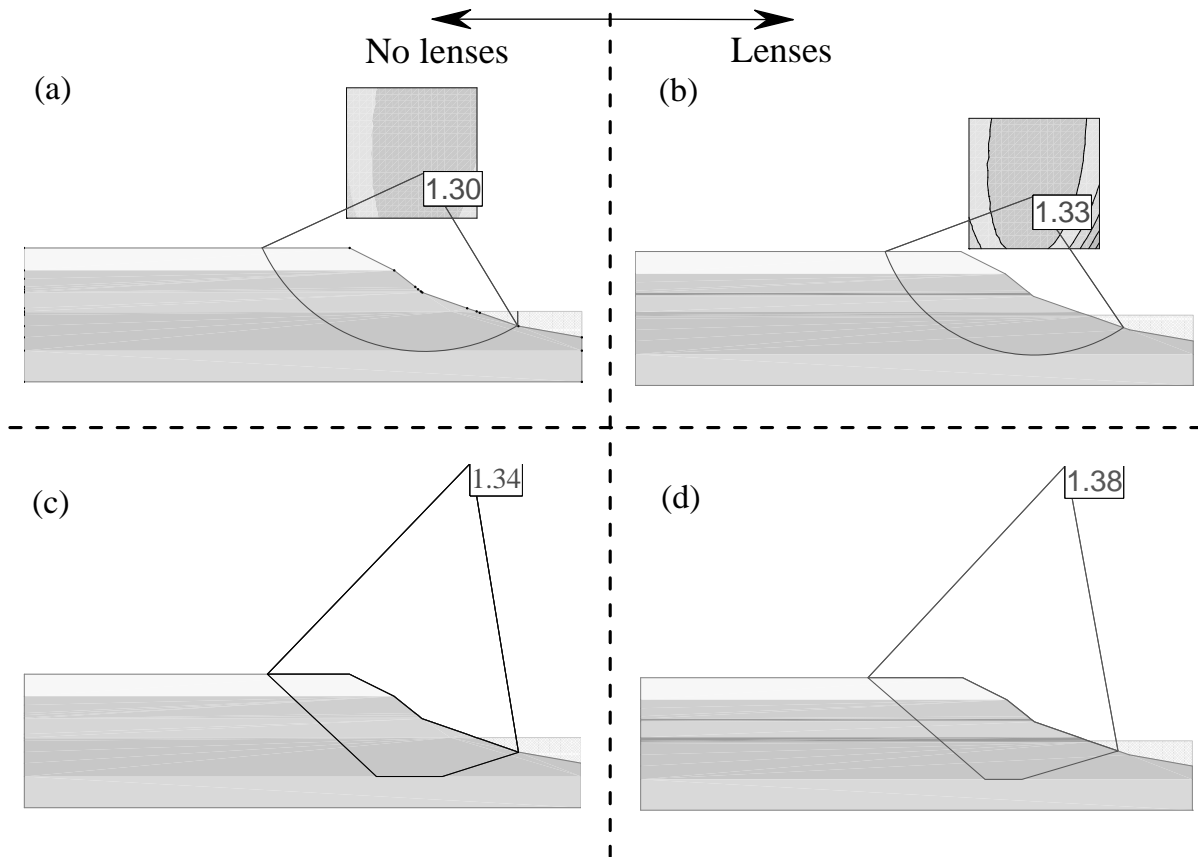


Figure 3.9. Stability FS of Turnagain Heights slope before the 1964 earthquake: (a) circular slip surface (no lenses); (b) circular slip surface (with lenses); (c) non-circular slip surface (no lenses); (d) non-circular slip surface (with lenses)

before the 1964 earthquake. Since Spencer's and M-P methods give very close results (i.e., the maximum difference in FS is 0.02), only the results based on Spencer's method is presented. Note that both the presence of lenses and the non-circular slip surface assumption tend to increase the slope stability. However, the resulted difference in stability FS is not significant, i.e., the computed FS varies from 1.30 to 1.38. The relatively safe condition implied by such FS is confirmed by the fact that the slope did not fail

during three major earthquakes from 1943 to 1954, whose magnitude is from 6.3 to 7.3 and epicentral distance varies 35 to 60 miles (U.S. Coast and Geodetic Survey, 1964). Additionally, the slope survived through the first two minutes of the 1964 earthquake. Most recently, in 2016 an earthquake with a magnitude of 7.1 and epicentral distance of 162 miles hit Anchorage and no failure was reported around the Turnagain Heights area.

3.4.3. Required Strength Reduction in BCF Clays for Landslide Initiation

Figure 3.10 presents varying FS obtained from stability analyses when the strength is gradually reduced in the upper stiff clay and upper soft clay layers. The required strength reduction for slope failure initiation is also labeled in the figure. It can be seen that two different slice methods give very close FS, and the required amount of strength reduction is slightly different under different assumptions regarding the presence of lenses and slip surface shape. Quantitatively, to independently trigger the landslide, the needed strength deterioration for the upper stiff clay is 68% to 76%, depending on the slip surface shape and whether lenses are present. On the other hand, a higher amount of strength reduction in upper soft clay layer (i.e., 80% to 88%) is required to initiate the slope failure.

Also included in Figure 3.10 is the range of the sensitivity interpreted from in-situ tests as mentioned above (gray band) for the upper stiff clay and upper soft clay layers. It is clear that the required strength reduction is compatible with the measured sensitivity at the corresponding layer, which implies the degradation of clay during earthquake and consequent strength loss is sufficient to lead to the landslide at Turnagain Heights, even if other actions (e.g., inertia force during earthquake) are not considered. Concerning the effects of slip surface shape and lenses, the presence of lenses tends to increase the required

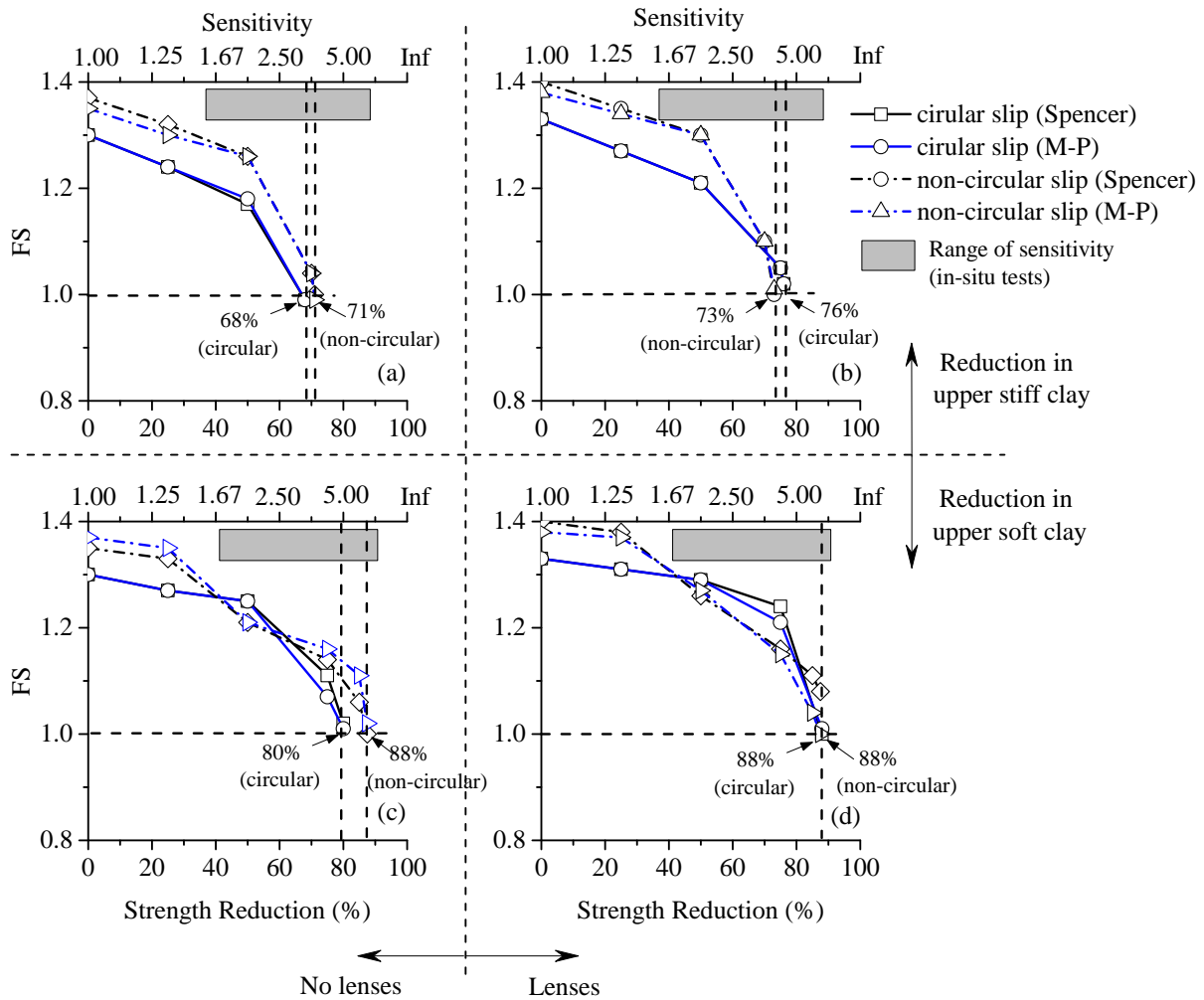


Figure 3.10. Required strength reduction for slope failure initiation: (a) reduction in upper stiff clay (no lenses); (b) reduction in upper stiff clay (with lenses); (c) reduction in upper soft clay (no lenses); (d) reduction in upper soft clay (with lenses)

strength reduction, while among the four cases considered, there is not a dominant failure slip surface mode. In other words, whether one slip surface shape is more critical than the other depends on whether lenses are present and in which layer the strength deterioration occurs.

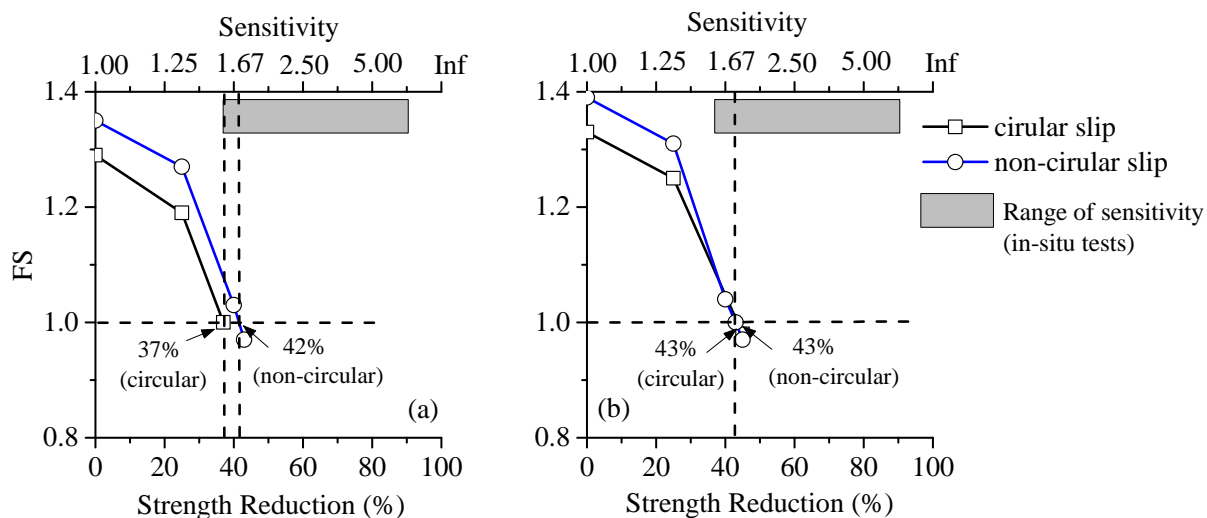


Figure 3.11. Required strength reduction for slope failure initiation: (a) simultaneous reduction in upper stiff clay and upper soft clay (no lenses); (b) simultaneous reduction in upper stiff clay and upper soft clay (with lenses)

Figure 3.11 shows the needed strength reduction to initiate slope failure when strength in both the upper stiff and soft clay layers is reduced simultaneously. It is worth mentioning that the figure only shows the results based on the Spencer method, as both methods give very close results. It can be seen that 37% to 43% strength degradation is required to initiate the slope failure, which is lower than that when the reduction is conducted in an individual layer, as one would expect. Also, this required strength loss is compatible with the sensitivity of BCF clay.

3.4.4. Effects of Earthquake Induced Excess Pore Pressure in Lenses

Seed and Wilson (1967) attributed the initiation of Turnagain Heights landslide to the liquefaction of lenses within BCF clays. This conclusion motivates a study regarding the effects of excess pore pressure in lenses on the stability of Turnagain Heights. In the SLIDE

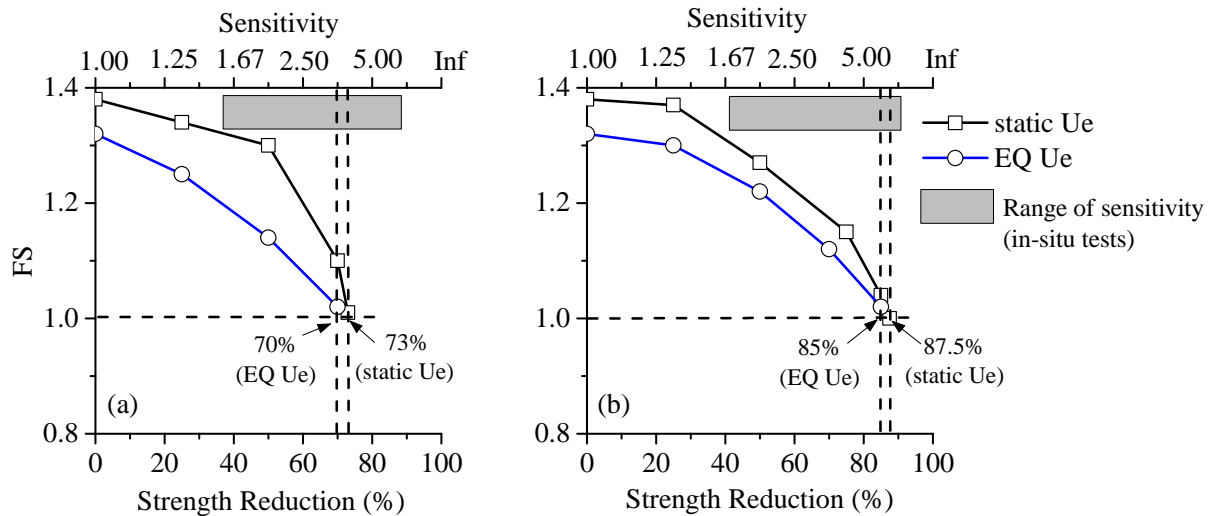


Figure 3.12. Required strength reduction for slope failure initiation with and without earthquake-induced excess pore pressure in sand/silt lenses: (a) reduction in upper stiff clay; (b) reduction in upper soft clay

software, excess pore pressure cannot be assigned manually, but is indirectly controlled by the B-bar method (Rocscience Inc., 2015). In this analysis, B-bar value of 1.7 and 2.0 are assigned to upper and lower lenses, respectively, which leads to an excess pore pressure ratio R_u of around 1.0. Such excess pore pressure is high enough to create a zero strength (i.e., liquefaction) in both lenses. Figure 3.12 compares the required strength reduction for landslide initiation under the two conditions: (1) only pore pressure determined by seepage analysis is considered (i.e., static Ue in Figure 3.12); (2) the above pore pressure is superposed with earthquake-induced excess pore pressure (i.e., EQ Ue in Figure 3.12). In such a comparison, only non-circular slip surface is considered, since failure surface that concentrates in a thin, weak layer is the most critical failure mode if the landslide is triggered by the liquefaction of lenses. Besides, only FS computed by Spencer's method is presented.

Figure 3.12 shows that the initial stability FS has decreased when the excess pore pressure above is considered, which is a result of the loss of resistance in lenses. However, the presence of excess pore pressure does not significantly alter the required amount of strength degradation in BCF clay for the sake of failure initiation, i.e., the maximum change is 3%. This result suggests that the liquefaction of lenses may not be the primary reason that triggered the Turnagain Heights landslide, since even when the lenses have lost all their resistance, the Turnagain Heights landslide could not have happened without significant reduction of the strength of BCF clay. It is worth mentioning that this conclusion is made under the particular material strength and lenses locations interpreted from the in-situ tests at the Lynn Ary Park.

3.4.5. Slip Surface at Failure

The computed slip surface at failure induced by strength degradation are presented in Figure 3.13 (circular slip surface) and Figure 3.14 (non-circular slip surface). For the purpose of comparison, the estimated location of slip surface (Seed and Wilson, 1967) is shown as the hatched zone. It is found that when strength reduction only occurs within the upper stiff clay layer, the computed circular and non-circular failure surface are restrained in the top sand layer and upper stiff clay layer. This depth of failure surface is inconsistent with the estimated location of sliding surface by Seed and Wilson (1967), which implies that the failure of Turnagain Heights is not likely to be solely caused by the strength reduction in the upper stiff clay layer. Moreover, in the experiments on BCF clay that belongs to the same geological Facies (i.e., Facies IV) as the upper stiff clay, negligible strength reduction was observed during post-cyclic shearing, after soil specimens

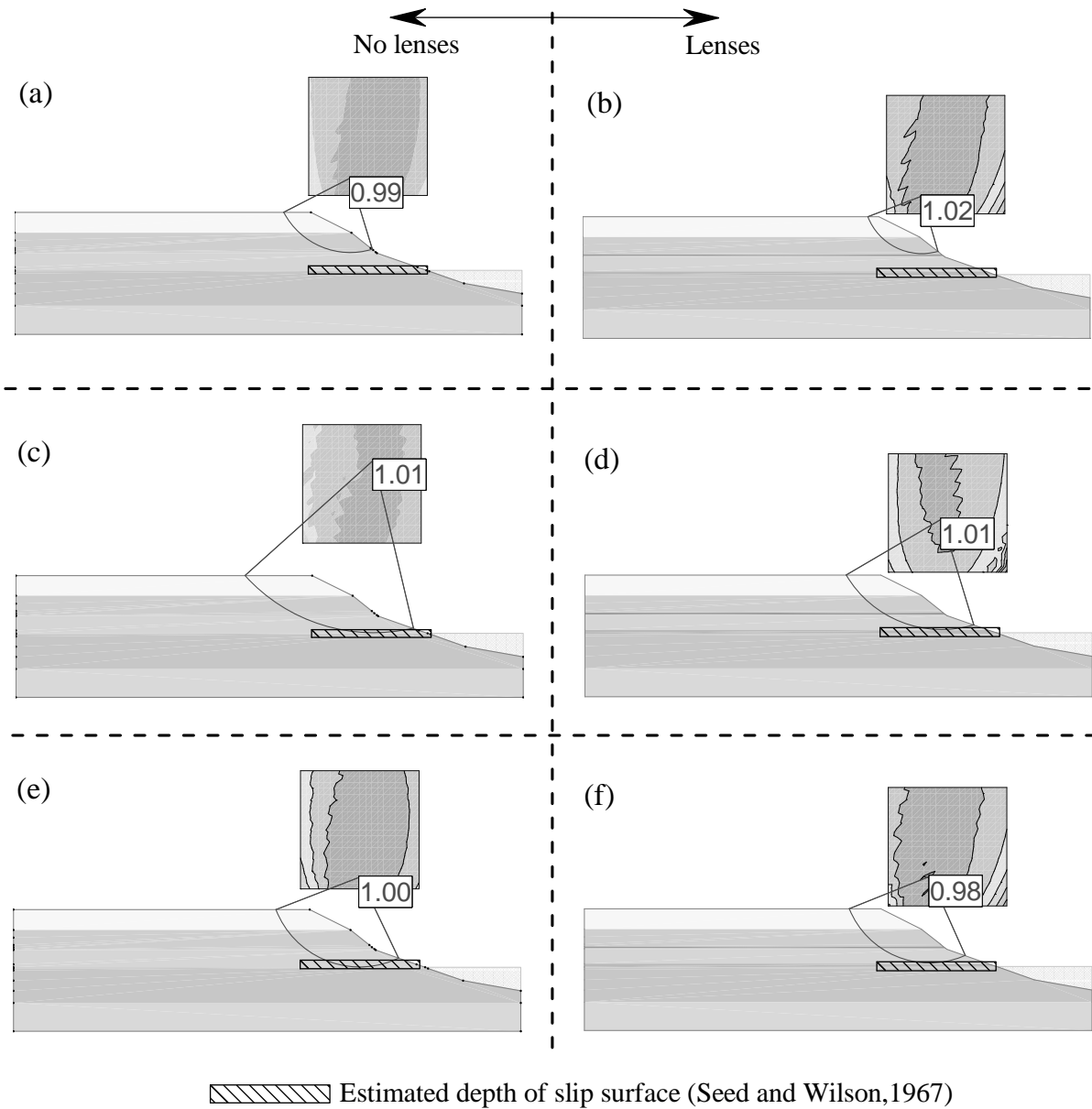


Figure 3.13. Circular slip surface at failure: (a) reduction in upper stiff clay (no lenses); (b) reduction in upper stiff clay (with lenses); (c) reduction in upper soft clay (no lenses); (d) reduction in upper soft clay (with lenses); (e) simultaneous reduction in both layers (no lenses); (f) simultaneous reduction in both layers (with lenses)

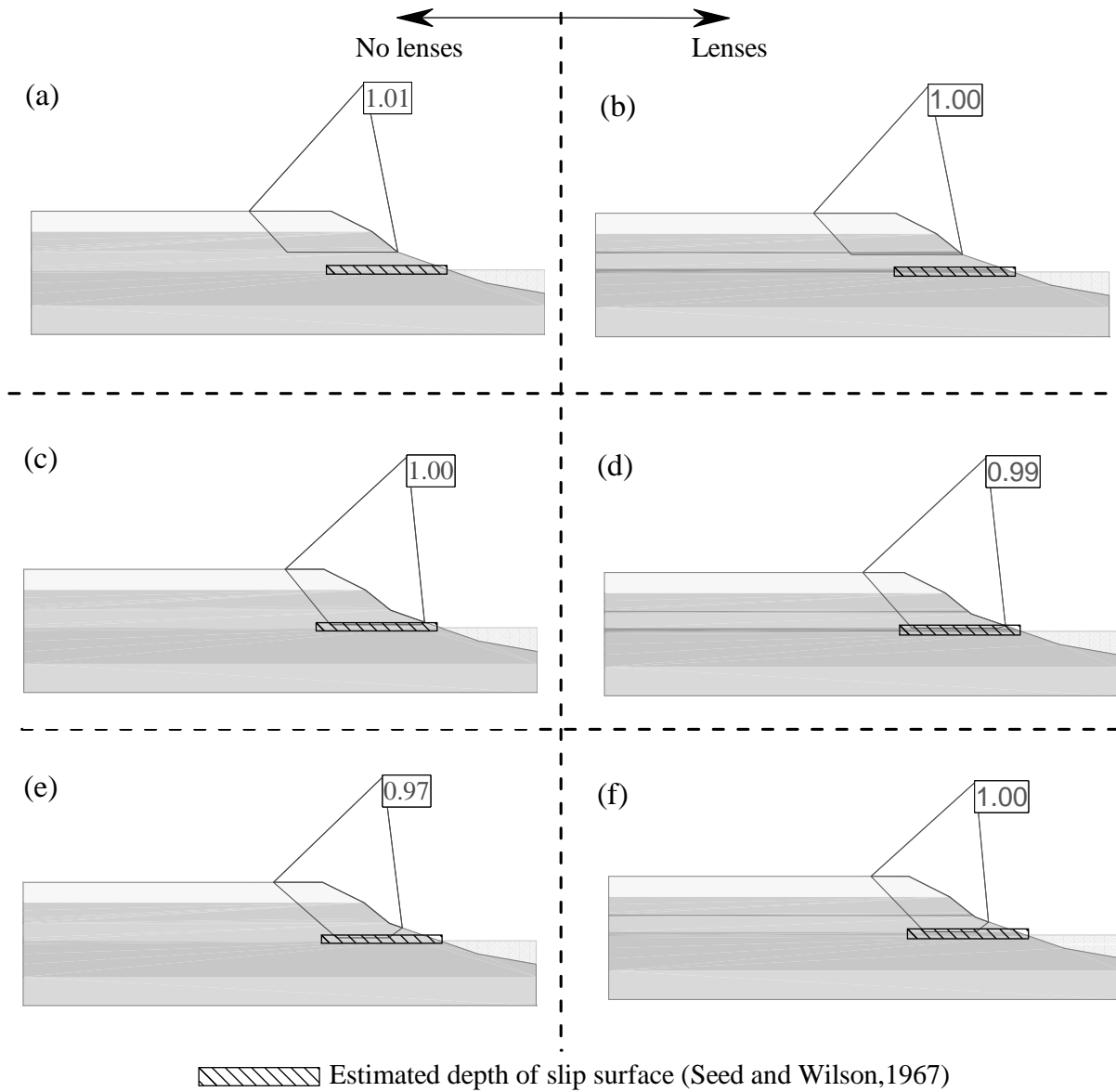


Figure 3.14. Non-circular slip surface at failure: (a) reduction in upper stiff clay (no lenses); (b) reduction in upper stiff clay (with lenses); (c) reduction in upper soft clay (no lenses); (d) reduction in upper soft clay (with lenses); (e) simultaneous reduction in both layers (no lenses); (f) simultaneous reduction in both layers (with lenses)

had experienced 40 loading cycles of $CSR = 0.2$ (Zapata-Medina, 2012). This evidence also supports the above implication. On the other hand, the failure surface induced by gradually decreasing strength in the upper soft clay layer or simultaneous strength reduction in both layers is in good agreement with the estimated sliding surface in the field, regardless of the assumptions of slip surface shape and lenses. The above findings imply that to form a sliding surface that extends to the reasonable depth determined by the field investigation, the strength reduction in the upper soft clay layer is necessary. It is worth mentioning that the above slip surface are computed under the condition that inertia forces during earthquake is not considered. It is likely that the location of slope failure surface is also affected by this inertia actions.

3.4.6. Implications Regarding Degradation During the Earthquake and Limitations of the Analysis

The above stability analysis provides an estimation of the strength reduction of the BCF clay layers needed to initiate the Turnagain Heights landslide. The results are obtained under the assumption of static failure, as the inertial actions induced by the earthquake have not been considered. This simplification implies less reduction than the estimation in this work may be sufficient to trigger slope failure during the earthquake. Accordingly, the analyses results (i.e., 68% to 76% reduction for the upper stiff clay, 80% to 88% reduction for the upper soft clay, and 37% to 43% uniform reduction for both layers) are the upper bound on the BCF clay strength degradation during the 1964 earthquake.

For the purpose of simplicity, the present analysis is based on the assumption that the strength of clay is homogeneously reduced throughout a single layer. Accordingly, the

required strength reduction obtained in the analysis represents an averaged value for the whole layer. Nevertheless, non-uniform strength deterioration within a layer is possible. In other words, a portion of clay may exhibit higher strength reduction than that at other parts of the same layer. This possibility implies that, to trigger the landslide, strength reduction that is higher than the averaged value presented in this work, may be required at some local locations of a layer.

The strength degradation during cyclic loading is a function of cyclic loading parameters (e.g., amplitude and number of cycles) and stress-strain behavior of natural clay. Therefore, to study the above non-uniform strength degradation, future work can be conducted in three steps: first, one need to conduct a wave propagation analysis to obtain the time history of cyclic shear stress, particularly the number of significant cycles and an equivalent shear stress, at representative locations of a slope, based on the ground motion at the bedrock. Then, a constitutive model can be used to quantify the strength degradation of natural clay at different locations of the slope in accordance to particular cyclic loading. Finally, the computed available strength after cyclic loading can be input into the slope stability analysis to estimate the stability condition of the slope.

Additionally, given the stress-strain behavior of sensitive clays are characterized by strain-softening, the Turnagain Heights landslide may result from a progressive failure (Bjerrum, 1967; Peck, 1967). In other words, local soil element failure leads to a growth of strains of the neighboring soils, which consequently induces their strength degradation and failure. Similar to a chain reaction, the propagation of the collapse zone eventually causes the failure of the total slope. Such progressive failure can not be modeled by the analysis method (i.e., slice method) in this work, as stability condition (i.e., FS) is

constant along the slip surface. A suitable method to model progressive slope failure will be the finite element method, for instance, the work of Eberhardt et al. (2004). Also, the finite element method can more reasonably reproduce soil behavior during dynamic loading (e.g., earthquake). In general, a reasonably accurate finite element analysis of a geotechnical problem heavily relies on the constitutive model that reproduces the stress-strain behavior of soil. In this specific case, the basic requirements for the model is to reasonably reproduce the cyclic behavior of clay and consequently quantify the clay strength loss during cyclic loading.

It is clear that at the core of both the study of uniform strength degradation in BCF clay layer and the finite element simulation of the progressive slope failure during dynamic events is a constitutive model that can quantify the cyclic strength degradation of natural clay during cyclic loading. The development and validation of such a model will be presented in Chapter 4 and Chapter 5.

3.5. Summary and Conclusions

This chapter presents a back analysis of an upper bound on the strength degradation of BCF clay needed to initiate failure of the Turnagain Height landslide during the 1964 earthquake. In-situ tests were conducted at the Lynn Ary Park, Anchorage, which is adjacent to the Turnagain Heights landslide scarp. This chapter presents the soil strength profile and stratigraphy at the Turnagain Heights area, which is generated based on the in-situ tests. The sensitivity of BCF clay is evaluated based on the same field investigations. This chapter also discusses the correlation between the interpreted sensitivity and soil index properties and pore fluid chemical compositions. Lastly, this chapter presents the

slope stability analysis of Turnagain Heights based on the strength parameters obtained from the in-situ tests, in which the stability condition before the 1964 earthquake and an upper bound on strength reduction of BCF clay to trigger the slope failure are presented. The following main conclusions can be drawn from this chapter:

- (1) The strength profile interpreted from FV and CPT tests suggests that BCF soil at the tested site (i.e., Lynn Ary Park) is overconsolidated at the top of the layer, and gradually becomes normally consolidated with depth. Also, this trend of stress history is supported by the classification of soil behavior type based on the normalized CPT data. BCF clay at this site can be divided into four sublayers based on their undrained strength variation: upper stiff clay, upper soft clay, lower soft clay and lower stiff clay.
- (2) The sensitivity of BCF clay interpreted from the in-situ tests at the Lynn Ary Park ranges from 2 to 10, with the majority of data falls between 2 and 6. This sensitivity, together with the liquidity index indicates that the BCF clay at the Lynn Ary Park is not very sensitive. Moreover, the sensitivity of the upper stiff clay and upper soft clay layers is noticeably larger than that of the lower soft clay and lower stiff clay layers.
- (3) A comparison between the pore fluid chemical composition concentration profile at the Lynn Ary Park and the variation of sensitivity suggests that the high sensitivity of the upper stiff clay and upper soft clay layers may be caused by the low concentration of total cation and the low percentage of the divalent cations.
- (4) The stability analysis based on the strength parameters interpreted from the in-situ tests shows that the Turnagain Heights slope was at a relatively safe condition

before the 1964 earthquake (i.e., $FS=1.30 - 1.38$). Furthermore, stability analysis which decreases the strength of BCF clay reveals that 68% to 76% strength reduction for the upper stiff clay is needed to trigger slope failure under static condition, while a higher strength reduction is required for the upper soft clay layer (80% to 88%). If a strength degradation uniformly occurs in both the above layers, a relatively lower reduction (37% to 43%) is sufficient to initiate the slope failure. These strength reductions represent an upper bound on the amount of degradation required to initiate failure during cyclic loading, and these results are compatible with the sensitivity interpreted from the in-situ tests implying that the degradation of BCF clays during the earthquake individually was sufficient to result in the landslide at Turnagain Heights.

- (5) The consideration of interbedded sand/silt lenses in the analysis tends to strengthen the stability of the slope slightly. And the study shows without significant reduction of the BCF clay strength, the liquefaction of such lenses during the earthquake is not able to trigger the landslide.
- (6) The current stability analyses provide an upper bound of the required strength reduction of BCF clay to initiate the landslide. Given that other unfavorable conditions (e.g., inertial forces in an earthquake) are not considered in this work, the actual strength loss is expected to be lower than the computed values. Furthermore, the above upper bound is obtained based on the assumption that the 1964 earthquake uniformly reduced the strength of clay throughout individual BCF layers. If inhomogeneous strength reduction occurred, the greater strength reduction than the analyses results might be required at local locations.

CHAPTER 4

**FORMULATION OF A CONSTITUTIVE MODEL FOR
CYCLICALLY LOADED RECONSTITUTED CLAY**

4.1. Introduction

The strength loss of natural clay during cyclic loading is the key phenomenon that is investigated in this thesis. As discussed in Chapter 2, such a degradation of material strength is related to the deterioration of soil structure and the changes of effective stress states caused by the excess pore pressures generated during undrained cyclic loading. Constitutive models that reasonably represents mechanical behaviors of natural clay during monotonic loading share an important assumption that the degradation of soil structure is driven by plastic deformations. Therefore, successful modeling of natural clay degradation during cyclic loading relies on accurate simulation of plastic deformation and pore pressure build-up during cyclic loading, as well as formulating an appropriate relation between accumulated plastic strain and resulting structure degradation.

To meet the above requirements, a constitutive model is developed in two steps. A basic model is developed within the bounding surface framework to capture the intrinsic behavior of natural clay under cyclic loading, for which the effects of structure are negligible. This model is applicable to reconstituted clays or insensitive natural clays. Then, the basic model is extended to consider structure effects typical of natural clays and the structural deterioration during cyclic loading. The present chapter has been focused on the formulation and validation of the basic model. The extended model will be discussed in Chapter 5.

As discussed in Chapter 2, a number of constitutive models developed within the framework of bounding surface plasticity can reproduce important features of clay behavior under cyclic loading. However, the image stress flow rule commonly used by these models may underestimate the magnitude of cyclic pore pressure build-up and possibly

lead to an incorrect prediction of whether the pore pressure increases or decreases during cyclic loading (shown later in this chapter.) Moreover, to the author's knowledge, no model is currently available that can reproduce both cyclic shakedown and softening. Furthermore, the clay's small strain stiffness responses are usually ignored in cyclic loading models, which may cause an underestimation of soil's non-linearity and energy dissipation when the cyclic loading is characterized by relatively small shear strains. Correspondingly, in the proposed basic model, the above issues are addressed explicitly in certain model components. A new plastic flow rule is proposed to improve the simulation of pore pressure accumulation in the bounding surface framework. Second, a new form of plastic modulus is employed which can reproduce cyclic shakedown and softening phenomenon in a unified manner. Lastly, a non-linear elasticity model is adopted which can reproduce the nonlinearity of soil when the magnitude of cyclic strains is relatively small.

This chapter is organized as follows: the formulation of the basic model in triaxial space is presented, which is followed by the demonstration of the calibration of model parameters and internal variables. Then, a series of parametric studies are presented to illustrate the roles of new model components. Lastly, the capacity of the basic model to replicate intrinsic clay behavior during cyclic loading is validated with respect to experimental evidence of reconstituted Georgia clay and insensitive Bootlegger Cove Formation (BCF) clays.

4.2. Formulation of the Basic Model

In this section, the key components of the basic model are presented, including the bounding surface, plastic flow rule, plastic modulus, discrete projection center, and elasticity model.

To clarify key features of the model, the formulation is presented in triaxial space, for which stress quantities $p = (\sigma_a + 2\sigma_r)/3$, $q = (\sigma_a - \sigma_r)$ and strain quantities $\varepsilon_v = \varepsilon_a + 2\varepsilon_r$, $\varepsilon_d = 2(\varepsilon_a - \varepsilon_r)/3$ are used. The subscripts a and r denote the axial and radial direction of a triaxial sample, and the subscript v and d denote the volumetric and deviatoric components, respectively. All the stress variables are considered effective stresses. In addition, both stress and strain, as usual in geomechanics, are assumed positive in compression.

4.2.1. Bounding Surface, Radial Mapping and Loading Surface

Experimentally defined yield envelopes of natural clay are more or less centered on the $K_{0,NC}$ line (Tavenas and Leroueil, 1977; Leroueil and Vaughan, 1990), as does the yield surface of reconstituted clay that has experienced the K_0 consolidation (Gens, 1982; Parry and Nadarajah, 1973). These observations indicate that the plasticity anisotropy of natural clay primarily results from the anisotropic consolidation history during the initial deposition and can be assumed an intrinsic property. To reproduce such an anisotropy, the yield surface proposed by Dafalias et al. (2006) has been adopted as the bounding surface in this work. In triaxial stress space, the bounding surface is expressed as:

$$F = (\bar{q} - \bar{p}\alpha)^2 - (N^2 - \alpha^2)\bar{p}(p_0 - \bar{p}) \quad (4.1)$$

A schematic diagram of the bounding surface is shown in Figure 4.1, which is a rotated

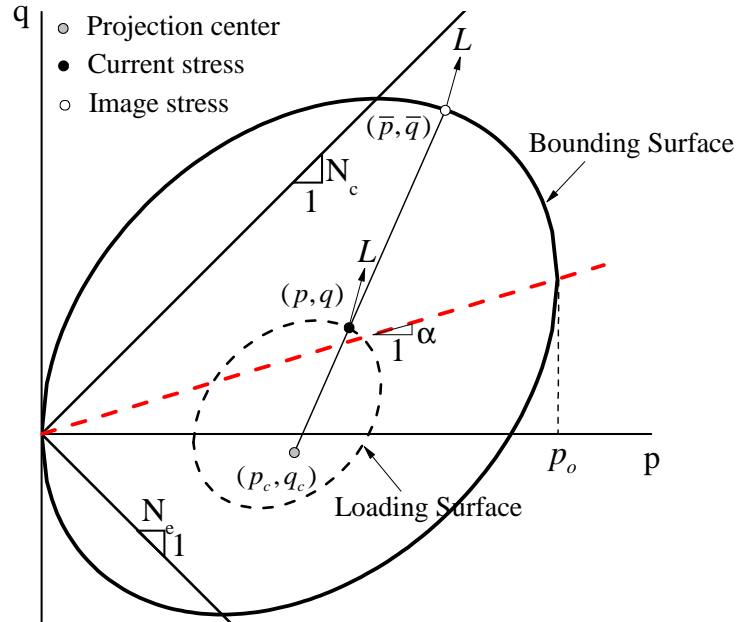


Figure 4.1. Schematic illustrations of important surfaces in the basic model in triaxial stress space: bounding surface and loading surface

and distorted ellipse. The degree of rotation and distortion is determined by the value of α , which is an internal variable representing the clay fabric anisotropy. Another internal variable, p_0 governs the size of the bounding surface, and grows or shrinks according to void ratio change in the same way as the Modified Cam-Clay model (Wood, 1990). The model constant N denotes the stress ratio (i.e., $\eta = q/p$ in triaxial space) at the peak of the bounding surface. Similar to the model proposed by Taiebat et al. (2010), the value of N is different in compression and extension loading:

$$N = \begin{cases} N_c & \text{if } \bar{q} \geq \bar{p}\alpha \\ N_e & \text{if } \bar{q} < \bar{p}\alpha \end{cases} \quad (4.2)$$

where N_c and N_e are model parameters. The need for this flexibility has been confirmed by the work of Jiang and Ling (2010), in which the equation 4.1 was used as the yield surface to fit the yield stresses of 17 types of natural clays.

The variables \bar{p} and \bar{q} in Equation 4.1 denote the pair of image stress, i.e., the open circle in Figure 4.1. In this work, such an image stress is defined by the radial mapping rule proposed by Dafalias (1986b). As shown in Figure 4.1, a projection center, (p_c, q_c) always inside the bounding surface is used to radially project the current stress, (p, q) to (\bar{p}, \bar{q}) on the bounding surface. The relation between the projection center, current stress and image stress can be expressed as:

$$\bar{p} = p_c + b(p - p_c); \quad \bar{q} = q_c + b(q - q_c) \quad (4.3)$$

where the variable b quantifies the ratio of the distance from the image stress to the projection center over the distance between the current stress and the projection center. The value of b can be obtained by substituting equation 4.3 into equation 4.1, with the current stress (p, q) being known.

Similar to other bounding surface models, the loading direction at the current stress is assumed to be the gradient of the bounding surface at the image stress (i.e., \mathbf{L} in Figure 4.1) :

$$\mathbf{L} = \partial F / \partial \bar{\boldsymbol{\sigma}} \quad (4.4)$$

Substituting equation 4.1 into equation 4.4, the loading direction in triaxial space is expressed as:

$$\mathbf{L} = \left(\frac{\partial F}{\partial \bar{p}}, \frac{\partial F}{\partial \bar{q}} \right) \quad (4.5)$$

$$\frac{\partial F}{\partial \bar{p}} = \bar{p}(N^2 - \bar{\eta}^2); \quad \frac{\partial F}{\partial \bar{q}} = 2\bar{p}(\bar{\eta} - \alpha) \quad (4.6)$$

where $\bar{\eta}$ is the image stress ratio defined as \bar{q}/\bar{p} .

Such assumption combined with the radial mapping rule, implicitly defines a loading surface (i.e., the dash line surface in Figure 4.1) passing through the current stress and being homologous to the bounding surface and with the projection center being the center of homology (Dafalias, 1986b). Consequently, the variable b in equation 4.3 can also be interpreted as the similarity ratio between the bounding surface and loading surface. Based on equation 4.3, one can prove that b decreases monotonically when the current stress moves toward the bounding surface and $b = 1$ when the current stress point is on the bounding surface (i.e., it coincides with the image stress).

4.2.2. Proposed Mixed Plastic Flow Rule and Plastic Potential Surface

As discussed in section 2.5.2, the image stress flow rule is extensively employed by models developed within the bounding surface plasticity framework. In other words, the plastic flow direction is the gradient of a plastic potential passing the image stress (i.e., R_i in Figure 4.2). If the plastic potential is assumed to be the same as the bounding surface, then an associative flow rule is generated.

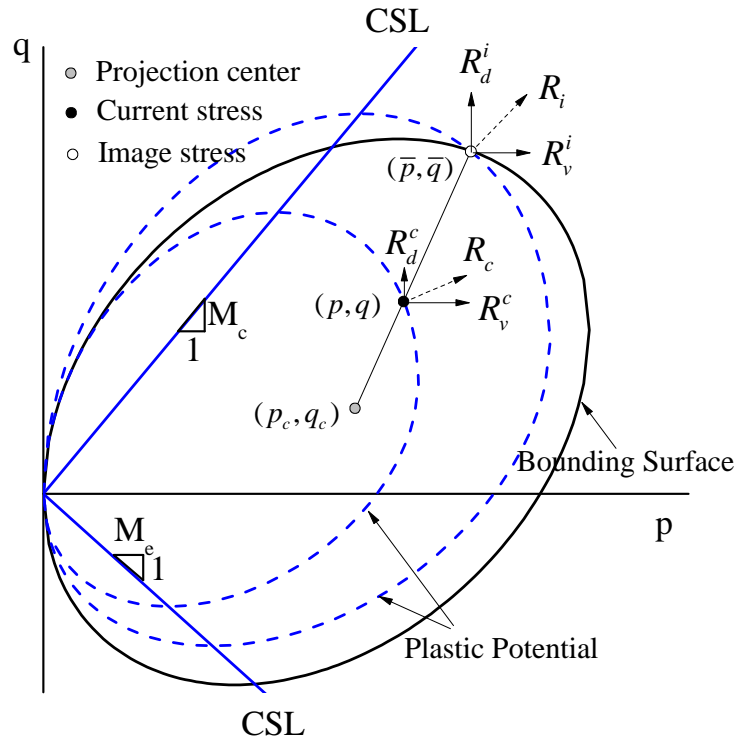


Figure 4.2. Schematic illustration of plastic flow direction defined at image stress and current stress

The proposed mixed flow rule is inspired by experimental observations of cyclic loading on BCF clays (Zapata-Medina, 2012). Based on the concept of critical state (Schofield and Wroth, 1968), the critical state line in triaxial stress space divides the stress space into two zones: plastic contraction and plastic dilation. When the current stress state is inside the contraction zone, monotonic shearing that mobilizes plasticity will induce positive excess pore pressure under undrained conditions, and when the current stress state is inside the zone of plastic dilation, negative excess pore pressure will be generated. In the experiments of BCF clay, the effective stress paths of tests characterized by positive excessive pore pressure build-up mostly fall into the zone of plastic contraction. This observation indicates the need to explicitly consider the role of the current stress state in the

determination of the plastic flow direction, especially the state of plastic contraction or dilation. Therefore, the proposed flow rule incorporates characteristics of plastic volume change defined at the current stress into the existing image stress flow rule. This proposition is also consistent with other experimental evidence, which shows the dependence of soil plastic flow direction on the current stress state (Taylor, 1948; Schofield and Wroth, 1968; Graham et al., 1983).

The plastic flow direction in triaxial space is composed of volumetric and deviatoric components:

$$R = (R_v, R_d) \quad (4.7)$$

In the mixed flow rule, the volumetric component is a combination of gradient of plastic potential defined at the image stress and current stress, while the deviatoric component is solely determined by the image stress:

$$R_v = R_v^i g_i + R_v^c (1 - g_i); \quad R_d = R_d^i \quad (4.8)$$

where superscripts i and c denote the gradient of plastic potential defined at the image stress and current stress, respectively, as shown in Figure 4.2. The distribution variable g_i is postulated as:

$$g_i = \left(\frac{1}{b} \right)^w \quad (4.9)$$

where b is the similarity ratio introduced in equation 4.3. As one will see in the section 4.2.3, the variable b obtains a value that tends to be infinite after stress reversal (i.e., unloading or reloading) and then gradually decreases as the current stress moves

towards the bounding surface. Therefore, equation 4.8 and 4.9 together imply that the current stress state plays a prevailing role in the determination of plastic flow direction after stress reversal, and the image stress plays an increasingly important role when the current stress is moving towards the image stress. Moreover, when a stress point is on the bounding surface (i.e., $b = 1$), the plastic flow rule, based on equation 4.8, is exclusively determined by the image stress. Therefore, equation 4.9 guarantees a smooth transition in plastic flow direction between the stress states inside and on the bounding surface. The material constant w is introduced to control the relative contribution of the aforementioned two flow directions. A larger value of w will put more weight on the plastic flow direction determined at the current stress. It is noteworthy that image stress flow rule can be recovered as a special case (i.e., $w = 0$) of the proposed flow rule.

The proposed mixed flow rule is general and can be applied to various forms of plastic potential. The plastic potential surface originally proposed by Dafalias (1986a), which can consider the influence of fabric anisotropy, is adopted in this work, as shown in Figure 4.2:

$$g = (q - \alpha p)^2 - (M^2 - \alpha^2)p_a(p_a - p) \quad (4.10)$$

The variable p_a in equation 4.10 is a dummy variable and varies so that the plastic potential surface can pass through either the image stress or current stress. M is the stress ratio at critical state. It is assumed the value of M depends on the location of image stress in the same way as the parameter N :

$$M = \begin{cases} M_c & \text{if } \bar{\eta} \geq \alpha \\ M_e & \text{if } \bar{\eta} < \alpha \end{cases} \quad (4.11)$$

where M_c and M_e denote the critical state stress ratio in triaxial compression and extension, respectively. Since the condition of $\bar{\eta} \geq \alpha$ indicates compression loading while extension loading corresponds to $\bar{\eta} < \alpha$, equation 4.11 is able to capture the varying failure stress ratio as a function of mode of shearing. By comparing equation 4.10 and 4.1, one can find the rotation and distortion of the plastic potential surface is characterized by the same variable α as the bounding surface. This assumption is made to simplify the model. A similar assumption has been employed in both classical elastoplasticity models (e.g., Wheeler et al. (2003) and Jiang and Ling (2010)) and bounding surface models (e.g., Liang and Ma (1992) and Seidalinov and Taiebat (2014)). When an upper bound of rotation variable α is enforced, which is lower than current stress ratio η (e.g., the models proposed by Wheeler et al. (2003) or Dafalias et al. (2006)), the above simplification in classical elastoplasticity models may lead to undesired consequences, e.g., a higher positive excess pore pressure and an excessive elastic zone computed in the initial stage of CK₀TXC and CK₀TXE on NC clay, respectively (Taiebat et al., 2010). Nevertheless, based on the comparison of model simulations made with the above simplification and one made with the assumption that the rotation variable of a yield surface and plastic potential are different, Taiebat et al. (2010) concluded that such a simplification can provide an acceptable level of accuracy.

Based on the adopted plastic potential, the volumetric and deviatoric components of the flow direction defined at the image stress can be expressed as

$$R_v^i = \frac{\partial g}{\partial \bar{p}} = \bar{p}(M^2 - \bar{\eta}^2); \quad R_d^i = \frac{\partial g}{\partial \bar{q}} = 2\bar{p}(\bar{\eta} - \alpha) \quad (4.12)$$

Correspondingly, the volumetric component of flow direction at the current stress is given by:

$$R_v^c = p(M^2 - s_l \eta^2) \quad (4.13)$$

Note that the variable s_l is introduced to reproduce plastic contraction after stress reversal and a subsequently monotonic decrease of plastic contraction, as observed in experiments on clay and gravel (Sheu, 1985; Kong et al., 2016). A similar strategy has been employed by Dafalias and Manzari (2004) to model the cyclic behavior of sand. The value of s_l depends on the loading direction and current stress ratio:

$$s_l = \begin{cases} 1 & \text{if } (\bar{\eta} - \alpha)\eta \geq 0 \\ -1 & \text{if } (\bar{\eta} - \alpha)\eta < 0 \end{cases} \quad (4.14)$$

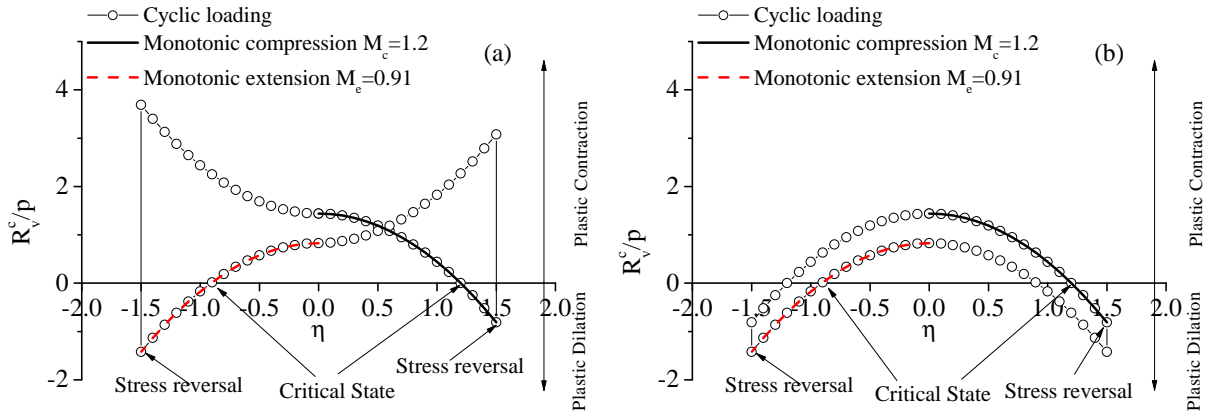


Figure 4.3. Schematic illustration of normalized R_v^c evolution during cyclic loading: (a) s_l varies based on equation 4.14; (b) $s_l = 1$

The concept behind variable s_l is seen in Figure 4.3(a), in which the evolution of normalized R_v^c with respect to p during a loading cycle is illustrated. The positive and negative value of variable R_v^c/p denote plastic contraction and dilatation, respectively. The

stress path starts from $\eta = 0$ and follows a compression loading path (i.e., $d\eta > 0$ and $\bar{\eta} > \alpha$). Such a loading path, during which η reaches 1.5, is followed by a unloading path (i.e., $d\eta < 0$ and $\bar{\eta} < \alpha$) to $\eta = -1.5$. After this, stress reversal occurs again and brings the stress ratio, η back to zero. Figure 4.3 also includes the evolution of R_v^c/p in monotonic compression and extension loading, which will be predicted by classical elastoplasticity models based on the same plastic potential shown in equation 4.10 (e.g., SANICLAY model by Dafalias et al. (2006)). From Figure 4.3(a), one can see that the normalized R_v^c during the first loading branch of the cyclic loading is the same as monotonic compression and material behavior changes from plastic contraction to plastic dilation as the increase of stress ratio. The stress ratio corresponding to the above phase transition is the same as the critical state. Upon unloading, soil jumps to plastic contraction even if the state before unloading is plastic dilation. This is consistency with the experimental observations in undrained cyclic loading, which show positive pore pressure is generated during unloading even if clay samples have the tendency to dilate before unloading (Sheu, 1985; Zergoun and Vaid, 1994). During continuous unloading, material's tendency to contract progressively reduces. After the stress ratio passes zero, predicted evolution of R_v^c follows the same path as monotonic extension tests until the occurrence of the next stress reversal, after which plastic contraction will be predicted again. Kong et al. (2016) conducted cyclic triaxial tests on gravel and extracted the stress-dilation relation in both loading and unloading. They found during unloading that follows a monotonic compression loading, soil exhibits strong plastic contraction even if it is close to critical state before unloading. If this unloading continues, they found, degree of plastic contraction decreases and the stress-dilatancy curve will gradually converge to the one corresponding to monotonic extension

loading. The same trend is also observed in tests that begin with monotonic extension loading. Such an experimental observation provides additional justification to the relation shown in Figure 4.3(a). In Figure 4.3(b), the above analysis is repeated with $s_l = 1$. It can be seen that upon unloading/reloading, soil will remain plastic dilation if this state has been reached before the stress reversal. Furthermore, during monotonic loading which follows stress reversal, the degree of plastic contraction first gradually increases then decreases, which is inconsistent with experimental observations.

To provide more insight about the proposed flow rule, plastic flow directions computed based on various flow rule assumptions in a simulation of undrained cyclic tests on an isotropically consolidated NC clay are presented in Figure 4.4. The black arrows in the figure indicates the plastic flow directions and the solid curve represents the corresponding effective stress path. It can be seen from Figure 4.4(a) that the plastic flow directions computed based on the image stress flow rule point approximately along the vertical direction during the second cycle indicating small plastic volumetric strain rates. Consequently, the computed effective stress stops migrating towards the origin of stress space. Figure 4.4(a) also shows that the aforementioned small plastic volumetric strain rate results from that the image stress is close to the critical state line. Figure 4.4(b) presents the same simulation based on the proposed mixed flow rule, in which as the current stress approaches the critical state line, plastic flow changes from contraction to dilation (i.e., the plastic flow arrow points to the right first, then changes to the left). The computed phase transition between contraction and dilation happens at stress ratio lower than that of the critical state, as observed in experiments (Sangrey et al., 1969; Zergoun, 1991). This observation heights the need to mix the flow direction defined at

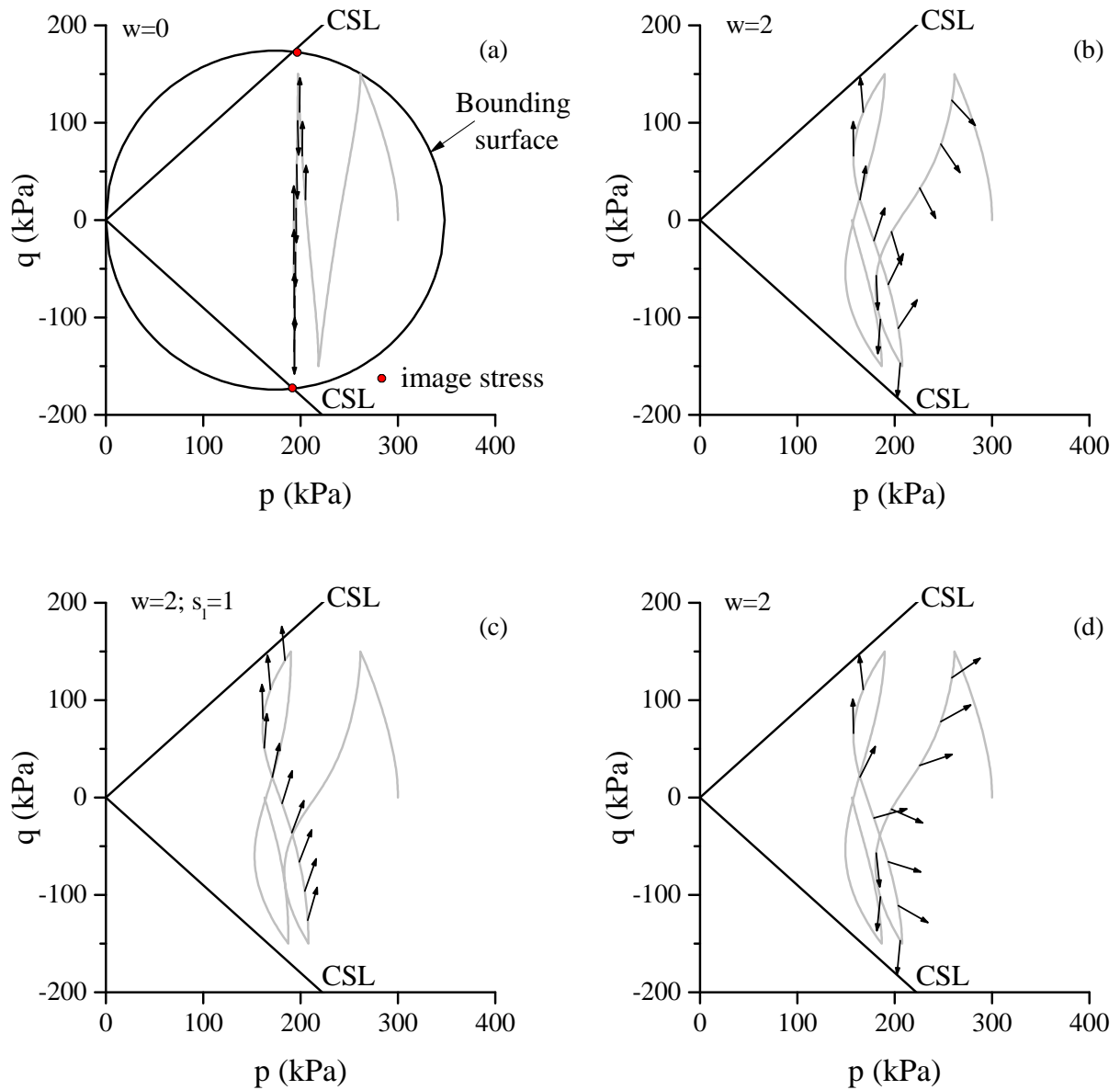


Figure 4.4. Plastic flow direction in a undrained cyclic loading tests under different assumptions of plastic flow rules: (a) image stress flow rule; (b) proposed flow rule; (c) proposed flow rule with $s_l = 1$; (d) mixed flow rule with deviatoric component

the current stress with that defined at the image stress, because, otherwise, the stress ratio for the phase transition will be the same as the critical state, as shown in Figure 4.3.

Figure 4.4(b) also shows that after stress reversal, the plastic flow features plastic contraction, which also applies to the case that soil tends to dilate before the stress reversal. From a modeling point of view, such a plastic contraction after stress reversal is the key to capturing the pore pressure build-up in cyclic loading (Dafalias and Manzari, 2004). Moreover, the degree of the above plastic contraction progressively decreases until the occurrence of the phase transition, which is reflected by the increasing inclination of flow direction arrow with respect to the p axis. As a result of the above features, the typical butterfly shape stress path is reproduced by the simulation based on the mixed flow rule. Figure 4.4(c) presents the simulation when $s_l = 1$ is fixed in the proposed flow rule. After stress reversal, the inclination of plastic flow direction first decreases then increases. This phenomenon reflects, as expected, the degree of plastic contraction after stress reversal unrealistically first increases then decreases.

In fact, one may find that in the proposed flow rule, the current stress only plays a role in the determination of the volumetric component of plastic flow direction. The reason can be seen in Figure 4.4(d), which presents the simulation results under the condition that the deviatoric component of flow direction is a similar combination as the volumetric component i.e.,:

$$R_d = R_d^i g_i + R_d^c (1 - g_i) \quad (4.15)$$

with

$$R_d^c = \frac{\partial g}{\partial q} = 2p(\eta - \alpha) \quad (4.16)$$

Take the first unloading as an example, the plastic flow direction gradually changes from pointing upwards to a downward direction, which implies the deviatoric component of the

plastic flow direction, R_d , changes its sign. The reason is that the value of R_d^c changes its sign when the stress path passes the rotation axis, i.e., $\eta = \alpha$. Note that before a stress reversal the deviatoric component of loading direction, L_d , remains the same sign. Therefore, the deviatoric components of the plastic flow direction and loading direction will point to the opposite directions during certain stages, which may induce artificial material instability that has no physical meanings (compared with the instability that corresponds to static liquefaction of loose granular material (Buscarnera and Whittle, 2013)). Furthermore, this will create a non-smooth stress-strain curve that only preserves the continuity of a C^0 class.

Finally, it is worthy noting that when a stress point reaches the bounding surface and stays on the bounding surface (i.e., a monotonic loading path), the well-verified plastic flow rule proposed by Dafalias (1986a) is recovered by the proposed flow rule, irrespective of the value of parameter w . This is the key to allowing the proposed model to capture complex soil cyclic behavior, while maintaining advantages of the earlier constitutive models in terms of modeling soil responses in monotonic loading.

4.2.3. Discrete Projection Center and Its Evolution Law

Being a key element, the choice of projection center can significantly impact the plastic behavior of soil predicted by a bounding surface model. As discussed in Chapter 2, a fixed projection center will lead to over-damping in simulations of cyclic loading. Therefore, a discrete projection center is employed in the proposed model. The concept of discrete projection center is illustrated in Figure 4.5, in which the projection center will be updated to the current stress once a stress reversal is detected. In this work, stress reversal is

triggered when:

$$\mathbf{L}\dot{\boldsymbol{\sigma}}_{trial} < 0 \quad (4.17)$$

The same criteria has been successfully used in various models (Pastor et al., 1990; Wang et al., 1990; Andrianopoulos et al., 2010; Seidalinov and Taiebat, 2014).

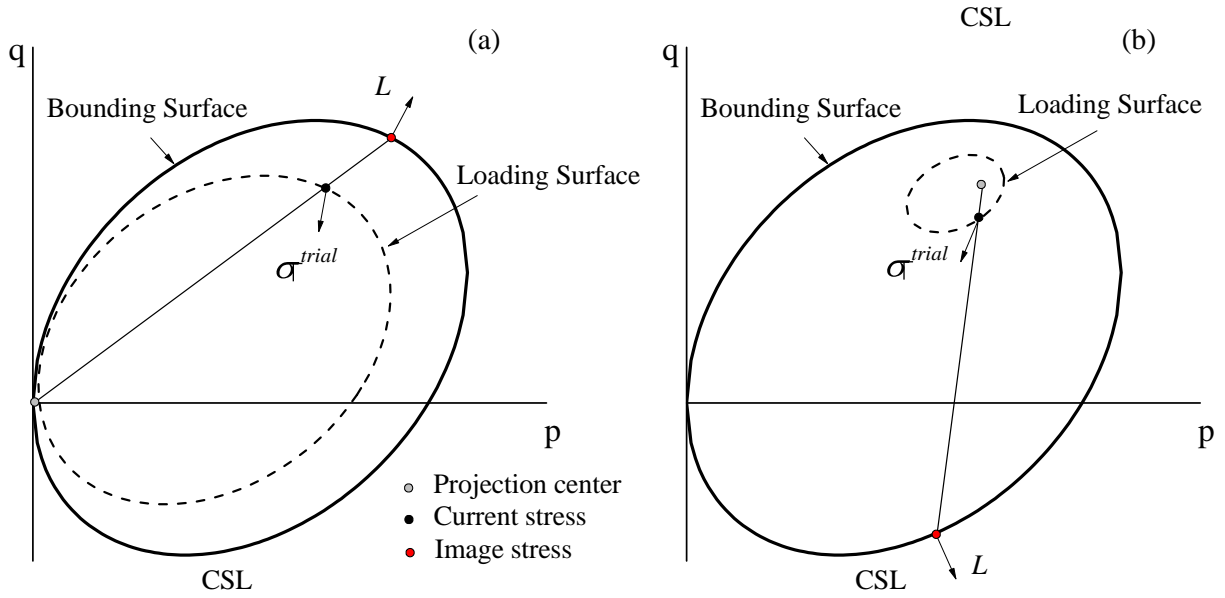


Figure 4.5. Schematic illustration of projection center update at stress reversal : (a) the detection of stress reversal at current step (step i); (b) forming of new loading surface at next step (step $i + 1$)

One can find, by referring to equation 4.3, the image stress loses its definition and b value is infinity after the projection center is updated to the current stress, i.e., the projection center coincides with the current stress. As a result, a singularity will happen if the current step is still treated as a normal elastoplasticity computation. To overcome it, the step (e.g., step i), whose trial stress rate $\dot{\boldsymbol{\sigma}}_{trial}$ triggers the stress reversal and update of the projection center, is assumed to involve only the elastic update of stress, i.e., $\dot{\boldsymbol{\sigma}} = \dot{\boldsymbol{\sigma}}_{trial}$ and internal variables are frozen. Such an elastic update will separate the

current stress from the projection center so that normal elastoplasticity computation can continue from the next step (i.e., step $i + 1$). Comparison of the loading surfaces in Figure 4.5(a) and (b) reveals that the similarity ratio b is significantly enlarged after the update of the projection center. Consequently, the magnitude of plastic modulus increases, which predicts stiffer response than what would be predicted if a material is being monotonically loaded. Subsequently, as the current stress moves towards the bounding surface, the b value decreases, the plastic modulus decreases and softer stress strain response is reproduced. As a result, the discrete projection center can realistically reproduce soil's non-linearity during unloading and reloading and correspondingly stress-strain hysteresis observed in cyclic loading tests, when the cyclic shear stress is relative large and plastic deformation is the dominant component of total deformation. When cyclic shear stress is relative small and elastic strain dominates, soil's non-linearity and hysteresis loop are mainly reproduced by non-linear elasticity model that will be introduced later.

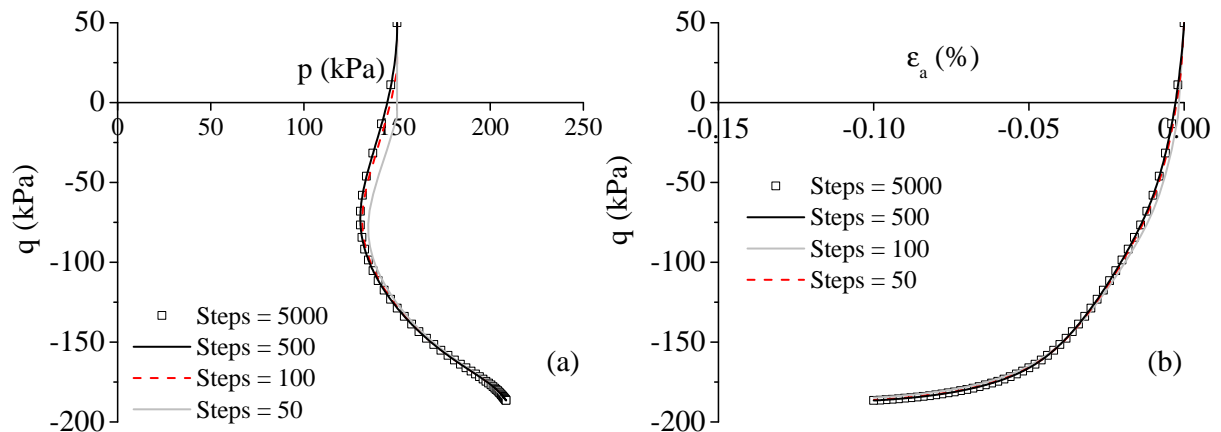


Figure 4.6. Influence of computation step size on computed stress-strain response after the stress reversal

While the proposed strategy can successfully overcome the singularity after the stress reversal, it inevitably makes the computed stress-strain response after a stress reversal dependent on the step size in a computation. Figure 4.6 evaluates the influences of the step size on the computed stress-strain response of a undrained extension test. As the projection center is initially assigned at the origin of stress space, the stress reversal will be triggered at the beginning of the simulation. Note that in this particular case the computed results are relatively insensitive to the selected step size. Moreover, as the step number increases, the computed response converges to a unique one, which suggests once the step size in a computation is small enough, the corresponding stress-strain response obtained from the model is not step-size dependent anymore.

For the sake of the uniqueness of the image stress, the projection center is required to be inside or on the bounding surface, despite of changes in size, shape and inclination of the bounding surface. To achieve this, an evolution rule is proposed that governs the change of the projection center between consequent stress reversals. First, two variables X_p and X_d are introduced to define the position of the projection center relative to the bounding surface, as shown in Figure 4.7:

$$X_p = \frac{p_c}{p_0}; \quad X_d = \frac{q_c - q_a}{q_b - q_a} \quad (4.18)$$

where q_b is the deviatoric stress at the intersection between the bounding surface and the vertical line passing the projection center, i.e., $p = p_c$. It is noteworthy that the intersection considered is the one above the bounding surface rotation axis, $q = p\alpha$. The variable q_a is the intersection between the rotation axis and the vertical line $p = p_c$. It is clear that X_p and X_d define the relative position of the projection center along

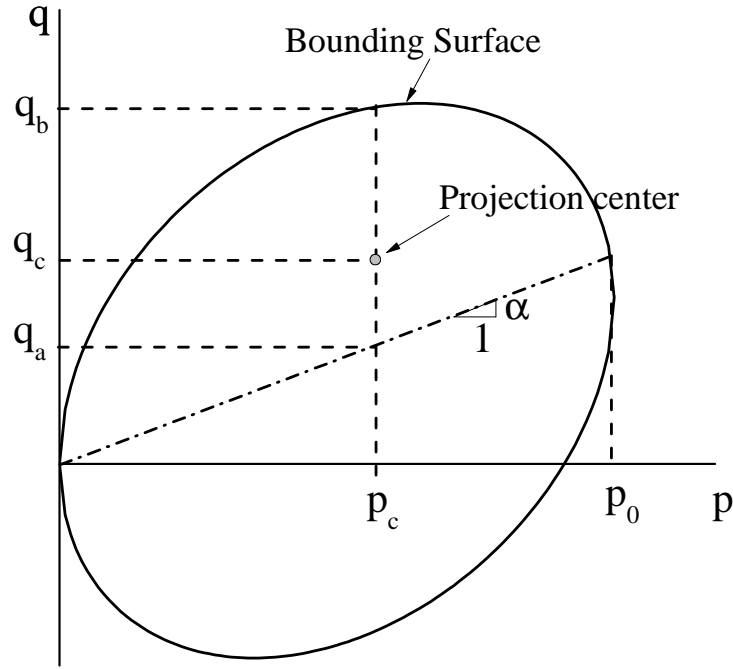


Figure 4.7. Schematic illustration of projection center location relative to the bounding surface

the hydrostatic axis (i.e., p axis) and along the deviatoric plane, respectively. Through differentiating equation 4.18 and assuming X_p and X_d are constant, the rate form of projection center evolution rule is obtained as a function of changes of internal variables p_0 and α :

$$\dot{p}_c = \frac{p_c}{p_0} \dot{p}_0; \quad \dot{q}_c = \frac{q_c}{p_0} \dot{p}_0 + \frac{N_c^2 p_c - \alpha q_c}{N_c^2 - \alpha^2} \dot{\alpha} \quad (4.19)$$

It is observed that the change of p_c is only related to the size change of the bounding surface, while the evolution of q_c is a result of the combination of changes in size, inclination and distortion of the bounding surface. It is worth mentioning that the SANICLAY-B model employed a similar evolution law for the projection center (Seidalinov and Taiebat, 2014). Compared with it, the law in equation 4.19 can guarantee that the projection

center remains the same location relative to the bounding surface even when the size and inclination of the bounding surface change simultaneously.

4.2.4. Internal Variables Hardening Laws and Plastic Modulus

Isotropic hardening: The evolution of internal variable p_0 is governed by the same isotropic hardening law as the Modified Cam Clay (Wood, 1990):

$$\dot{p}_0 = \left(\frac{1+e}{\lambda-\kappa} \right) p_0 \dot{\varepsilon}_v^p = \langle \Lambda \rangle \bar{p}_0; \quad \bar{p}_0 = \left(\frac{1+e}{\lambda-\kappa} \right) p_0 R_v \quad (4.20)$$

where λ and κ are model constants, which represent the slope of isotropic virgin compression line and rebound line in $e - \ln p$ plane, respectively. e is the current void ratio indicating the logarithm strain is used. The variable \bar{p}_0 is a components of vector \mathbf{r} in equation 2.5, which guides the direction for p_0 evolution.

Rotation hardening: The change of anisotropy of both the bounding surface and plastic potential surface is governed by the rotation hardening law proposed by Dafalias et al. (2006):

$$\begin{aligned} \dot{\alpha} &= \left(\frac{1+e}{\lambda-\kappa} \right) C \left(\frac{\bar{p}}{p_0} \right)^2 |\dot{\varepsilon}_v^p| |\bar{\eta} - \chi\alpha| (\alpha_b - \alpha) = \langle \Lambda \rangle \bar{\alpha} \\ \bar{\alpha} &= \left(\frac{1+e}{\lambda-\kappa} \right) C \left(\frac{\bar{p}}{p_0} \right)^2 |R_v| |\bar{\eta} - \chi\alpha| (\alpha_b - \alpha) \end{aligned} \quad (4.21)$$

Similar to the SANICLAY-B model (Seidalinov and Taiebat, 2014), in equation 4.21, the originally used current stress quantities has been replaced by the corresponding image stress quantities. This is done with the intention to ensure that the plastic modulus at the image stress, \bar{K}_p , can be directly derived from the consistency condition of the bounding surface. Also, this modification implies the evolution of α is determined by

the image stress instead of the current stress. While all unintended effects are unclear now, it is believed that such a modification will not significantly change basic responses associated with equation 4.21, originally designed for monotonic loading, as the plastic strain is relatively small when the stress is inside the bounding surface and the image stress coincides with the current stress when the stress point is on the bounding surface, at which time major plastic strain develops. The model parameter C in equation 4.21 quantifies the rate of rotation. The parameter χ governs the upper bound of α during constant stress ratio loading. In other words, the evolution of α will stop ($\dot{\alpha} = 0$) when its value reaches $\bar{\eta}/\chi$. Since except $(\alpha_b - \alpha)$, all terms in equation 4.21 are positive, α will evolve towards the variable α_b . Besides, variable α_b serves as an upper bound of α , which is required for equation 4.1 and 4.10 to have real-value roots. In triaxial space, α_b is determined by:

$$\alpha_b = \begin{cases} \min(M_c, N_c) & \text{if } \bar{\eta}/\chi \geq \alpha \\ \max(-M_e, -N_e) & \text{if } \bar{\eta}/\chi < \alpha \end{cases} \quad (4.22)$$

Since p_0 and α are the only two internal variables for the basic model, the vector \mathbf{r} in equation 2.5 is correspondingly constructed as:

$$\mathbf{r} = [\bar{p}_0, \bar{\alpha}] \quad (4.23)$$

Plastic Modulus: A specific feature of bounding surface models is that the plastic modulus, K_p is related to the plastic modulus at image stress, \bar{K}_p through a function of the distance between the current stress and image stress. When the radial mapping rule

is employed, K_p can be generally expressed as:

$$K_p = \bar{K}_p + f(b) \quad (4.24)$$

where \bar{K}_p is obtained by enforcing that the image stress remains on the bounding surface (i.e., the consistency condition of the bounding surface):

$$\bar{K}_p = - \left(\frac{\partial F}{\partial p_0} \bar{p}_0 + \frac{\partial F}{\partial \alpha} \bar{\alpha} \right) \quad (4.25)$$

variables \bar{p}_0 and $\bar{\alpha}$ are given by equation 4.20 and 4.21, respectively. And:

$$\frac{\partial F}{\partial p_0} = -\bar{p}(N^2 - \alpha^2); \quad \frac{\partial F}{\partial \alpha} = -2\bar{p}(\bar{q} - p_0\alpha) \quad (4.26)$$

The term $f(b)$ in equation 4.24 quantifies the higher plastic modulus when stress point is inside the bounding surface, and essentially governs the soil stiffness during cyclic loading. The $f(b)$ needs to satisfy two requirements. First, $f(b) = 0$ when $b = 1$ (i.e., current stress is on the bounding surface) implying once the current stress reaches and stays on the bounding surface, plastic modulus K_p equals to \bar{K}_p . Second, $f(b)$ should be a monotonic function of the variable b . In this way, when the current stress moves towards the bounding surface and consequently the b value decreases, $f(b)$ provides a smooth stiffness degradation from higher stiffness corresponding to stress state inside the bounding surface to the value determined by the consistency condition of the bounding surface.

In this work, the function $f(b)$ takes the following form:

$$\begin{aligned} f(b) &= h(1+e)p_0^3(b-1)m_s \\ m_s &= \frac{1}{1+d}; \quad \dot{d} = c_d|\dot{\varepsilon}_d^p|(1 + \langle -c_d/|c_d| \rangle d) \end{aligned} \quad (4.27)$$

The term $(1+e)$ is in accordance with the same term appearing in equation 4.20 and 4.21 and renders the hardening of internal variables a function of plastic void ratio change, independent of the strain measure used (Dafalias and Herrmann, 1986). The term p_0^3 introduces proper unit to the function $f(b)$, i.e., the same unit as \bar{K}_p . The variable h is a shape-hardening factor that provides additional freedom in adjustment of plastic modulus magnitude, and it is proposed to be dependent on shear modes (i.e., compression or extension) in a similar way as the model parameter N :

$$h = \begin{cases} h_c & \text{if } \bar{\eta} \geq \alpha \\ h_e & \text{if } \bar{\eta} < \alpha \end{cases} \quad (4.28)$$

with h_c and h_e being two model constants. This feature is desirable in terms of capturing anisotropic cyclic stiffness of clays.

The novelty of the proposed function $f(b)$ comes from the variable m_s , which is introduced to model cyclic shakedown and softening in a unified manner. When the model parameter $c_d > 0$, the evolution of d is based on the form $\dot{d} = c_d|\dot{\varepsilon}_d^p|$. Under this condition, driven by the accumulation of plastic deviatoric strain, plastic modulus K_p will be gradually diminished as d increases. As a result, cyclic stiffness degradation is reproduced, which eventually will lead to a softening form of failure. It is worth mentioning that similar form of plastic modulus has been employed by Seidalinov and Taiebat (2014)

to reproduce cyclic softening. On the other hand, when $c_d < 0$, the evolution form of d changes to $\dot{d} = c_d |\dot{\epsilon}_d^p| (1 + d)$. This implies that as plastic deviatoric strain accumulates, the value of d will asymptotically decrease to its bound, which is -1. As a consequence, m_s will progressively grow to infinity, which increases the plastic modulus and thereby decelerates the development of plastic deformation. Finally, when the plastic modulus is large enough, the purely elastic responses during cyclic loading can be recovered, i.e., the cyclic shakedown.

As suggested by experimental evidence (Sangrey et al., 1969; Lefebvre et al., 1989; Zergoun and Vaid, 1994), there exists a threshold of applied cyclic shear stress, below which cyclically loaded clay will reach the cyclic shakedown while above the threshold clays will fail eventually due to cyclic softening. This fact clarifies the advantage of modeling cyclic shakedown and softening in a unified manner. Based on equation 4.27, a further proposition of c_d as a function of stress state or other variables is expected to capture the observed transition between aforementioned two responses when cyclic shear stress varies.

4.2.5. Evolution Law of Similarity Ratio b

After the update of the current stress, internal variables and the projection center in each elasoplasticity computation step, appropriate update of the value of b is needed. Otherwise, the image stress calculated based on equation 4.3 will not be on the bounding surface (i.e., violation of the consistency condition of the bounding surface).

For each elastoplasticity computation step, the consistency condition for both the loading surface ($f = 0$) and bounding surface ($F = 0$) should be satisfied simultaneously:

$$\dot{f} = \frac{\partial f}{\partial p} \dot{p} + \frac{\partial f}{\partial q} \dot{q} - \langle \Lambda \rangle K_p = 0 \quad (4.29a)$$

$$\dot{F} = \frac{\partial F}{\partial \bar{p}} \dot{\bar{p}} + \frac{\partial F}{\partial \bar{q}} \dot{\bar{q}} - \langle \Lambda \rangle \bar{K}_p = 0 \quad (4.29b)$$

By equaling the Λ in equation 4.29(a) and (b), and considering the assumption of loading direction (i.e., equation 4.4), one can obtain:

$$\frac{1}{K_p} \left(\frac{\partial F}{\partial \bar{p}} \dot{\bar{p}} + \frac{\partial F}{\partial \bar{q}} \dot{\bar{q}} \right) = \frac{1}{K_p} \left(\frac{\partial F}{\partial p} \dot{p} + \frac{\partial F}{\partial q} \dot{q} \right) \quad (4.30)$$

where $\dot{\bar{p}}$ and $\dot{\bar{q}}$ can be obtained by differentiating equation 4.3:

$$\dot{\bar{p}} = \dot{p}_c + b(\dot{p} - \dot{p}_c) + (p - p_c)\dot{b}; \quad \dot{\bar{q}} = \dot{q}_c + b(\dot{q} - \dot{q}_c) + (q - q_c)\dot{b} \quad (4.31)$$

By substituting equation 4.31 into equation 4.30, the rate form of b value evolution can be expressed as a function of the rate of stress and projection center:

$$\dot{b} = \frac{C_1}{C_2} \quad (4.32)$$

where:

$$C_1 = - \left(\frac{\partial F}{\partial \bar{p}} (\dot{p}_c + b(\dot{p} - \dot{p}_c)) + \frac{\partial F}{\partial \bar{q}} (\dot{q}_c + b(\dot{q} - \dot{q}_c)) \right) + \frac{\bar{K}_p}{K_p} \left(\frac{\partial F}{\partial p} \dot{p} + \frac{\partial F}{\partial q} \dot{q} \right); \quad (4.33)$$

$$C_2 = \frac{\partial F}{\partial \bar{p}} (p - p_c) + \frac{\partial F}{\partial \bar{q}} (q - q_c)$$

4.2.6. Nonlinear Small Strain Elasticity Model

It needs to be emphasized that the vast majority of elastoplasticity models aiming at modeling clay's cyclic responses in the literature rely on the plastic strain to reproduce soil's nonlinear and cyclic hysteresis, and usually use elasticity models that do not consider small strain stiffness of soil. This approach works seemingly well for models developed to capture soil behavior at larger cyclic strain, for which elastic component is only a small portion of the total strain. Nevertheless, if such models are used to reproduce the soil response that involves small cyclic strain (say smaller than 0.1%), one finds that experimentally observed non-linear behaviors will be underestimated (Papadimitriou and Bouckovalas, 2002). On the other hand, Masing's study about material behavior during cyclic loading (Masing, 1926) and experimental work on clays (Vucetic and Dobry, 1991; Vucetic, 1994; Finno and Zapata-Medina, 2013) suggest that at a stress reversal, the shear modulus assumes a value equal to shear modulus that represents shear stiffness at very small strain level, which is denoted as G_0 . As discussed in the section 4.2.3, plastic deformation predicted by the proposed model is generally negligible right after stress reversal due to the update of the projection center, and consequently elastic deformation is dominant. Therefore, to reproduce soil behavior in accordance with the Masing's rules, an elasticity model that can recover shear modulus G_0 at stress reversal is needed. Based on above considerations, the small-strain overlay model proposed by Benz et al. (2009) is incorporated into the proposed model. This relatively simple model is able to reproduce the recovery of G_0 at each stress reversal and non-linear stiffness variation at small strains. After such an integration, the non-linear behavior of full cyclic strain levels can be captured by the proposed model. In other words, at small to medium strain levels (e.g.,

$1e^{-5}$ to $1e^{-2}$), soil's nonlinear stress-strain response and hysteresis during cyclic loading is governed by the elasticity model, while at medium to large strain levels (e.g., greater than $1e^{-2}$) is primarily controlled by the bounding surface plasticity. For the sake of brevity, only major aspects of the adopted model and modifications will be described in this section. For more details, readers are referred to the Ph.D. thesis of Benz (2007).

Modified Hardin-Drnevich function is used to quantify the degradation of elastic shear modulus driven by shear strain history:

$$G_{sec} = \frac{G_0}{1 + 0.385\gamma_{hist}/\gamma_{0.7}} \quad (4.34)$$

As illustrated in Figure 4.8, the elastic secant shear modulus gradually decrease from its maximum value G_0 with the increase of shear strain history, γ_{hist} . In triaxial space, shear strain γ is defined as $\varepsilon_a - \varepsilon_r$.

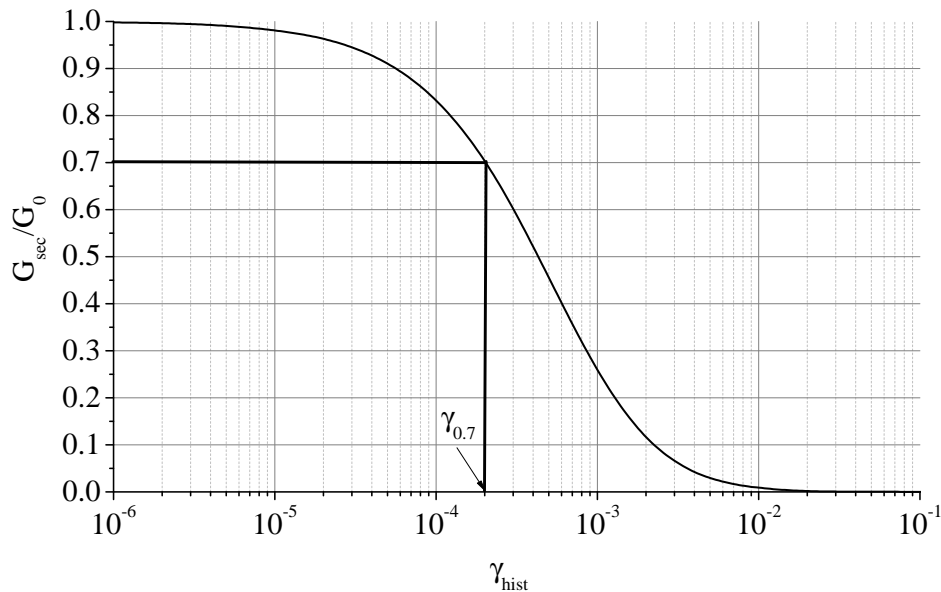


Figure 4.8. Modified Hardin-Drnevich elastic shear stiffness degradation curve and definition of the parameter $\gamma_{0.7}$

By definition, the non-negative variable γ_{hist} equals $|\bar{\gamma}_{hist}|$, whose value is updated through:

$$\bar{\gamma}_{hist}^{i+1} = \begin{cases} \bar{\gamma}_{hist}^i + \Delta\gamma^{i+1} & \text{if } \bar{\gamma}_{hist}^i \Delta\gamma^{i+1} \geq 0 \\ \Delta\gamma^{i+1} & \text{if } \bar{\gamma}_{hist}^i \Delta\gamma^{i+1} < 0 \end{cases} \quad (4.35)$$

where i and $i + 1$ denote the quantities corresponding to the previous and current computation steps and $\Delta\gamma$ is the shear strain increment. Equation 4.35 implies that γ_{hist} will progressively increase during monotonic loading and be reset to zero upon strain reversal. As a result, the elastic shear stiffness given by equation 4.34 will keep decreasing along monotonic loading and regain its maximum value, G_0 , upon unloading or reloading. This is consistent with the original suggestion by Hardin and Drnevich (1972) that the non-linearity of soil is most appropriately described in terms of its strain history. Similar reversal triggering criteria have been successfully used by the family of MIT models to reproduce elastic hysteresis (Whittle and Kavvas, 1994; Pestana and Whittle, 1999), in which volumetric strain reversal and shear strain reversal are used to trigger the recovery of stiffness at very small strain level in drained and undrained loading, respectively. It is noteworthy that in the proposed model, the bounding surface plasticity and elasticity model employ stress and strain reversal criteria, respectively. Nevertheless, these two conditions will generally be triggered at the same time. In the three-dimensional version of the adopted elasticity model, shear strain history is memorized as the form of tensor and the strain history is mapped to the principal direction of current strain increment so that the stiffness variation in accordance to angular change in loading path (i.e., stress path rotation angle) (Finno and Cho, 2010; Finno and Kim, 2012) can be reproduced (Benz, 2007).

In the original work of Benz et al. (2009), the shear modulus G_0 is only related to the mean effective stress, p through a power law. However, experimental work has shown that, in addition to the confining pressure, the value of G_0 is also closely related to the void ratio (Finno and Cho, 2010; Finno and Kim, 2012; Zapata-Medina et al., 2014). Therefore, the following empirical relation suggested by Zapata-Medina (2012) is selected in this work:

$$G_0 = A_g \frac{(e_g - e_0)^2}{1 + e_0} \left(\frac{p}{p_a}\right)^{n_g} p_a \quad (4.36)$$

where A_g , e_g , and n_g are model constants. p_a is the atmosphere pressure and e_0 is the initial void ratio at the beginning of consolidation.

The model parameter $\gamma_{0.7}$ in equation 4.34 defines the shear strain threshold at which the elastic secant shear modulus reduces to $0.7G_0$ in primary loading. Consequently, $\gamma_{0.7}$ controls the deterioration rate of elastic stiffness.

The degradation relation for the secant shear modulus presented in Equation 4.34 needs to be converted to that for tangent modulus, which could be used in elastoplasticity constitutive models:

$$G_{tan} = G_0 \left(\frac{\gamma_{0.7}}{\gamma_{0.7} + 0.385\gamma_{hist}} \right)^2 \quad (4.37)$$

Additionally, a constant Poissons ratio ν is assumed to obtain the corresponding bulk modulus K from G_{tan} :

$$K = \frac{2(1 + \nu)}{3(1 - 2\nu)} G_{tan} \quad (4.38)$$

To avoid an excessive reduction of elastic stiffness caused by large plastic shear strain, a cut-off value of shear modulus, G_{min} is introduced. Tangent shear modulus will stop degrading once G_{tan} equals G_{min} . In this work, G_{min} is proposed to be given by the

Cam-Clay elasticity model:

$$G_{min} = \frac{3(1 - 2\nu)}{2(1 + \nu)} K_{min}; \quad K_{min} = \frac{1 + e}{\kappa} p \quad (4.39)$$

Such an employment of G_{min} not only prevents unrealistically low elastic stiffness, but also provides a transition of elastic stiffness from small strain range to large strain range, during which soil elasticity behavior is governed by the well-defined Cam-Clay elasticity model.

Finally, the stress rate can be related to the elastic strain rate through:

$$\dot{p} = K \dot{\epsilon}_v^e; \quad \dot{q} = 3G \dot{\epsilon}_d^e; \quad (4.40)$$

Note that equation 4.40 implies that there is no cross-coupling between volumetric and deviatoric components in this elasticity model.

As demonstrated by Zytynski et al. (1978), the currently employed hypo-elasticity model, which has a stress-dependent shear modulus linked to bulk modulus via a constant Poisson's ratio, is not energy-conservative. Nevertheless, a hyper-elasticity model (i.e., conservative in energy) with desired stiffness degradation will inevitably increase the model complexity and number of parameters. In addition, as shown later in this chapter, the proposed model is able to provide satisfactory simulations of clays cyclic behavior. Furthermore, several constitutive models that implement hypo-elasticity model achieved encouraging successes in modeling cyclic soil behavior (Li and Meissner, 2002; Seidalinov and Taiebat, 2014; Gao and Zhao, 2015). Therefore, this adopted elasticity model is considered appropriate and a simple energy-conservative elasticity model equipped with non-linear stiffness degradation will be one of the areas for future research.

Table 4.1. Parameters in the basic model and their roles

	Designation	Description of Its Role
Elasticity (small strain)	$e_g/A_g/n_g$	Interpolation parameters for shear modulus at very small strain, G_0
	$\gamma_{0.7}$	Degradation rate of elastic stiffness with respect to shear strain
Elasticity (large strain)	κ	Slope of rebound line in $e - \ln(p)$ plane
	ν	Poisson's ratio
Critical State	M_c/M_e	Stress ratio at critical state
Isotropic Hardening	λ	Slope of virgin compression line in $e - \ln(p)$ plane
Rotation Hardening	C	Rate of surface rotation
	χ	Upper bound of rotation during constant stress ratio loading
Bounding surface shape	N_c/N_e	Shape of bounding surface
Cyclic loading	h_c/h_e	Cyclic stiffness
	w	Pore pressure build-up in cyclic loading
	c_d	Cyclic shakedown/softening

Table 4.2. Initial conditions in the basic model

Designation	Description of Its Role
p_0	Size of the bounding surface
α	Inclination and distortion of the bounding surface
e_0	Initial void ratio

4.2.7. Summary of Model Parameters and Initial Conditions

All the parameters and the required initial condition for the basic model are summarized in Table 4.1 and Table 4.2, respectively.

4.3. Parametric Analyses of the Primary Constitutive Hypotheses

This section presents qualitative evaluations of the basic model, which is conducted via a series of parametric studies. The purpose of this work is to emphasize the roles of the

primary constitutive hypotheses and their associated model parameters. One important contribution in this work is the newly proposed mixed plastic flow rule. Its advantage as well as the role played by the parameter w is elucidated in this section. Moreover, the influence of parameter c_d on accelerating or decelerating deformation development during cyclic loading is demonstrated, and illustrate the model's capacity to reproduce cyclic shakedown and softening in a unified manner. The importance of considering small strain stiffness in simulating clay cyclic behavior is illustrated as well.

The model parameters used in the three evaluations above are summarized in set-1, set-2 and set-3 of Table 4.3, respectively. The initial conditions (i.e., stress and internal variables) is summarized in Table 4.4. It is noteworthy that all simulations in the present chapter and next chapter are based on the implementation of the constitutive model in a triaxial space constitutive driver that can integrate stress-strain response under mixed-control conditions. The details of model implementation, stress integration method, and the constitutive driver will be presented in Chapter 6.

4.3.1. The Role of Mixed Plastic Flow Rule

Figure 4.9 compares the simulated effective stress paths during undrained cyclic loading on isotropically consolidated NC clay with different values of w . The corresponding pore pressure build-up versus number of loading cycles is presented in Figure 4.10. In all cases, gradual accumulation of positive pore pressures and the consequent decrease of mean effective stress p are simulated. In addition, as one expects, the rate of pore pressure build-up decreases with increasing number of loading cycles. What parameter w affects are the speed of pore pressure accumulation and its final upper bound. To be specific, a

Table 4.3. Model parameters in the qualitative evaluations

		Set-1	Set-2	Set-3
Elasticity (small strain)	e_g	2.64	2.64	2.64
	A_g	160	160	160
	n_g	0.635	0.635	0.635
	$\gamma_{0.7}$	1.6E-04	1.6E-04	1.6E-04
Elasticity (large strain)	κ	0.018	0.018	0.018
	ν	0.2	0.2	0.2
Critical State	M_c	1.2	1.2	1.2
	M_e	0.9	0.9	0.9
Isotropic Hardening	λ	0.12	0.12	0.12
Rotation Hardening	C	16	16	16
	x	1.75	1.75	1.75
Bounding Surface Shape	N_c	1	1	1
	N_e	1	1	1
Cyclic Loading	h_c	20	20	20
	h_e	20	20	20
	w	varies	5	5
	c_d	0	varies	0

Table 4.4. Initial conditions in the qualitative evaluations

p_0 (kPa)	α	S_b	p (kPa)	q (kPa)	e_0
300	0.00	0	300	0	0.75

larger value of w leads to a faster pore pressure accumulation as well as to an increase in the magnitude of excess pore pressure at the end of the simulation. In terms of model calibration, this observation suggests that parameter w can be defined by fitting the pore pressure build-up in cyclic loading tests. The use of $w = 0$ (i.e., image stress flow rule) leads to an early stabilization of the effective stress path and the smallest excess pore pressures. As a higher value of w indicates more weight is placed on the flow direction

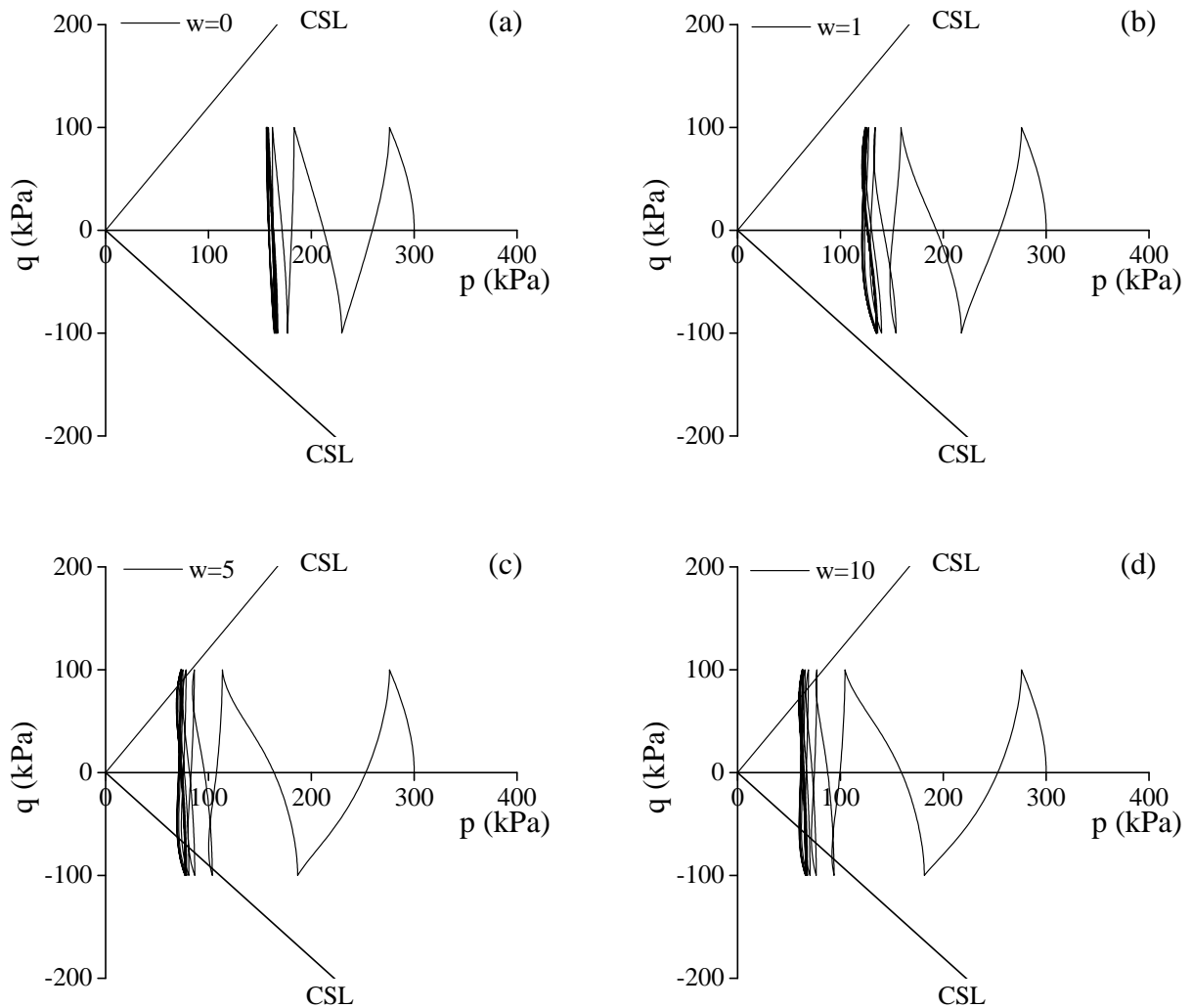


Figure 4.9. Simulated effective stress paths during CIU CYC-TX test: (a) $w=0$; (b) $w=1$; (c) $w=5$; (d) $w=10$

defined at the current stress state, the higher pore pressure build-up is attributed to the explicit consideration of the current stress in determination of plastic flow direction. In simulations with $w = 5$ and $w = 10$, the effective stress path reaches the critical state line and even exceeds it. Similar behavior have also been seen in experiments (Sheu, 1985; Zergoun, 1991). By comparing the results observed in the simulations with $w = 5$ and

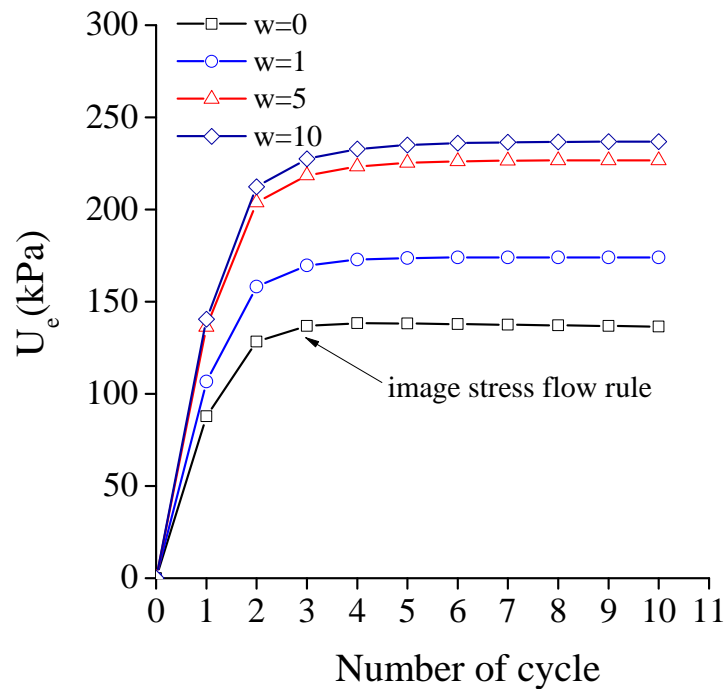


Figure 4.10. Simulated pore pressure build-up during CIU CYC-TX test with different values of parameter w

$w = 10$, one is able to find that there exists a upper bound in terms of simulated pore pressure build-up, which seems to be independent of the value w . In other words, even if w keeps increasing, the simulated pore pressure accumulation cannot grow further. The reason is that under high value of w , plastic contraction or dilation is determined primarily by the current stress. Once the stress path in cyclic loading is close to the critical state line, soil tends to dilate at the later stages of loading (i.e., after stress path passes the critical state line) while tends to contract during unloading. This leads to the oscillation of effective stress path and prevents further accumulation of pore pressure.

4.3.2. The Role of Shakedown/Softening Parameter c_d

As discussed before, the model parameter c_d affects the amount of accumulated deformation during cyclic loading. Furthermore, a change of c_d value is able to switch soil response from cyclic shakedown to softening. Figure 4.11 demonstrates these influences, in which the peak strains of each loading cycle in simulations of a undrained cyclic loading on isotropically normally consolidated clay are presented. The compression and extension peak strain are depicted separately for the sake of clarity. In addition, the accumulated strain (i.e., residual strain at the end of each loading cycle) in the simulations is also provided (Figure 4.11(b)). In general, higher values of c_d induce a more rapid development of deformation in cyclic loading, which are reflected in both peak strain and residual strain at the end of each cycle. When a negative value of c_d is assigned (i.e., $c_d = -30$), the increase of residual strain within 10 cycles is very small and its growth rate is very low after 10 loading cycles as well. Meanwhile, the development of peak strain in both compression and extension tends to stabilize with the increasing number of cycles. All these features indicate the phenomenon of cyclic shakedown. On the other hand, in the simulations under positive values of c_d (i.e., $c_d = 5$ and $c_d = 15$), both residual strain and peak strain keep growing with the loading cycle number. Moreover, such a deformation development is unstable after certain loading cycles, which is characterized by the accelerating growth of residual strain and peak strain. Under such a cyclic softening condition, one can expect that the soil would fail once more loading cycles are applied.

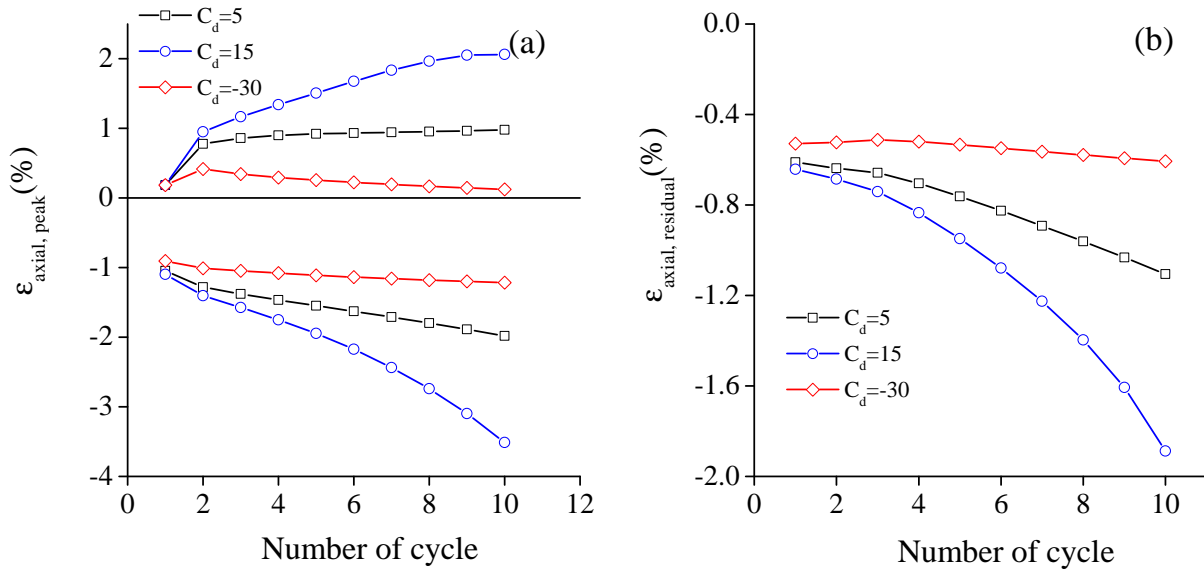


Figure 4.11. Simulated peak and residual strains during CIU CYC-TX test with different values of c_d : (a) peak compression and extension strains in each cycle; (b) residual strain at the end of each cycle

4.3.3. The Role of Small Strain Stiffness

To consider the small strain stiffness of soil, this work incorporates a non-linear small strain elasticity model (Benz, 2007), whose key features include the recovery of shear modulus G_0 after stress reversal and subsequent stiffness degradation with increasing magnitude of deformation. In this section, efforts are made to clarify the effects of soil's small strain stiffness during cyclic loading and probably more importantly, under what condition these effects can be ignored without introducing significant errors. Figure 4.12 and 4.13 present simulation results of undrained cyclic loading with large ($q_{cyc} = 180\text{kPa}$) and small ($q_{cyc} = 15\text{kPa}$) cyclic stress amplitudes, respectively. For each of the above cyclic stresses, simulations are repeated for two scenarios, i.e., considering and ignoring small

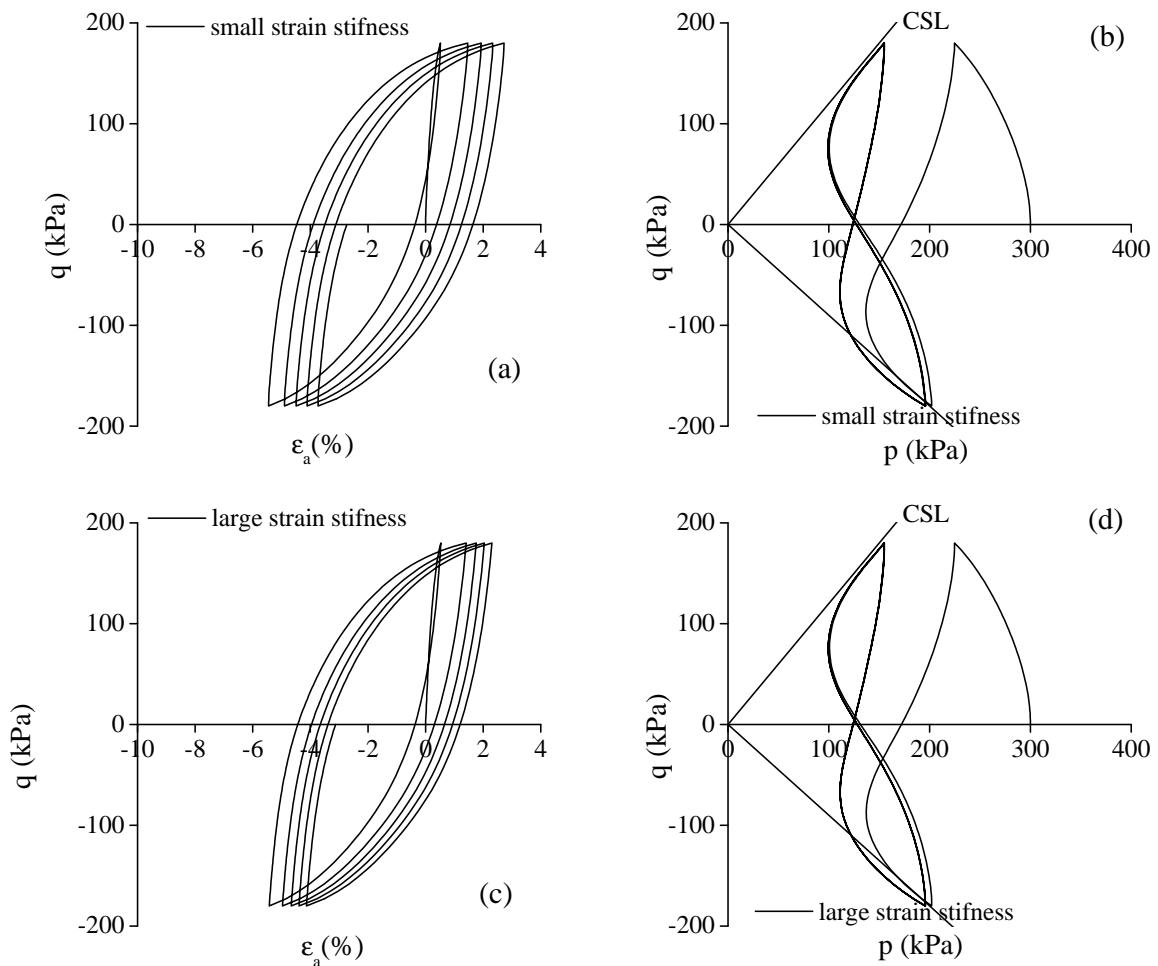


Figure 4.12. Simulated cyclic stress-strain and effective stress paths during CIU CYC-TX test with large cyclic stress amplitude: (a)-(b) consider small strain elasticity; (c)-(d) ignore small strain elasticity

strain elasticity. when small strain elasticity is not considered, the Cam-Clay elasticity model with parameters κ and ν is used to determine material's elastic behavior.

The mobilization of large plastic deformations expedites the degradation of elastic stiffness while has the elastic strain component a small fraction of the total strains. As a result, soil's nonlinearity, stress-strain hysteresis loop and pore pressure generation are dominantly governed by plasticity. Therefore, as shown in Figure 4.12, ignoring small

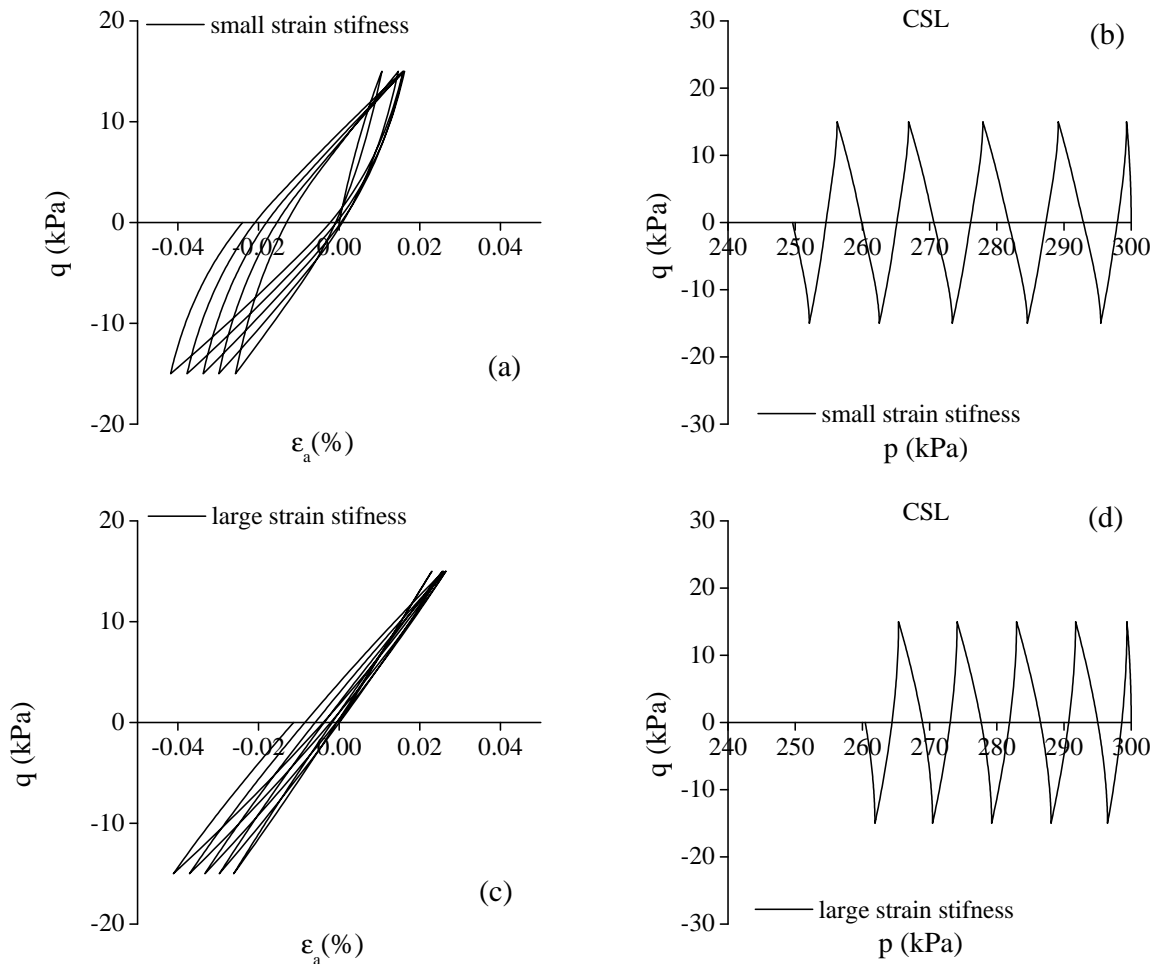


Figure 4.13. Simulated cyclic stress-strain and effective stress paths during CIU CYC-TX test with small cyclic stress amplitude: (a)-(b) consider small strain elasticity; (c)-(d) ignore small strain elasticity

strain stiffness does not introduce a significant difference in terms of stress-strain and pore pressure responses during cyclic loading. However, when the cyclic stress is relatively small (like the case shown in Figure 4.13) or the material yield stress is relatively high, plastic deformation that develops during cyclic loading will be small. As a result, the elastic component of deformation is more pronounced and sometimes even dominant. Figure 4.13 shows, under this condition, small strain elasticity model helps to reproduce the soil's

non-linearity and thus to simulate a better stress-strain hysteresis loop than the simplified model. From an energy point of view, the above hysteresis loop can significantly affect the amount of energy dissipation and thereby changes kinematic energy that is converted to soil particle velocity, especially if the number of cycle is large. While in this specific case, both models predict similar growth of peak strain, noticeable differences exist in terms of residual strain and this difference is expected to growth with increasing number of cycles. The comparison of the two effective stress paths shown in Figure 4.13(b) and (d) indicates that the simulation that considers small strain stiffness predicts a higher amount of pore pressure accumulation and consequently a higher reduction in effective stress. This is likely due to the coupling between pore pressure generation and material elastic stiffness under undrained condition. Since effective stress can significantly affect strength and stiffness of soil, ignoring small strain elasticity may make predictions unconservative (i.e., reduction in stiffness and strength may be overlooked by the simulation) under a loading condition of low stress amplitude but high cycle numbers (e.g., wave action).

In terms of usage of the model, it is suggested that when the anticipated plastic strain in cyclic loading is the dominant component of the total strain, simulations with simple large strain elasticity model (e.g., Cam-Clay elasticity) are acceptable and the impact of this simplification are expected to be minor.

4.4. Calibration of Model Parameters and Initial Conditions

4.4.1. Calibration of Model Parameters

As the basic model is formulated to reproduce intrinsic clay behavior, the calibration of relevant parameters should be based on experimental observations on reconstituted clay,

insensitive clay or sensitive clay that has been consolidated to sufficiently high stress levels (i.e., inter-particle bonds have been completely eliminated). The procedure to calibrate model parameters is demonstrated as follow, on the basis of experimental data for tests on relatively insensitive BCF clay (Zapata-Medina, 2012).

- Parameters λ and κ

The parameter λ represents the slope of virgin compression line in $e - \ln(p)$ plane and can be calibrated from either an isotropic compression test or a 1D compression test. In 1D compression tests, if the measurement of lateral effective stress is absent, which is the case for BCF clays, λ can be estimated from compression index C_c (Figure 4.14(a)). This estimation is based on the assumption that the K_0 value is constant for NC clay. Under this condition, mean effective stress, p is proportional to axial effective stress σ'_a with a constant, i.e., $p = (1 + 2K_{0,NC})\sigma'_a/3$. Further, λ is related to C_c via:

$$\lambda = \frac{e_1 - e_2}{\ln p_2 - \ln p_1} = \frac{e_1 - e_2}{\ln \sigma'_{a,2} - \ln \sigma'_{a,1}} = C_c / \ln(10) \quad (4.41)$$

where 1 and 2 in subscript denote two points in the virgin compression line.

The parameter κ is the slope of rebound line in $e - \ln(p)$ plane and it can be estimated in a way similar to λ via recompression index C_r , i.e., $\kappa = C_r / \ln(10)$. Nevertheless, the κ estimated with this method is less reliable due to the variation of the K_0 values during 1D unloading (Dafalias et al., 2006). Zapata-Medina (2012) conducted reconsolidation tests on BCF clay samples in the triaxial cell, in which samples were 1D consolidated (i.e., no lateral deformation) to its maximum past pressure then unloaded under conditions of zero lateral strain to its in-situ stress, as shown in Figure 4.14(b). Since both axial and

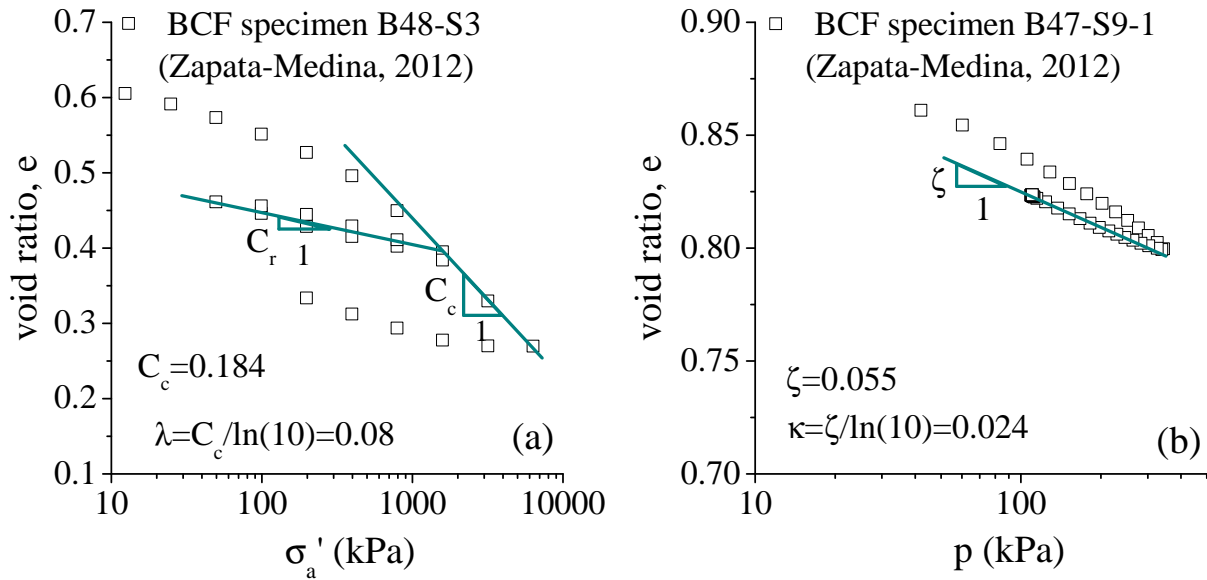


Figure 4.14. Calibration of parameters λ and κ

radial effective stresses were measured in the reconsolidation, the relation between e and p during unloading is used to calibrate κ .

- Parameter ν

As suggested by Dafalias et al. (2006), The Poisson ratio ν is calibrated from the effective stress path of 1D unloading, as shown in Figure 4.15. The material response during the initial stage of 1D unloading is assumed to be elastic. As a result, the slope ξ of the initial portion of the effective stress path is related to ν through: $\nu = (3 - \xi) / (\xi + 6)$.

- Parameters A_g , n_g , e_g and $\gamma_{0.7}$

This set of parameters controls small strain stiffness responses simulated by the model. With the initial void ratio being known, A_g , n_g and e_g can be calibrated by fitting equation 4.36 to the measured G_0 values at different mean effective stress levels. For BCF clay, bender element tests were used to measure G_0 during reconsolidation (Zapata-Medina, 2012). This set of data is used to calibrate the above three parameters, as shown in Figure

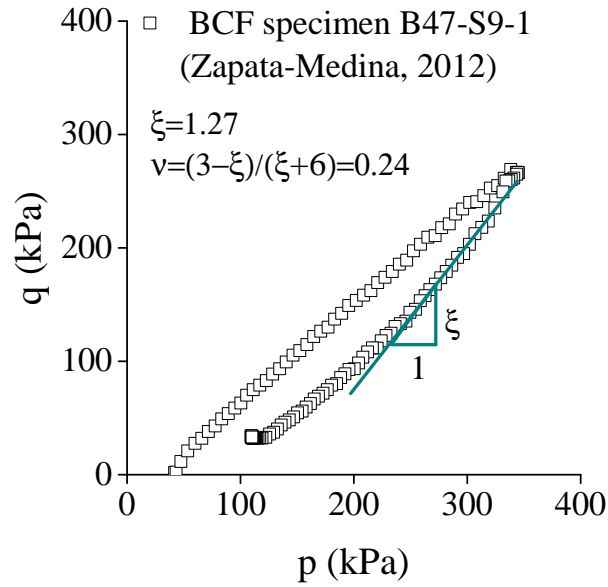


Figure 4.15. Calibration of parameter ν

4.16 (a). The parameter $\gamma_{0.7}$ controls the degradation rate of the elastic stiffness and its value can be calibrated by fitting the stiffness degradation curve during unloading stage in a cyclic loading test. The data in unloading is preferred, as plastic deformations are relatively small, and the decrease of material stiffness is primarily caused by the elastic stiffness degradation. Figure 4.16 (b) presents the measured secant shear modulus of the first unloading of a cyclic loading test on BCF clay and model simulations with different values of $\gamma_{0.7}$. It is clear that the adopted elasticity model captures the soil stiffness recovery to G_0 at the instance of stress reversal. Moreover, Note that the value of $\gamma_{0.7}$ mainly affects the rate of stiffness degradation while does not significantly affect the stiffness at large strains. The value $\gamma_{0.7} = 7e^{-4}$ is chosen for BCF clay, as it can satisfactorily reproduce the observed stiffness evolution, particularly for the axial strain range from 0.1% to 1%, which is more important for the simulations of strains accumulation under cyclic loading. For comparison, Figure 4.16(b) includes the simulation under the condition that

small strain stiffness is ignored, which significantly underestimates soil stiffness during unloading. It is noted that the shape of the degradation curve computed by the model is different from the experimental data. Nevertheless, given the simplicity of this elasticity model, its performance is still considered satisfactory.

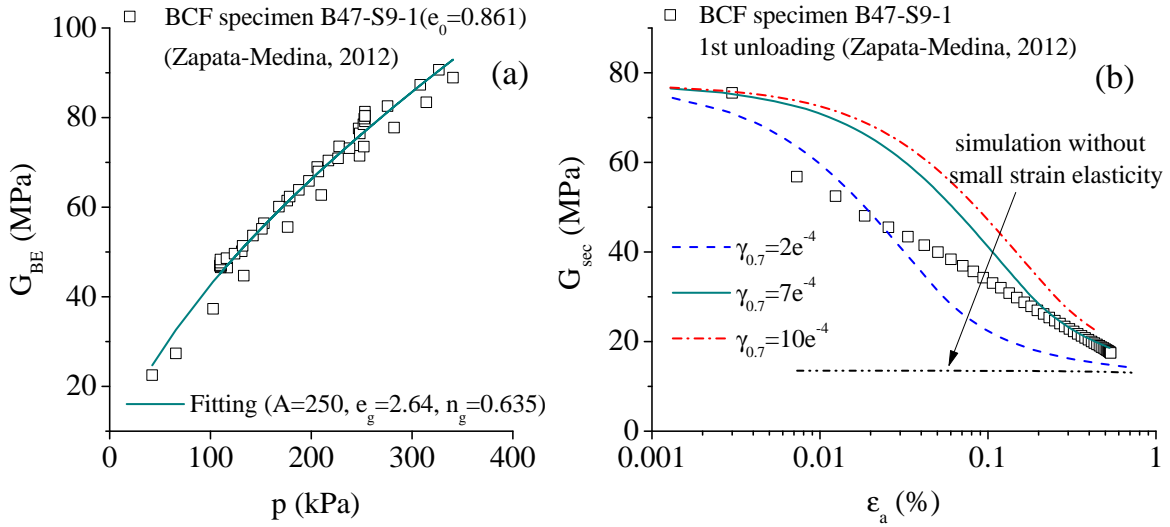


Figure 4.16. Calibration of small strain stiffness parameters: (a) A_g , n_g and e_g ; (b) $\gamma_{0.7}$

- Parameters M_c and M_e

M_c and M_e denote the stress ratio at critical state in triaxial compression and extension, respectively. For BCF clay, the effective stress path during a CK_0 TXC and TXE tests (Figure 4.17) are used to calibrate M_c and M_e , respectively. If only compression test data are available, it is suggested that M_e can be estimated via critical state friction angle, which is related to M_c :

$$\phi_{cs} = \arcsin\left(\frac{3M_c}{6 + M_c}\right); \quad M_e = \frac{6 \sin \phi_{cs}}{3 + \sin \phi_{cs}} \quad (4.42)$$

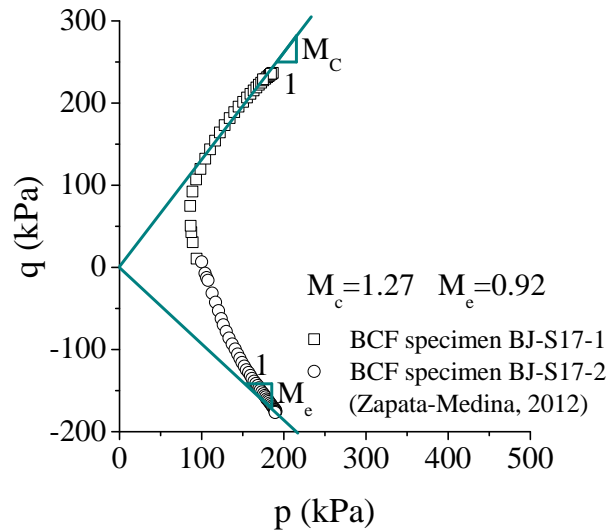


Figure 4.17. Calibration of parameters M_c and M_e

- Parameters N_c and N_e

The parameters N_c and N_e control the shape of the bounding surface. Dafalias et al. (2006) proposed an analytical solution to calibrate N_c (in their work, N_c and N_e are assumed to be the same) based on data of a CK_0U TXC test on NC clay:

$$\frac{p_f}{p_{k0}} = \left(\frac{N^2 - \eta_{k0}^2}{N^2 - 2\eta_{k0}M_c + M_c^2} \right)^{1-(\kappa/\lambda)} \quad (4.43)$$

where p_f and p_{k0} is the mean effective stress at critical state and at the end of K_0 consolidation, respectively. The variable η_{k0} is the stress ratio at the end of K_0 consolidation. Also, N_c can be calibrated by fitting the bounding surface with the effective stress path of CK_0 TXC on NC clay (Taiebat et al., 2010). Regarding N_e , it can be calibrated by matching peak undrained strength in extension through a trial-and-error procedure. Unfortunately, data of CK_0 TXC or TXE test on NC BCF clays is not available. Therefore, N_c and N_e were initially assumed to be equal to M_c and M_e , respectively, i.e., $N_c = 1.27$

and $N_e = 0.92$. Further adjustments were made to match post-cyclic undrained shear strength in compression (test B47-S9-1) and extension (test B48-S6-2), and eventually $N_c = 1.22$ and $N_e = 0.8$.

- Parameter χ

The parameter χ governs the upper bound of the internal variable α during constant stress ratio loading. This value can be calibrated by an analytical solution proposed by Dafalias et al. (2006):

$$\chi = \frac{2\eta_{k0}\varepsilon(1 - \kappa/\lambda)}{B\varepsilon\eta_{k0}^3 + \eta_{k0}^2 + 2[(1 - \kappa/\lambda) - BM_c^2]\varepsilon\eta_{k0} - M_c^2} \quad (4.44)$$

where:

$$B = -\frac{2(1 + \nu)\kappa}{9(1 - 2\nu)\lambda} \quad (4.45)$$

η_{k0} is the stress ratio during K_0 consolidation on NC clay and can be related to the $K_{0,NC}$ value through $\eta_{k0} = 3(1 - K_{0,NC})/(1 + 2K_{0,NC})$. The reported K_0 values for NC BCF clays are between 0.45 and 0.53 (Zapata-Medina, 2012) and the averaged value 0.49 has been chosen, which corresponds to $\eta_{k0} = 0.77$. The term ε in the above equation is the ratio between volumetric strain rate and deviatoric strain rate during 1D compression, i.e., $\varepsilon = \dot{\varepsilon}_v/\dot{\varepsilon}_d = 3/2$. Finally, $\chi = 1.98$ is determined for BCF clays.

- Parameters h_c and h_e

The parameters h_c and h_e control the amount of plastic strain developed when the stress point is inside the bounding surface, and consequently govern the material stiffness during cyclic loading. Therefore, these two parameters can be calibrated by fitting the stress-strain curves of the first several cycles during a cyclic loading (Figure 4.18), which

are less impacted by the the cyclic shakedown/softening parameter c_d . Currently, this fitting procedure is conducted through a trial-and-error procedure. However, to efficiently and more objectively calibrate these two parameters, it is recommended to employ the parameter optimization technique (e.g., Finno and Calvello (2005) and Calvello and Finno (2004)).

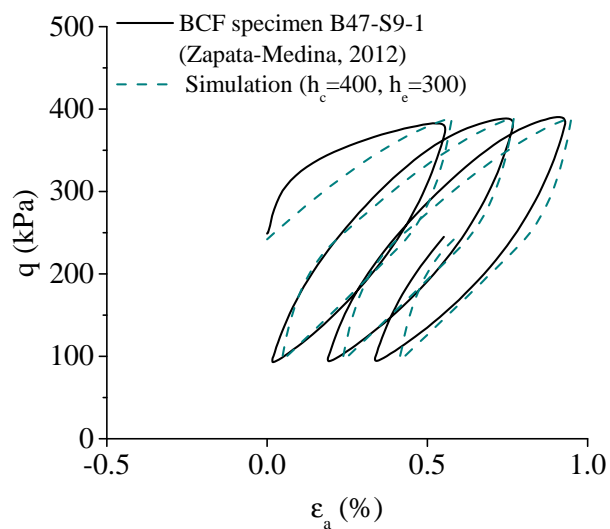


Figure 4.18. Calibration of parameters h_c and h_e

- Parameter C

The parameter C determines the rate of rotation and distortion of both the bounding surface and the plastic potential surface. Hence, as suggested by Dafalias et al. (2006), the most appropriate test for its calibration is CK₀U TXE on NC clay. This test can induce significant surface rotation, as the initial stress ratio η_{in} is far from the final stress ratio η_f . Due to the absence of suitable experimental data for BCF clays, the CK₀U TXE on OC clay has been used to estimate C . As is shown in Figure 4.19, simulations with different values of C all stop at the same stress ratio, which is determined by M_e .

However, the undrained shear strength is sensitive to the selection of parameter C . Note that $C = 8$ is chosen for BCF clays, as the corresponding simulation reproduces the undrained shear strength. Compared with experimental data, the soil's plastic deformation and corresponding negative excess pore pressure are underestimated by the model. This difference is caused by the relatively high h_e value, which is calibrated based on stress-strain responses during cyclic loading as discussed earlier. The above discrepancy may be attributed to the natural variation in different samples or the fact that the soil can exhibit higher stiffness in cyclic loading, in which the loading rate of 1Hz is considerably higher than 0.5% per hour used for the monotonic tests on BCF clay, i.e., clay's time-dependent effects.

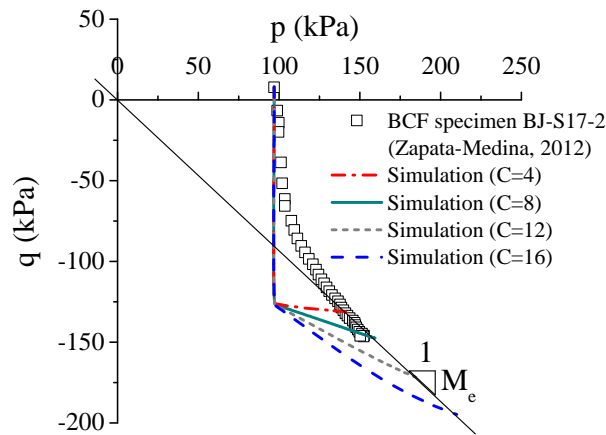


Figure 4.19. Calibration of parameter C

- Parameter c_d

The parameter c_d controls the strain development in cyclic loading, so one should calibrate c_d by fitting strain accumulation data of cyclic loading tests. Figure 4.20 presents the accumulation of axial strain in a cyclic loading test on BCF clay. Note that while the axial strain was keeping increasing, the rate of strain accumulation was decreasing,

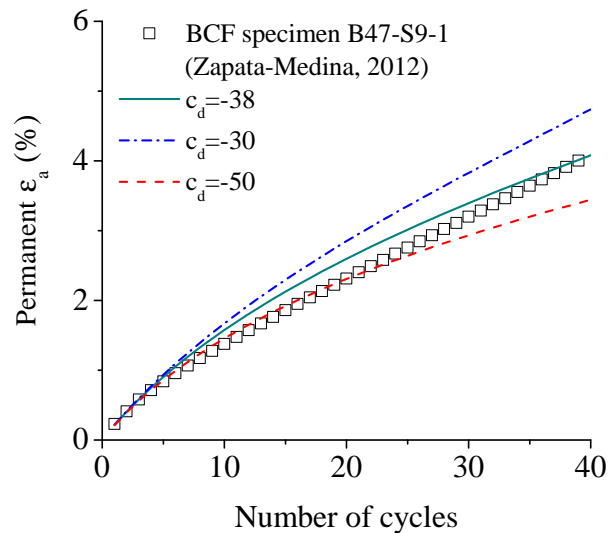


Figure 4.20. Calibration of parameter c_d

implying cyclic shakedown. Among the three simulations, it is found that the simulation using $c_d = -38$ can best reproduce the cyclic shakedown in the experiment. Additionally, in the last several cycles, the experimentally observed rate of strain development (i.e., the increasing amount of permanent strains within each cycle) is well captured by the simulation with $c_d = -38$. This match suggests that the model will capture strain development even if more cycles are applied.

- Parameter w

The parameter w controls the amount of pore pressure build-up during undrained cyclic loading. As a result, pore pressure accumulation in a cyclic test on BCF clay (Figure 4.21) is used to calibrate w . Note that after 40 cycles, a small amount of positive excess pore pressure builds up in the experiment. In contrast, the image stress flow rule (i.e., $w = 0$) leads to a considerable negative pore pressure build-up. The employment of the mixed flow rule (i.e., a non-zero value of w) improves model simulation and decreases

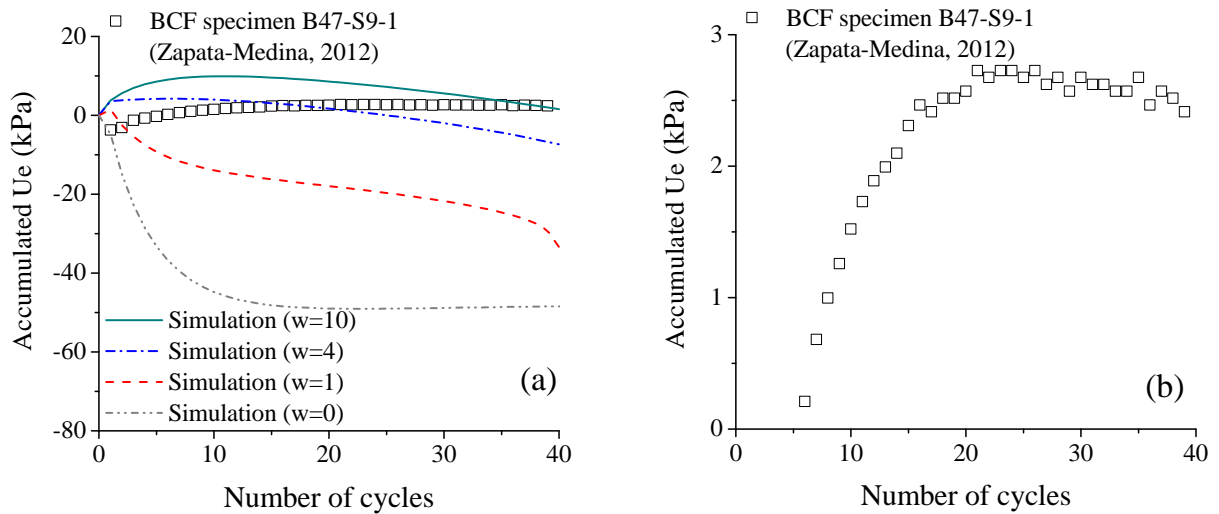


Figure 4.21. Calibration of parameter w : (a) pore pressure build up; (b) experimental data under magnified scale

the amount of accumulated negative pore pressure. As discussed by Andersen et al. (1980), stress concentration due to end restraints in triaxial tests can lead to a non-uniform pore pressure distribution within a sample. Due to the clays low permeability, the time for pore pressure to equalize within a sample is relatively long. This fact suggests that the pore pressure distribution within a high-frequency cyclically loaded clay sample (for BCF clays, the frequency is 1Hz) is more close to being uniform during the later cycles. Accordingly, during the later cycles, the pore pressure measured at the bottom of a specimen is more liable to reflect material responses at a stress point. Based on this consideration, more weight is put on fitting the pore pressure build-up in later cycles and $w = 10$ is selected for BCF clays. Moreover, Figure 4.21(b) zooms the same experimental observation to a magnified scale, in which one can observe a trend that positive pore pressure gradually increases to its peak then starts to decrease. This trend is correctly reproduced by the simulation with $w = 10$.

4.4.2. Calibration of Initial Internal Variables

In the basic model, there are two internal variables p_0 and α . The determination of their initial values that correspond to the in-situ conditions is discussed in this section.

- Internal variable α

In general, one can find a series of yield points in stress space by performing stress-probe tests with different stress ratio. The value of α is obtained by fitting the bounding surface to the yielding points. Unfortunately, such information is not always available in the practice. To address this issue, an analytical solution is proposed to estimate the in-situ value of α based on conventional soil properties that can be readily determined: $K_{0,NC}$ value or the stress ratio at critical state M_c .

To derive the analytical solution, the following two assumptions are made: (1) clay during its deposition (1D consolidation) experiences a loading path that has a constant stress ratio η_{k0} ; (2) at the end of sedimentation, α has reached its upper limit α_{lim} , which is determined by the rotation hardening rule in equation 4.21, i.e., $\alpha_{lim} = \eta/\chi$. If these two assumptions are valid, then the in-situ α value is given by:

$$\alpha = \alpha_{lim} = \eta_{k0}/\chi; \quad \eta_{k0} = 3(1 - K_{0,NC})/(1 + 2K_{0,NC}) \quad (4.46)$$

If $K_{0,NC}$ is not measured in experiments, one can use the stress ratio at critical state M_c to estimate η_{k0} . Based on the Jacky's equation, $K_{0,NC}$ is related to friction angle at critical state through the following expression:

$$K_{0,NC} = 1 - \sin(\phi_{cs}) \quad (4.47)$$

Furthermore, considering the relation between critical state friction angle ϕ_{cs} and stress ratio at critical state M_c :

$$M_c = \frac{6 \sin(\phi_{cs})}{3 - \sin(\phi_{cs})} \quad (4.48)$$

one is able to derive the following expression of η_{k0} :

$$\eta_{k0} = \frac{3M_c}{6 - M_c} \quad (4.49)$$

Correspondingly, a saturated α value in the field is related to M_c by:

$$\alpha = \alpha_{lim} = \frac{\eta_{k0}}{\chi} = \frac{3M_c}{\chi(6 - M_c)} \quad (4.50)$$

Equation 4.46 or 4.50 provides an estimation of scalar-valued α in triaxial space. To generalize the scalar α to the tensor $\boldsymbol{\alpha}$ in multiaxial space, first one observes that given the asymmetric condition in the field, $\boldsymbol{\alpha}$ obeys the following form:

$$\boldsymbol{\alpha} = \begin{bmatrix} \alpha_1, 0, 0 \\ 0, \alpha_2, 0 \\ 0, 0, \alpha_3 \end{bmatrix} \quad (4.51)$$

This form implies the principal direction of $\boldsymbol{\alpha}$ is coincident with the Cartesian coordinate axes. If axis-1 is along the vertical direction in the field, then under the the asymmetrical condition, $\alpha_2 = \alpha_3$. Due to its nature of deviatoric stress ratio, the trace of $\boldsymbol{\alpha}$ is zero, i.e., $\alpha_1 + \alpha_2 + \alpha_3 = 0$. Additionally, in triaxial space, the scalar α is related to the components of $\boldsymbol{\alpha}$ via $\alpha = \alpha_1 - \alpha_3$. Based on the above relations and after some

algebra, the components of α is uniquely obtained:

$$\alpha_1 = \frac{2}{3}\alpha_{lim}; \quad \alpha_2 = \alpha_3 = -\frac{1}{3}\alpha_{lim} \quad (4.52)$$

- Internal variable p_0

Similar to the internal variable α , the most reliable way to estimate in-situ p_0 value is to fit the bounding surface to the experimentally defined yield points in the stress space. Considering the usual absence of the above information, an analytical solution is proposed to estimate initial value of p_0 based on maximum past pressure σ'_p found in the 1D compression test and $K_{0,NC}$ value.

First, the pair of (p, q) stresses that correspond to σ'_p is obtained by:

$$p_p = (\sigma_a + 2\sigma_r)/3 = (1 + 2K_{0,NC})\sigma'_p/3; \quad q_p = \sigma_a - \sigma_r = (1 - K_{0,NC})\sigma'_p \quad (4.53)$$

As the above stress pair lies on the bounding surface, the value p_0 can be obtained by substituting (p_p, q_p) and previously determined α and N_c value into the bounding surface expression (i.e., equation 4.1). N_c is used as the aforementioned stress point is expected to be lie on the compression side of the bounding surface. After some algebra, the following expression of p_0 is obtained:

$$p_0 = p_p + \frac{(q_p - p_p\alpha)^2}{(N_c^2 - \alpha^2)p_p} \quad (4.54)$$

4.5. Validation of The Basic Model

This section discusses the validation of the basic model with experimental observations of reconstituted Georgia kaolin (Sheu, 1985) and relatively insensitive BCF clay (Zapata-Medina, 2012), for which the effects of soil structure are relatively small.

4.5.1. Reconstituted Georgia Kaolin Clay

Sheu (1985) conducted a series of undrained cyclic loading tests on reconstituted clay specimens, which were created by mixing Georgia kaolin with salty water. For more details about the process of sample preparation and testing, readers are referred to the thesis of Sheu (1985). In the following validation, four undrained cyclic loading tests were simulated, which have different amplitudes of cyclic shear stress, i.e., $q_{cyc} = 121.4$ kPa, $q_{cyc} = 136$ kPa, $q_{cyc} = 140.7$ kPa and $q_{cyc} = 165.5$ kPa.

Model Parameters and Initial Conditions

Table 4.5 summaries model parameters for the reconstituted Georgia kaolin. The parameters $h_c = 50$ and $h_e = 50$ are obtained by fitting the stress-strain curves of the first three loading cycles in the undrained cyclic loading test with $q_{cyc} = 140.7$ kPa. The parameter $c_d = 25$ and $w = 5$ are chosen to match the observed strain development and pore pressure build-up in the above test, respectively. Other parameters shown in Table are obtained from Seidalinov (2012), who calibrated a bounding surface model based on isotropic consolidation tests and monotonic undrained shearing tests on the same reconstituted Georgia kaolin. In experiments, reconstituted specimens were isotropically consolidated to $p = 340$ kPa before cyclic loading. Therefore, internal variable $p_0 = 340$ kPa and $\alpha = 0$ is selected. It is worth mentioning that as no accurate measurement of small strain behavior is available, and observed strain is relatively large, the small strain elasticity model is switched off, and isotropic elasticity is used instead.

Model Simulation and Performance

Figure 4.22 show experimental observations in the test $q_{cyc} = 140.7$ kPa and those computed with the proposed model. To highlight advantages of the proposed plastic flow

Table 4.5. Model parameters for reconstituted Georgia kaolin

Adopted from Seidalinov (2012)									This work			
λ	κ	ν	M_c	M_e	N_c	N_e	C	χ	h_c	h_e	c_d	w
0.121	0.037	0.2	0.87	0.86	0.8	0.8	3	1.69	50	50	25(13*)	5

Note: * $c_d = 13$ value is used when image stress flow rule is employed

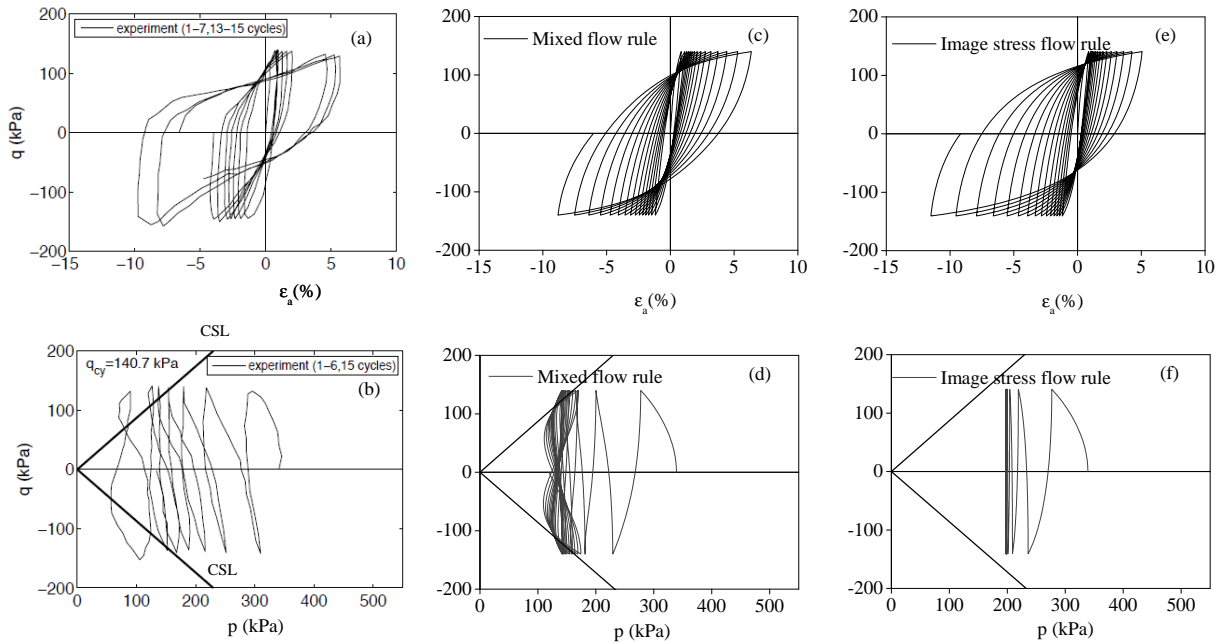


Figure 4.22. Comparison between experimental observations and model simulations in a undrained cyclic loading with $q_{cyc} = 140.7\text{kPa}$: (a)-(b) experimental observations; (c)-(d): simulations of the proposed model; (e)-(f): simulations under image stress flow rule

rule, the model simulations based on image stress flow rule (i.e., $w = 0$) is also included. It is worth mentioning that to achieve similar strain development in cyclic loading, the parameter $c_d = 13$ is used when image stress flow rule is employed. It can be seen that the proposed model can reasonably reproduce the deformation development during cyclic loading. The computed stress-strain loop gradually rotate clockwise indicating the cyclic softening, as observed in the experiment. Moreover, the experimental data show that

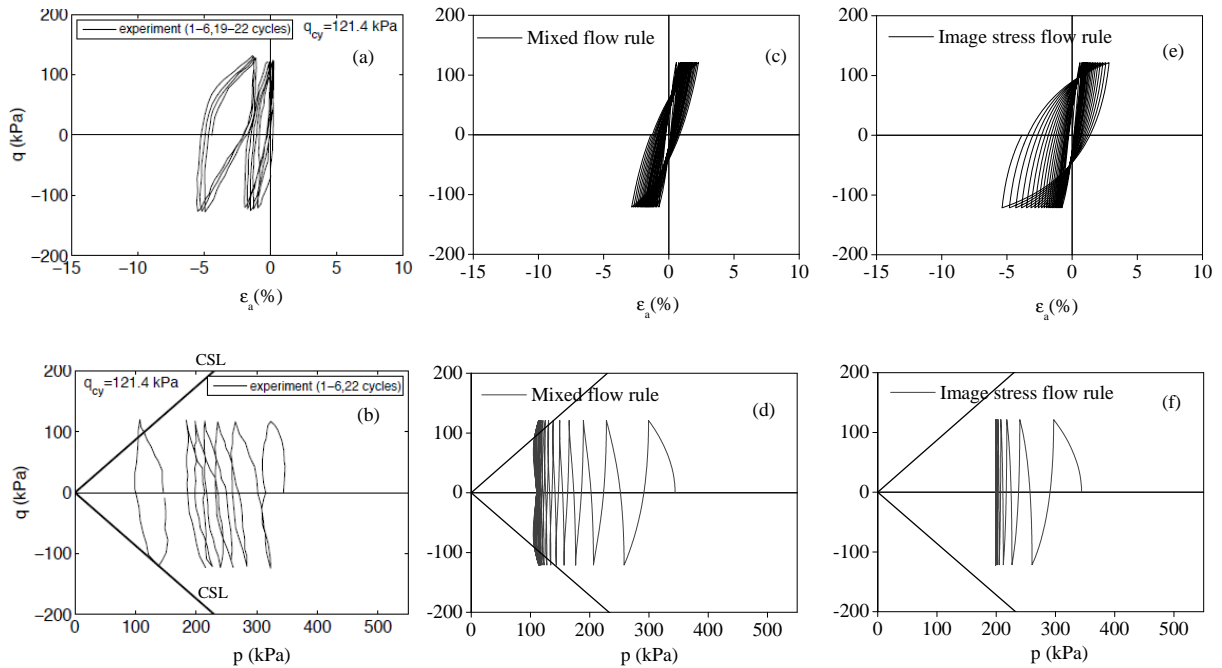


Figure 4.23. Comparison between experimental observations and model simulations in a undrained cyclic loading with $q_{cyc} = 121.4 \text{ kPa}$: (a)-(b) experimental observations; (c)-(d): simulations of the proposed model; (e)-(f): simulations under image stress flow rule

when the effect stress is lower enough due to pore-pressure build-up, the soil exhibited a sudden drop of stiffness whenever the stress path passes p-axis. In the model simulation, similar stiffness degradation is reproduced, but it develops more smoothly than observed in the experiment. This difference implies that the plastic modulus interpolation function (i.e., equation 4.27) may need some modifications, and particularly the experimental data suggest the need to explicitly incorporate the effective stress into the interpolation function. Figure 4.22 (b) and (d) show that pore pressure build-up is also reasonably represented by the proposed model. Like the experimental observations, the computed effective stress paths continuously shift towards the origin of the stress space and form a “butterfly” shape loop when the effective stress paths are close to the critical state line.

Moreover, the proposed mixed flow rule successfully solves the undesired early stabilization of pore pressure build-up observed in the simulations by the image stress flow rule.

To evaluate the predictability of the model, Figures 4.23 through 4.25 compare the model simulations and experimental observations in other three tests, which were not used in the parameters calibration. It can be seen that with the same parameters, the proposed model can reasonably predict the deformation development and pore pressure build-up in the other three cyclic loading tests. Note that the computed strains at the peak of the applied cyclic shear stress in tests $q_{cyc} = 136\text{kPa}$ and $q_{cyc} = 165.5\text{kPa}$ is lower than that observed in experiments, because the aforementioned abrupt drop of stiffness is not reproduced by the model.

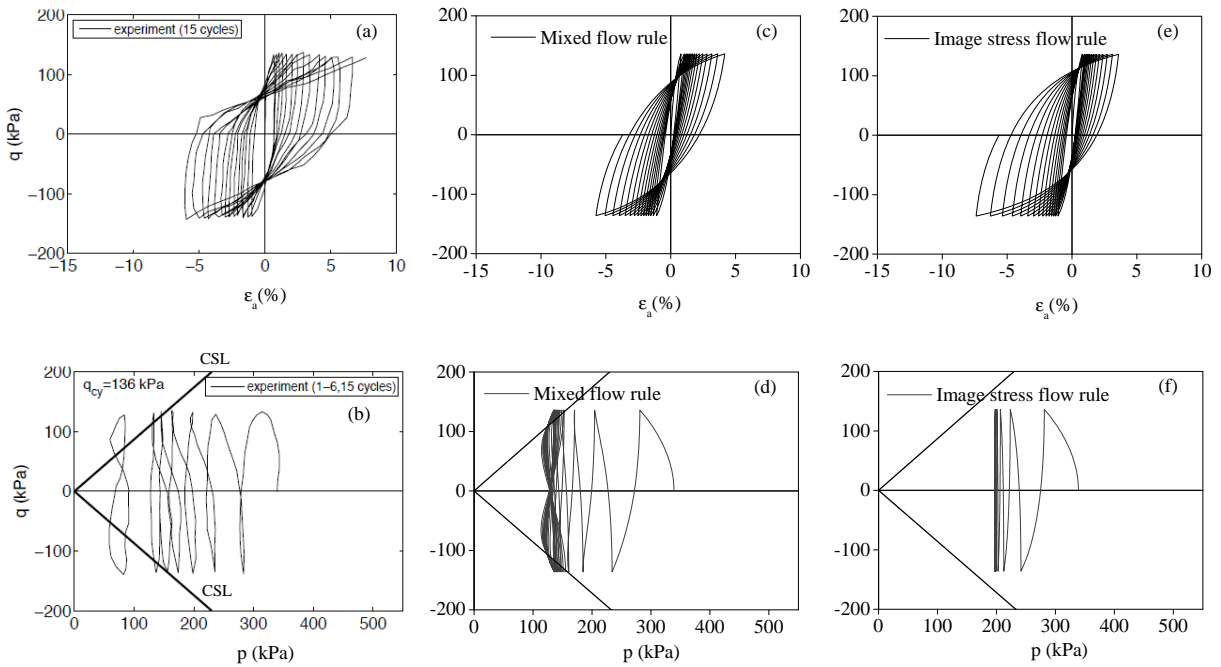


Figure 4.24. Comparison between experimental observations and model simulations in a undrained cyclic loading with $q_{cyc} = 136\text{kPa}$: (a)-(b) experimental observations; (c)-(d): simulations of the proposed model; (e)-(f): simulations under image stress flow rule

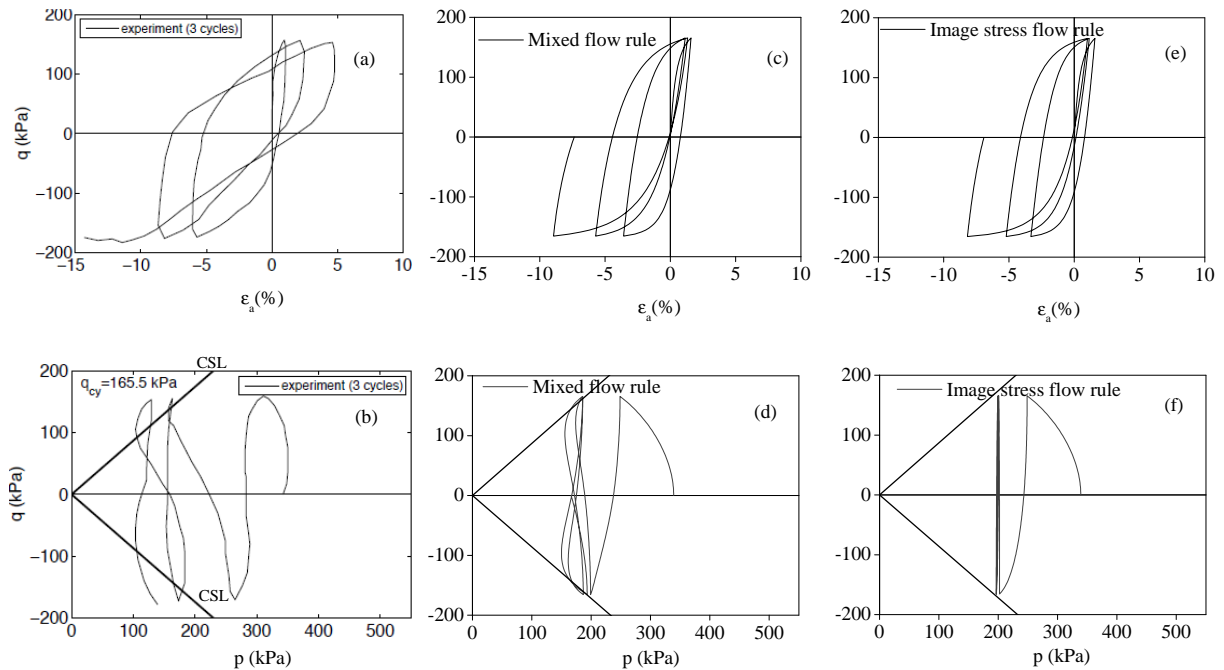


Figure 4.25. Comparison between experimental observations and model simulations in a undrained cyclic loading with $q_{cyc} = 165.5\text{kPa}$: (a)-(b) experimental observations; (c)-(d): simulations of the proposed model; (e)-(f): simulations under image stress flow rule

Figure 4.23 shows that an asymmetrical strain development was observed in the $q_{cyc} = 121.4\text{kPa}$ test, in which strain accumulated in the extension direction (i.e., decreasing axial strain). In contrast, symmetrical strains accumulate in the simulation with the proposed model. Figure 4.24 to 4.25 show symmetric strain development was observed in all other three tests and these symmetrical strain growths are successfully reproduced by the proposed model. Therefore, the above discrepancy is likely to be caused by specimen variation.

Figure 4.26 quantitatively evaluates the model's capacity to capture pore pressure build-up for the above four tests. It can be seen that the proposed model can satisfactorily reproduce the gradual accumulation of pore pressure observed in experiments, except for

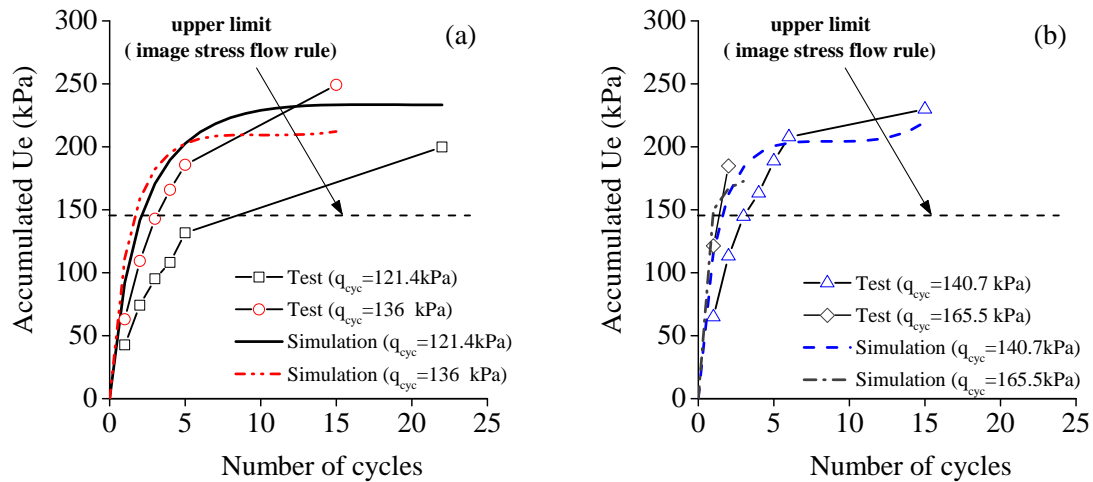


Figure 4.26. Comparison between experimental observations and model simulations of pore pressure build-up in cyclic loading: (a) pore pressure accumulation in tests $q_{cyc} = 121.4\text{kPa}$ and $q_{cyc} = 136\text{kPa}$; (b) pore pressure accumulation in tests $q_{cyc} = 140.7\text{kPa}$ and $q_{cyc} = 165.5\text{kPa}$

the test $q_{cyc} = 121.4\text{kPa}$, in which computed pore pressure accumulation is higher than the observed value. Despite this undesirable discrepancy, the proposed model, with its mixed flow rule, significantly improves the simulation of cyclic pore pressure build-up, compared with image stress flow rule (dotted line shown in Figure 4.26).

Figure 4.27 illustrates the proposed model's capacity to capture cyclic softening, in which experimentally observed peak axial strains in each cycle are compared with the model simulations. The tests $q_{cyc} = 136\text{kPa}$ and $q_{cyc} = 140.7\text{kPa}$ are shown, because the numbers of cycles in these tests are relatively large, and presents a clear trend. It can be seen that the proposed model can both qualitatively and quantitatively reproduce the strains development with increasing number of cycles, and clearly characterize a softening mode of failure.

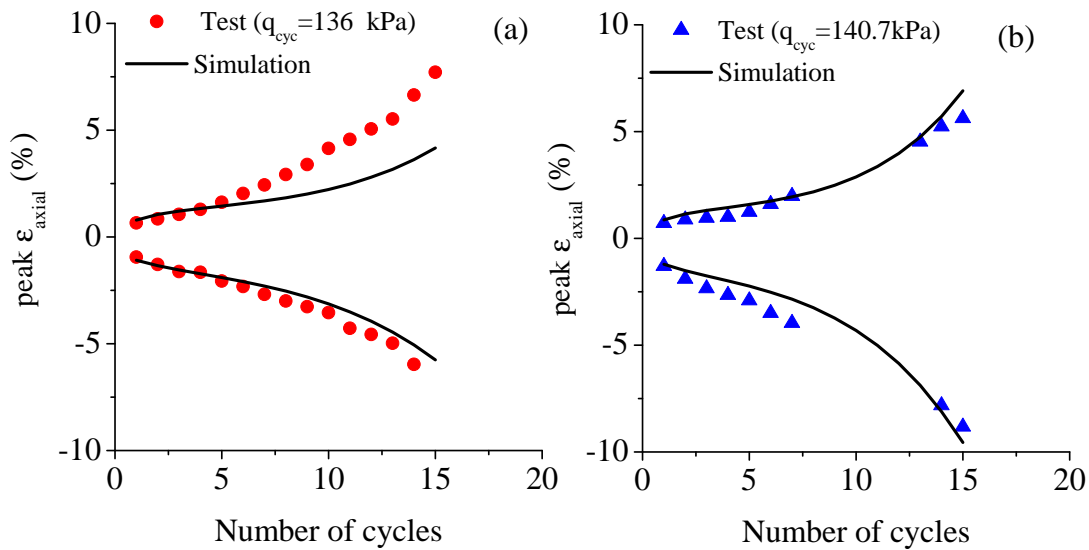


Figure 4.27. Comparison between experimental observations and model simulations of strains development in cyclic loading: (a) peak strains development in tests $q_{cyc} = 136\text{kPa}$; (b) peak strains development in tests $q_{cyc} = 140.7\text{kPa}$

4.5.2. Insensitive BCF clay

A series of triaxial cyclic loading tests, as well as post-cyclic shearing tests were conducted at Northwestern on undisturbed BCF clay specimens (Zapata-Medina, 2012), which were identified as the Facie IV of BCF (Updike and Olsen, 1988) and characterized as insensitive structured clays. The experimental data provide a unique opportunity to evaluate the proposed model in two aspects. First, the model is examined regarding its capacity to reasonably represent the cyclic behavior of both lightly and more heavily overconsolidated clay, which are created by different construction stress paths. This feature is required when one attempts to evaluate the stability of structures that impose significant loads on soils. Zapata-Medina (2012) simulated the construction of an open-cell wharf structure located at the Port of Anchorage in the Plaxis3D. He identified construction-induced

stress changes of stiff OC BCF clays at various locations relative to the wharf structure (i.e., landward, cell toe and seaward in Figure 4.28). The soil beneath the structure (e.g., landward) becomes lightly overconsolidated after construction-induced excess pore water pressures have dissipated. When an earthquake then impacts such a structure, the foundation soil beneath the structure will have a much different response than that immediately adjacent to the structure, which remained little affected by the construction of the retaining structure (e.g., seaward in Figure 4.28). Second, the experimental observations in post-cyclic shearing enable an evaluation of the model's capacity to adequately predict post-cyclic shear strength, which is an important property for engineering applications but has received little attentions in other constitutive modeling efforts.

In the experiments, the stress changes shown in Figure 4.28 were reproduced on clay samples via drained stress-controlled loading, after samples had been reconsolidated to their in-situ stress conditions. The free field condition (i.e., no construction activity) is characterized by sample B47-S7-2. After applying the construction stress paths, stress-controlled undrained cyclic loading equivalent to the Contingency Level Earthquake (CLE) at the project was applied to specimens. This loading corresponded to a cyclic stress ratio (CSR) of 0.2, and 40 cycles of a frequency of 1Hz. After cyclic loading, the samples were immediately subjected to strain-controlled undrained monotonic shearing until failure. More details about the experimental procedures and experimental equipment can be found in the thesis of Zapata-Medina (2012).

Model Parameters and Initial Conditions

Table 4.6 summarizes model parameters for the relatively insensitive BCF clay, whose calibration has been explained in the section 4.4. The parameter λ were calibrated from

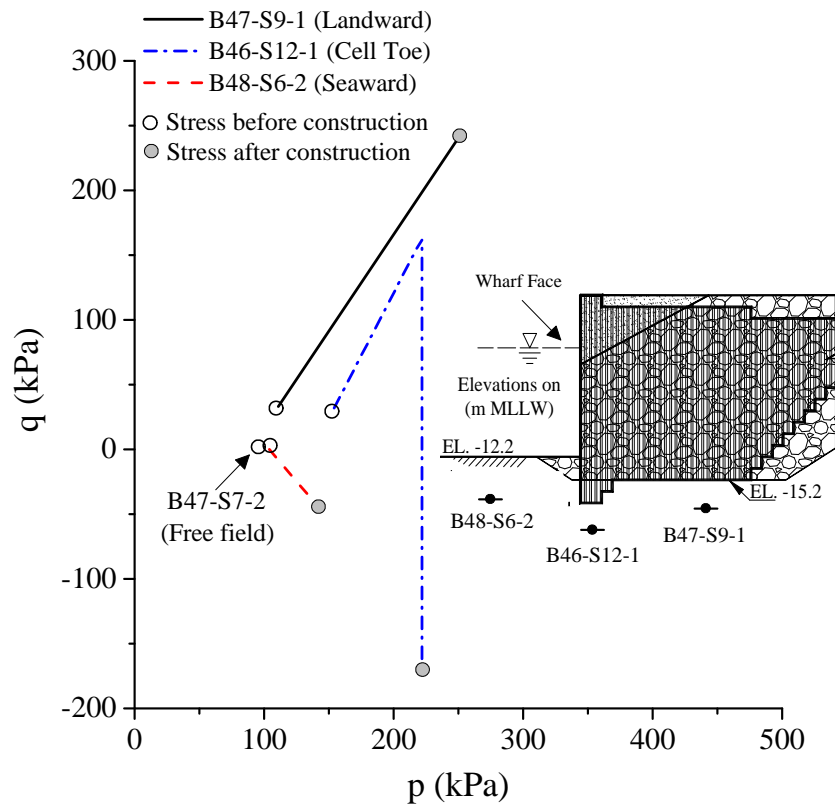


Figure 4.28. Simulated construction-induced stress changes for different samples and their relative positions to the wharf structure

Table 4.6. Model parameters for insensitive BCF clay

λ	κ	M_c	M_e	N_c	N_e	C	χ	h_c	h_e	c_d	w	A_g	e_g	n_g	$\gamma_{0.7}$
0.08	0.022	1.27	0.92	1.22	0.8	8	1.98	400	300	-38	10	250	2.64	0.635	7.00E-04

a 1D compression test on the specimen that has similar compression and recompression indexes as the one in test B47-S9-1. The parameters M_c , M_e and C are calibrated from two monotonic tests, and the parameter N_e is calibrated by matching the post-cyclic undrained strength in the test B48-S6-2. All other parameters were calibrated from the test B47-S9-1.

The initial values of internal variables p_0 and α that corresponds soil in-situ conditions were estimated by the following way. The stress pair (p, q) that corresponds to the maximum stress experienced by the soil was estimated based on σ'_p found in oedometer tests and the $K_{0,NC}$ values found in reconsolidation. The relevant relations are shown in equation 4.53. Then, these stress points were plotted in stress space, and a bounding surface based on the predefined parameters N_c and N_e was constructed to fit these points, as shown in Figure 4.29. However, it was found under this bounding surface configuration, the cyclic loading could not be completed in some simulations. In other words, after several loading cycles, undrained shear strength predicted from the model is less than the peak shear stress applied during cyclic loading. This discrepancy suggests that the size of the bounding surface (i.e., p_0 value) may have been underestimated, which may occur as a result of the underestimation of σ'_p in oedometer tests due to the sample disturbance (Holtz et al., 2010) or variations in σ'_p of the BCF. On the other hand, the $K_{0,NC}$ value that was obtained during reconsolidation tests in the triaxial cell is more consistent. Therefore, the stress states shown in Figure 4.29 provide a more reliable estimation of stress ratio at maximum past stress states, and thus the inclination of the bounding surface, but a less accurate estimation of the bounding surface size. Based on these observations, $\alpha = 0.3$ was fixed and $p_0 = 550$ kPa was calibrated by the model performance in B47-S9-1 cyclic loading test. Table 4.7 summarizes the initial internal variables for each tests. It is worth mentioning that for the B46-12-1, a higher p_0 value is required, with which cyclic loading same as the experiment can be completed in the simulation. Such difference may be attributed to the natural variation between samples, which were obtained from different elevations and boreholes.

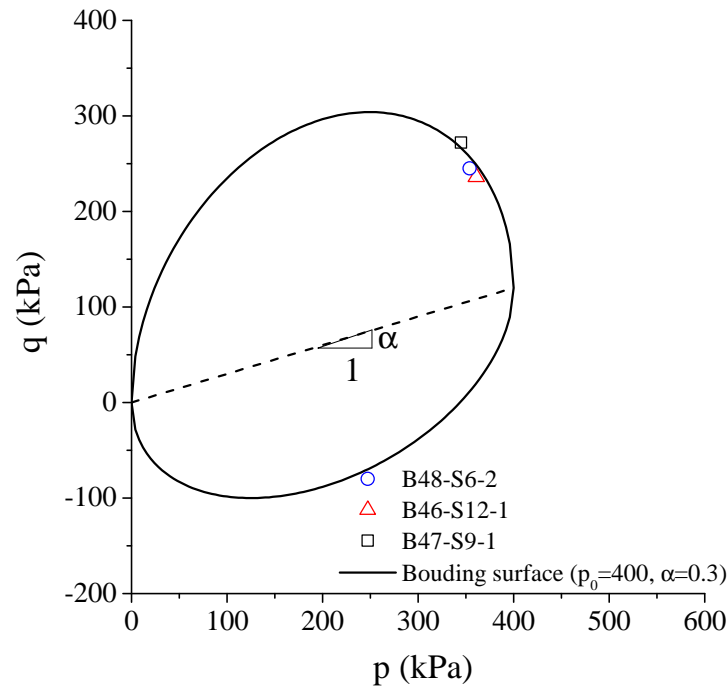


Figure 4.29. Estimation of initial value of internal value α from maximum past pressure

Table 4.7. Initial values of internal variables for insensitive BCF clay

Sample	Elevation (m)	p_0 (kPa)	α
B47-S9-1	-23.8	550	0.3
B47-S7-2	-20.7	550	0.3
B48-S6-2	-21	550	0.3
B46-S12-1	-28.3	850	0.3

The above p_0 values are decided by mainly considering model performance during cyclic loading. To check whether such values are reasonable, simulations of reconsolidation tests were conducted based on the model parameters in Table 4.6 and the internal variables in Table 4.7. Figure 4.30 presents the relevant comparisons. It can be seen that with the selected initial p_0 and α , the model can satisfactorily reproduce the BCF clay's 1D

compression and unloading behavior in four reconsolidation tests. Moreover, except for sample B47-S7-2, experimental data (i.e., the curvature of the compression curve) in the loading branch of all other three tests indicate the yield stress had not been reached during loading, which confirms that the bounding surface in Figure 4.29 is smaller than the actual one. For test B47-S7-2, the yield point can be identified in the initial loading, because the applied vertical stress is much higher than the other three cases. The model simulation well captures such yielding behavior, which suggests the selected p_0 value is reasonable. Some difference among experiments results and model simulations can be seen in the case of B46-S12-1, in which the model computes less void ratio reduction during the initial loading. This discrepancy may be caused by the natural variations in samples as one single set of parameters is used in the four simulations. Otherwise, this difference may suggest an overestimation of p_0 value, which is a compromise for the model's better performance in cyclic loading.

Model Simulations and Performance

In the simulations, similar to actual experiments, three continuous stages were employed: (a) construction-induced stress changes were reproduced; (b) 40 stress-controlled loading cycles with triaxial CSR=0.2 were applied under undrained condition; (c) strain-controlled undrained post-cyclic shearing was applied.

Figure 4.31 shows the experimentally observed and computed stress-strain responses during cyclic loading tests on samples in Figure 4.28. Note that dash-dot and dash line denote 1st cycle and 40th cycle data, respectively. The cyclic stress-strain data in test B47-S9-1 are used in the model calibration, so the corresponding simulation is labeled “computation” and simulations for other three tests are labeled “predication”.

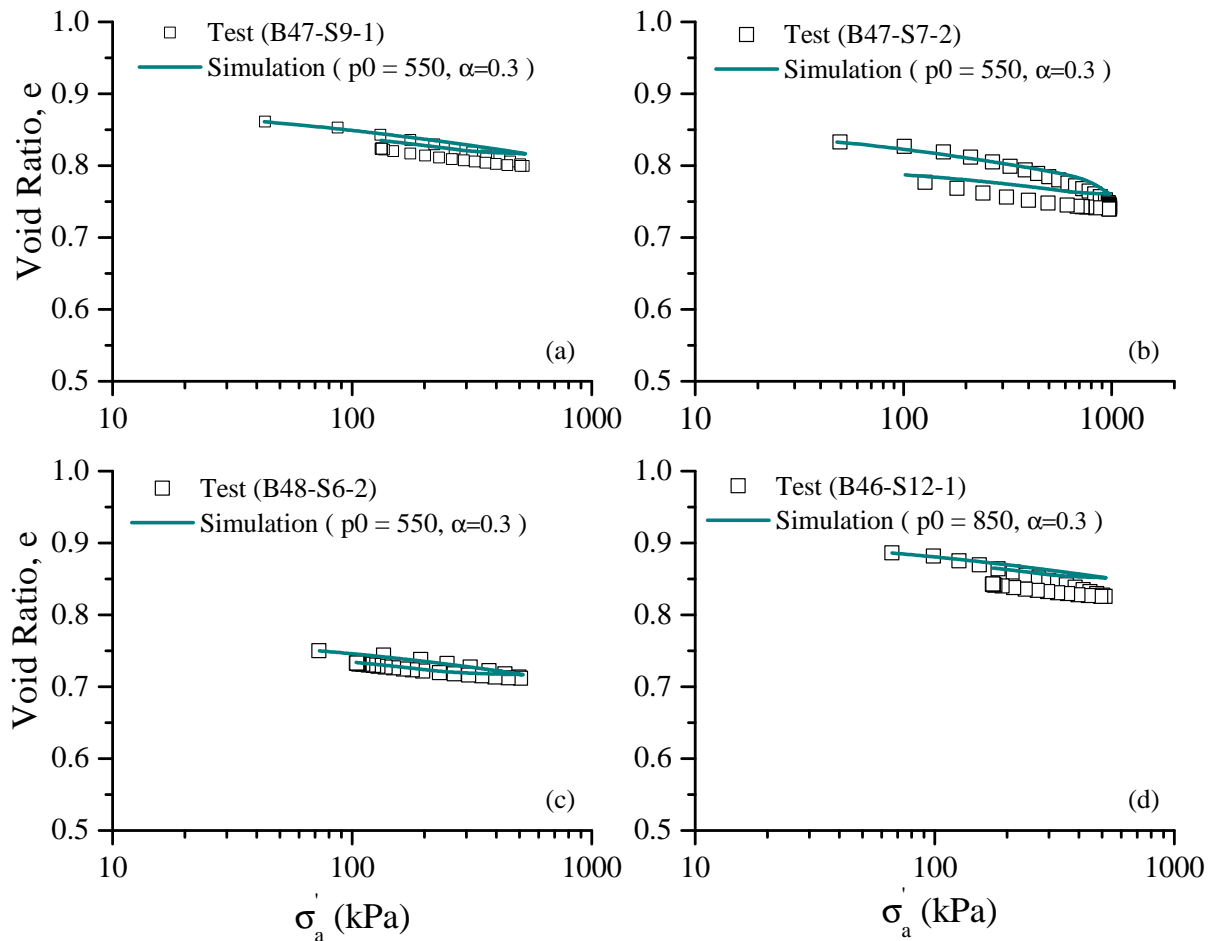


Figure 4.30. Comparison between experimental observations and model simulations in reconsolidation tests: (a) sample B47-S9-1; (b) sample B47-S7-2; (c) sample B48-S6-2; (d) sample B46-S12-1

Experimental data in Figure 4.31 show that the construction activities, and associated soil stress changes significantly affect the strain accumulation during cyclic loading. The same CSR defined the cyclic loading for each sample, but resulting in substantial differences in applied cyclic stresses. The specimen B47-S9-1 was subjected to a consolidation history similar to other samples but then subjected to a drained compression loading path representative of a foundation soil beneath a retaining structure such that the specimen

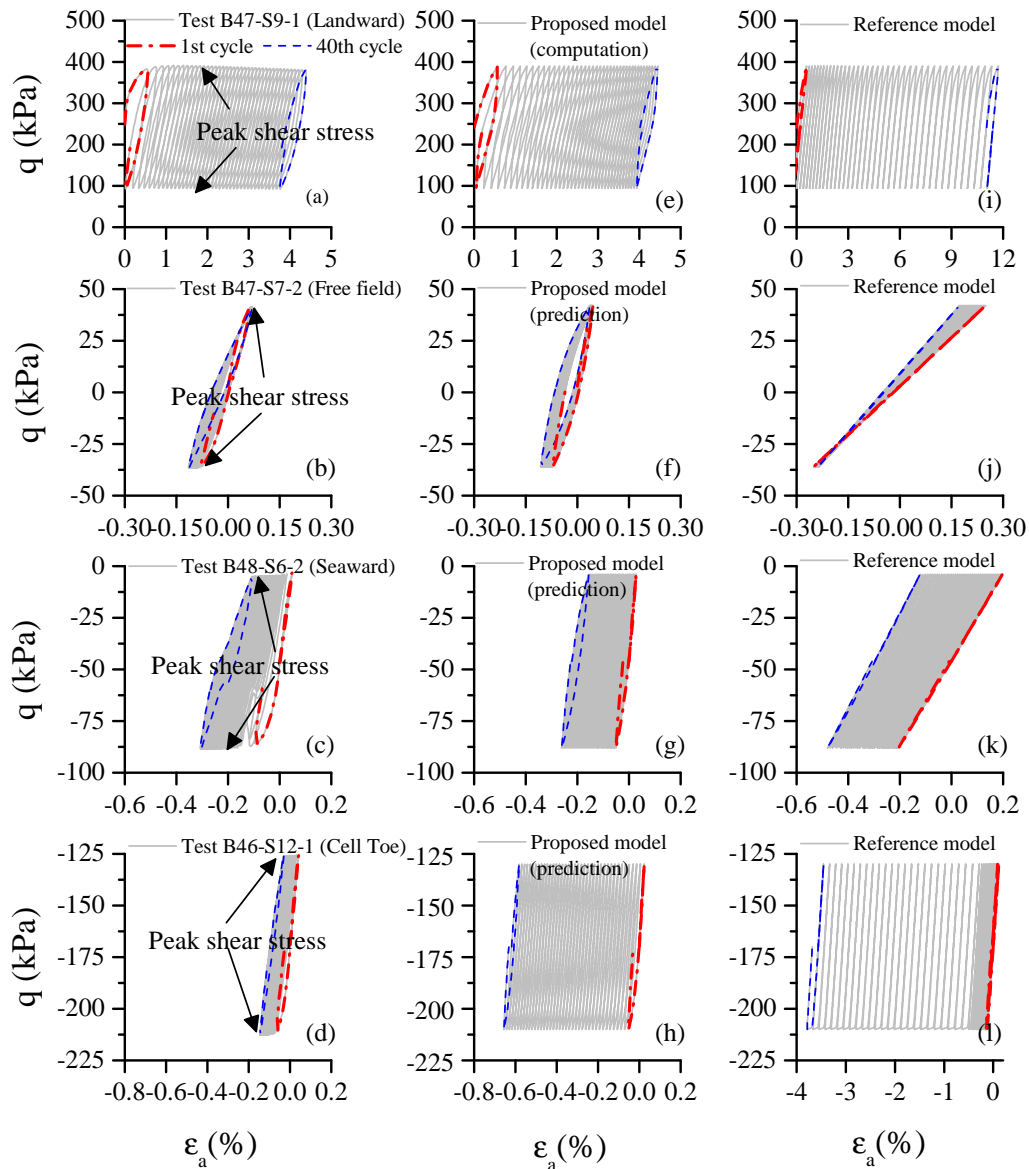


Figure 4.31. Comparison between experimental observations and model simulations of stress-strain response during undrained cyclic loading tests: (a)-(d) experimental data; (e)-(h) simulations by the proposed model; (i)-(l) simulations by the reference model

was lightly overconsolidated after applying the load. It can be seen that the strains which accumulated in this lightly overconsolidated specimen are significantly larger than those

that developed in the samples that were more heavily-overconsolidated (i.e., B47-S7-2 and B48-S6-2). The simulation results in Figure 4.31 shows the above construction effect is reasonably reproduced by the proposed basic model.

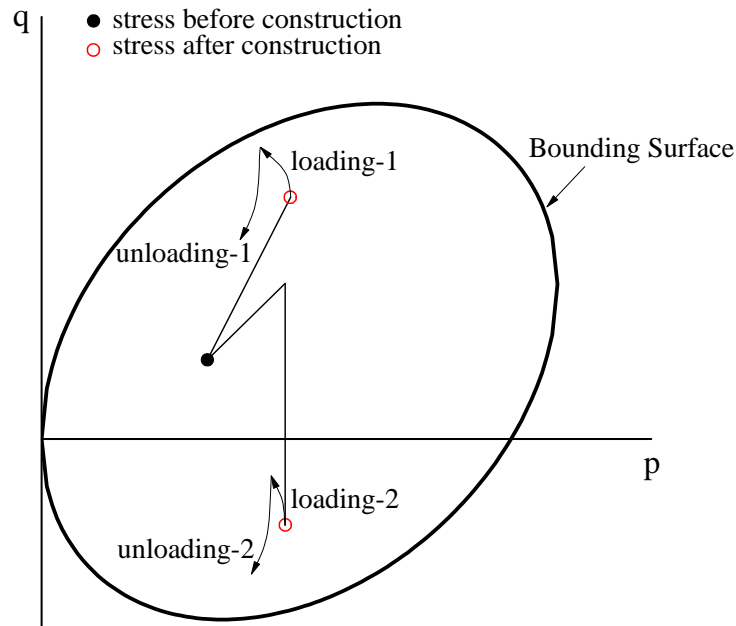


Figure 4.32. Schematic illustrations of the effects of pre-cyclic construction paths on the computed strain accumulation directions

It is found that the construction stress path can also impact the preferential direction of cyclic strain accumulation. For instance, compressive strains (i.e., positive axial strain) accumulated in specimen B47-S9-1, while strains featuring extension (i.e., negative axial strain) accumulated in specimen B46-S12-1 and B48-S6-2. Again, the model simulations correctly capture the direction of strain accumulation. Figure 4.32 illustrates how the proposed model reproduces the above influences of the construction-induced stress changes. After a construction stress path induces a higher shear stress in compression (e.g., sample B47-S9-1), the loading branch featuring compression (loading-1 in Figure 4.32) induces

more permanent deformation than unloading (unloading-1 in Figure 4.32), because the computed amount of plastic deformation is proportional to the proximity of a stress point to the bounding surface. On the other hand, after soil experiences a construction path that brings stress point closer to the extension side of the bounding surface (e.g., sample B46-S12-1), unloading featuring extension (unloading-2 in in Figure 4.32) induced more irrecoverable deformation than loading (loading-2 in in Figure 4.32) in the compression direction, which finally produced a strain accumulation in extension.

The direction of strain accumulation has partially resulted from the effect of recent stress history (Finno and Cho, 2010; Finno and Kim, 2012). The first one-half cycle for specimen B48-S6-2 and B46-S12-1 had a relatively large stress path rotation from its prior construction path. As a result, the corresponding shear stiffness at the first loading branch is much higher than the loading branch of subsequent cycles, which results in less deformation during the first loading. However, this difference in shear stiffness between the first loading and subsequent ones is less noticeable for B47-S9-1, as the stress path rotation of the first loading branch is much smaller. This effect of recent history on shear stiffness is achieved by the adopted small strain elasticity model, in which upon stress reversal (i.e., greater stress path rotation), elastic shear modulus recovers to G_0 .

Moreover, as a result of the small strain elasticity model, the shape of stress-strain hysteresis loop observed in tests is reasonably well reproduced by the model simulations. This achievement is more pronounced when the strains developed during cyclic loading are relatively small. Note that less success is seen in the prediction of the test on sample B46-S12-1, in which the amount of strain accumulation is overestimated. Nevertheless,

considering the actual difference between observed and predicted final strain accumulation, i.e., 0.18% versus 0.65%, the simulation is still acceptable.

To highlight the benefits of new model components, simulations are also included in Figure 4.31 under the conditions that the image stress flow rule is employed ($w = 0$), cyclic shakedown is not considered ($c_d = 0$) and small strain elasticity model is switched off. These computations are referred to as “Reference model” simulations. It can be seen that the reference model significantly overestimates the amount of strain accumulation in the tests of B47-S9-1 and B46-S12-1. This discrepancy partially results from the fact that cyclic shakedown and small strain stiffness behavior are not taken into consideration. Additionally, the accumulation of negative excess pore pressure shown in Figure 4.33 indicates that negative plastic volumetric strain keeps accumulating in the simulations of the reference model, which induced a gradually shrinking bounding surface. Accordingly, computed plastic deformation and the amount of strain accumulation are increased.

Furthermore, in simulations of tests B47-S7-2 and B48-S6-2 by the reference model, the slope of stress-strain curve gradually increases during cyclic loading, which indicates the soil stiffness is increasing as more cycles are applied. This cyclic hardening is contrary to the cyclic softening observed in the experiments and is attributed to the accumulation of negative pore pressure which increases the effective stress and the computed elastic stiffness which is proportional to the effective stress. These observations highlight the coupling between clay strain accumulation and pore pressure build-up in a undrained cyclic loading and the importance of the appropriateness of the plastic flow rule, as the reasonably accurate predictions of strain and pore pressure accumulation heavily rely on it.

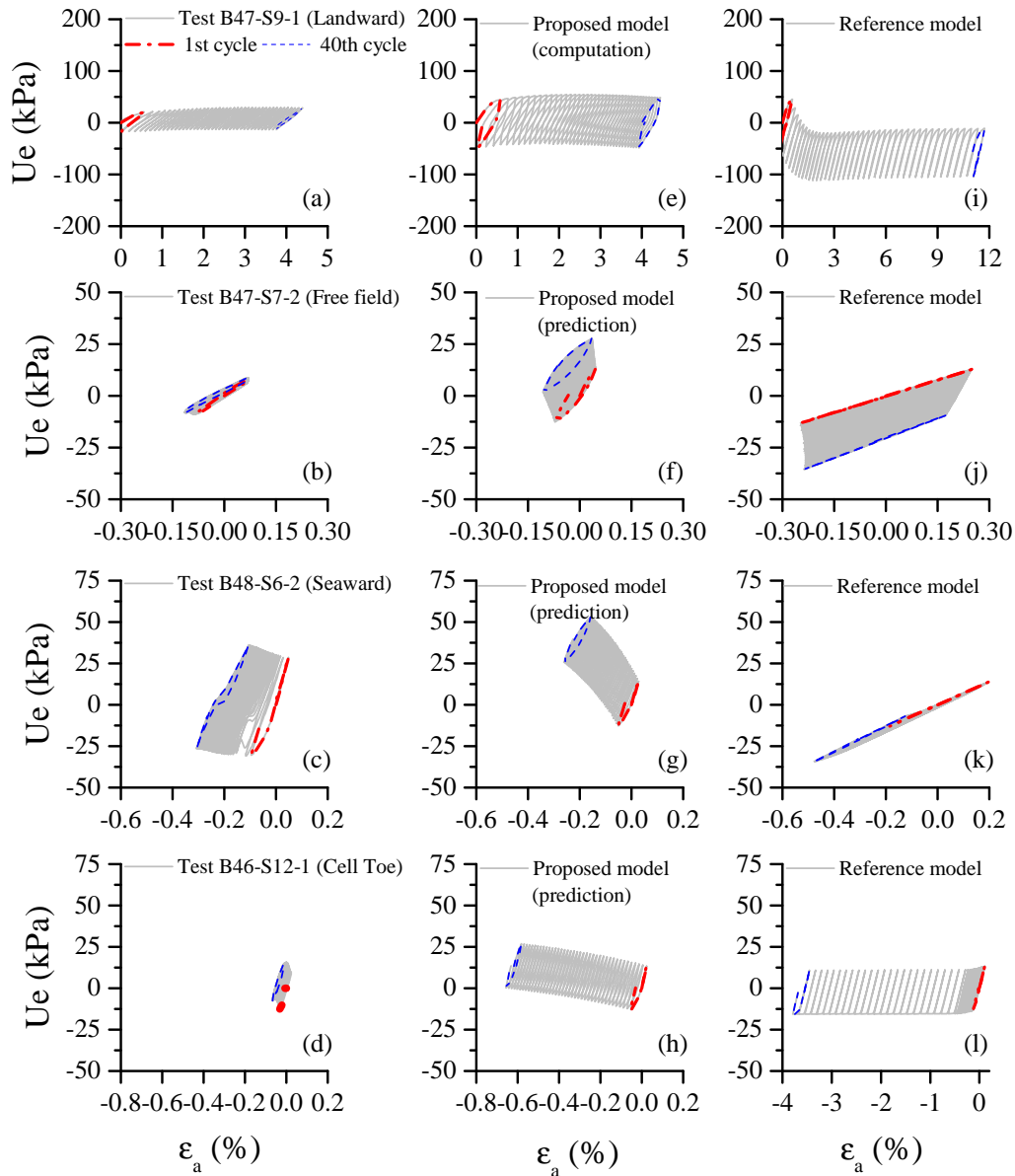


Figure 4.33. Comparison between experimental observations and model simulations of strain-pore pressure response during undrained cyclic loading tests: (a)-(d) experimental data; (e)-(h) simulations by the proposed model; (i)-(l) simulations by the reference model

Figure 4.33 shows the pore pressure responses during the above cyclic loading. Note that the reference model, which uses the image stress flow rule, simulates the accumulations of negative pore pressure. On the other hand, the proposed model can satisfactorily

reproduce the build-up of positive pore pressure during cyclic loading for all tests. The final amount of pore pressure build-up simulated by the proposed model is 5 to 25 kPa higher than experiments. As discussed earlier, one possible explanation for the discrepancy above is that non-uniform pore pressure within a specimen cannot reach equalization during cyclic loading of 1Hz. As a result, the pore pressure measured at the bottom of a sample cannot represent soil constitutive responses, which the model tries to reproduce. Besides, to verify the above hypothesis, cyclic loading tests with lower cyclic loading rates, which can ensure the equalization of pore pressure, are needed in the future. Finally, It worth mentioning that the above comparisons illustrate the strong predictability of the proposed model. The model can reasonably predict cyclic stress-strain responses in tests that were not used in the model calibrations and especially these tests have very different pre-cyclic stress history compared with the test that was directly used to calibrate model parameters.

Figure 4.34 shows the tests results of post-cyclic undrained shearing and the simulations of the basic model. It can be seen the computed responses reasonably agree with the experimental observations regarding strain-stress-pore pressure response during post-cyclic shearing. The difference between computed and measured undrained strength varies from 2% to 10%, which is accurate enough for the model to be used in assessing the stability of geotechnical facilities after cyclic loadings (e.g., earthquake or offshore wave actions). Also, the trend of pore pressure evolution during shearing is correctly captured by the model.

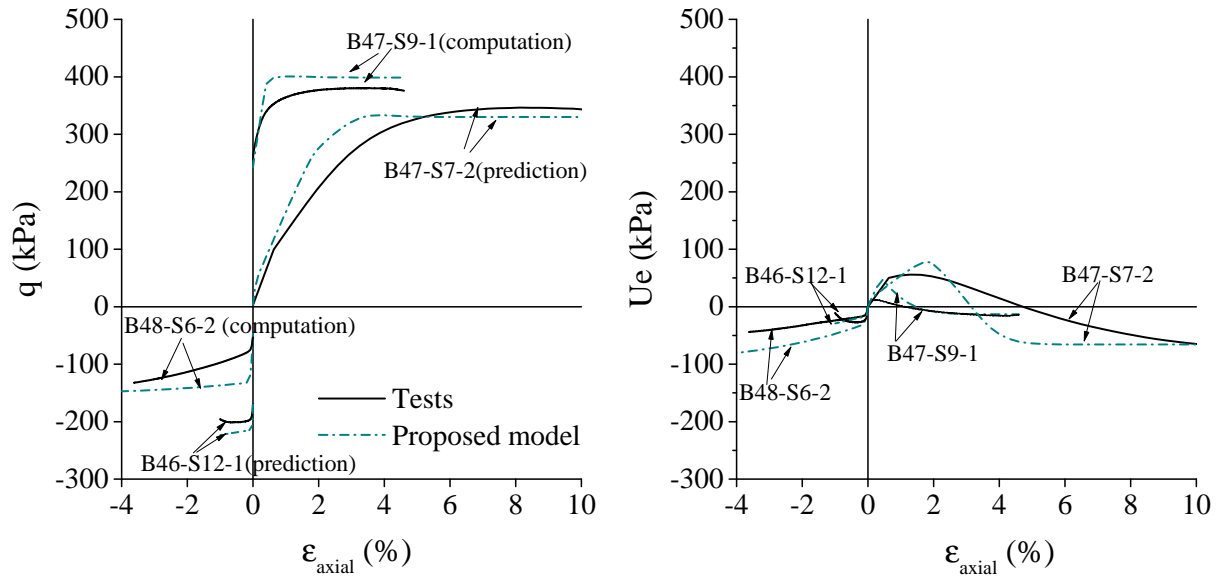


Figure 4.34. Comparison between experimental observations and model simulations in post-cyclic undrained shearing: (a): stress-strain response; (b) strain-pore pressure response

4.6. Summary and Conclusions

This chapter presents the formulation of the basic constitutive model in triaxial space, which is developed within a bounding surface plasticity framework. Compared with existing bounding surface plasticity models for cyclic clay behavior, three major enhancements are proposed, including the mixed plastic flow rule, a new form of plastic modulus to uniformly reproduce cyclic softening and shakedown, and the adoption of a small strain elasticity model. The results from a series of parametric studies are discussed, which elucidate the roles of new model components. The steps required to calibrate model parameters and estimate the initial values of the internal variables are presented. Finally, the basic model is validated with respect to experimental observations of two relatively

unstructured types of clay: reconstituted Georgia kaolin and relatively insensitive BCF clay. The following main conclusions can be drawn from this chapter:

- (1) The verification with experimental observations shows that the proposed basic model is general, versatile and can reliably represent observed responses. With a single set of parameters, the proposed basic model is capable of reproducing strain and pore pressure accumulation during cyclic loading with different shear stresses and various complex stress histories before cyclic loading.
- (2) The proposed mixed plastic flow rule incorporates characteristics of plastic flow direction defined by the current stress state into the existing image stress flow rule. The employment of this new flow rule successfully solves the undesirable early stop of pore pressure build-up inherent with the use of flow rule based on the image stress. Further, compared with the image stress flow rule, the proposed flow rule ensures that a correct trend of pore pressure build-up is reproduced. The new parameter w provides model users additional flexibility in controlling the amount of pore pressure build-up during undrained cyclic loading.
- (3) The proposed plastic modulus formulation enables the model to reproduce in a unified manner both cyclic softening and cyclic shakedown, which are observed in tests on the reconstituted Georgia kaolin and insensitive BCF clay, respectively.
- (4) When large plastic deformation develops and forms the majority of total deformation, ignoring small strain stiffness will not cause significant differences in computed responses. When cyclic strains are relatively small, incorporation of the small strain elasticity model will better simulate the cyclic stress-strain hysteresis loop, corresponding energy dissipation, and the recent stress history

effects. Ignoring small strain stiffness under some circumstance can limit the amount of deformation accumulation and underestimate pore pressure build-up in cyclic loading, which may eventually lead to unsafe predictions if the number of cycles is large.

- (5) Experiments on relatively insensitive BCF clay show construction-induced stress changes significantly affect clay behavior during cyclic loading, including the amount and directional preference of strain accumulation. This feature is delicately reproduced by the proposed model. The proposed model also can satisfactorily capture the stress-strain-pore pressure responses observed in post-cyclic shearing on relatively insensitive BCF clay, which enables the model to be used in assessing the stability of geotechnical facilities after cyclic loading.

CHAPTER 5

**EXTENSION OF THE BASIC CONSTITUTIVE MODEL
FOR CYCLICALLY LOADED STRUCTURED CLAY**

5.1. Introduction

To consider structure effects typical of natural clays and their deterioration during cyclic loading, the basic constitutive model presented in chapter 4 is extended. The formulation and validation of this extended model are the focus of the present chapter.

Within various constitutive models that achieve encouraging success in modeling structured soil and its destructuration, very few of them (e.g., Yu et al. (2007b)) have studied the influence of the soil's structure on material plastic flow, which is a keystone for models to capture plasticity behavior of structured soil. A new form of plastic potential surface has been employed in the extended model, which explicitly considers clay fabric anisotropy and inter-particle bonds. To provide more insights concerning the issue above, the effects of structure on plastic flow has been studied through the stress-dilatancy relation derived from the above plastic potential surface. Further, available experimental evidence is used to evaluate and validate the appropriateness of the proposed plastic potential surface.

The capacity of the extended model is assessed via comparing model simulations with experimental observations on eight different natural clays. To provide a comprehensive evaluation, the selected clays are characterized by a wide range of index properties; tested samples have various stress history (i.e., OCR ranges from 1 to 5); loading programs include both monotonic and cyclic loading, drained and undrained conditions and compression and extension shearing. Notably, the validation on experiments of Grande Baleine clay, Cloverdale clay and sensitive BCF clay examines the ability of the model to track clay structure degradation and correspondingly reproduce strength reduction during cyclic loading.

This chapter is organized as follow: First, the extension of the basic model and relevant formulation in triaxial space is presented. Then, the effects of soil structure on stress-dilatancy relation are discussed. Besides, calibration of newly introduced model parameters is demonstrated, which is followed by the method to estimate new internal variables. Finally, the validation of the extended model with experimental observations is discussed.

5.2. Extension of the Basic Model to Consider the Effects of Soil Structure

In this section, the extension of the basic model is discussed. This extension enables the model to reproduce salient features in the stress-strain behavior of natural clays, including enlarged yielding stress, substantially higher compressibility during post-yielding compression, strain-softening during shearing, and most importantly, the progressive convergence of natural clays behavior to the corresponding intrinsic behavior.

The emphasis of this section is given to the concepts of intrinsic surface and structure surface, proposition of a new plastic potential surface, and destructuration law that governs the structure degradation with plastic deformations. Also, the modifications of plastic modulus and the evolution rule of projection center are discussed. It is worth mentioning that model components that remain the same as ones in the basic model will not be repeated.

5.2.1. Intrinsic Surface, Structure Surface, and Plastic Potential Surface

The intrinsic surface and structure surface in the extended model are illustrated in Figure 5.1. Following the logic behind the term “intrinsic behavior” introduced by Burland

(1990), the intrinsic surface governs the behavior of clays, in which the effects of structure are negligible. Therefore, the intrinsic surface takes the same form as the bounding surface in the basic model. The structure surface is the real bounding surface in the extended model, which is constructed based on the intrinsic surface and two additional internal variable p_m and p_t . Being the macroscopic manifestation of inter-particle bonds, p_m is introduced to reproduce the enlarged yield surface (bounding surface in this work) of natural clay while p_t is used to model the true cohesion that exists in natural clay (Rampello et al., 1993). Furthermore, as portrayed in Figure 5.1(a), the structure surface is assumed to have the same shape, rotation and distortion as the intrinsic surface, i.e., both surfaces are characterized by the same value of α . As the internal variable α is determined by the stress history, the above assumption implies that the plasticity anisotropy is an intrinsic property of natural clay and is solely determined by stress history, which is consistent with experimental evidence (Tavenas and Leroueil, 1977; Leroueil and Vaughan, 1990; Gens, 1982; Parry and Nadarajah, 1973).

For the sake of convenience, a translated coordinate $p^* - q$ is introduced, which horizontally translates the bounding surface by p_t from the original $p - q$ coordinate. In the new coordinate, the structure surface is expressed as:

$$F_s = (\bar{q} - \alpha \bar{p}^*)^2 - (N^2 - \alpha^2) \bar{p}^* (p_{s0}^* - \bar{p}) \quad (5.1)$$

with the loading direction defined at the image stress as:

$$\partial F_s / \partial \bar{p}^* = \bar{p}^* (N^2 - \bar{\eta}^{*2}); \quad \partial F_s / \partial \bar{q} = 2 \bar{p}^* (\bar{\eta}^* - \alpha) \quad (5.2)$$

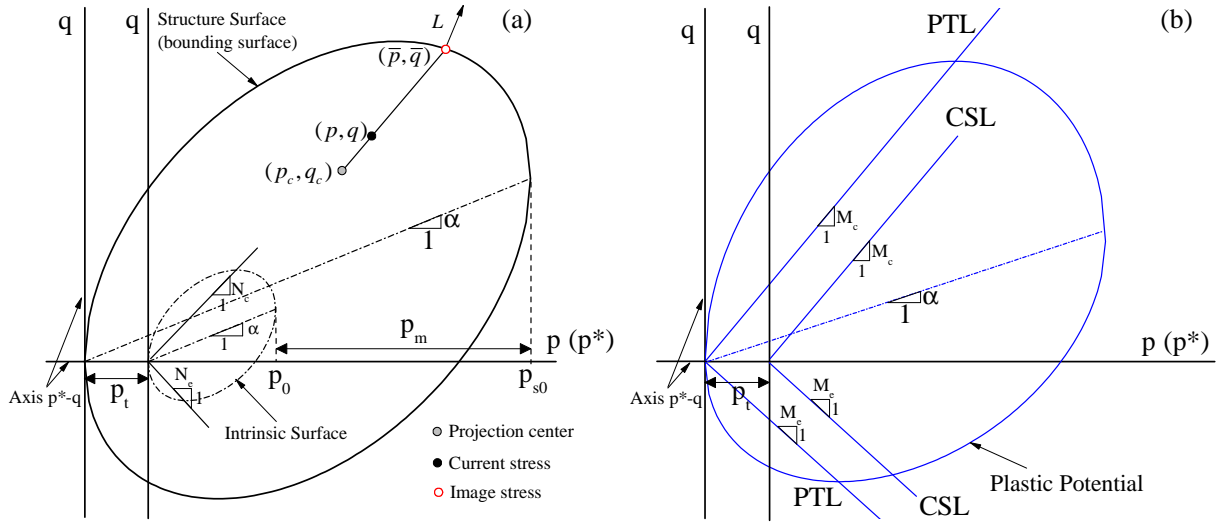


Figure 5.1. Schematic illustration of important surfaces in the extended model: (a) intrinsic surface and structure surface; (b) plastic potential surface

Superscript ' $*$ ' in the above equations denotes the variable after axis translation, i.e., $\bar{p}^* = \bar{p} + p_t$, $p_{s0}^* = p_{s0} + p_t$ and $\bar{\eta}^* = \bar{q}/\bar{p}^*$. The variables p_{s0} , p_m and p_t shown in Figure 5.1 are related to each other through:

$$\begin{aligned} p_{s0} &= p_0 + p_m \\ p_m &= S_b p_0 \\ p_t &= r_c p_m \end{aligned} \quad (5.3)$$

S_b is a new internal variable which quantifies the amount of inter-particle bonds. For the sake of simplicity, the variable p_t is assumed to be linearly related to p_m through the model parameter r_c .

For the extended model, the mixed flow rule proposed in the basic model (i.e., equation 4.8) is inherited. However, the plastic potential surface has been modified:

$$g_s = (q - \alpha p^*)^2 - (M^2 - \alpha^2)p^*(p_a - p^*) \quad (5.4)$$

with its derivatives being:

$$\partial g_s / \partial p^* = p^*(M^2 - \eta^{*2}); \quad \partial g_s / \partial q = 2p^*(\eta^* - \alpha) \quad (5.5)$$

As shown in Figure 5.1(b), modified plastic potential surface is also anchored at the origin of coordinate $p^* - q$. Due to this axis translation, the line passing through the peak of the plastic potential surface is shifted to the left. This line is renamed as phase transition line (PTL), since this line is the collection of stress state at the boundary between plastic dilation and contraction. The designation of critical state line (CSL) is not used, as critical state, strictly speaking, is the state of continuous and purely frictional shearing (Schofield and Wroth, 1968), as opposed to the cohesive-frictional nature of structured clay due to the existence of inter-particle bonds (Rampello et al., 1993). Therefore, critical state can only be reached after inter-particle bonds have been completely eliminated. Considering the relations in equation 5.3, the location of phase transition line in stress space depends on the amount of inter-particle bonds. When bonds deteriorate, the phase transition line will shift to the right due to the decrease of the internal variable p_t and thereby creates a changing boundary between plastic contraction and dilation. As a result, soil's dilatancy predicted by the model is not only a function of stress state but also relies on the amount of inter-particle bonds. Eventually once all inter-particle bonds have been broken (i.e., $p_m = 0$ and $p_t = 0$), the phase transition line will converge back to the critical state

line and plastic potential surface will become the one in the basic model. At the same time, the structure surface coincides with intrinsic surface and the constitutive behavior predicted by the extended model is identical to the ones obtained from the basic model. This is consistent with the idea that the behavior of structured clay will be identical to that of reconstituted clay once the loading or deformation is large enough to remove all the structure (Burland, 1990).

5.2.2. Internal Variables Hardening Laws and Plastic Modulus

The destructuration law proposed by Taiebat et al. (2010) is adopted in this work to govern bond deterioration, i.e., the evolution of the internal variable S_b :

$$\begin{aligned} \dot{S}_b &= -(k_i S_b) \dot{\varepsilon}_{de} = \langle \Lambda \rangle \bar{S}_b; \\ \dot{\varepsilon}_{de} &= \sqrt{(1-A)(\dot{\varepsilon}_v^p)^2 + A(\dot{\varepsilon}_d^p)^2}; \quad \bar{S}_b = -(k_i S_b) \sqrt{(1-A)(R_v)^2 + A(R_d)^2} \end{aligned} \quad (5.6)$$

This rate form of destructuration law implies S_b value will exponentially decrease with the growth of destructuration strain ε_{de} , and the constant k_i controls the rate of destructuration. The decrease of S_b and its competition with the hardening that is associated with density increase are keys for the model to capture higher post-yield compressibility, strain-softening and other peculiar features of natural clay. The definition of destructuration strain implies both volumetric and deviatoric plastic strains contribute to the bond deteriorations. This is consistent with the experimental evidences that loss of bonds are observed in both compression and shearing tests. Parameter A is responsible for allocating relative contributions of deviatoric and volumetric plastic strains. Additionally, the form of ε_{de} ensures that inter-particle bonds monotonically decreases, independently of

the sign of the plastic strain. In terms of plastic volumetric strains, it implies that both plastic contraction and dilation will induce the degradation of natural clay.

The isotropic hardening law for internal variable p_0 in the basic model (i.e., equation 4.20) is assumed to be valid for natural clays. However, the rotation hardening law needs slight modifications. The term $(\bar{p}/p_0)^2$ and $(\bar{\eta} - \chi\alpha)$ in equation 4.21 is replaced by $(\bar{p}^*/p_{s0}^*)^2$ and $(\bar{\eta}^* - \chi\alpha)$, respectively, due to facts that structure surface is the bounding surface and the rotation axis is passing the origin of translated coordinate $p^* - q$. Correspondingly, the vector \mathbf{r} in equation 2.5 for the extended model is :

$$\mathbf{r} = [\bar{p}_0, \bar{\alpha}, \bar{S}_b] \quad (5.7)$$

The term \bar{K}_p in plastic modulus equation of the basic model (i.e., equation 4.24) is modified based on the consistency condition of the structure surface:

$$\bar{K}_p = - \left(\frac{\partial F_s}{\partial p_{s0}^*} \bar{p}_{s0}^* + \frac{\partial F_s}{\partial \alpha} \bar{\alpha} + r_c \frac{\partial F_s}{\partial \bar{p}^*} (p_0 \bar{S}_b + S_b \bar{p}_0) \right) \quad (5.8)$$

where:

$$\frac{\partial F_s}{\partial p_{s0}^*} = -\bar{p}^*(N^2 - \alpha^2); \quad \frac{\partial F_s}{\partial \alpha} = -2\bar{p}^*(\bar{q} - p_{s0}^* \alpha); \quad (5.9)$$

$$\bar{p}_{s0}^* = (1 + (1 + r_c)S_b)\bar{p}_0 + (1 + r_c)p_0\bar{S}_b$$

In the extended model, function $f(b)$ in plastic modulus equation takes the following form:

$$f(b) = \frac{h(1 + e_0)p_{s0}^{*3}}{\langle b/(b-1) - s \rangle} m_s \quad (5.10)$$

Compared with the counterpart in the basic model (i.e., equation 4.27), the only change is that p_0 has been replace by p_{s0}^* . Since p_{s0}^* is larger than p_0 , this modification is able to

reproduce higher cyclic stiffness of natural clay due to the bonds between soil particles. Moreover, as the degradation of inter-particle bonds (i.e., S_b decreases) will lead to the decrease of p_{s0}^* , equation 5.10 explicitly considers the effect of particle bond breakage on the gradual stiffness reduction of natural clay during cyclic loading.

5.2.3. Projection Center Evolution Rule and Elasticity Model

In the extended model, the variable X_p and X_d in equation 4.18 is redefined in terms of structure surface:

$$X_p = \frac{p_c^*}{p_{s0}^*}; \quad X_d = \frac{q_c - q_a}{q_b - q_a} \quad (5.11)$$

Through differentiating equation 5.11 and setting $\dot{X}_p = 0$ and $\dot{X}_d = 0$, the evolution of projection center is again expressed as a function of changes of internal variables:

$$\dot{p}_c = \frac{p_c^*}{p_{s0}^*} \dot{p}_{s0}^* - \dot{p}_t; \quad \dot{q}_c = \frac{q_c}{p_{s0}^*} \dot{p}_{s0}^* + \frac{N_c^2 p_c^* - \alpha q_c}{N_c^2 - \alpha^2} \dot{\alpha} \quad (5.12)$$

where:

$$\dot{p}_{s0}^* = (1 + (1 + r_c)S_b)\dot{p}_0 + (1 + r_c)p_0\dot{S}_b; \quad \dot{p}_t = r_c(S_b\dot{p}_0 + p_0\dot{S}_b) \quad (5.13)$$

While different elastic properties have been observed for some natural clays, generally changes are not very significant (Burland, 1990; Smith et al., 1992). Specifically, Cotecchia and Chandler (1997) compared normalized shear modulus with respect to confining stress at small to intermediate strains of natural Pappadai clay samples and corresponding reconstituted ones. Little difference was observed. Therefore, the nonlinear small strain elasticity model in the basic model is used to describe the elasticity behavior of natural

clays, and for simplicity the relevant parameters are assumed to be independent of soil structure.

5.3. The Influence of Natural Clay Structure on Plastic Flow

In the extended model, the plastic potential surface proposed by Dafalias (1986a), which explicitly considers the influence of fabric anisotropy, is further modified via axis translation. The new plastic potential surface (i.e., equation 5.4) is a function of both fabric anisotropy (i.e., internal variable α) and inter-particle bonds (i.e., internal variable p_t), which are critical components of the natural clay structure. In this section, the stress-dilatancy relation derived from the plastic potential surface above has been used to elucidate the roles of soil structure on material plastic flow. Accordingly, relevant experimental evidence is used to examine the appropriateness of the above plastic potential.

As suggested by Wood (1990), the stress-dilatancy relation is presented in the form of a stress-dilatancy diagram, in which stress ratio η and plastic dilatancy angle β are used. And β is defined as:

$$\tan \beta = \frac{\dot{\varepsilon}_d^p}{\dot{\varepsilon}_v^p} \quad (5.14)$$

As shown in Figure 5.2, for the condition of positive $\dot{\varepsilon}_d^p$, angle $0 < \beta < \pi/2$ indicates plastic contraction (i.e., $\dot{\varepsilon}_v^p > 0$), $\beta > \pi/2$ indicates plastic dilation (i.e., $\dot{\varepsilon}_v^p < 0$) and $\beta = \pi/2$ implies the state of zero plastic volumetric strain rate (i.e., critical state for reconstituted clay) is reached. To highlight the influence of soil structures on plastic flow, let us consider the situation that $\dot{\varepsilon}_d^p > 0$ and the stress point is on the bounding surface (i.e., plastic flow direction is solely determined by plastic potential surface and current

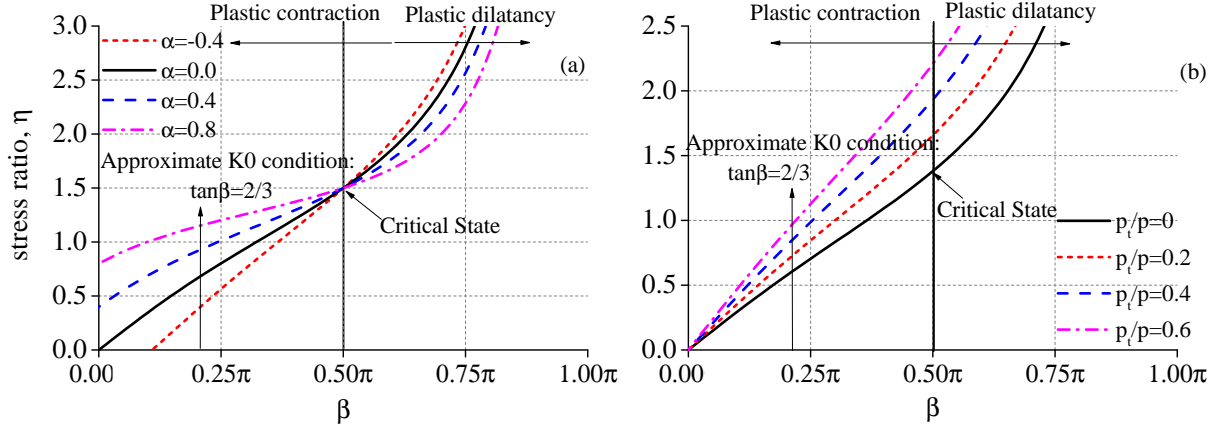


Figure 5.2. The influences of variable α and p_t/p on stress-dilatancy curve: (a) varying α under $p_t/p = 0$; (b) varying p_t/p under $\alpha = 0$

stress state). Based on the plastic potential surface in equation 5.4, $\tan \beta$ could be written as:

$$\tan \beta = \frac{\partial g / \partial q}{\partial g / \partial p} = \frac{2(\eta^* - \alpha)}{M^2 - \eta^{*2}} \tag{5.15}$$

with

$$\eta^* = q/p^* = \eta/(1 + p_t/p) \tag{5.16}$$

It is worth mentioning when fabric anisotropy and inter-particle bond are ignored (i.e., $\alpha = 0$ and $p_t = 0$), the stress-dilatancy relation of Modified Cam-Clay model is recovered. Figure 5.2 presents theoretical stress-dilatancy curves based on equation 5.15. For the sake of clarity, the effects of α and p_t are illustrated separately in Figure 5.2(a) and (b), respectively. Nevertheless, in reality, these two factors will work together. Figure 5.2(a) shows the increase of α induces a clockwise rotation of the diagram around a fixed point, which represents the state of critical state. In other words, the stress ratio at critical state is independent of the value of α . As a result of the rotation, the plastic volume change will increase given the same stress ratio. Furthermore, the predicted stress-dilatancy diagram

under non-zero value of α will intersect axis $\eta = 0$ at a non-zero β . This implies that due to the existence of fabric anisotropy, after yielding the increase of isotropic stress in the absence of deviatoric stress can cause not only compression but also distortion. While the intersections between stress-dilatancy curves and axis $\beta = 0$ indicates purely compressive, non-distortional plastic deformation occurs for non-isotropic stress state (i.e., non-zero stress ratio η) due to fabric anisotropy.

Another signature of any plastic flow rule is the K_0 value predicted for normally consolidated state. If the elastic strain rate is ignored, which is a reasonable assumption when clay is normally consolidated, the angle β for K_0 condition (i.e., $\dot{\epsilon}_r = 0$) is approximately constant and equals:

$$\tan \beta = \frac{\dot{\epsilon}_d}{\dot{\epsilon}_v} = \frac{2/3\dot{\epsilon}_a}{\dot{\epsilon}_a} = \frac{2}{3} \quad (5.17)$$

As depicted in Figure 5.2(a), the increase of α induces a growth of stress ratio that corresponds to K_0 condition. Considering the relation between stress ratio and $K_{0,NC}$ value:

$$K_{0,NC} = \frac{\sigma_r}{\sigma_a} = \frac{3 - \eta}{2\eta + 3} \quad (5.18)$$

one can conclude that a positive value of α , which is compatible with the stress condition in naturally deposited soil, will lead to lower K_0 value compared with theoretical prediction that ignores influence of fabric anisotropy (i.e., $\alpha = 0$). This trend is supported by the experimental observation conducted by Nadarajah (1973), in which measured K_0 values in consolidation tests is remarkably lower than the value predicted by Modified Cam Clay model, which does not consider plasticity anisotropy. This difference could significantly affect the estimation of in-situ stresses in the field.

One should be aware of that stress-dilatancy diagrams presented in Figure 5.2(a) are obtained through freezing the internal variables. However, in the real simulations, internal variable α will also change in accordance to its hardening law. Therefore, the stress-dilatancy simulated by the model will form a curve connecting the $\eta - \beta$ curves that represents varying states of fabric anisotropy. This also implies, due to existing fabric anisotropy, predicted stress-dilatancy relation by the model is not unique but depends on initial conditions and subsequent loading paths, unlike the stress-dilatancy relation in Cam-Clay model or Rowe's dilatancy theory (Rowe, 1962; Roscoe et al., 1963), which is solely a function of stress states.

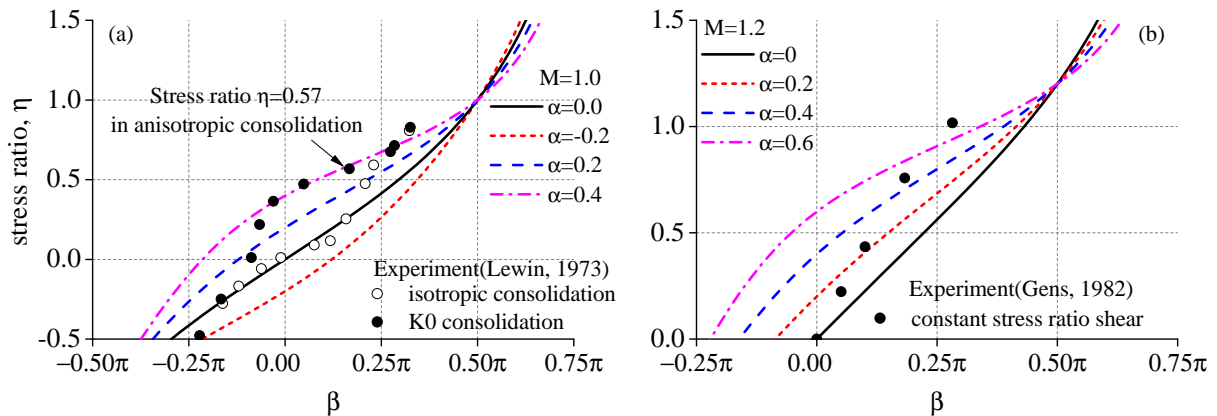


Figure 5.3. Experimentally observed stress-dilatancy relations and their comparisons with theoretical predictions: (a) reconstituted clay samples under isotropic and K_0 consolidation history (Lewin, 1973); (b) reconstituted clay samples under constant stress ratio consolidation (Gens, 1982)

Further evaluation of theoretical predictions with respect to experimental evidences is presented in Figure 5.3. Tests on reconstituted clays are selected for above purpose, in which presumably the effects of inter-particle bonds are negligible. Lewin (1973) prepared two groups of reconstituted samples that were consolidated from slurry, in which one group was isotropically consolidated and the other one is anisotropically consolidated

with a constant stress ratio $\eta = 0.57$. This anisotropic consolidation is intended to give approximately zero lateral strain (i.e., K_0 path). After consolidation, each sample was brought to different stress ratio under the condition of constant mean effective stress and dilatancy relation were measured during subsequent drained constant stress ratio shearing. To interpret soil dilatancy, Lewin (1973) assumed elastic strain generated during shearing is negligible so that the total strain increment was essentially equal to plastic strain. The test results are presented in Figure 5.3(a), accompanied by stress-dilatancy diagrams computed based on equation 5.15 with the value of M and different values of α shown in the figure. For isotropically consolidated samples (open symbol), the experimentally observed stress-dilatancy relation of the stress states near the isotropic condition (i.e., $\eta = 0$), is well captured by the theoretical prediction that assumes a zero value of α (i.e., Modified Cam-Clay model). However, as the stress ratio increases, experimental data keeps deviating from the prediction based on an isotropic flow rule. Specifically, given the same stress ratio, samples exhibited a higher degree of plastic contraction than the prediction that ignores anisotropy effect. Moreover, measured data points forms a curve connecting the $\eta - \beta$ curve of $\alpha = 0$ and curves of increasing values of α , which suggests that the aforementioned discrepancy is due to the anisotropic fabric developed during a non-isotropic loading history. The influence of anisotropic stress history on plastic flow is even pronounced for the samples after K_0 consolidation. For these samples, plastic distortion (i.e., $\beta \neq 0$) were observed at the isotropic stress state and pure plastic volumetric change corresponds to a positive value of stress ratio (i.e., $\eta \approx 0.4$). The same trend can be also observed in the theoretically predicted stress-dilatancy curve under a positive value of α , which is consistent with samples' K_0 -consolidation history. Moreover,

observed dilatancy data at stress ratios close to that at the end of K_0 consolidation can be well fitted by predicted stress-dilatancy curve with positive value of $\alpha = 0.4$. With the decreasing of stress ratio, these stress-dilatancy data forms a curve that starts from the above predicted curve and ends with prediction corresponding to a negative value of α ($\alpha = -0.2$ in this case). As a loading path featuring decreasing stress ratio η will induce a progressive reduction of α value in the proposed model (recall the hardening rule in section 4.2.4), predicted plastic flow in the model is expected to follow the same trend as experiments. Another significant observation is that data points from two groups eventually converge together at both high and low stress ratio. This suggests the previous consolidation stress history has been swept out by subsequent loading path and the stress-dilatancy relation is solely determined by current stress state and its corresponding fabric anisotropy. From a numerical modeling point of view, the above observation confirms the appropriateness of incorporating the current stress state as the saturation value of internal variable α in its hardening law (i.e., equation 4.21). Figure 5.3(b) presents the stress-dilatancy data obtained from constant stress ratio tests conducted on reconstituted clay (Gens, 1982), in which the total strain increment after the soil yields was used to obtain the stress-dilatancy relation. Again, with the increase of stress ratio, measured points form a similar curve as the previous example.

Concerning the effects of inter-particle bond on plastic flow in the model, equation 5.15 reveals that the relative ratio between inter-particle bonds and stress level, i.e., p_t/p , plays an important role in determining the response. This ratio implies the influence of bond on stress-dilatancy relation is more pronounced for low stress level than high stress level. To illustrate this concept, the stress-dilatancy diagram predicted based on

equation 5.15 under various values of p_t/p is presented in Figure 5.2(b). As a result of the increase of ratio p_t/p , predicted stress-dilatancy curves gradually rotate to the left with coordinate origin as the fixed point. This implies that purely plastic volumetric deformation will be predicted for isotropic stress state, regardless of the amount of inter-particle bonds. Due to above shift, stress ratio corresponding to zero plastic volumetric strain rate (i.e., $\beta = \pi/2$) increases. Moreover, material plastic contraction is intensified and plastic dilation is delayed. In other words, given the same stress ratio, a higher value p_t/p leads to lower value of β , and thereby higher degree of plastic contraction as well as a larger amount of pore pressure for undrained shearing. This higher pore pressure physically could be attributed to natural clay's larger void size compared with reconstituted state and corresponding material's higher tendency to contract after inter-particle bonds start to break. On the other hand, under the same stress ratio, the plastic dilatancy predicted by the flow rule without bond effect will change to plastic contraction if the ratio p_t/p is high enough. Figure 5.2(b) also shows the predicted K_0 value for the normally consolidated state is also affected by inter-particle bonds. The increase of p_t/p ratio will increase the stress ratio corresponding to 1D compression condition and consequently decrease $K_{0,NC}$ value. Such a theoretical prediction implies that $K_{0,NC}$ of natural clays is not only a function of fabric anisotropy, but also a function of inter-particle bonds and confining stress. Ignoring the effects of fabric and inter-particle bonds may both lead to an overestimation of the K_0 value in the field, which further leads to an underestimation of in-situ shear stress and potentially overestimates the additional shear stress, which can be sustained by the clay material.

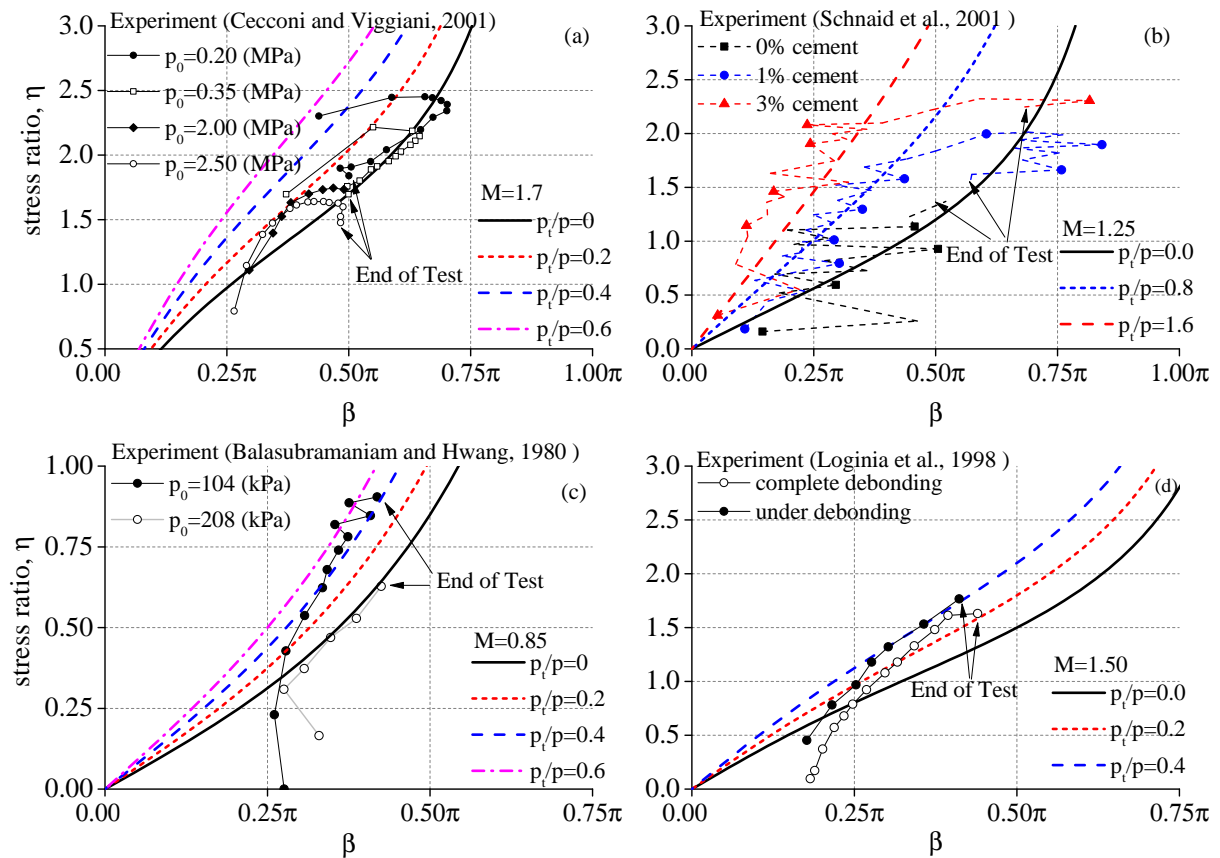


Figure 5.4. Experimentally observed stress-dilatancy relations and their comparisons with theoretical predictions: (a) pyroclastic weak rock (Cecconi and Viggiani, 2001); (b) artificially cemented sand (Schnaid et al., 2001); (c) Bangkok clays (Balasubramaniam and Hwang, 1980); (d) Gravina di Puglia calcarenite (Lagioia et al., 1996)

After the discussion of influences of inter-particle bonds on predicted stress-dilatancy relation in the model, experimental observations and their comparisons with theoretical predictions are able to provide deeper understanding of material behavior. Cecconi and Viggiani (2001) conducted a series of triaxial tests on pyroclastic weak rock, which exhibits the degradation of inter-particle bonds during shearing. Figure 5.4(a) presents the corresponding stress-dilatancy curves interpreted from CID TXC tests that begin with

four different confining stress (i.e., p_c). In calculating dilatancy, elastic axial strain was ignored while elastic volumetric strain was calculated based on κ value obtained in compression tests (Cecconi and Viggiani, 2001). Interpreted results show that the condition of $\beta = 0$ (i.e., zero plastic volumetric strain rate) are attained at a different stress ratio for different samples and the general trend is that increasing initial confining stress p_c will decrease the stress ratio corresponding to zero plastic volumetric strain rate. If the amount of inter-particle bonds could be assumed to be equal for all samples, then above observation supports the aforementioned left shift of predicted stress-dilatancy curves due to the increasing p_t/p value. The initial portion of observed stress-dilatancy curves also suggests that the effect of p_t/p is correctly (at least qualitatively) considered in the proposed flow rule. In other words, data from tests with lower initial confining stress tend to start from predictions that represent higher values of p_t/p . Furthermore, experimentally observed stress-dilatancy curves qualitatively form curves that starts from theoretical predictions corresponding to higher value p_t/p and ends with ones of lower value of p_t/p . As model simulations of same loading paths as experimental tests will involve a increase in p value (before softening) and a decrease in p_t value once plasticity is activated, it is reasonable to expect that the similar connecting paths can be reproduced by the employed flow rule. One may notice that the initial portion of stress-dilatancy curves for tests with $p_c = 2.00$ and 2.50 MPa does not follow the aforementioned trend. This may be due to the fact that elastic axial strain rate is ignored in experimental results interpretation, which may lead to an overestimation of plastic shear strain rate $\dot{\varepsilon}_d^p$ and thereby corresponding β value. This error tends to be more pronounced at stage of lower stress ratio, as the effective

stress path progresses most nearly tangentially to the yield surface (Wood, 1990). A final observation from Figure 5.4(a) is that stress-dilatancy curves obtained from different tests tend to converge to a single theoretical prediction. This suggests that there exists an intrinsic stress-dilatancy relation that is independent of bonds between particles and this intrinsic behavior is recovered when all bonds have been eliminated.

Figure 5.4(b) presents the stress-dilatancy relations interpreted by Yu et al. (2007b) from CID TXC tests on three artificially cemented sand with different cement percentage conducted by Schnaid et al. (2001). Unlike previous case, all cemented sand samples were sheared from the same isotropic consolidation stress. When interpreting dilatancy from test results, elastic strain rate was ignored (Yu et al., 2007b). Experimental observations show stress-dilatancy curve shifts to the left when cement amount increases, which is consistent with theoretical predictions of increasing values of p_t/p , which is due to an increase in p_t value that reflects higher amount of cementation in the model. Further verification of proposed plastic flow rule comes from the fact that continuous shear deformation and presumably breakage of inter-particle bonds cause measured stress-dilatancy curve of cemented sand bending to the right, which forms a path connecting predicted curves representing decreasing values of p_t/p . When shear deformation is large enough, observed stress-dilatancy relations of sand with 1% and 3% cement eventually can be characterized by the same theoretical prediction (i.e., the one with $p_t/p = 0$) as the sand without cement. This further supports aforementioned idea that the intrinsic stress-dilatancy exists.

Experimental work on Bangkok weathered soft clays and Gravina di Puglia calcarenite provide additional supports of the predicted left shift of the stress-dilatancy curve due to the existence of inter-particle bonds. Balasubramaniam and Hwang (1980) conducted a

series of triaxial tests on Bangkok weathered soft clays, which exhibits relatively strong destructuration phenomenon during consolidation tests. Figure 5.4(c) presents the interpreted stress-dilatancy curves from two CID TXC tests with two initial confining stresses, $p_c = 104$ kPa and $p_c = 208$ kPa. Dilatancy was interpreted by the author of this work, by ignoring elastic shear strain and estimating elastic volumetric strain based on κ value measured from 1D compression test. Isotropic compression test results on Bangkok clays suggest all inter-particle bonds are eliminated at the moment of effective mean stress p being increased to 208 kPa, which makes stress-dilatancy obtained from subsequent shearing representative of the intrinsic response. Compared with this, stress-dilatancy data for the test with $p_c = 104$ kPa exhibits the same left shift as previously discussed. Gravina di Puglia calcarenite is a soft rock that exhibits inter-particle bonds degradation during loading or deformation. Two stress-dilatancy curves in Figure 5.4(d) are interpreted from CID TXC tests by Lagioia et al. (1996), in which consolidation to an effective mean stress $p = 3.5$ MPa is believed to have eliminated all bonds. Again, a left shift of the stress-dilatancy curve induced by inter-particle bonds is observed. It is noteworthy that for both Bangkok clay and Gravina di Puglia calcarenite, the aforementioned curves that connect stress-dilatancy diagrams with different p_t/p ratios are not observed. While the exact reason is not clear at this stage, possible explanation is the change of fabric due to the increasing stress ratio rotates the stress-dilatancy curve clockwise, thereby making it difficult to observe the trend of stress-dilatancy diagram shifting to the right due to degradation of inter-particle bonds. It is likely that such a change of fabric induced by anisotropic loading is less pronounced for soft rock and cemented sand shown in Figure 5.4 (a) and (b).

Lastly, one should be aware of that the above discussed influences of inter-particle bonds on plastic flow are not applicable to all natural clays that exhibit destructuration. For instance, Rampello et al. (1993) studied the plastic flow of intact and reconstituted Vallericca clay and no noticeable difference was observed. In addition, Walker and Raymond (1969) investigated the plastic flow of natural Leda clay under different confining pressure and concluded that the stress-dilatancy curves of clay under different confining stress fall within a narrow band. Nevertheless, from a numerical modeling point of view, the above observations could be reproduced by simply setting parameter $r_c = 0$, through which the plastic flow rule in the basic model and extended model will be identical.

5.4. Calibration of Model Parameters and Initial Conditions for the Extended Model

Table 5.1 and Table 5.2 summarize the parameters and required initial conditions for the extended model, respectively. Besides the parameters in the basic model, three destructuration parameters k_i , A and r_c are introduced in the extended model. Also, a new internal variable S_b is introduced to represent the amount of inter-particle bonds. For natural clay, it is recommended that the parameters for the basic model are calibrated from tests in which samples are consolidated to high stresses if the reconstituted samples are not available.

The calibration of the additional parameters and the new internal variable is illustrated based on the experimental evidence on the Bothkennar clay (Smith et al., 1992). This demonstration clarifies the roles of the new model parameters.

5.4.1. Calibration of Destructuration Parameters

- Parameter k_i

The parameter k_i controls the rate of the destructuration. Its value is calibrated by fitting post-yield compression curves of intact natural clay specimens in isotropic consolidation, 1D compression or anisotropic consolidation. Figure 5.5(a) shows a compression curve in the $e - \log(\sigma'_v)$ plane from a 1D compression test on intact Bothkennar clay and simulation results with three different values of k_i . Note that a higher value of k_i leads to a greater compressibility at the post-yielding stage. Moreover, as k_i increases, the compression line of natural clay converges more rapidly to the intrinsic compression line (ICL) (Burland, 1990), which implies smaller load and less deformation are required to

Table 5.1. Model parameters and their roles in the extended model

	Designation	Description of Its Role
Elasticity (small strain)	$e_g/A_g/n_g$	Interpolation parameters for shear modulus at very small strain, G_0
	γ_{07}	Degradation rate of elastic stiffness with respect to shear strain
Elasticity (large strain)	κ	Slope of rebound line in $e - \ln(p)$ plane
	ν	Poisson's ratio
Critical State	M_c/M_e	Stress ratio at critical state
Isotropic Hardening	λ	Slope of virgin compression line in $e - \ln(p)$ plane
Rotation Hardening	C	Rate of surface rotation
	χ	Saturation value of rotation
Bounding surface shape	N_c/N_e	Shape of bounding surface
Cyclic loading	h_c/h_e	Cyclic stiffness
	w	Pore pressure build-up in cyclic loading
Destructuration	c_d	Cyclic shakedown/ratcheting
	k_i	Destructuration rate with respect to plastic strain
	A	Relative contribution of plastic volumetric and deviatoric strain to destructuration
	r_c	True cohesion in natural clay

Table 5.2. Initial conditions in the extended model

Designation	Description of Its Role
p_0	Size of the intrinsic surface
α	Inclination and distortion of the structure surface and intrinsic surface
S_b	Amount of inter-particle bonds
e_0	Initial void ratio

break all bonds between particles. It also implies that a higher k_i value indicates a more sensitive clay. For Bothkennar clay, $k_i = 12$ is an appropriate value.

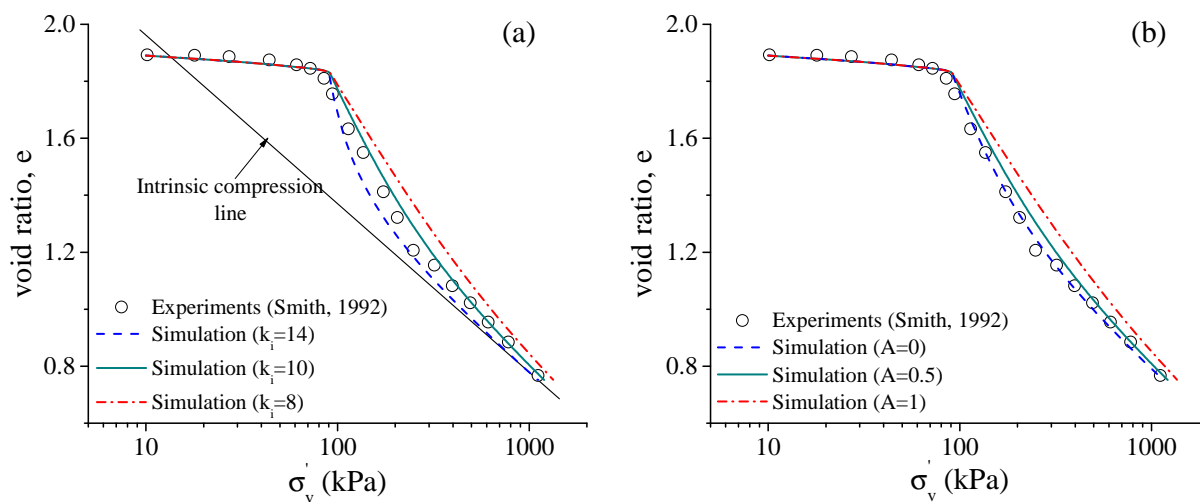


Figure 5.5. Calibration of the parameters k_i and A in a 1D compression test on the Bothkennar clay: (a) varying values of k_i ; (b) varying values of A

- Parameter A

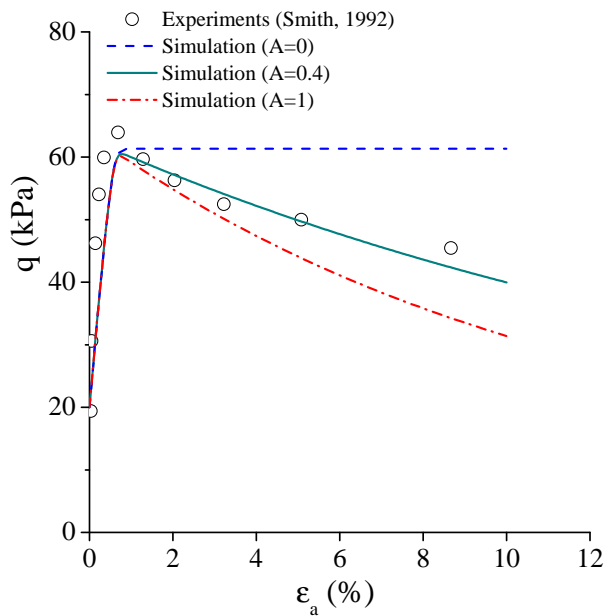


Figure 5.6. Calibration of the parameter A in a CK_0U TXC test

The parameter A controls the relative contributions of plastic volumetric and deviatoric strains to the destructuration. When A equals zero, the destructuration solely is induced by the volumetric plastic strain whereas purely deviatoric destructuration is achieved when A equals one. Figure 5.5 (b) illustrates the sensitivity of simulated compression curves to the parameter A . It can be seen that a higher A value results in a slower structure deterioration, which implies along this specific loading path the volumetric plastic strain is higher than the deviatoric plastic strain. Nevertheless, such difference is likely to be small, as the simulated results are relatively insensitive to the parameter A . Therefore, for the Bothkennar clay, the value of A is calibrated from a CK₀U TXC test, as shown in Figure 5.6. Note that the change in A value significantly alters the rate of strain softening in undrained shearing. Accordingly, $A = 0.4$ is selected for the Bothkennar clay. It is worth mentioning that the peak strength and stress-strain curves before the peak strength are insensitive to the value of A .

- Parameter r_c

The parameter r_c quantifies true cohesion in natural clay. Figure 5.7(a) shows simulated effective stress paths of a CAU TXC test for three different values of r_c and the corresponding initial phase transition lines (PTL). Note that when r_c equals zero, the corresponding PTL coincides with the critical state line (CSL). Figure 5.7(a) shows that a higher value of r_c results in a higher computed peak strength. Moreover, for a non-zero r_c , the peak mobilized stress ratio in the simulation is higher than the critical state stress ratio. As positive excess pore pressure monotonically increases in the above simulations, the above higher mobilized friction is not attributed to soil's tendency to dilate but the true cohesion in natural clay. The experimental observations on natural Vallericca clay

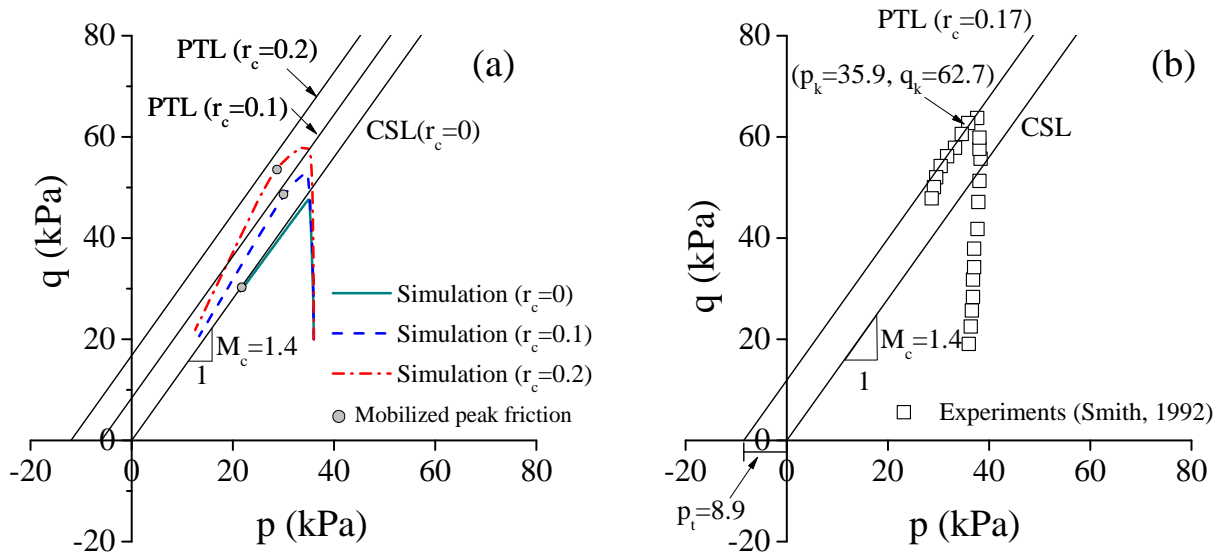


Figure 5.7. Calibration of the parameter r_c : (a) simulated effective stress paths for different r_c ; (b) calibrate r_c for the Bothkennar clay

(Rampello et al., 1993) have shown that in addition to friction, dilatancy and cohesion are two factors that contribute to the mobilized friction in natural clay. Note that the stress point that represents the peak mobilized friction (closed circle in Figure 5.7(a)) is close to the initial PTL, which inspires the way to calibrate r_c . As an approximation, it is assumed that the stress point (p_k, q_k) that corresponds to peak mobilized friction lies on the initial PTL, as shown in Figure 5.7(b). Smith et al. (1992) reported the critical state stress ratio M_c equals 1.4 for the Bothkennar clay. So one can find the intercept of PTL, p_t , equals 8.9 kPa. As will be shown later, the initial internal variable S_b and p_0 for the Bothkennar clay equal 6.1 and 8.3 kPa, respectively. Based on the definition of p_t , (i.e., $p_t = r_c S_b p_0$), $r_c = 0.17$ is obtained for the Bothkennar clay.

5.4.2. Estimation of Initial Values for Internal Variables

- Internal variable S_b

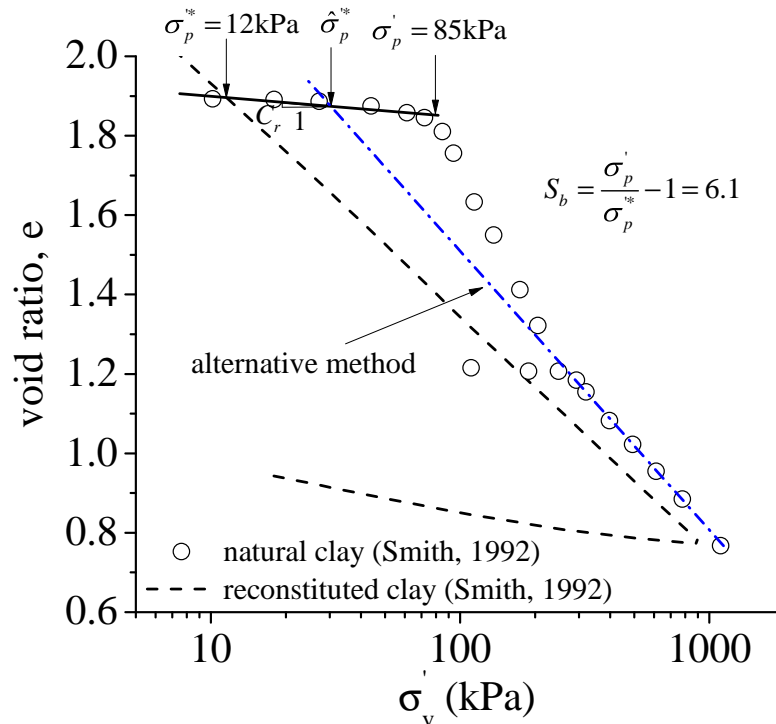


Figure 5.8. Estimation of internal variable S_b in 1D compression tests on the Bothkennar clay

The internal variable S_b represents the amount of inter-particle bonds in natural clay. Its value can be estimated based on the results of compression tests on intact natural clay and corresponding reconstituted clay. The specific steps are illustrated in Figure 5.8, which shows the results of 1D compression tests on intact and reconstituted Bothkennar clay in the $e - \log(\sigma'_v)$ plane. One needs to determine the max past pressure σ'_p of the intact natural clay. Then, a line is drawn starting from the point of σ'_p with a slope equals to the recompression index C_r . The intersection between this line and the compression curve for the reconstituted clay is defined as the intrinsic maximum past pressure σ_p^{I*} .

Considering the similarity between the structure surface and the intrinsic surface, one assumes that $\sigma'_p/\sigma_p'^* \approx p_{s0}/p_0$ and therefore:

$$S_b = \sigma'_p/\sigma_p'^* - 1 \quad (5.19)$$

For the Bothkennar clay, $S_b = 85/12 - 1 = 6.1$.

If reconstituted specimens are not available, a compression test on natural clay samples wherein the applied pressure is sufficiently high to eliminate inter-particle bonds fully can be used to estimate S_b value. In the high-pressure regime of the above test, the compression curve can be assumed to have converged to the ICL. A straight line that connects data points at the later stage of compression test (e.g., dot-dash line shown in Figure 5.8) is approximately the same as the ICL. Accordingly, the intrinsic maximum past pressure $\sigma_p'^*$ can be found from the intersection of this line and the line with a slope of C_r through σ'_p . However, when employing this method, one should be very careful to ensure all structure has been eliminated at the end of compression test. Otherwise, as illustrated in Figure 5.8, the S_b value will be underestimated due to the overestimation of intrinsic yielding stress $\hat{\sigma}_p'^*$.

- Internal variable p_0

For natural clay, the stress pair (p, q) that corresponds to the maximum past pressure σ'_p should lie on the structure surface instead of the intrinsic surface. Therefore, the analytical solution to estimate p_0 in the basic model (i.e., equation 4.54) is modified to be:

$$p_0(1 + S_b) = p_p + \frac{(q_p - (p_p + r_c S_b p_0)\alpha)^2}{(N_c^2 - \alpha^2)(p_p + r_c S_b p_0)} \quad (5.20)$$

This equation is a non-linear and its exact solution exists but is tedious. It is suggested to solve this equation by numerical iterative methods (e.g., Newton method). If r_c value is zero or small enough to be ignored, then equation 5.20 can be simplified as:

$$p_0 = \frac{p_p}{(1 + S_b)} + \frac{(q_p - p_p \alpha)^2}{(N_c^2 - \alpha^2)p_p(1 + S_b)} \quad (5.21)$$

Note that when r_c value is not negligible, equation 5.21 can provide a first guess of p_0 . Further adjustment can be made to match the yield stress in compression tests (e.g., 1D compression).

5.5. Validation of the Extended Model

Table 5.3. Index properties and USGS classification of the investigated natural clays

	Norrk- öping clay	Valler- icca clay	Shanghai clay	Wuzhou clay	Both- kennar clay	Grande Balenein clay	Sensitive BCF clay	Clover- dale clay
PL (%)	25	26	22	28	31	22	20	26
LL (%)	68	55	44	63	80	34	31	50
PI (%)	43	29	22	35	49	12	11	24
W_n (%)	76	27	52	68	70	59	30	50
LI	1.19	0.03	1.36	1.14	0.80	3.08	0.91	1.0
USCS	CH	CH	CL	CH	CH	CL	CL	CL
S_t^*	-	-	4 - 5	-	4	> 300	5 - 6	16

Note: * the sensitivity was measured with the Swedish fall cone and laboratory vane for the Grande Balenein clay and Cloverdale clay, respectively.

Comparisons between computed results with the extended model and experimental observations of eight different natural clays are presented to validate the proposed model. Table 5.3 summarizes the basic index properties of these clays. Figure 5.9 shows their liquid limit and plasticity index on Casagrande's plasticity chart. Note that all points

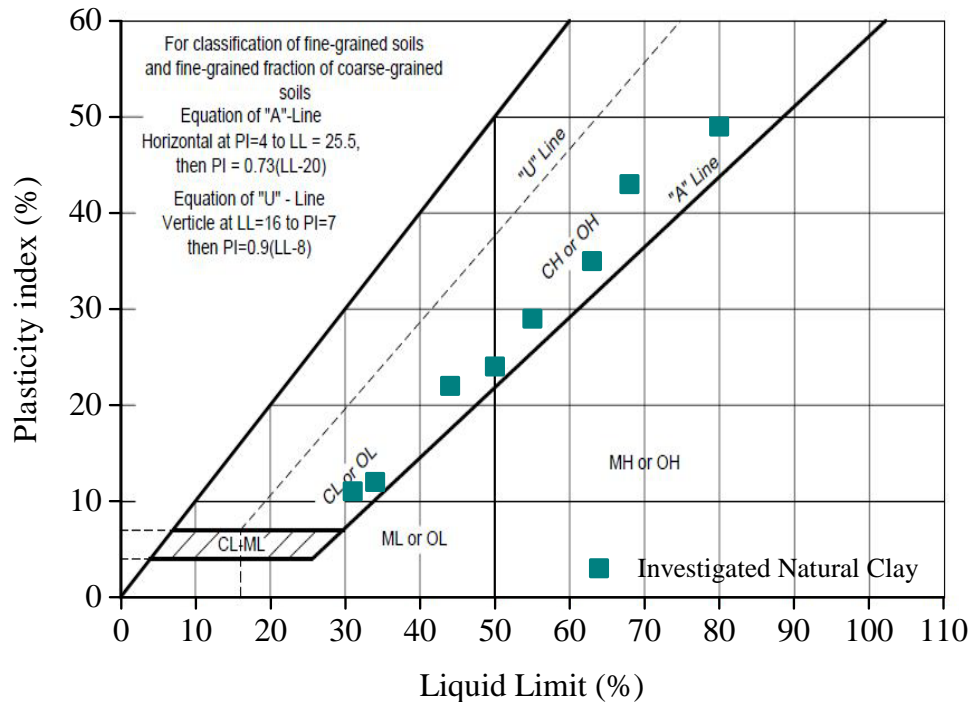


Figure 5.9. Atterberg limits for investigated natural clays on the Casagrande plasticity chart

in the chart are above “A-line”, which indicates that all the soils are either CL or CH according to the USCS designation. Moreover, because the clays have a relatively wide range of liquid limit and plasticity index, they are expected to exhibit relatively diverse behavior. Furthermore, the liquidity index of these natural clays varies from 0.03 to 3.08. Considering the correlation between soil sensitivity and liquidity index (Bjerrum, 1954; Mitchell, 1993), these clays are likely to have a varied degree of sensitivities as well. Thus, the corresponding evaluation provides a comprehensive picture of the model performance and ensure that the proposed model is quite general.

5.5.1. Norrköping clay

Norrköping clay is an inorganic clay from southern Sweden. Its clay content is about 62%, and the silt content is about 36%. Illite is the dominant clay mineral (Rouainia and Wood, 2000). The test results in the following comparisons were reported by Westerberg (1995), while the data was digitized from the work of Rouainia and Wood (2000).

Model Parameters and Initial Conditions

Table 5.4. Model parameters for Norrköping clay

λ	κ	ν	M_c	M_e	N_c	N_e	C	χ	h_c	h_e	c_d	w	k_i	A	r_c
0.35	0.047	0.2	1.6	1.4	1.15	1.1	10	1.73	25	25	0	1	16	0.9	0

Table 5.4 summarizes the model parameters for the Norrköping clay. The parameters λ and κ are estimated from the compression index C_c in the high pressure regime of a 1D compression test (due to the absence of reconstituted specimens) and the recompression index C_r , respectively. It is worth mentioning that for most of natural clays simulated in this work, the parameter κ is obtained from the initial loading curve prior σ'_p in compression tests. For the Bothkennar clay, the value of κ is calibrated through the initial unloading curve (unloading range is 800 kPa vertical effective stress) from an 1D compression test on a reconstituted sample. Poissons ratio ν is assumed to be 0.2. The parameters M_c and M_e were calibrated from the effective stress paths of a CK₀U TXC test and a CK₀U TXE test. The parameters N_c and N_e are calibrated by fitting the peak strength in the above two undrained shearing tests. The parameter C is determined by fitting the effective stress path of the above CK₀U TXE test. The parameter χ is obtained by the analytical solution of equation 4.44. The parameter k_i is calibrated by

fitting the post-yield compression curve in the aforementioned 1D compression test. The parameter A is determined by fitting the strain-softening rate in the CK₀U TXC test and CK₀U TXE test. The parameter r_c is assumed to be zero, as the peak mobilized friction in shearing under low and high consolidation pressures are quite similar. The parameter h_c is calibrated by fitting the stress-strain response in a CIU TXC test on an overconsolidated sample. The parameter h_e is assumed to equal h_c . The results of cyclic tests on the Norrköping clay are not available, so the parameters c_d and w take their default values, which are 0 and 1, respectively. It is worth mentioning that due to the absence of relevant measurements, small strain stiffness response is not considered in the following simulations.

Table 5.5. Initial conditions for Norrköping clay simulations

p_0 (kPa)	α	S_b	e_0	p (kPa)	q (kPa)
16	0.63	1.5	2.05	10	0

Initial values of the internal variables, void ratio and stress state are summarized in Table 5.5. Because 1D compression tests on reconstituted Norrköping clay were not reported, $S_b = 1.5$ was estimated through the alternative method shown in Figure 5.8. The initial value of α is estimated through equation 4.50 based on the parameter M_c . The variable p_0 is estimated through equation 5.21 based on an estimated maximum past pressure $\sigma'_p = 54.1$ kPa and a $K_{0,NC}$ value calculated from the parameter M_c (i.e., equation 4.47 and 4.48). The initial (p, q) stress shown in Table 5.5 is assumed to represent the residual stress of clay samples (i.e., the effective stress within a specimen that prevents it from falling apart after the specimen has been sampled and trimmed).

Comparisons between experimentally observed and computed results are presented in two groups: model simulation and model prediction. The comparisons for tests that have been used to define the above model parameters are shown in the “model simulation,” whereas those for tests that have not been used are shown in the “model prediction.”

Model Simulation

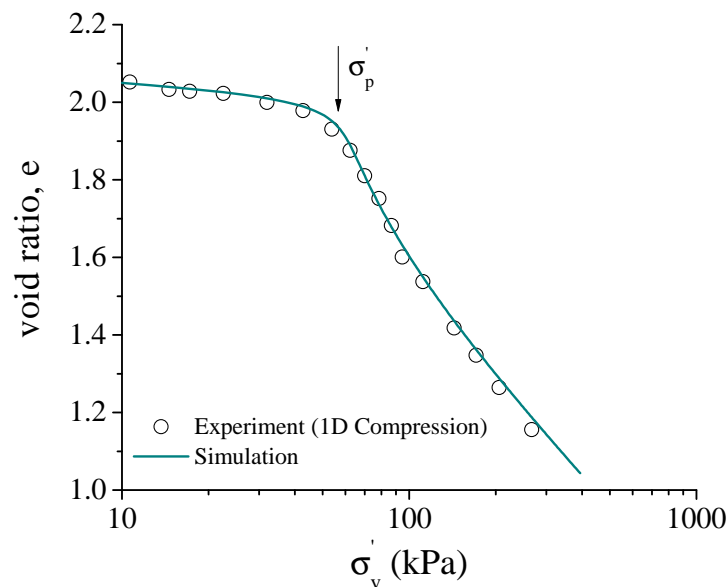


Figure 5.10. Comparison between the experimental observation and model simulation for a 1D compression test on the Norrköping clay

Figure 5.10 compares the experimental observation and model simulation for a 1D compression test. It can be seen that the model simulation fits well with the observed 1D compression behavior. The yield stress is well reproduced in the simulation, which shows the internal variable p_0 calculated from the proposed analytical solution (i.e., equation 5.21) is reasonable. Moreover, both the experimental data and simulation result show a decrease in compressibility at higher vertical effective stress.

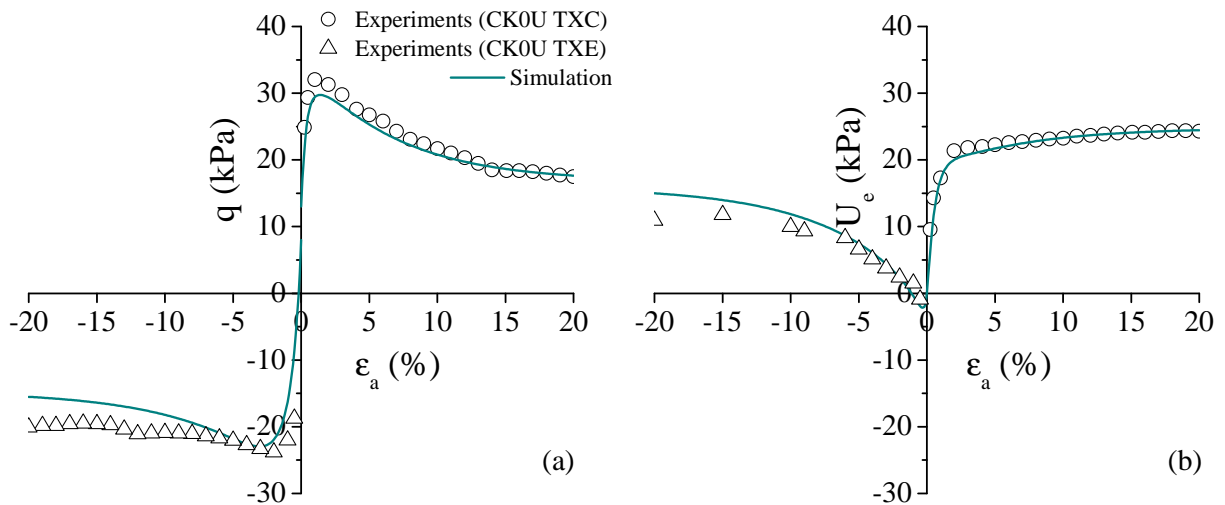


Figure 5.11. Comparison between the experimental observations and model simulations for a CK₀U TXC test and a CK₀U TXE test on the Norrköping clay: (a) stress-strain response; (b) strain-pore pressure response

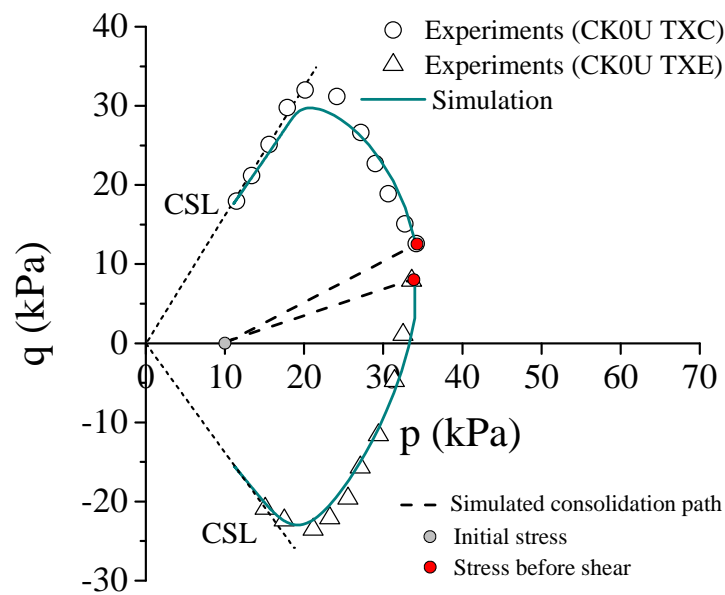


Figure 5.12. Comparison between the experimental observations and model simulations for a CK₀U TXC test and a CK₀U TXE test on the Norrköping clay: effective stress path

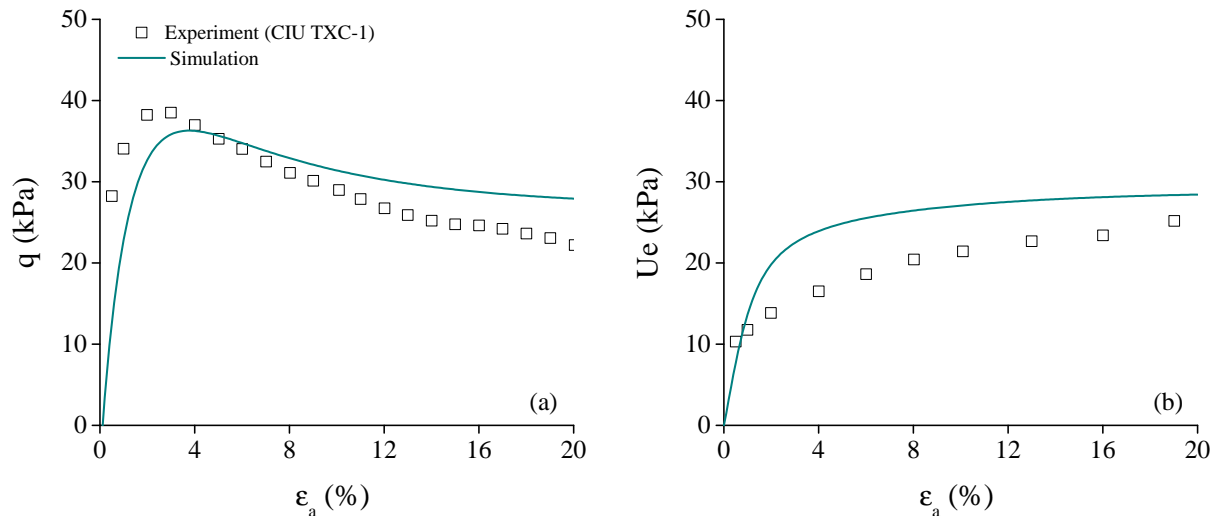


Figure 5.13. Comparison between the experimental observations and model simulations for a CIU TXC test on a Norrköping clay with $OCR=2$: (a) stress-strain response; (b) strain-pore pressure response

Figure 5.11 and Figure 5.12 shows the stress-strain responses and effective stress paths of a CK_0U TXC test and a CK_0U TXE test and the corresponding model simulations. The dashed line in the figure represent the reconsolidation stress path that is reproduced by the simulations. The critical state line was computed from the parameters M_c and M_e . As shown in Figure 5.11 (a), the destructuration induced by monotonic shearing is indicated by the noticeable strain-softening in both compression and extension tests. The model simulates this feature very well. The experimental data show the strain-softening in the compression loading is greater than that in the extension, so does the model simulation. Moreover, the simulation reasonably reproduces the shear-induced excess pore pressure.

Figure 5.13 presents the observed and computed results in a CIU TXC tests on an OC specimen that was isotropically consolidated to $p = 70, q = 0$, then unloaded to $p = 35, q = 0$ to create an $OCR=2$. Note that the model reasonably reproduces the stress-strain-pore pressure responses observed in the experiment. The computed excess

pore pressure increases faster than that observed, and the final amount of excess pore pressure is slightly overestimated in the simulation.

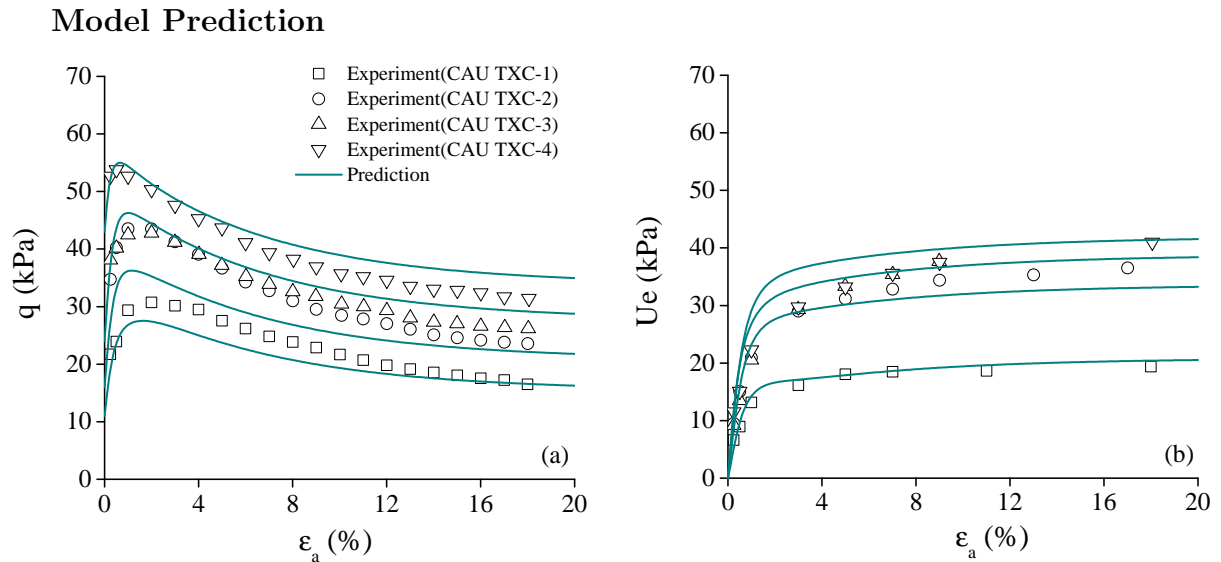


Figure 5.14. Comparison between the experimental observations and model predictions for four CAU TXC tests on the Norrköping clay: (a) stress-strain response; (b) strain-pore pressure response

Figure 5.14 and Figure 5.15 present the observed stress-strain responses and effective stress paths in four CAU TXC tests and the corresponding model predictions. It can be seen that the predictions reasonably agree with the experimental results regarding the peak strength, strain-softening and gradually increasing excess pore pressure. With the increase in consolidation stress, more soil structure is eliminated. The four tests shown in Figure 5.14 and Figure 5.15 presumably represent the responses of clays that have different degrees of structure deterioration. The model's success in predicting these behavior shows its capacity to successfully track structure changes during consolidation and reproduce the shearing behavior of soil with different degrees of structure degradation. Less success is seen in the simulation of the CAU TXC-2, in which model underestimates the peak

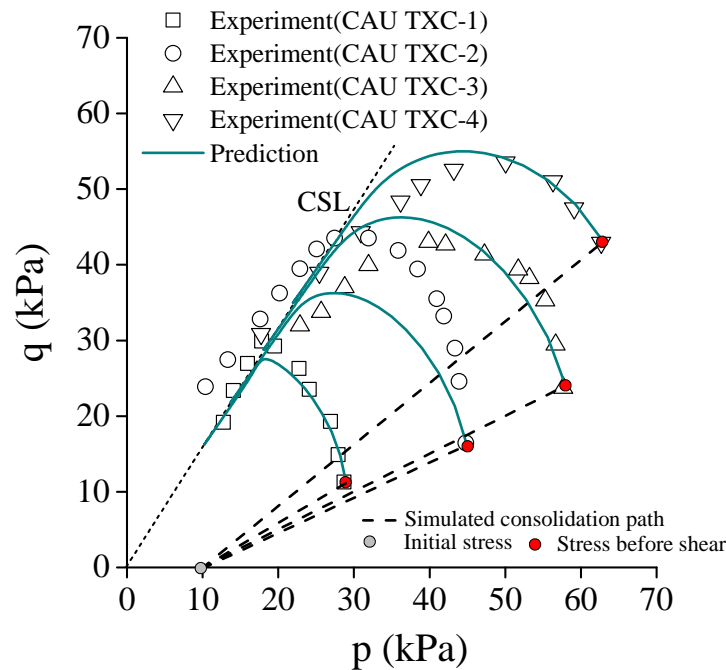


Figure 5.15. Comparison between the experimental observations and model predictions for four CAU TXC tests on the Norrköping clay: effective stress path

strength. This difference is likely to be caused by natural variations in specimens because the observed strength in the CAU TXC-2 is almost the same as that in the CAU TXC-3 for which the sample was consolidated to stress greater than the TXC-2.

Figure 5.16 compares the predicted and experimentally observed responses in a CIU TXC test on a heavily OC sample that was isotropically consolidated to $p = 175, q = 0$, then unloaded to $p = 35, q = 0$ to create an OCR=5. It can be seen that the model prediction generally reproduces the observation. The predicted strain-softening rate agrees well with that observed, but the peak strength is overestimated by 35%. This discrepancy is probably a result of the large bounding surface that is created by the preceding

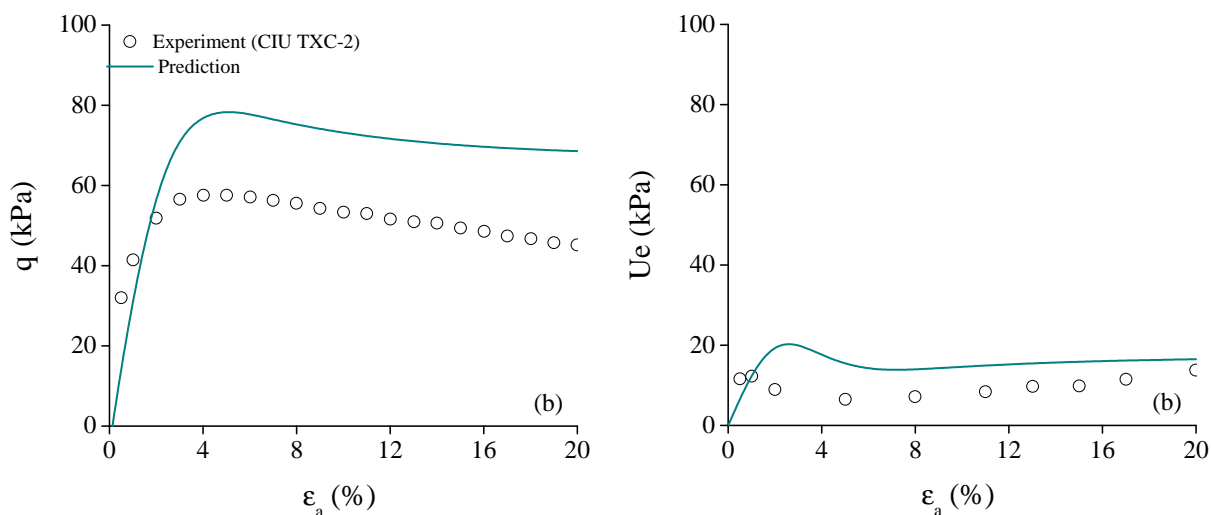


Figure 5.16. Comparison between the experimental observations and model predictions for a CIU TXC test on a Norrköping clay of OCR=5: (a) stress-strain response; (b) strain-pore pressure response

reconsolidation to high stress. The predicted excess pore pressure first increases, then decreases, and then gradually increases again, as observed in the test.

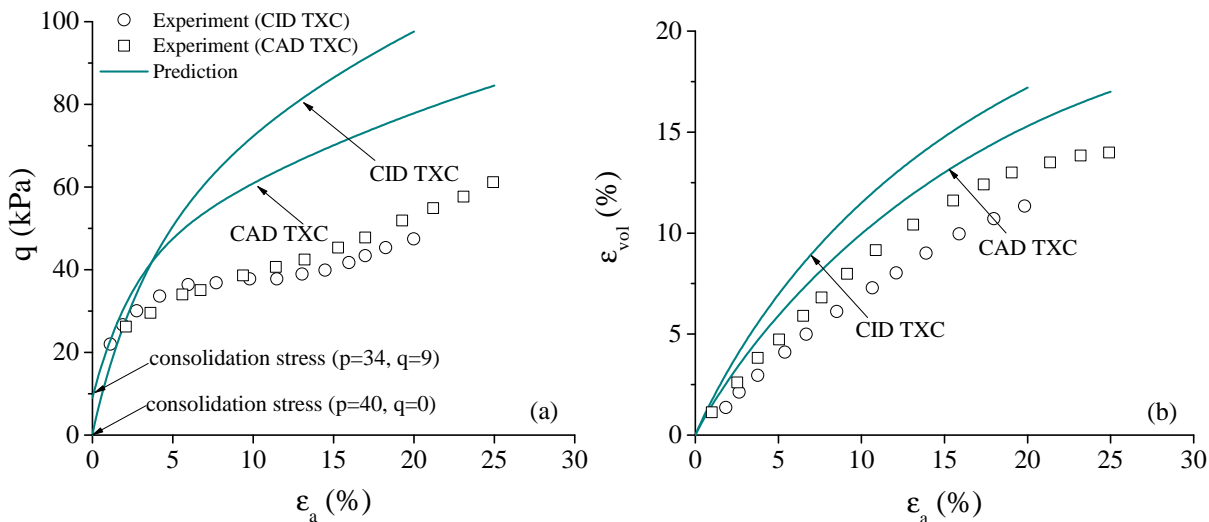


Figure 5.17. Comparison between experimental observations and model predictions for CID TXC and CAD TXC tests on the Norrköping clay: (a) stress-strain response; (b) volume change

Results of two drained triaxial compression tests (CAD TXC and CID TXC) are shown in Figure 5.17. The significant point made in this figure is that for structured clays, when strain-softening is seen in undrained shearing tests, strain-hardening can develop in drained tests. This feature is shown in both experiments and model predictions. In the model, hardening in drained tests results from the fact that destructuration induced softening has been compensated by the hardening associated with density increase. In the undrained tests, however, as volume change is restrained, the above hardening is limited. In CAD TXC, the predicted strain-hardening rate reasonably agrees with the experimental data and the computed yield stress and the strength are higher than that observed. A relatively poor agreement is seen between the predicted stress-strain curve of CID TXC test and the corresponding experimental data, in which the strain-hardening and strength are considerably overestimated. Figure 5.17 (b) shows that the volumetric responses of both drained tests are generally reproduced by the model, but a better agreement is seen in the CAD TXC.

5.5.2. Vallericca Clay

Vallericca clay is a natural Plio-Pleistocene marine clay. It is stiff, over-consolidated with a medium plasticity and activity. This clay is characterized by a calcium carbonate content of 30% (Kavvas and Amorosi, 2000). The following experimental tests on Vallericca clay were conducted by Amorosi (1996), and the corresponding data was obtained by digitizing the work of Kavvas and Amorosi (2000).

The shearing tests were divided into medium-high-pressure (MP) and high-pressure (HP) based on the applied stress level in reconsolidation (Kavvas and Amorosi, 2000).

In each group, specimens were anisotropically reconsolidated to sufficiently high pressure to create normally consolidated samples, which were then either sheared (undrained and drained) or unloaded to generate different OCR values.

Model Parameters and Initial Conditions

Table 5.6. Model parameters for the Vallericca clay

λ	κ	ν	M_c	M_e	N_c	N_e	C	χ	h_c	h_e	c_d	w	k_i	A	r_c
0.147	0.018	0.2	1.05	0.78	1.1	1	4	1.63	50	50	0	1	20	0.5	0.0

The model parameters for the Vallericca clay are summarized in Table 5.6. The parameters λ and κ are calibrated from an isotropic compression test on an intact sample. The Poisson's ratio ν is assumed to be 0.2. The parameters M_c , N_c and C are estimated from the effective stress path of a CAU TXC test on an NC specimen in the HP group. Due to the absence of the results of extension tests, M_e is estimated through equation 4.42 and N_e is assumed to be 1.0. The parameter χ is obtained by the analytical solution of equation 4.44. The parameter k_i is obtained by fitting the post-yield compression curve in the above compression test. The parameter A is calibrated by fitting the strain-softening rate in a CAU TXC test on an NC specimen in the MP group. Because negligible difference is observed between the peak mobilized friction in shearing under low and high consolidation pressures, the parameter r_c is assumed to be zero. The parameter h_c is calibrated by fitting the stress-strain response in a CAU TXC test on an OC specimen in the HP group. The parameter h_e is assumed to equal h_c . The parameters w and c_d take their default values.

Table 5.7. Initial conditions for the Vallericca clay simulations

p_0 (kPa)	α	S_b	e_0	p (kPa)	q (kPa)
1840	0.39	0.35	0.75	400	0

Table 5.7 presents the initial conditions for simulations. The internal variable $S_b = 0.35$ was estimated based on the previously mentioned isotropic compression test. The initial value of α is estimated through equation 4.50 based on the parameter M_c . The variable p_0 is estimated through equation 5.21 based on an estimated maximum past pressure $\sigma'_p = 2100$ kPa and a $K_{0,NC}$ value calculated from the parameter M_c . Following Kavvasdas and Amorosi (2000), all simulations begin with the initial stress $p = 400$ kPa, $q = 0$ kPa.

Model Simulation

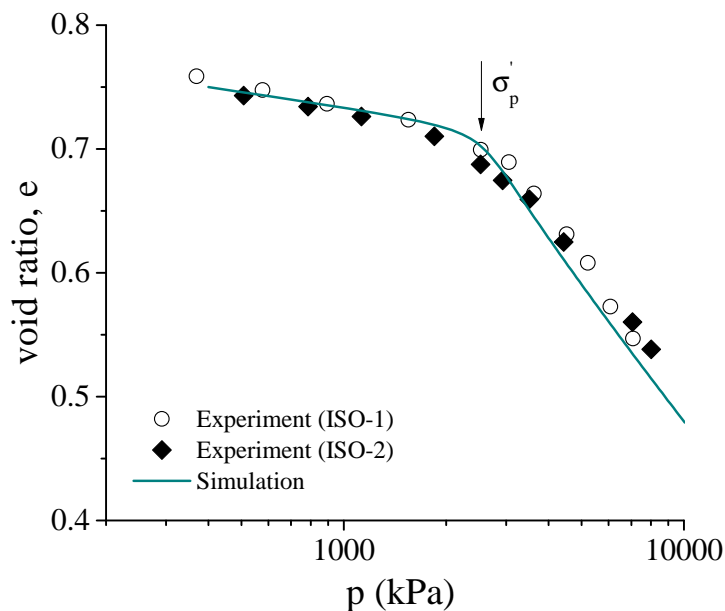


Figure 5.18. Comparison between experimental observations and model simulation for isotropic compression tests on the Vallericca clay

Figure 5.18 compares the experimental data and model simulation for isotropic compression tests. Good agreement can be seen between the experimental observations and the computed result. It is worth mentioning that the typical destructuration response (i.e., a decrease in the compressibility at higher stresses) is not observed in tests on the Vallericca clay. As discussed in Chapter 2, this behavior may result from a compact structure and more oriented fabric that were formed during soil deposition.

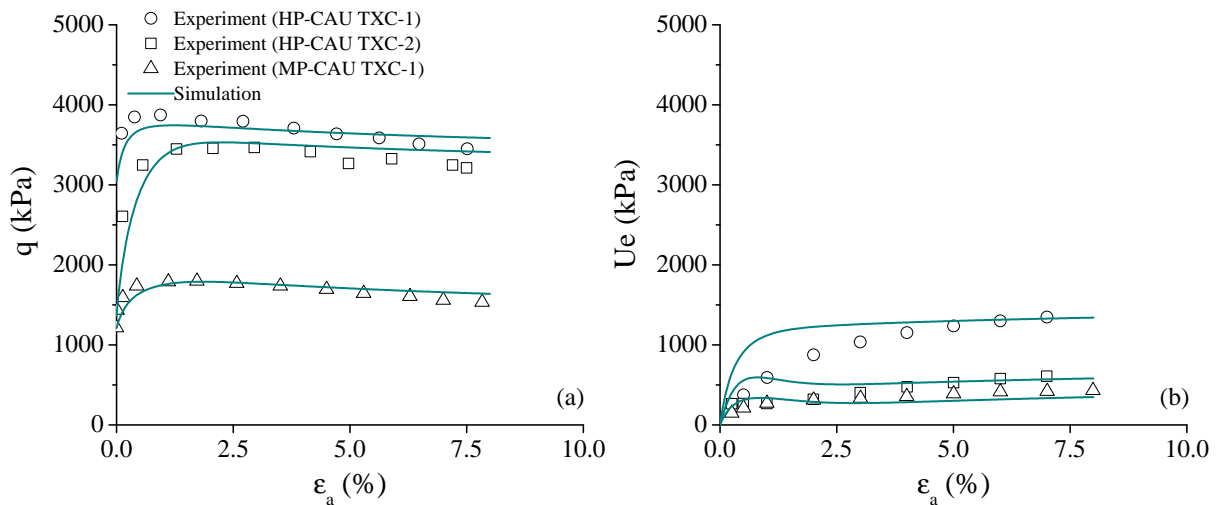


Figure 5.19. Comparison between the experimental observations and model simulations for CAU TXC tests on the Vallericca clay: (a) stress-strain response; (b) strain-pore pressure response

Figure 5.19 and Figure 5.20 present the experimentally observed and computed results in the three CAU TXC tests that were used in the model calibration. In general, the model simulations reasonably reproduce the experimental observations. Specimens in the HP group were consolidated to much higher pressure than their maximum past pressure. Therefore, presumably, most of the soil structure had been removed before the shearing and its stress-strain response is more likely to reflect the intrinsic behavior. The significant point of this comparison is that with a single set of parameters, the proposed model can

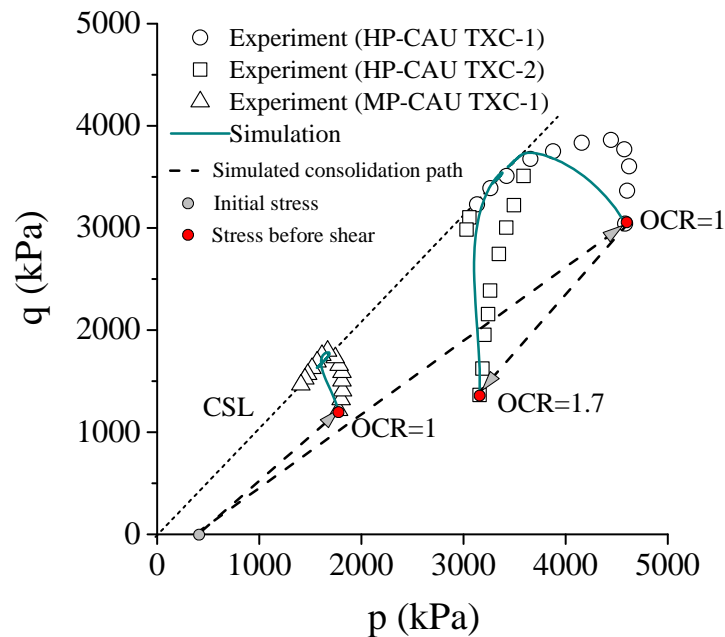


Figure 5.20. Comparison between the experimental observations and model simulations for CAU TXC tests on the Vallericca clay: effective stress path

satisfactorily reproduce the behavior of both structured and unstructured clays that have different stress histories. Note that the computed initial pore positive pore pressure for the two specimens in the HP group is greater than the observations.

Model Prediction

Figure 5.21 and Figure 5.22 present the experimental data and model predictions in three CAU TXC tests in the MP group. It is noted that the model predictions agree well with the observed stress-strain-strength responses in the tests, especially the peak strength and strain-softening. Experimental data show that the excess pore pressure increases first then decreases and then gradually increases again. Model predictions correctly reproduce this trend. Moreover, the strain levels that correspond to excess pore pressure starting to decrease are well predicted. The amount of the above decrease in excess pore pressure

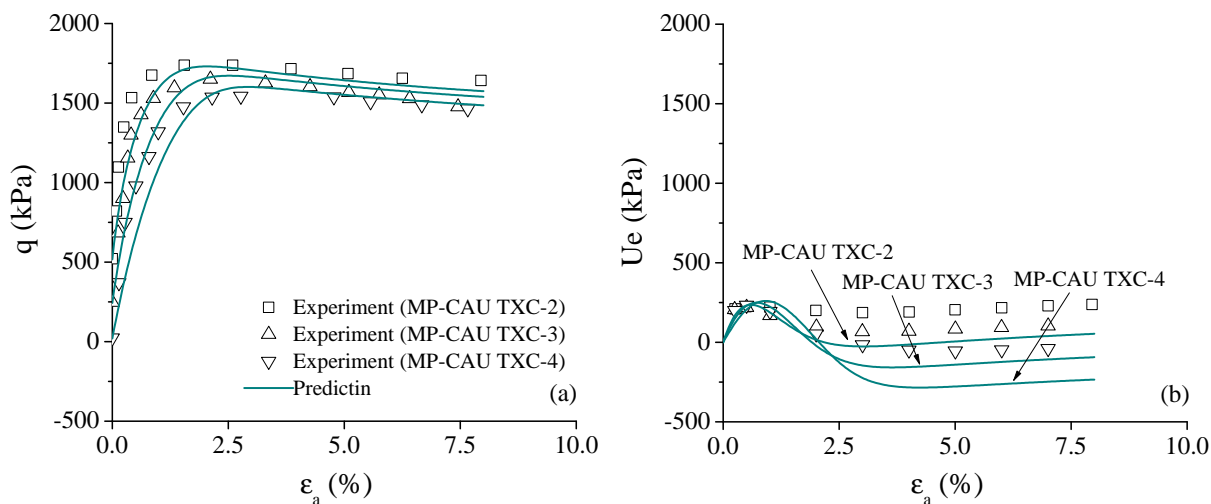


Figure 5.21. Comparison between the experimental observations and model predictions for CAU TXC tests on the Vallericca clay (MP group): (a) stress-strain response; (b) strain-pore pressure response

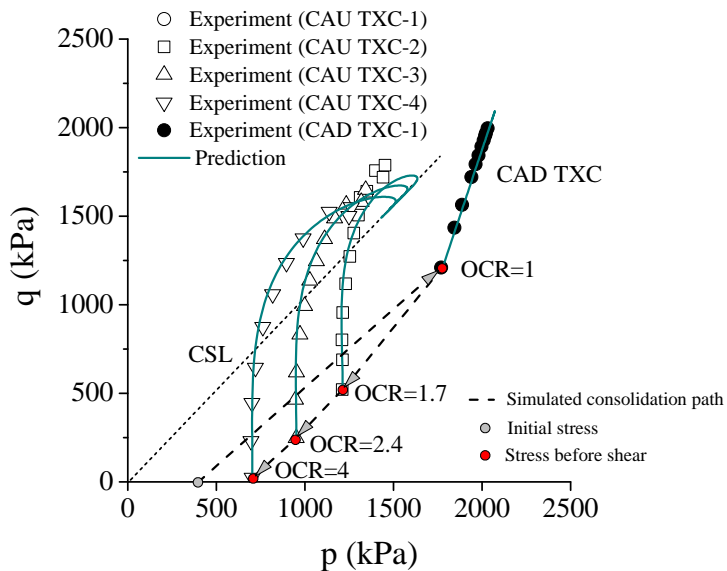


Figure 5.22. Comparison between the experimental observations and model predictions for CAU TXC tests on the Vallericca clay (MP group): effective stress path

is higher than that observed, which leads to an underestimation of the final excess pore pressure.

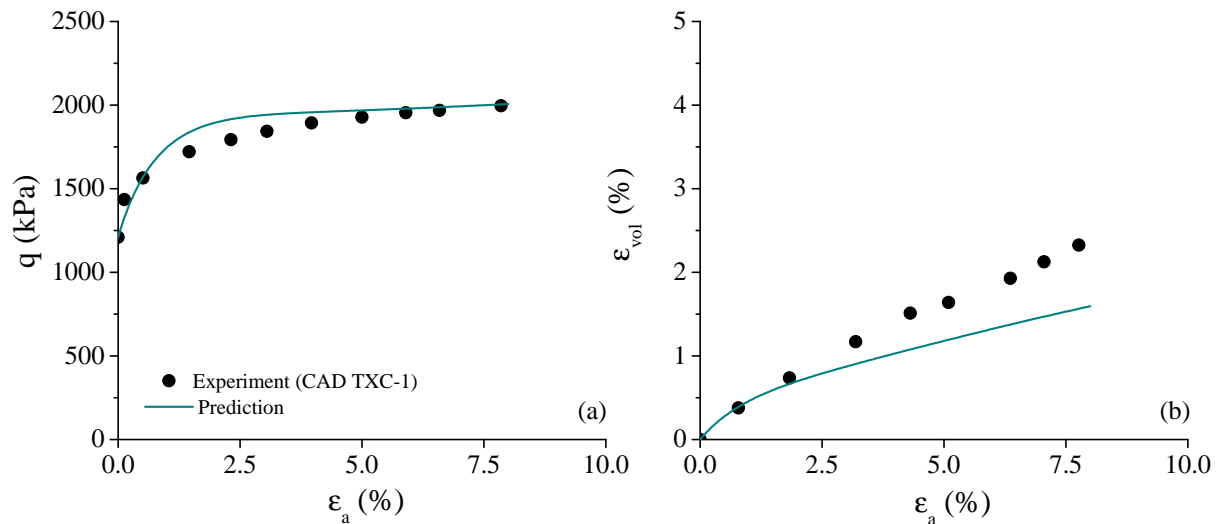


Figure 5.23. Comparison between experimental observations and model predictions for a CAD TXC test (MP group) on the Vallericca clay: (a) stress-strain response; (b) volume change

Figure 5.23 shows the observed and predicted responses in a CAD TXC test in the MP group, whose effective stress path is shown in Figure 5.22. The predicted stress-strain response agrees well with the observation and the volume change at relative high axial strains is underestimated.

Figure 5.24 and Figure 5.25 show the result of a CAU TXC test in the HP group, as well as the corresponding model predictions. It can be seen that the observed stress-strain and pore pressure responses are satisfactorily predicted by the model.

5.5.3. Bothkennar Clay

Bothkennar clay is a typical structured clay, whose intrinsic behavior and yielding behavior of intact specimens have been experimentally studied by Allman and Atkinson (1992) and

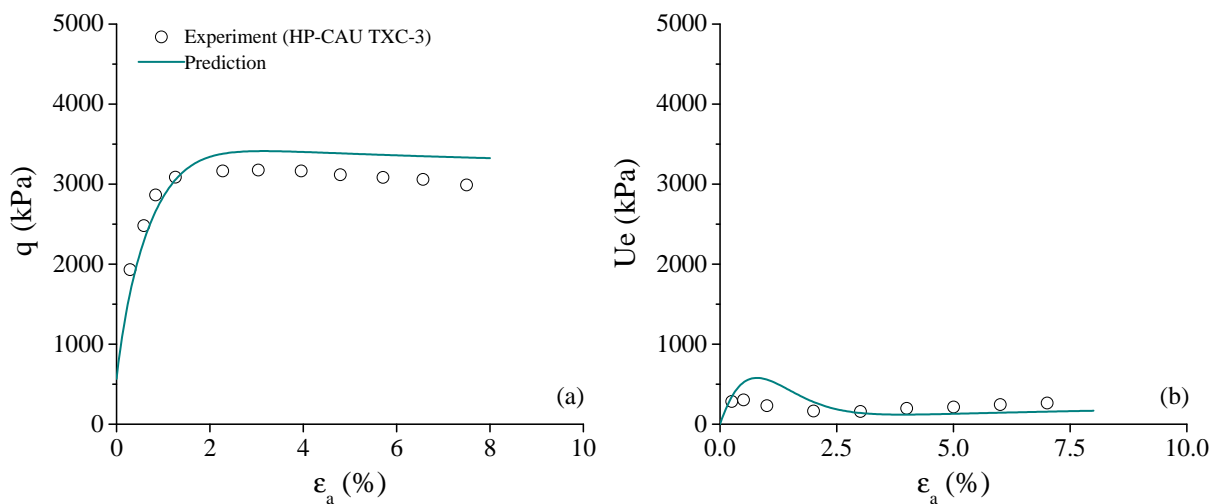


Figure 5.24. Comparison between the experimental observations and model predictions in a CAU TXC test (HP group) on the Vallericca clay: (a) stress-strain response; (b) strain-pore pressure response

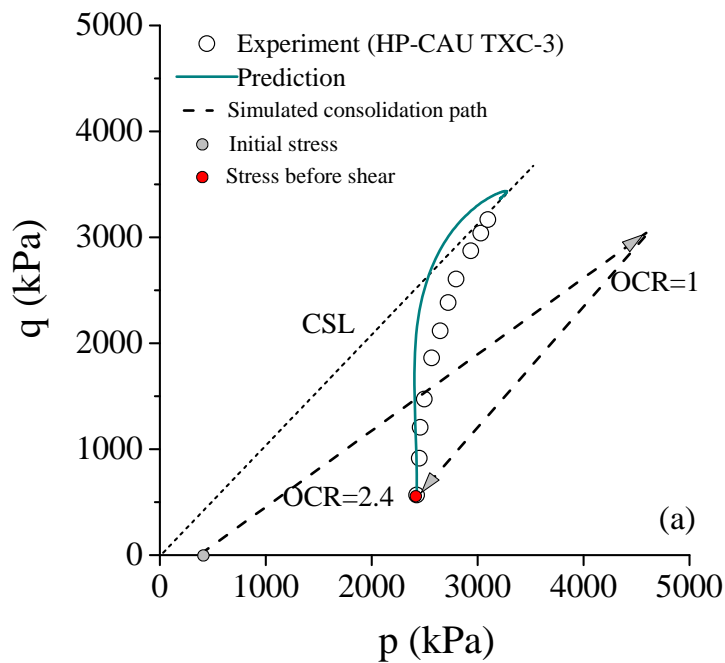


Figure 5.25. Comparison between the experimental observations and model predictions in a CAU TXC test (HP group) on the Vallericca clay: effective stress path

Smith et al. (1992), respectively. The data used in the following comparison were reported by Smith et al. (1992)

Model Parameters and Initial Conditions

Table 5.8. Model parameters for the Bothkennar clay

λ	κ	ν	M_c	M_e	N_c	N_e	C	χ	h_c	h_e	c_d	w	k_i	A	r_c
0.255	0.03	0.2	1.4	1.04	1.3	1	10	1.74	500	500	0	1	10	0.4	0.17

The model parameters for the Bothkennar clay are summarized in Table 5.8. The parameters λ and κ are calibrated from 1D compression test on a reconstituted specimen. The Poisson's ratio ν is assumed to be 0.2. The parameters $M_c = 1.4$ and $M_e = 1.04$ were reported by Smith et al. (1992). The parameters N_c and N_e are calibrated by fitting the peak strength of a CK₀U TXC test and a CK₀U TXE test on samples that have been K₀ consolidated to vertical effective stress more than twice as high as the σ'_p . The parameter C is obtained by fitting the effective stress path of the CK₀U TXE test. The parameter χ is calculated from the analytical solution of equation 4.44. The calibration of destructuration parameters k_i , A and r_c has been shown in the section 5.4.1. The parameter h_c is calibrated by fitting the stress-strain response in a CAU TXC test on an OC specimen. The parameter h_e is assumed to equal h_c . The parameters w and c_d take their default values.

Table 5.9. Initial conditions for the Bothkennar clay simulations

p_0 (kPa)	α	S_b	e_0	p (kPa)	q (kPa)
8.3	0.52	6.1	1.89	22	0

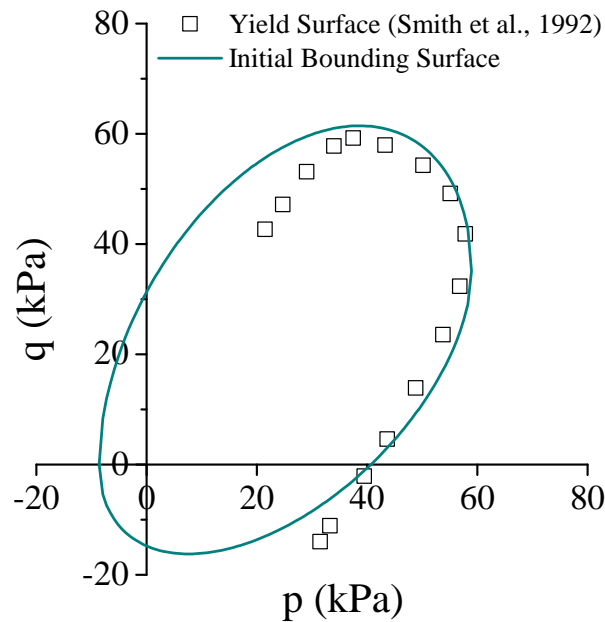


Figure 5.26. Comparison between computed initial bounding surface and experimentally observed yield stresses of the Bothkennar clay (Smith et al., 1992)

The initial conditions in model simulations are presented in Table 5.9. The estimation of the internal variable S_b has been shown in section 5.4.2. The initial value of α is estimated through equation 4.50 based on the parameter M_c . The variable p_0 is estimated through equation 5.21 based on an estimated maximum past pressure $\sigma'_p = 85$ kPa and a $K_{0,NC}$ value calculated from M_c . The initial stress $p = 22$ kPa, $q = 0$ kPa was reported by Smith et al. (1992).

As a preliminary validation of the model parameters and initial conditions, the computed initial bounding surface is compared with the yield stresses obtained in drained probe tests reported by Smith et al. (1992), as shown in Figure 5.26. Note that the computed bounding surface is in good agreement with the measured yield stress envelope. This agreement indicates that the proposed analytical solutions (i.e., equation 4.50 and

equation 5.21) can provide a reasonable estimation of the initial size and inclination of the bounding surface.

Model Simulation

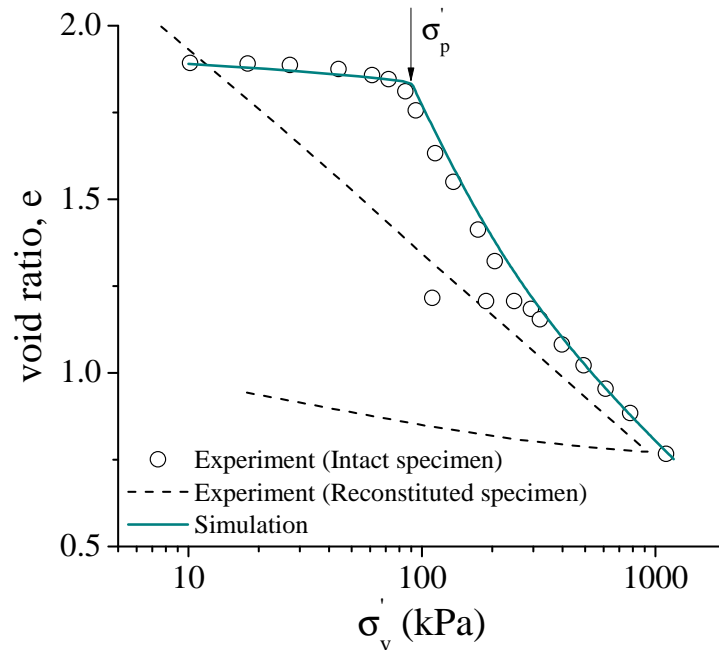


Figure 5.27. Comparison between the experimental observation and model simulation for a 1D compression on the Bothkennar clay

Figure 5.27 compares the experimental observation and the corresponding model simulation in a 1D compression test on intact Bothkennar clay. For the purpose of comparison, the result of a 1D compression test on a reconstituted specimen is included in the figure. Note that a good agreement is seen between the model simulation and the experimental data. Both the experimentally observed and computed results show that the compression curve of the intact sample gradually converges to the compression curve of the reconstituted sample, i.e., the intrinsic compression line (ICL) (Burland, 1990).

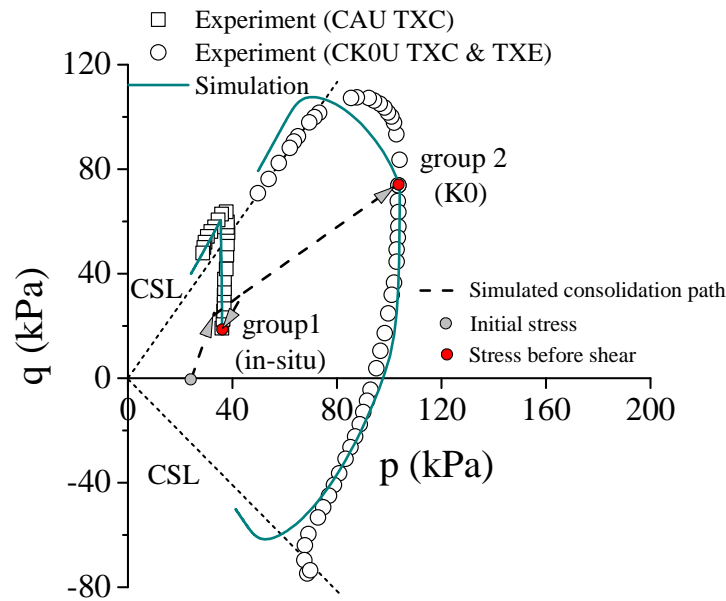


Figure 5.28. Comparison between the experimental observations and model simulations for triaxial shearing tests on the Bothkennar clay: stress path

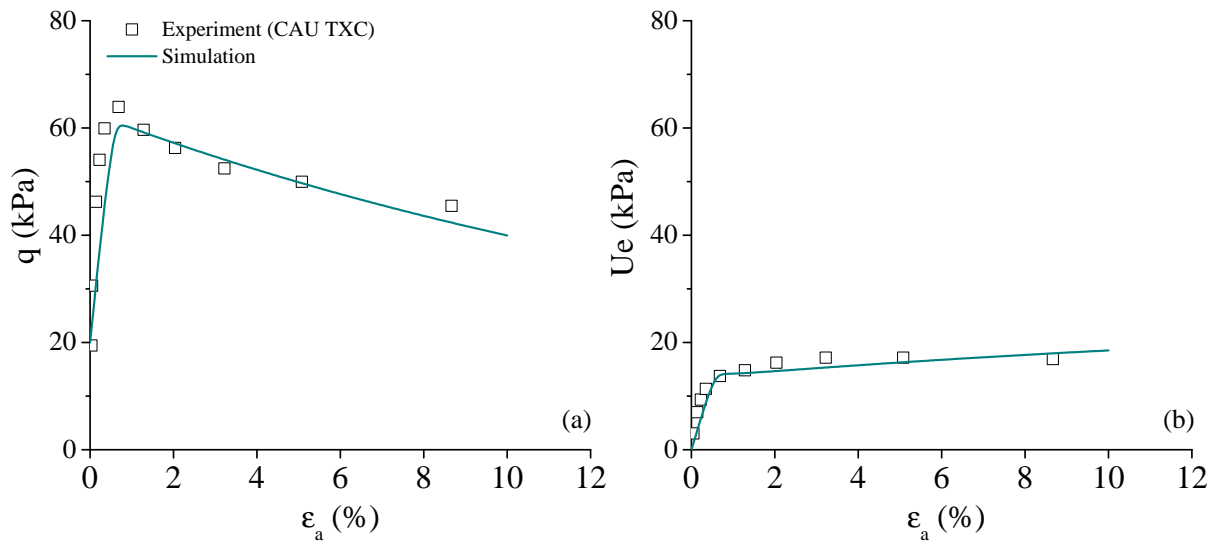


Figure 5.29. Comparison between the experimental observations and model simulation for a CAU TXC test on the Bothkennar clay: (a) stress-strain response; (b) strain-pore pressure response

Figure 5.28 presents the observed and computed effective stress paths in undrained triaxial shearing tests on specimens that had experienced different reconsolidation paths. In group 1, samples were reconsolidated back to in-situ stress along continuous stress paths that retraced their lightly overconsolidated stress history. In group 2, specimens were K_0 consolidated to normally consolidated state (Smith et al., 1992). In general, the model simulations achieve good agreement with the experimental observations. Note that the experimental data of the CK_0U TXE test show that the excess pore pressure starts to decrease (i.e., bending the effective stress path to the right) when stress ratio η reaches M_e , which is not seen in the model simulation. As discussed by Dafalias et al. (2006), this type of effective stress path can be reproduced when the rotation hardening is also dependent on the plastic deviatoric strain rate (e.g., the model proposed by Wheeler et al. (2003)). Out of the above three tests, Smith et al. (1992) only reported the stress-strain response for the CAU TXC test, which is presented in Figure 5.29. Note that the experimentally observed peak strength, strain-softening and gradual increase in excess pore pressure are well reproduced by the simulation.

Model Prediction

Figure 5.30 shows the effective stress paths in three other undrained shearing tests and the corresponding model predictions. In group 3, the specimen was isotropically consolidated to a normally consolidated state before the shearing, whereas the group 4 sample experienced passive consolidation that started from the in-situ stress (Smith et al., 1992). Note that the model predictions reasonably agree with the experimental observations. In the CIU TXC, the computed initial pore pressure is lower than that observed and the peak strength is overestimated by the model by 15%. Figure 5.31

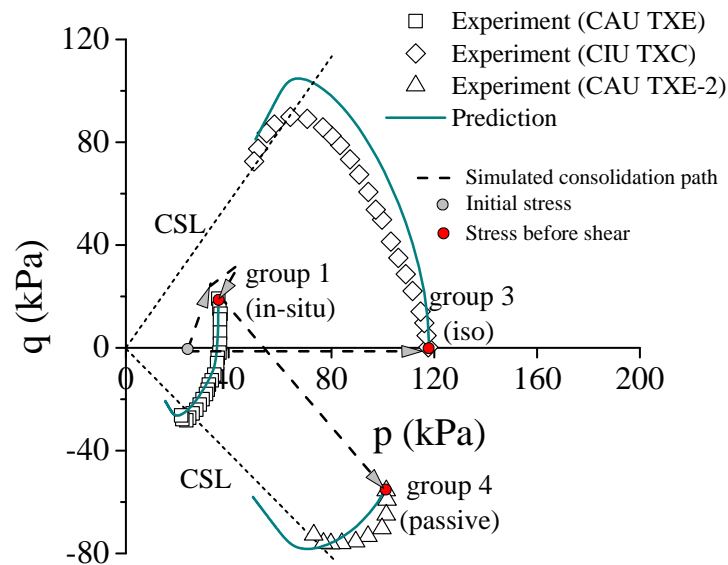


Figure 5.30. Comparison between the experimental observations and model predictions for triaxial shearing tests on the Bothkennar clay: stress path

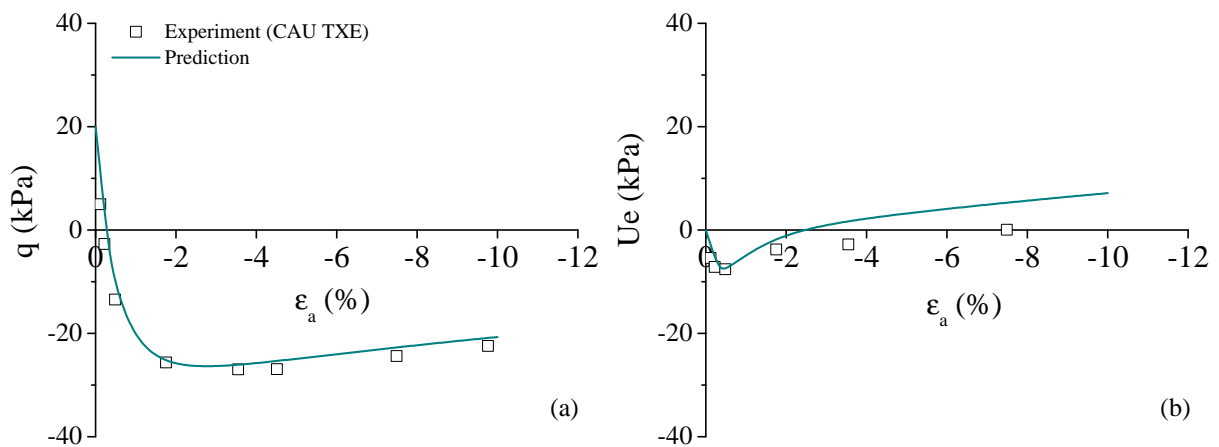


Figure 5.31. Comparison between the experimental observations and model prediction for a CAU TXE test on the Bothkennar clay: (a) stress-strain response; (b) strain-pore pressure response

compares the observed and predicted stress-strain response in the CAU TXE test. Note that the peak strength and strain-softening are predicted very well by the model whereas the excess pore pressure at large strains is slightly overestimated.

5.5.4. Shanghai Clay

Shanghai clay is a soft, normally consolidated material of relatively high sensitivity. Huang et al. (2011) reported results of a series of laboratory tests on the Shanghai clay and these data are used in the following comparisons.

Model Parameters and Initial Conditions

Table 5.10. Model parameters for the Shanghai clay

λ	κ	ν	M_c	M_e	N_c	N_e	C	χ	h_c	h_e	c_d	w	k_i	A	r_c
0.210	0.03	0.2	1.37	0.9	1.2	1.0	6	1.73	100	100	0	1	8	0.3	0.0

The model parameters for Shanghai clay are summarized in Table 5.10. The parameters λ and κ are calibrated from a 1D compression test on an intact sample. The Poisson's ratio ν is assumed to be 0.2. The parameters M_c , N_c and C are calibrated based on the effective stress path of a CIU TXC test on an NC sample. Because the results of extension test are not available, M_e is estimated through equation 4.42 and N_e is assumed to be 1.0. The parameter χ is calculated from the analytical solution of equation 4.44. The parameter k_i is obtained by fitting the post-yield compression curve in the above 1D compression test. The parameter A is calibrated by fitting the strain-softening rate in the above CIU TXC test. No noticeable difference is observed between the peak mobilized friction in shearing tests under low and high consolidation pressures, so the parameter r_c is assumed to be zero. The parameter h_c is obtained by fitting the stress-strain response in a CIU TXC test on an OC specimen. The parameter h_e is assumed to equal h_c . The parameters w and c_d take their default values.

Table 5.11. Initial conditions for the Shanghai clay simulations

p_0 (kPa)	α	S_b	e_0	p (kPa)	q (kPa)
32	0.51	1.16	1.40	20	0

The initial conditions of the following simulations are presented in Table 5.11. The internal variable S_b is estimated from the 1D compression test. The initial value of α is estimated through equation 4.50 based on the parameter M_c . The variable p_0 is estimated through equation 5.21 based on an estimated maximum past pressure $\sigma'_p = 97$ kPa and a computed $K_{0,NC}$ value from the parameter M_c . The initial stress $p = 20$ kPa, $q = 0$ kPa is assumed to represent the residual stress of the samples.

Model Simulation

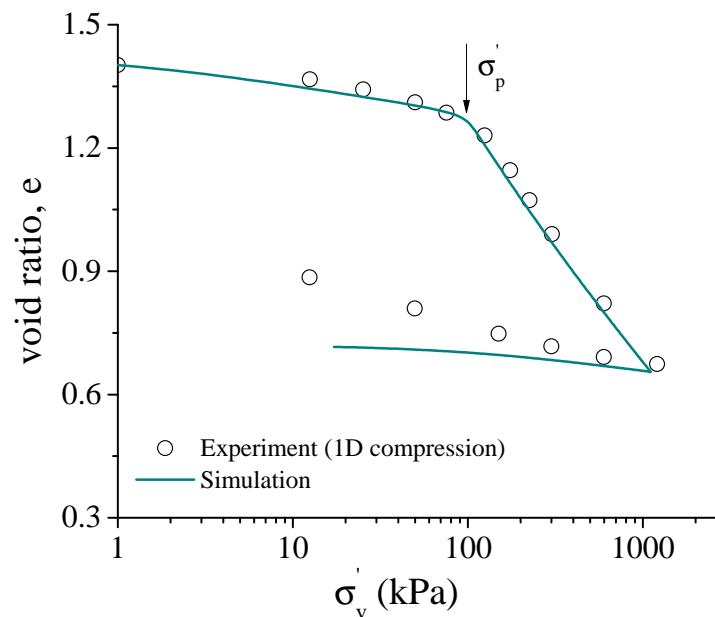


Figure 5.32. Comparison between the experimental observation and model simulation in a 1D compression test on the Shanghai clay

Figure 5.32 presents the comparison between the experimental data and model simulation for a 1D compression test on the Shanghai clay. It is clear that the model simulation successfully captures the yield stress and the post-yield compressibility. Note that the simulated swelling during unloading is lower than that observed in the test, which results in an underestimation of the void ratio at the end of unloading. The discrepancy may arise from two factors. First, a constant parameter κ and Poisson ratio ν will lead to a decreasing C_r in 1D unloading due to an increasing K_0 value. Second, the model underestimates the plasticity dilatancy during unloading.

Figure 5.33 and Figure 5.34 show the experimental data and model simulations in two CIU TXC tests that have been used to define the model parameters. Note that the model simulations satisfactorily reproduce material's stress-strain responses, particularly the peak strength, strain softening and excess pore pressure. The initial shear stiffness is overestimated by the model, which leads to lower strains that correspond to peak strength.

Model Prediction

Figure 5.35 and Figure 5.36 present results of two CAU TXC tests on the same material. Note that based on the parameters calibrated from the CIU TXC tests, the model predicts very well the response observed in the CAU TXC tests, which validates the capacity of the model to capture the effects of anisotropic stress history.

5.5.5. Wenzhou Clay

Wenzhou clay is a marine deposit characterized as slightly organic and highly plastic. Yin et al. (2015) reported the experimental tests data in the following comparisons.

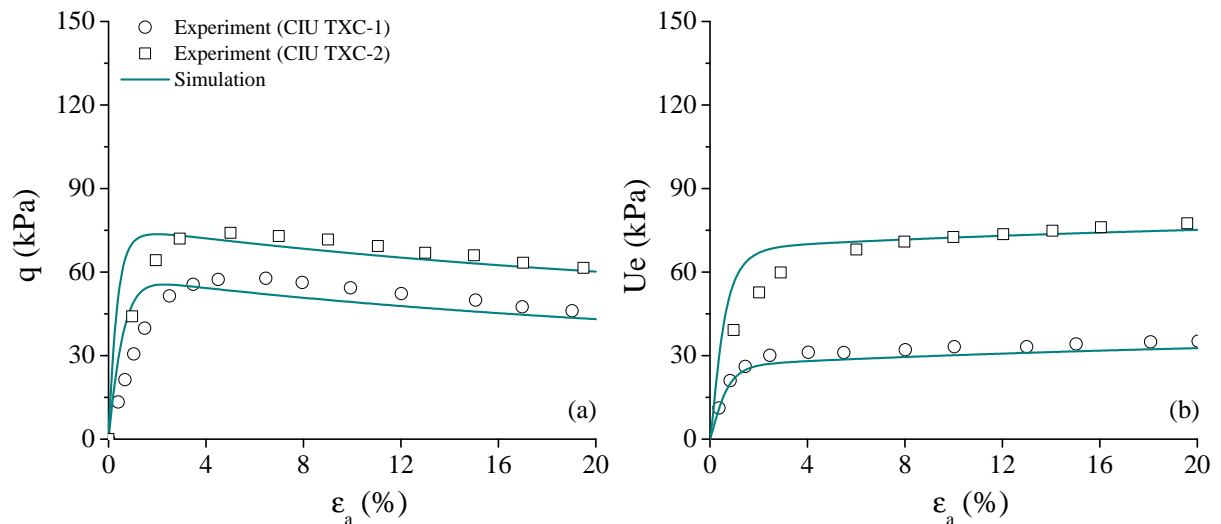


Figure 5.33. Comparison between the experimental observations and model simulations in two CIU TXC tests on the Shanghai clay: (a) stress-strain response; (b) strain-pore pressure response

Model Parameters and Initial Conditions

Table 5.12. Model parameters for the Wenzhou clay

λ	κ	ν	M_c	M_e	N_c	N_e	C	χ	h_c	h_e	c_d	w	k_i	A	r_c
0.275	0.03	0.2	1.23	0.87	1.2	1.1	10	1.73	100	100	0	1	12	0.75	0.0

The model parameters of the Wenzhou clay are shown in Table 5.12. The parameters λ and κ are calibrated from a 1D compression test on an intact sample. The Poisson's ratio ν is assumed to be 0.2. The parameters M_c and M_e are calibrated from the effective stress paths in a CK_0U TXC and a CK_0U TXE on samples that have been consolidated to pressure more than four times greater than σ'_p , respectively. The parameters N_c and N_e are obtained by fitting the peak strength in the two undrained tests. The parameter C is calibrated through fitting the effective stress path in the CK_0U TXE test. The parameter χ is calculated from the analytical solution of equation 4.44. The parameter k_i is obtained

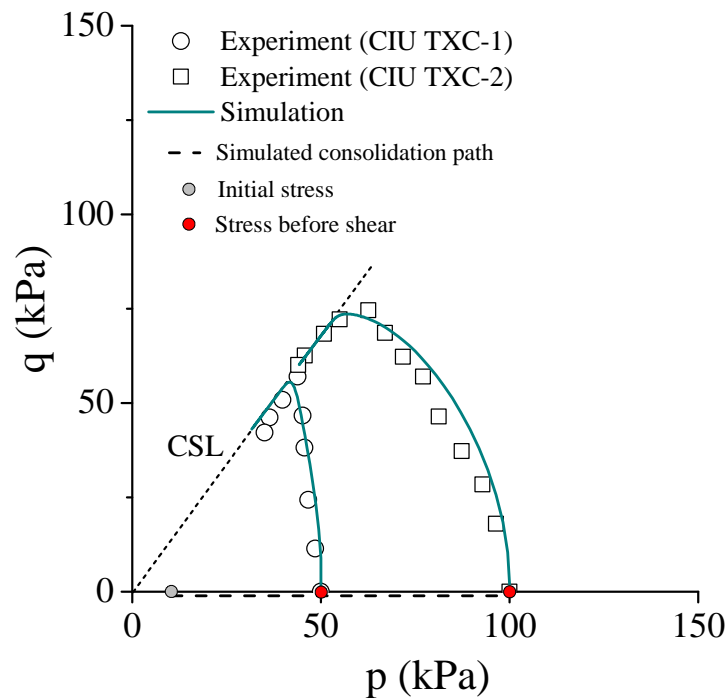


Figure 5.34. Comparison between the experimental observations and model simulations in two CIU TXC tests on the Shanghai clay: effective stress path

by fitting the post-yield compression curve in the 1D compression test. The parameter A is calibrated by fitting the strain-softening rate in the CK_0U TXC test. As negligible difference is observed between the peak mobilized frictions in shearing tests under low and high consolidation pressures, the parameter r_c is assumed to be zero. The experimental data on OC samples are not available, so the parameters h_c and h_e are assumed to be 100. The parameters w and c_d take their default values.

Table 5.13. Initial conditions for the Wenzhou clay simulations

p_0 (kPa)	α	S_b	e_0	p (kPa)	q (kPa)
21	0.45	1.4	1.89	20	0

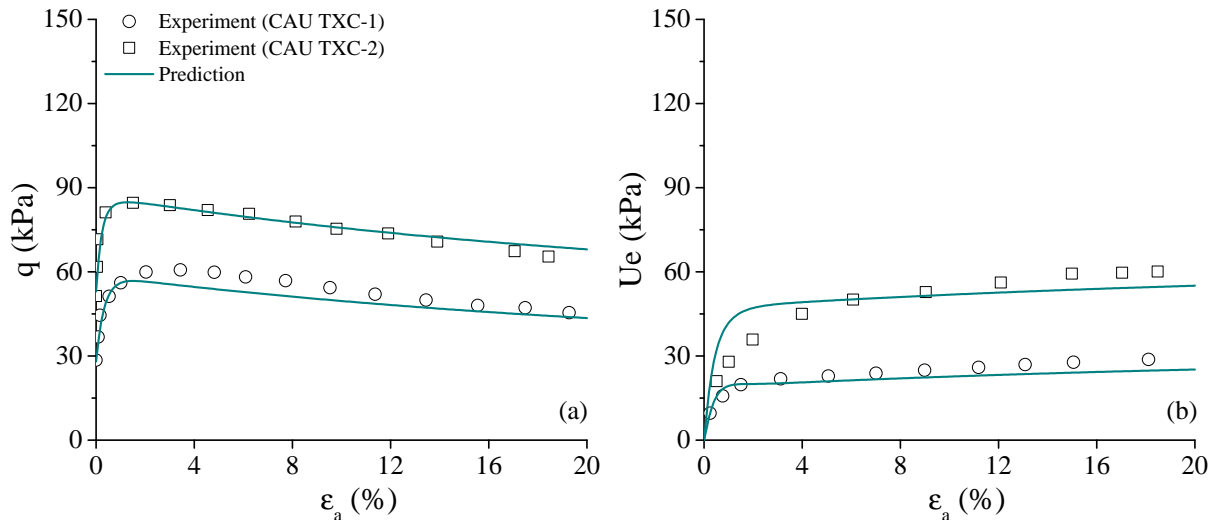


Figure 5.35. Comparison between the experimental observations and model predictions in two CAU TXC tests on the Shanghai clay: (a) stress-strain response; (b) strain-pore pressure response

The initial conditions of the following simulations are presented in Table 5.13. The internal variable S_b is estimated from the 1D compression test. The initial value of α is estimated through equation 4.50 based on the parameter M_c . The variable p_0 is estimated through equation 5.21 based on an estimated maximum past pressure $\sigma'_p = 70.4$ kPa and a calculated $K_{0,NC}$ value from the parameter M_c . The initial stress $p = 20$ kPa, $q = 0$ kPa is assumed to represent the residual stress of the samples.

Model Simulation

Figure 5.37 shows that excellent agreement is seen between the model simulation results and experimental observations in the 1D compression test.

Figure 5.38 and Figure 5.39 show the experimentally observed and computed results in the undrained shearing tests used in the model calibration. The simulated responses reasonably agree with that observed. In the CK_0U TXE, the computed shear modulus

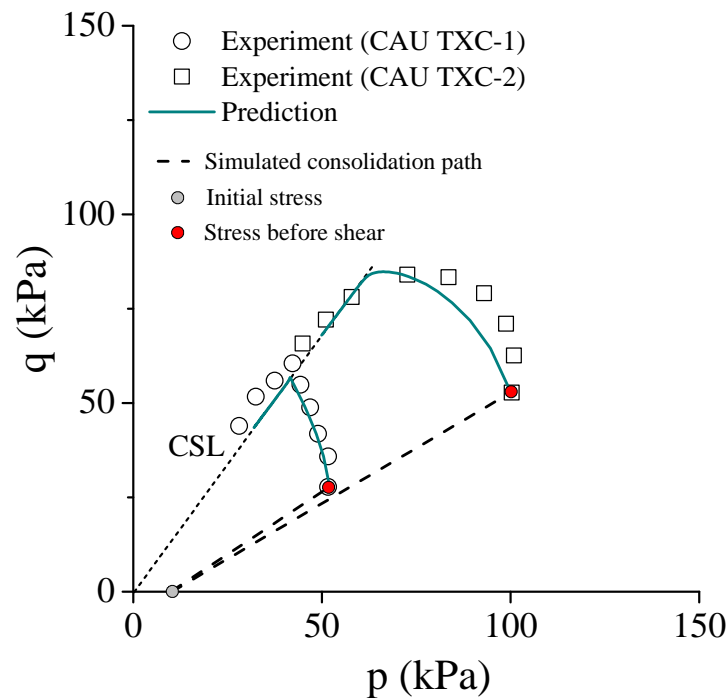


Figure 5.36. Comparison between the experimental observations and model predictions in two CAU TXC tests on the Shanghai clay: effective stress path

is higher than that observed, which leads to lower strains that correspond to the peak strength. Both the experimental data and model simulation show that the excess pore pressure in the CK_0U TXE first decreases then gradually increases. The computed increase of the pore pressure is slightly higher than that observed.

Model Prediction

Figure 5.40 and Figure 5.41 show the model predictions for other CK_0U TXC and TXE tests. In general, the predictions reasonably agree with the experimental observations. Experimental data show that strain-softening is stronger in compression loading, which presumably reflects the effect of preceding anisotropic consolidation. The model

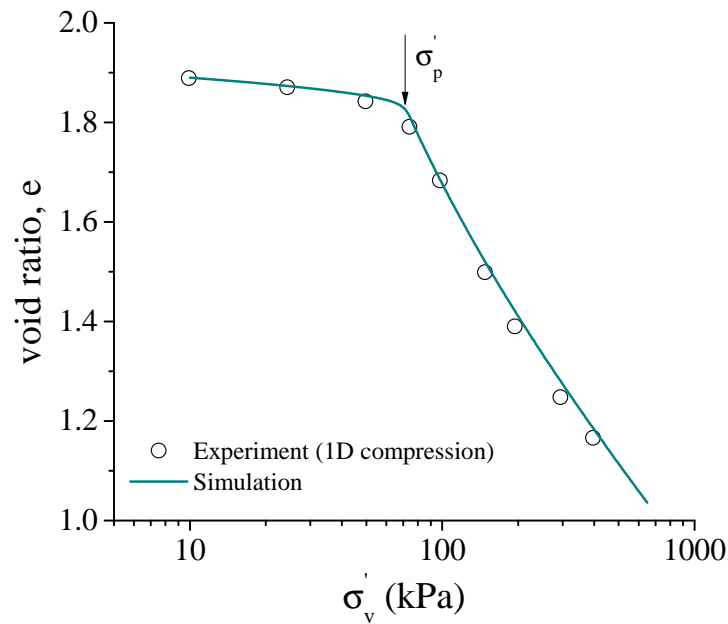


Figure 5.37. Comparison between the experimental observation and model simulation for a 1D compression test on the Wenzhou clay

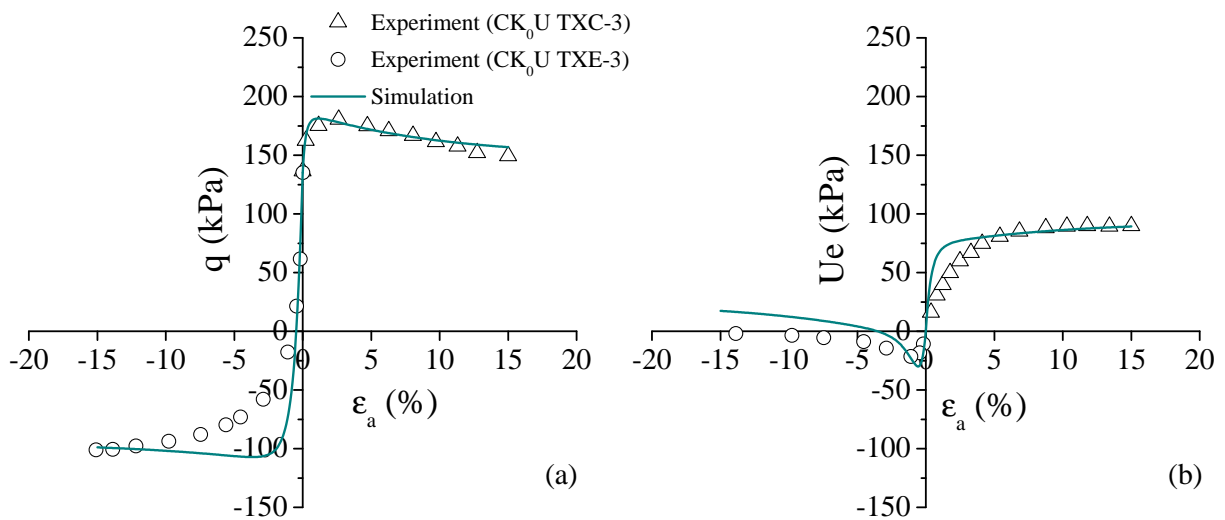


Figure 5.38. Comparison between the experimental observations and model simulations for a CK_0U TXC test and a CK_0U TXE test on the Wenzhou clay: (a) stress-strain response; (b) strain-pore pressure response

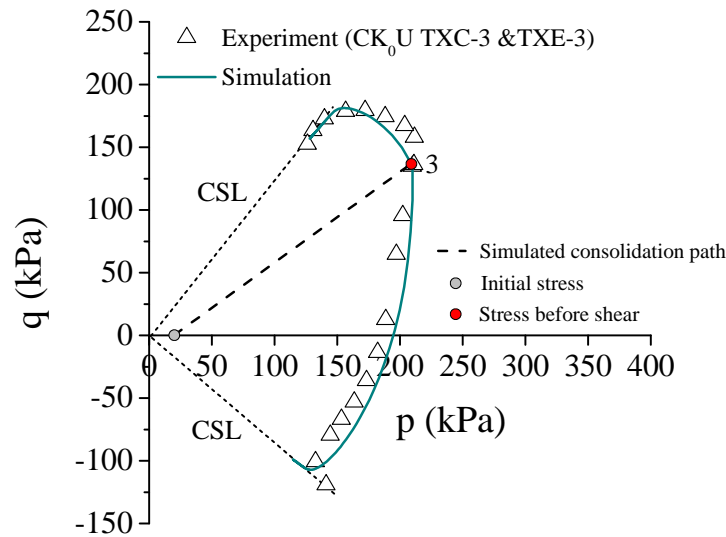


Figure 5.39. Comparison between the experimental observations and model simulations for a CK₀U TXC test and a CK₀U TXE test on the Wenzhou clay: effective stress path

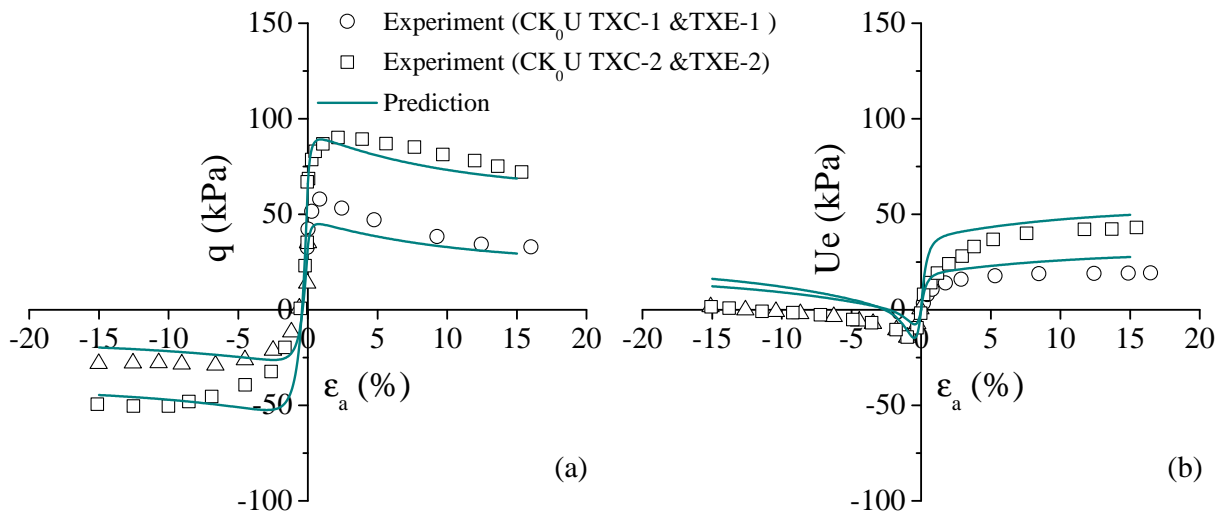


Figure 5.40. Comparison between the experimental observations and model predictions for two CK₀U TXC tests and two CK₀U TXE tests on the Wenzhou clay: (a) stress-strain response; (b) strain-pore pressure response

successfully predicts this feature. In the CK₀U TXC-1, the peak strength is underestimated about 22% by the model. In CK₀U TXE tests, the trend of excess pore pressure

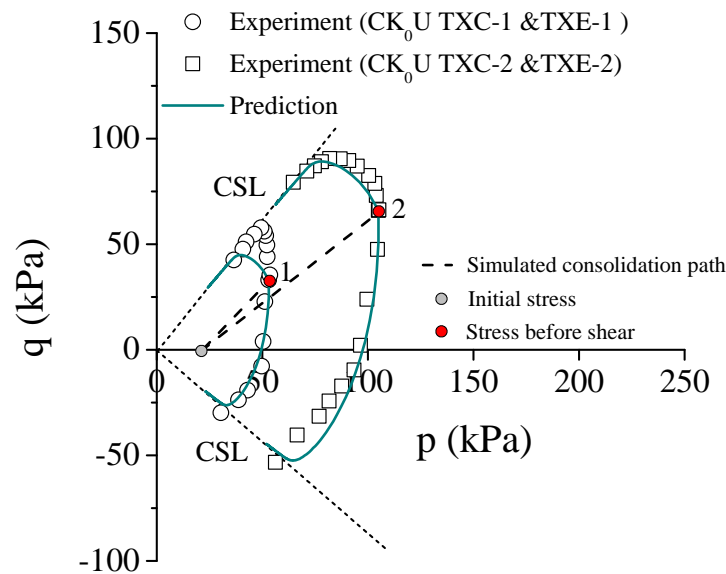


Figure 5.41. Comparison between the experimental observations and model predictions for two CK_0U TXC tests and two CK_0U TXE tests on the Wenzhou clay: effective stress path

development is reproduced by the model predictions, but the computed increase in excess pore pressure is higher than observed.

5.5.6. Grande Baleine Clay

Grande Baleine clay is a postglacial marine clay, which was deposited in the Tyrrell Sea about 7000 years ago. The plasticity of this clay is low, and its clay fraction reaches around 60%. One salient feature of Grande Baleine clay is its high natural water content compared with its liquid limit, as indicated by a liquidity index as high as 2.84. The behavior and destructuration of the Grande Baleine clay during monotonic loading and cyclic loading have been studied by Locat and Lefebvre (1985) and Lefebvre et al. (1989). Both these work presented the experimental data for the following evaluation. It is noteworthy that Lefebvre et al. (1989) reported observations in both cyclic loading tests and post-cyclic

undrained shearing tests. This set of observations provides key data for evaluating the model's capacity to simulate destructuration induced by cyclic loading and predict the available strength after cyclic loadings.

Model Parameters and Initial Conditions

Table 5.14. Model parameters for the Grande Baleine clay

λ	κ	ν	M_c	M_e	N_c	N_e	C	χ	h_c	h_e	c_d	w	k_i	A	r_c
0.136	0.007	0.2	1.49	1	1	1	12	1.73	200	550	-250	0	20	0.1	0.135

The model parameters for the Grande Baleine clay are summarized in Table 5.14. The parameters λ and κ are calibrated from 1D compression tests on reconstituted and intact specimen, respectively. The Poisson's ratio ν is assumed to be 0.2. To study the effects of destructuration on the shearing behavior, Lefebvre et al. (1989) conducted CIU TXC tests on samples had experienced two different reconsolidation. Samples in group 1 were reconsolidated to pressure twice as high as σ'_p to create a destructured, NC clay. For specimens in group 2, the applied reconsolidation stress was equal to in-situ vertical effective stress to preserve the intact clay structure. The parameters M_c , N_c and C are calibrated based on the effective stress path in a CIU TXC test in group 1. Results of extension tests are not available, so the parameter M_e is estimated through equation 4.42 and N_e is assumed to be 1.0. The parameter χ is calculated from the analytical solution of equation 4.44. The parameter k_i is obtained by fitting the post-yield compression curve in above 1D compression test on the intact sample. The parameter A is calibrated by fitting the strain-softening rate in the above CIU TXC test. The peak stress ratio in a CIU TXC test in group 2 and the M_c value are used to define the parameter r_c based on

the method shown in section 5.4.1. The parameters h_c , h_e , c_d and w are defined based on results of an undrained cyclic loading test.

Table 5.15. Initial conditions for Grande Baleine clay simulations

p_0 (kPa)	α	S_b	e_0	p (kPa)	q (kPa)
4.3	0.57	31.7	1.65	20	0

Table 5.15 shows the initial conditions for the model simulations of Grande Baleine clay behavior. The initial value of internal variable S_b is calibrated by comparing the compression curves of the reconstituted and intact samples. The initial value of variable α is estimated through equation 4.50 based on the parameter M_c . Based on an estimated maximum past pressure $\sigma'_p = 85$ kPa, equation 5.21 yields a value of p_0 equal to 2 kPa. Figure 5.42 compares the effective stress path for the group 2 CIU TXC and the computed initial bounding surface based on these initial conditions. It can be seen that the bounding surface would underestimate the peak strength in the CIU TXC. So the value of p_0 is determined by fitting the peak strength in the CIU TXC, as shown in Figure 5.42. Note that the initial phase transition line (PTL) passes the peak stress ratio in the test.

Model Simulation

Figure 5.43 shows the experimental data of a 1D compression test on intact Grande Baleine clay and the corresponding model simulation. For comparison, the result of 1D compression on a reconstituted sample is included in the figure. It can be seen that the computed compression curve reasonably reproduce the experimentally observed greater post-yield compressibility and its decrease due to the destructuration. Moreover, both the observed and computed compression curves tend to converge to the ICL at higher

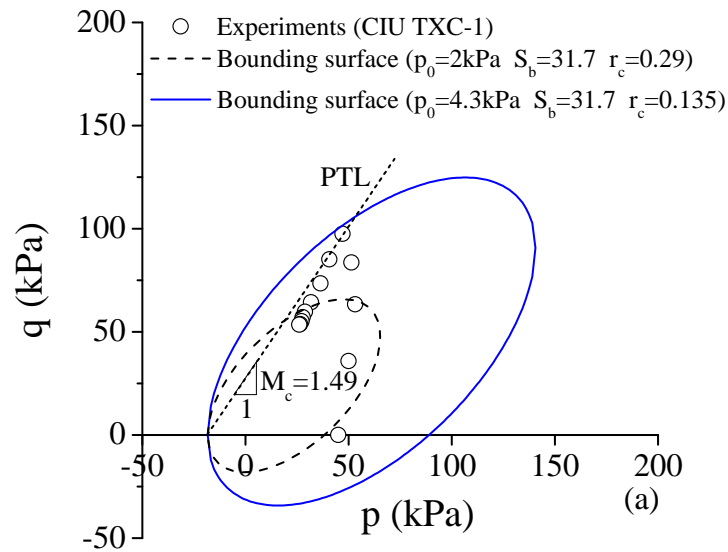


Figure 5.42. Comparison between the effective stress path in a CIU TXC test on an intact sample and the computed bounding surfaces with different values of internal variables

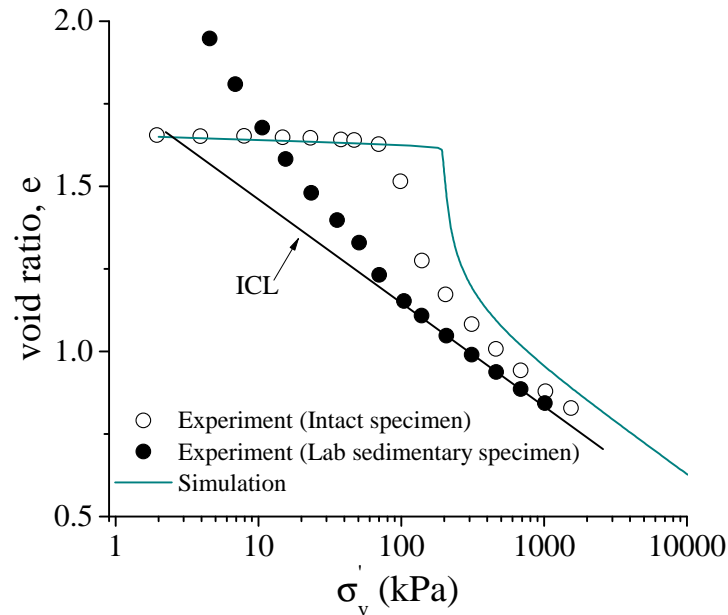


Figure 5.43. Comparison between the experimental observation and model simulation in a 1D compression test on the Grande Baleine clay

stresses. The simulated yield stress is higher than that observed, which is expected as the p_0 value used in the simulation is higher than that determined based on the observed maximum past pressure. This discrepancy may partially result from the natural variation between the samples for shearing tests by Locat and Lefebvre (1985) and the sample for the compression test by Locat and Lefebvre (1985), as these work reported different maximum past pressures.

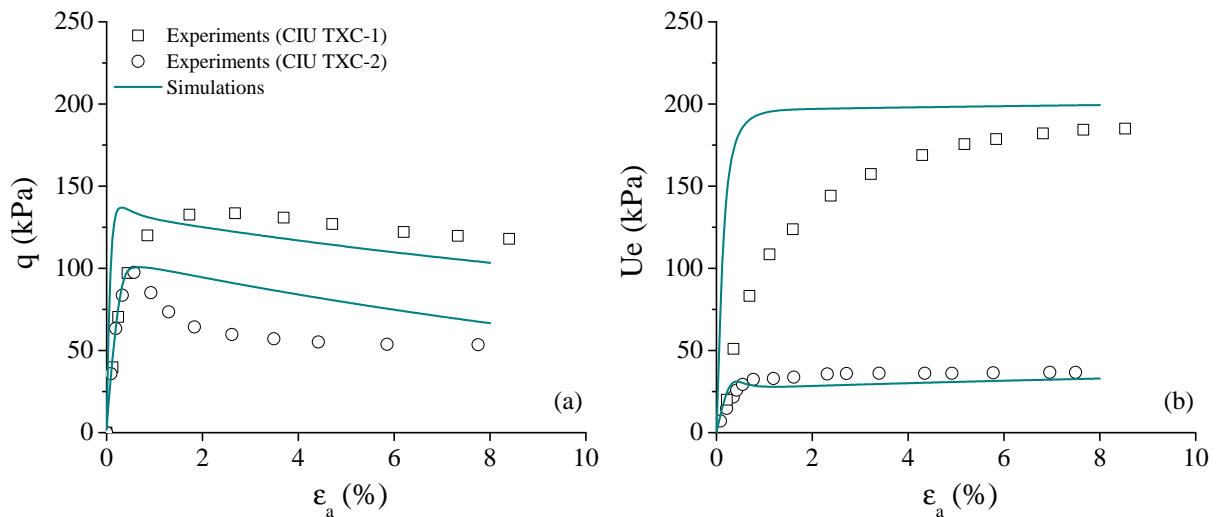


Figure 5.44. Comparison between the experimental observations and model simulations in two CIU TXC tests on the Grande Baleine clay: (a) stress-strain response; (b) strain-pore pressure response

Figure 5.44 and Figure 5.45 show the data from two CIU TXC tests. Note that CIU TXC-1 and CIU TXC-2 reflect the shearing responses of intact and destructured samples, respectively. In general, the model simulations reasonably agree with the observations. Note that in CIU TXC-1, a more rapid decrease of shear stress after peak strength is seen in the experiment. This abrupt drop of strength suggests localized deformation may have occurred, which cannot be captured by the model that is aimed at reproducing stress-strain behavior at the level of stress point. The comparison of the stress-strain curve

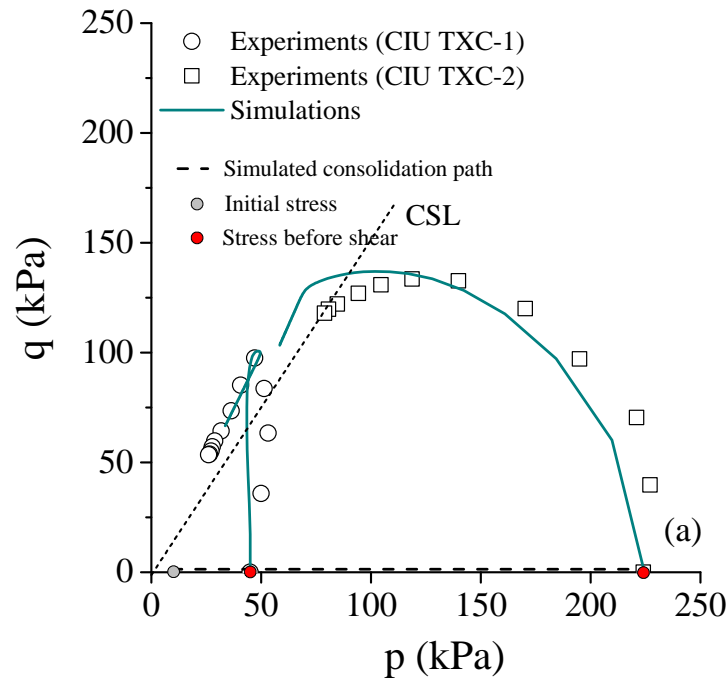


Figure 5.45. Comparison between the experimental observations and model simulations in two CIU TXC tests on the Grande Baleine clay: effective stress path

for the CIU TXC-2 shows that the initial shear stiffness is overestimated by the model, which results in an underestimation of strain levels that correspond to the peak strength. This discrepancy is likely to result from a higher elastic stiffness computed by the model, as indicated by the fact that the computed initial excess pore pressure is higher than that observed. This discrepancy stimulates a revisit of the assumption that the elastic property is independent of soil structure. The elastic stiffness calculated by the employed elasticity model is proportional to mean effective stress p . As a result, the computed elastic stiffness for CIU TXC-2 test is higher than that of CIU TXC-1 test, which can be seen in Figure 5.44, due to the difference in their consolidation stresses. However, experimental data show negligible difference in initial shear stiffness between the two tests

above. This observation suggests that in addition to stress level, the elastic properties may also depend on the structure deterioration. Such a relation was observed by Leroueil et al. (1979) in tests on Saint Alban clay. From a modeling point of view, to reproduce the above dependence, the elasticity model constants (e.g., κ) can be formulated as a function of the internal variable S_b (i.e., the amount of soil structure). A similar strategy has been implemented by Yu et al. (2007b) to model artificially cemented sand.

Figure 5.46 shows the results of an undrained one-way cyclic loading of cyclic shear stress q_{cyc} equal to 73.5 kPa on a sample that was isotropically consolidated to in-situ vertical effective stress ($\sigma_c=45$ kPa). Immediately following the cyclic loading, the sample was subjected to an undrained post-cyclic shearing. The corresponding data and model simulations are included in the figure.

It can be seen that the computed strain development and excess pore pressures build-up reasonably agree with the experimental data. In particular, the magnitude of strain accumulation after 71 cycles is well represented by the simulation. Moreover, the simulation reasonably reproduces the cyclic shakedown in the test, which is reflected by the location of stress-strain curves for 8th, 49th, and 71st cycle. The experimental data show little strain accumulated between the 49th cycle and 71st cycle while around 0.13% permanent strain developed during the same stage in the simulation. The computed shear stiffness in unloading is lower than that observed in the experiment, which may be attributed to the fact that small strain stiffness is not modeled. The model computes more excess pore pressure change for each cycle, which eventually leads to a lower magnitude of pore pressure build-up.

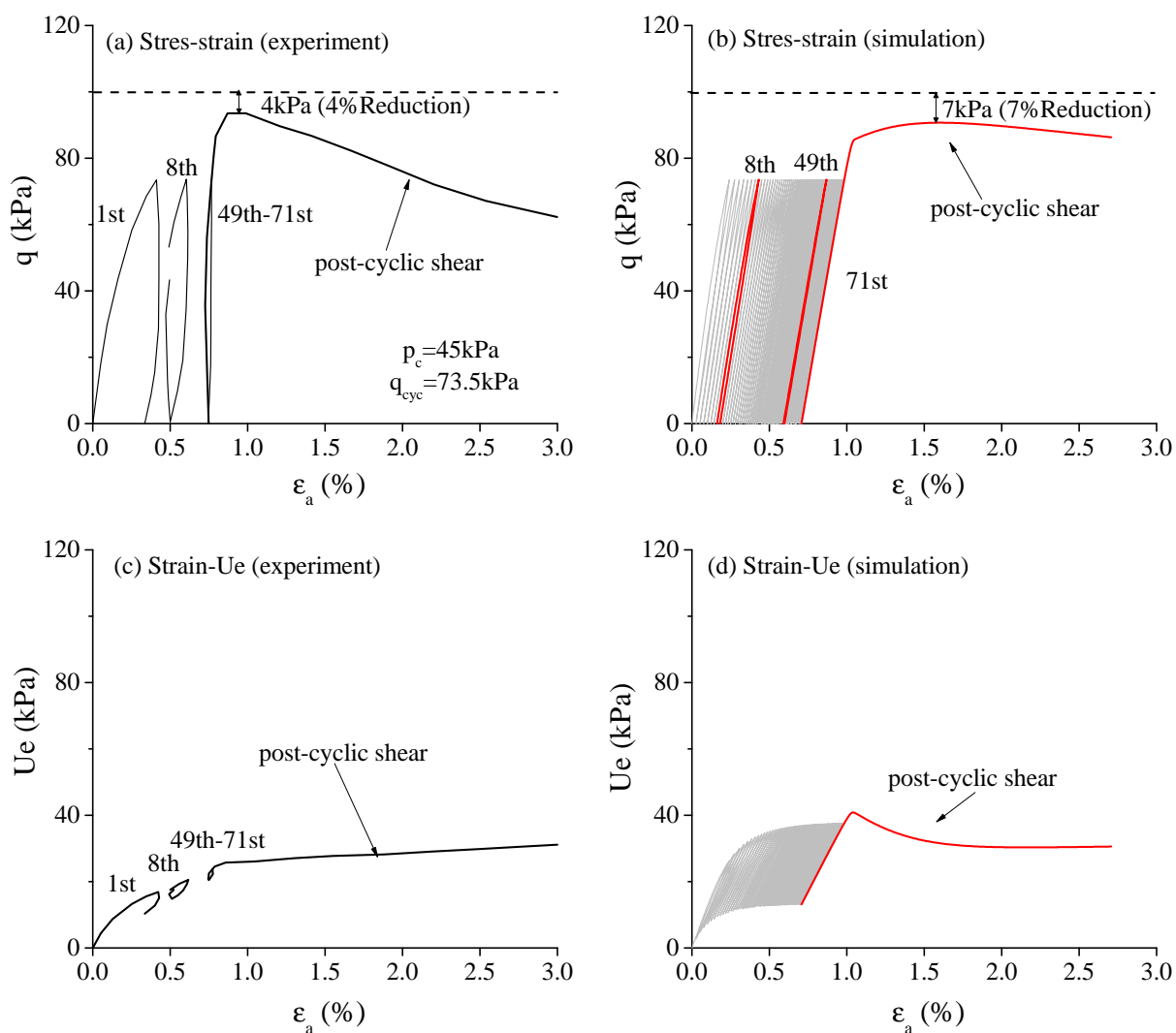


Figure 5.46. Comparison between experimental observations and model simulations in undrained cyclic test and post-cyclic shearing test on the Grande Baleine clay: (a)-(b) stress-strain response ; (c)-(d) strain-pore pressure response

The comparison of post-cyclic shearing response shows that the model accurately predicts the material strength after cyclic loading. Both experimental data and model simulation show that the natural Grande Baleine clay exhibits a negligible strength reduction (i.e., 4% and 7%, respectively) after 71 loading cycles. This insignificant strength

loss is consistent with the fact that only 0.7% axial strain accumulated in the cyclic loading. This correlation between strength reduction and strain accumulation is also reported for other clays (Thiers and Seed, 1969; Andersen et al., 1980). More importantly, this correlation confirms that soil structure degradation is directly related to the irrecoverable deformation of soil, which is one of the fundamental assumptions in formulating the model. Additionally, the strain-softening trend during post-cyclic shearing is captured by the simulation. Similar to the monotonic test, experimental data exhibits stronger brittle behavior than the simulation. The model's prediction of pore pressure response during post-cyclic loading is less successful. The prediction shows that the excess pore pressure starts to decrease after the peak, which is in contrast to a monotonic increase of the excess pore pressure in the experiment. Nevertheless, quantitatively speaking, the predicted amount of pore pressure during post-cyclic loading reasonably agrees with the experimental data.

In summary, the evaluation regarding the experimental evidence of the Grande Baleine clay shows that the proposed model can satisfactorily reproduce material behavior during cyclic loading and post-cyclic shearing based on model parameters primarily determined from monotonic tests. In particular, the available strength after cyclic loading is well reproduced by the model.

5.5.7. Cloverdale Clay

Cloverdale clay is a soft gray marine clay characterized by relatively high liquidity index (i.e., $LI = 1.0$) and sensitivity (i.e., $S_t = 16$ measured by laboratory vane shear). The sensitive nature of Cloverdale clay was probably caused by the surface infiltration (i.e.,

salt leaching) following ground uplift above the sea level (Zergoun, 1991). Zergoun (1991) and Zergoun and Vaid (1994) reported the results of monotonic loading tests, slow triaxial cyclic loading tests, and post-cyclic shearing on undisturbed Cloverdale clay specimens collected through block sampling. To ensure the equalization of pore pressure within specimens, an axial stress rate of 60 kPa per hour were employed in the stress-controlled cyclic loading tests. The reported data are used in the following evaluation regarding the model's capacity to represent both cyclic and post-cyclic clay behavior.

Model Parameters and Initial Conditions

Table 5.16. Model parameters for the Cloverdale clay

A_g	e_g	n_g	$\gamma_{0.7}$	κ	ν	λ	M_c	M_e	N_c	N_e	C	χ
400	2.64	0.635	10E-4	0.027	0.2	0.168	1.31	0.97	0.95	0.90	4	1.72
h_c	h_e	c_d	w	k_i	A	r_c						
105	125	29	5	18	0	0						

The model parameters of the Cloverdale clay are shown in Table 5.16. The parameters λ and κ are calibrated from the virgin compression curve and rebound curve in a 1D compression test on an intact sample, respectively. The Poisson's ratio ν is assumed to be 0.2. The parameter A_g is obtained by fitting the shear stiffness at the initial portion of unloading in an undrained cyclic loading test, which presumably is close to G_0 . The parameters e_g and n_g are assumed to be the same as those for the insensitive BCF clay presented in Chapter 4, as suitable experimental data are not available. The parameters M_c and M_e are calibrated from the effective stress paths in a CIU TXC and a CIU TXE tests on samples that have been isotropically consolidated to pressure more than three times greater than σ'_p , respectively. The parameters N_c , N_e and C are obtained by

fitting the stress path and peak strength in the two undrained tests. The parameter χ is calculated from the analytical solution of equation 4.44. The parameter k_i is obtained by fitting the post-yield compression curve in the 1D compression test. The parameter $A = 0$ is selected to fit the monotonic strain-hardening observed in the two undrained tests, which implies that the destructuration of Cloverdale clay solely results from plastic volume change. The parameter r_c is assumed to be zero. The parameters h_c and h_e are determined by fitting the stress-strain curve of the first cycle of the cyclic loading test, while the parameters c_d and w are calibrated by matching the strain developments and pore pressure accumulations in the same test.

Table 5.17. Initial conditions for the Cloverdale clay simulations

p_0 (kPa)	α	S_b	e_0	p (kPa)	q (kPa)
11	0.48	5.25	1.475	20	0

The initial conditions of the following simulations are presented in Table 5.17. The internal variable S_b is estimated from the 1D compression test. The initial value of α is estimated through equation 4.50 based on the parameter M_c . The variable p_0 is estimated through equation 5.21 based on an estimated maximum past pressure $\sigma'_p = 90$ kPa and a calculated $K_{0,NC}$ value from the parameter M_c . The initial stress $p = 20$ kPa, $q = 0$ kPa is assumed to represent the residual stress of the samples.

Model Simulation

Figure 5.47 shows the experimental observation of the 1D compression test on undisturbed Cloverdale clay and the corresponding model simulation. It can be seen that the

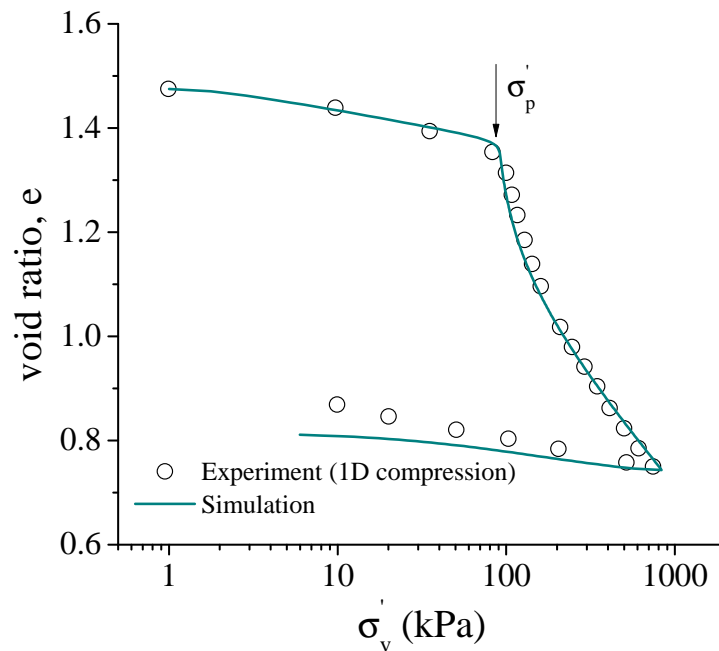


Figure 5.47. Comparison between the experimental observation and model simulation for a 1D compression test on Cloverdale clay

computed compression curve very well reproduces the observed yield stress, greater post-yield compressibility and its decrease due to the destructuration. However, the amount of swelling during unloading is slightly underestimated by the simulation.

Figure 5.48 presents the experimentally observed and computed stress-strain-pore pressure responses in the CIU TXC and CIU TXE tests, in which specimens were isotropically consolidated to $p = 200$ kPa before shearing. A good agreement can be seen between the model simulation and the observed responses.

Figure 5.48 shows the experimental data of the undrained cyclic loading on an isotropically consolidated NC specimen with its corresponding model simulation. Note that the model reasonably reproduces the effective stress path's gradually shifting towards the origin of stress space. Moreover, when the effective stress path is close to the critical state

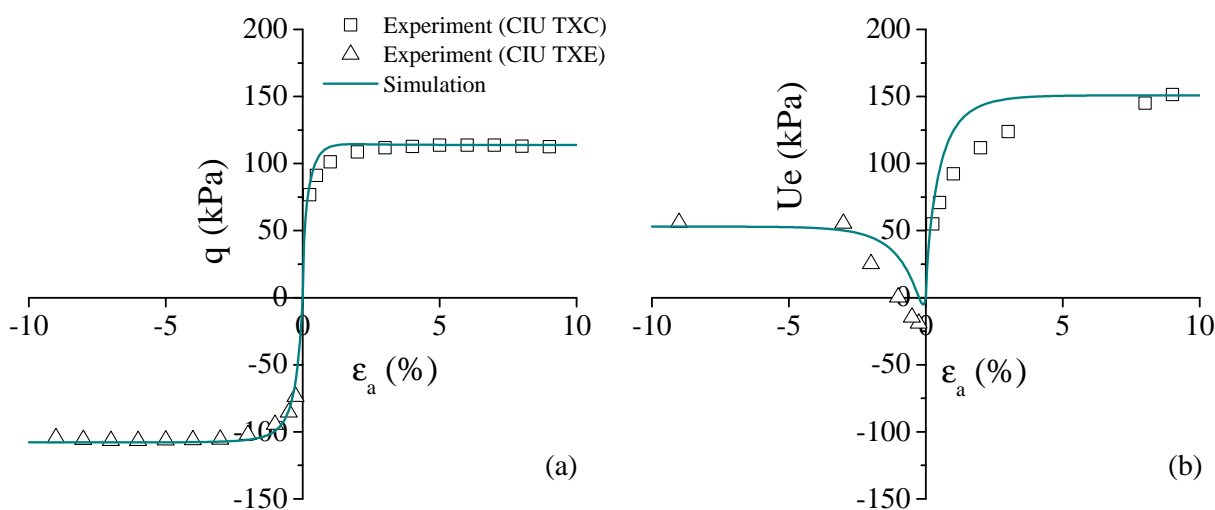


Figure 5.48. Comparison between the experimental observations and model simulations for CIU TXC and CIU TXE tests on NC Cloverdale clay: (a) stress-strain response; (b) strain-pore pressure response

line, the “butterfly” shape loop is formed, as does the experimental observation. However, the computed accumulation rate of pore pressure is higher than that observed in the test. The cyclic softening, indicated by the gradually clockwise rotating and broadening stress-strain loops, are also reasonably represented by the simulation. It can be noted that the computed areas of stress-strain hysteresis in the last several cycles are larger than that observed in the experiment, because the experiment shows an abrupt drop of stiffness once the effective stress path passes the p axis whereas the corresponding model simulation exhibits more smooth stiffness degradation.

Model Prediction

Figure 5.50 compares the experimentally observed and predicted stress-strain-pore pressure responses for CIU TXC and TXE tests on OC Cloverdale clay. It is noteworthy that the samples with different OCR were created by isotropic unloading after samples

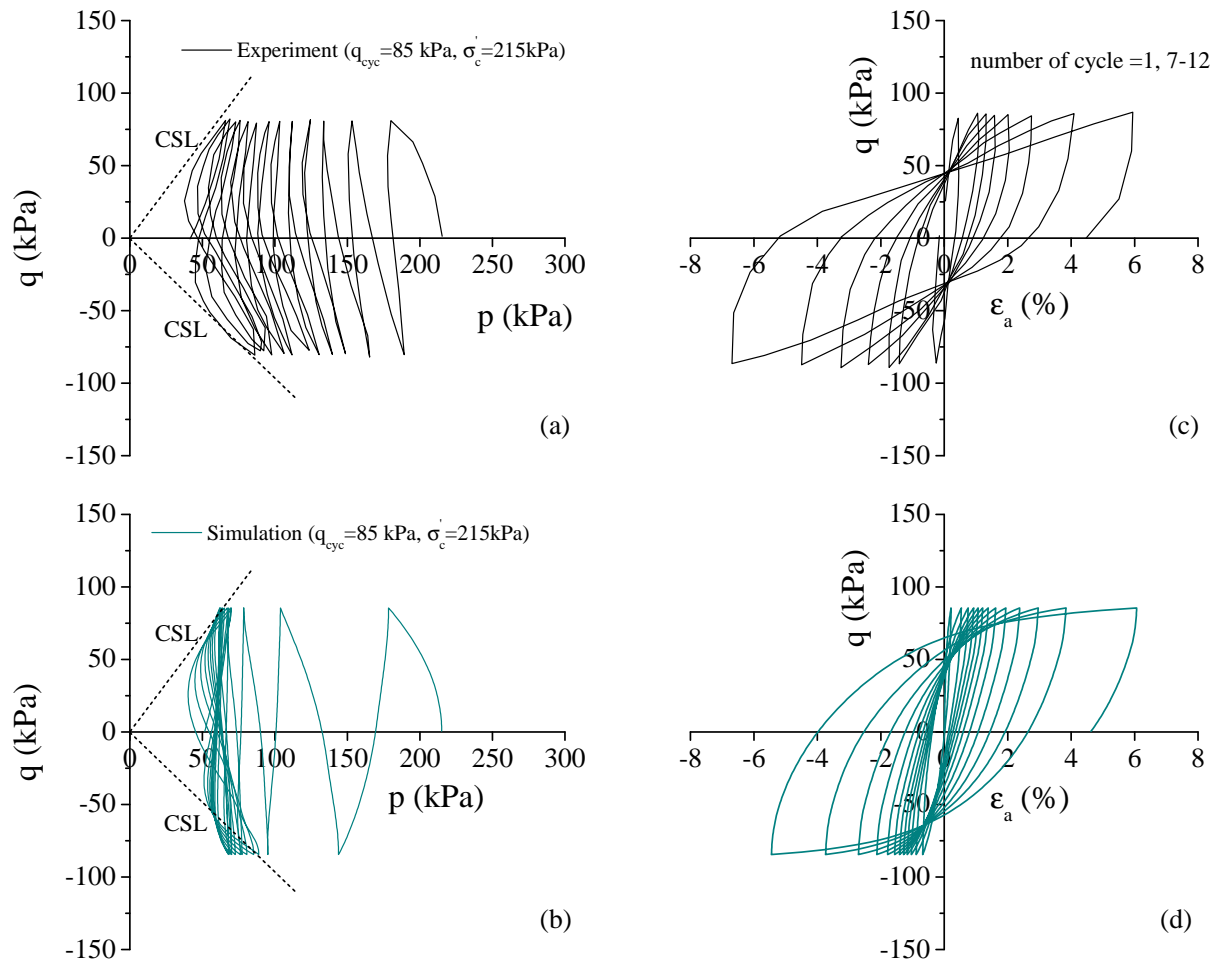


Figure 5.49. Comparison between the experimental observations and model simulations for an undrained cyclic loading test on NC Cloverdale clay: (a)-(b) effective stress path; (c)-(d) stress-strain response

have been isotropically loaded to $p = 200$ kPa. Note that a reasonable agreement is seen between the experimental data and model predictions.

Figure 5.51 and 5.52 present the experimental data regarding the effective stress paths and stress-strain responses in three undrained cyclic loading tests and their corresponding model predictions. In general, the model reasonably predicts the pore pressure accumulation indicated by the migration of effective stress path and the strain developments

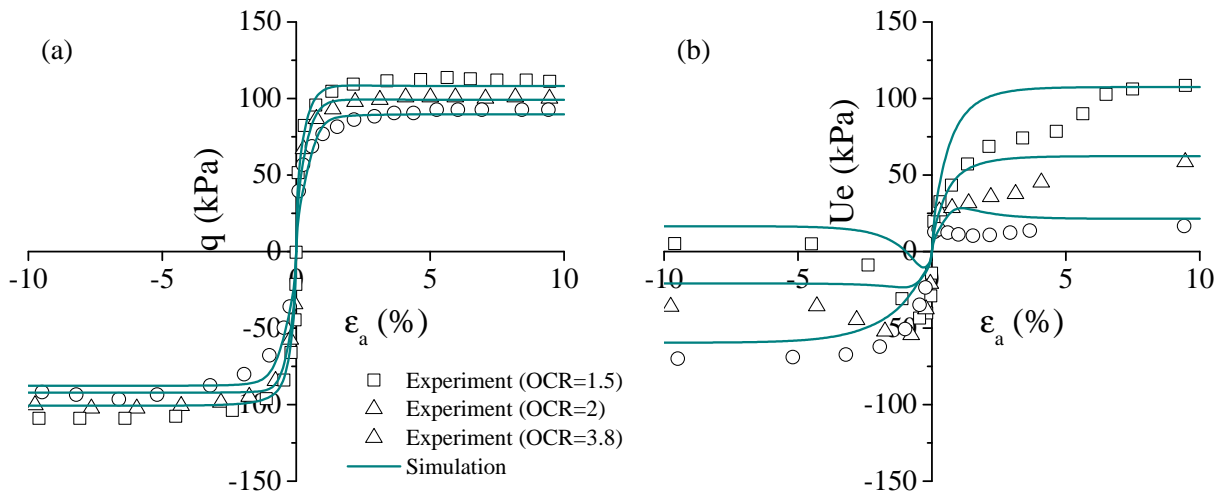


Figure 5.50. Comparison between the experimental observations and model simulations for three CIU TXC and TXE tests on OC Cloverdale clay: (a) effective stress path; (b) stress-strain response

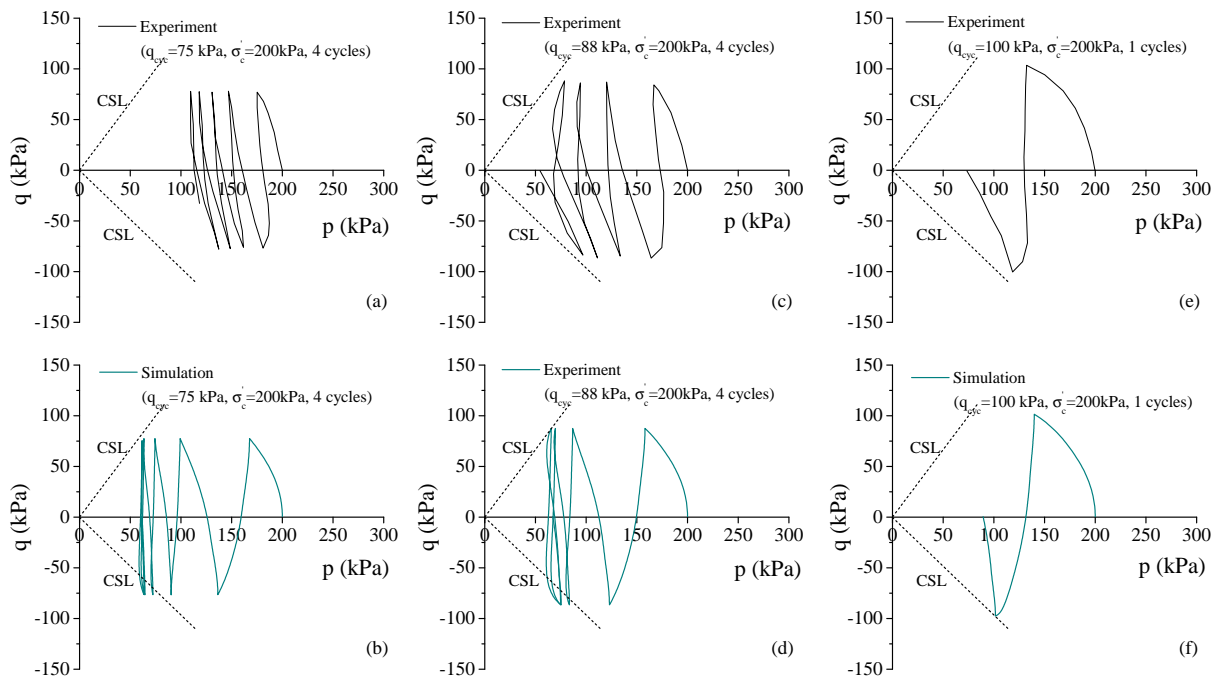


Figure 5.51. Comparison between the experimentally observed and computed effective stress paths for three cyclic loading tests on NC Cloverdale clay: (a)-(b) $q_{cyc} = 75$ kPa; (c)-(d) $q_{cyc} = 88$ kPa; (e)-(f) $q_{cyc} = 100$ kPa

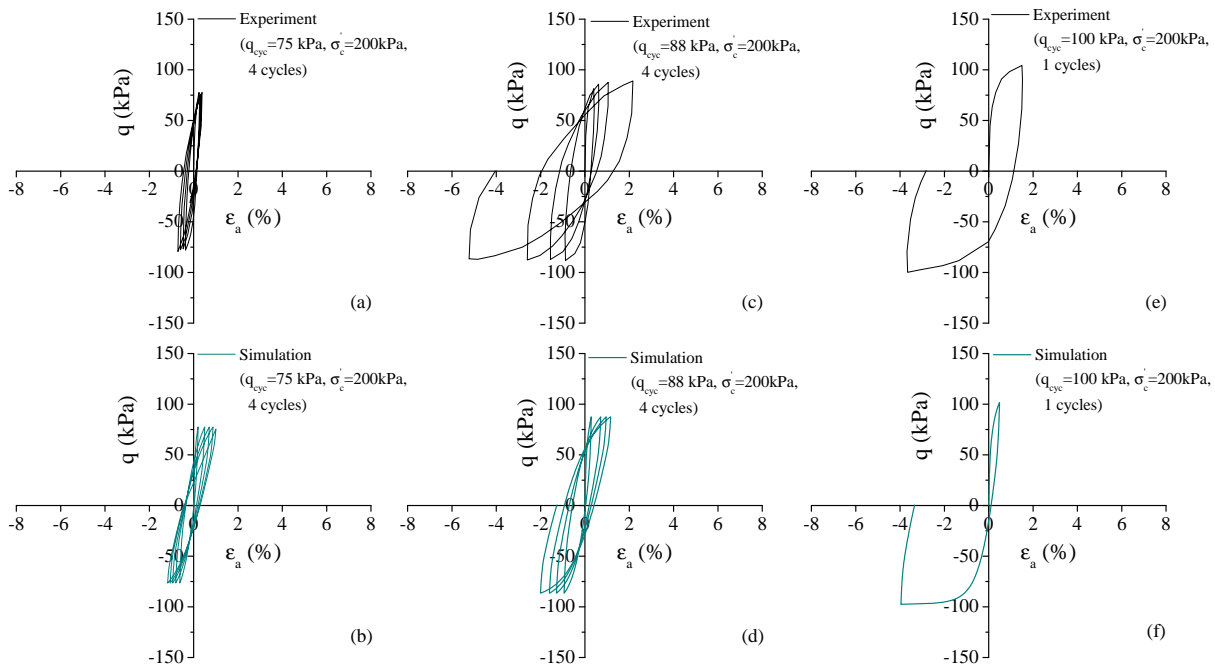


Figure 5.52. Comparison between the experimentally observed and computed stress-strain responses for three cyclic tests on NC Cloverdale clay: (a)-(b) $q_{cyc} = 75$ kPa; (c)-(d) $q_{cyc} = 88$ kPa; (e)-(f) $q_{cyc} = 100$ kPa

during cyclic loading tests characterized by different shear stresses. Note that for the test $q_{cyc} = 75$ kPa, the computed reduction of effective stress at the end of cyclic loading is higher than that observed in the test. For test $q_{cyc} = 88$ kPa, the computed axial strains at the peak cyclic shear stress during the last two cycles are lower than the observed values.

Figure 5.53 compares the experimentally observed pore pressure accumulation with the computed results based on the mixed flow rule and image flow rule. It is clear that the employment of the mixed flow rule considerably improves the simulation of cyclic pore pressure build-up. Note that for the test $q_{cyc} = 75$ kPa, simulations based on both the flow rules overestimate the amount of the pore pressure accumulation. For the test

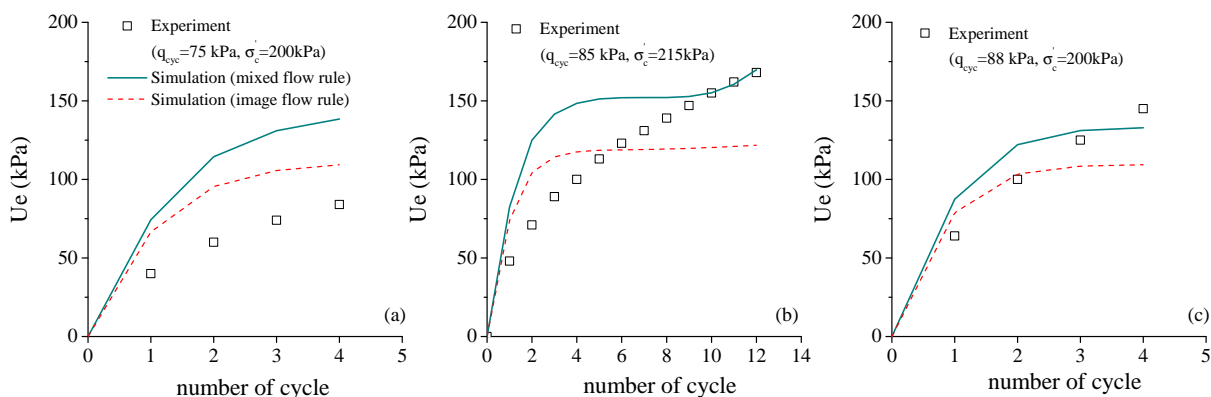


Figure 5.53. Comparison between the experimentally observed and computed pore pressure accumulation for three cyclic loading tests on NC Cloverdale clay: (a) $q_{cyc} = 75$ kPa; (b) $q_{cyc} = 85$ kPa; (c) $q_{cyc} = 88$ kPa

$q_{cyc} = 88$ kPa, the accumulation of pore pressure computed based on the mixed flow rule reaches a plateau after the 5th loading cycle and then starts to increase again after the 9th loading cycle, which corresponds to the acceleration of strain development shown in Figure 5.49. On the other hand, the experiment shows a progressive build-up of pore pressure.

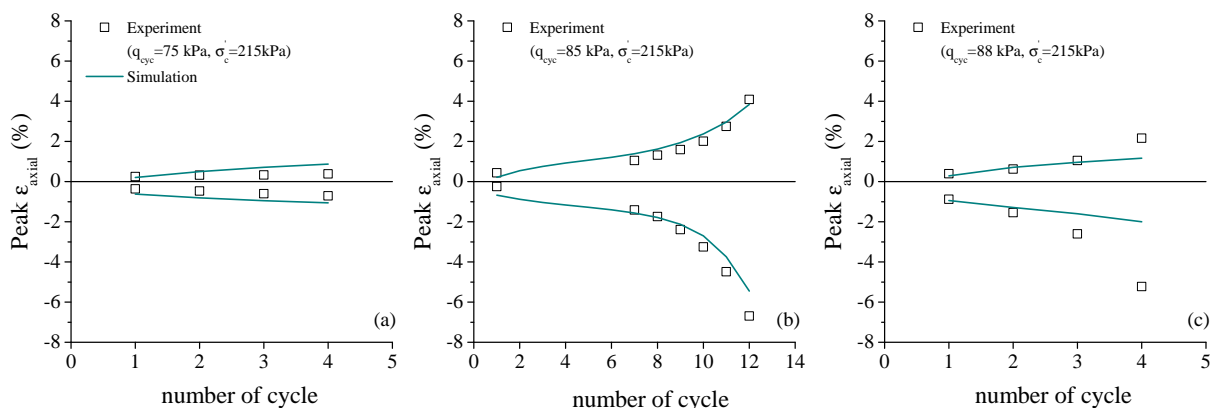


Figure 5.54. Comparison between the experimentally observed and computed strains at the peak cyclic shear stress for three cyclic loading tests on NC Cloverdale clay: (a) $q_{cyc} = 75$ kPa; (b) $q_{cyc} = 85$ kPa; (c) $q_{cyc} = 88$ kPa

Figure 5.54 quantitatively evaluates the model's capacity to reproduce strain development during cyclic loading with varying shear stresses. Note that a reasonable agreement is seen between the computed results and the experimental data.

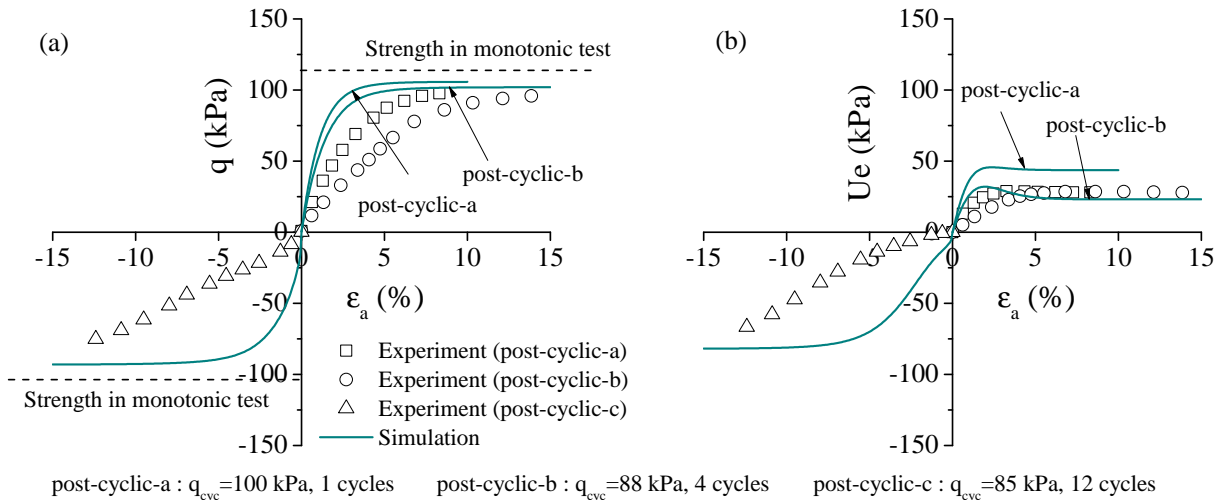


Figure 5.55. Comparison between the experimentally observed and computed stress-strain-pore pressure responses for three post-cyclic shearing on Cloverdale clay: (a) stress-strain response ; (b) strain-pore pressure response

Figure 5.55 presents the experimentally observed and predicted stress-strain-pore pressure responses of post-cyclic shearing after three of the aforementioned cyclic loading tests. Note that the model reasonably predicts the post-cyclic shear strength. Specifically, the maximum difference regarding shear strength in the three cases is 24%. Moreover, while cyclic degradation is observed in all three tests, the amount of strength reduction is not significant, i.e., the maximum strength reduction in experiments and model predictions are 70% and 88%, respectively. Such a moderate degree of strength loss is likely to result from the considerable destructuration during the consolidation before cyclic loading indicated by the compression curve in Figure 5.47. Moreover, the pore pressure build-up

during undrained cyclic loading creates an apparent over-consolidated state and thus the clay samples had a relatively high tendency to dilate during post-cyclic shearing as shown in Figure 5.56. This tendency to dilate and a consequent increase of the effective stress lead to a higher post-cyclic shear strength. This observation emphasizes that an accurate prediction of post-cyclic strength relies on the accurate prediction of cyclic pore pressure accumulation. Figure 5.55 also shows that the shear stiffness during post-cyclic shearing is overestimated by the model. This discrepancy suggests that the employed elasticity model needs improvements so that it can reproduce the stiffness loss of natural clay due to the change of effective stress state and soil structure.

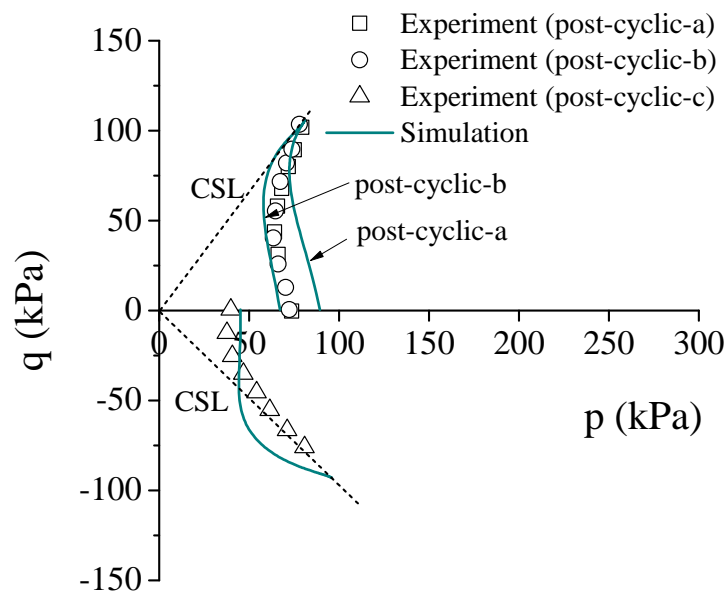


Figure 5.56. Comparison between the experimentally observed and computed effective stress paths for three post-cyclic shearing on Cloverdale clay

5.5.8. BCF Clay With a Sensitivity of 5 to 6

In this section, the capability of the proposed model to capture structure degradation of natural clay during cyclic loading is further evaluated by comparing model simulations with experimental data for BCF clays. Tested samples were collected at 13 m below the ground at the Lynn Ary Park, Anchorage, as discussed in Chapter 3. In contrast to the BCF clay studied in the validation of the basic model, the BCF clay explored in this section is more sensitive. The in-situ field vane tests show the sensitivity of the tested clays is approximately 5 to 6.

Model Parameters and Initial Conditions

Model parameters for the sensitive BCF clay are summarized in Table 5.18. It can be seen that most of the parameters are directly taken from those calibrated on the insensitive BCF clay presented in Chapter 4. Note that the parameters h_c , h_e , c_d and w have been changed based on the observed cyclic response of the sensitive BCF clay. Because cyclic loadings on the insensitive and sensitive BCF clay were characterized by different shear rates (1 cycle per second and 0.5% per hour, respectively), the above adjustments indicate that these parameters may depend on the loading rate. The parameter λ has been changed based on the compression curve during the consolidation portion of the test. The parameters k_i and A are obtained through a trial and error procedure to reproduce the strength degradation in a cyclic loading. The parameter r_c is assumed to be zero.

Table 5.19 shows the initial conditions for the model simulations of the sensitive BCF clay. Because the typical destructuration response is not observed in the 1D consolidation test, the initial value of variable S_b is evaluated by a trial and error procedure to match the observed responses in both consolidation and cyclic loading. The initial value of α is

Table 5.18. Comparison between model parameters for the insensitive and sensitive BCF clay

	Insensitive BCF clay	Sensitive BCF clay
A_g	250	250
e_g	2.64	2.64
n_g	0.635	0.635
γ_{07}	7.00E-04	7.00E-04
κ	0.022	0.022
ν	0.24	0.24
λ	0.08	0.186
M_c	1.27	1.27
M_e	0.92	0.92
N_c	1.22	1.22
N_e	0.8	0.8
C	8	8
χ	1.98	1.98
h_c	400	25
h_e	300	15
c_d	-38	-2
w	10	2
k_i	-	7
A	-	0.95
r_c	-	0

Table 5.19. Initial conditions for the sensitive BCF clay simulations

p_0 (kPa)	α	S_b	e_0	p (kPa)	q (kPa)
40	0.41	3	0.85	21	0

calculated through equation 4.50 based on the parameter M_c . The p_0 value is calculated from the equation 5.21 based on the yield stress $p = 132$ kPa and $q = 112$ kPa observed

in the consolidation portion of the test. The initial stress ($p = 21\text{kPa}$, $q = 0\text{kPa}$) is the measured residual stress.

Model Simulation

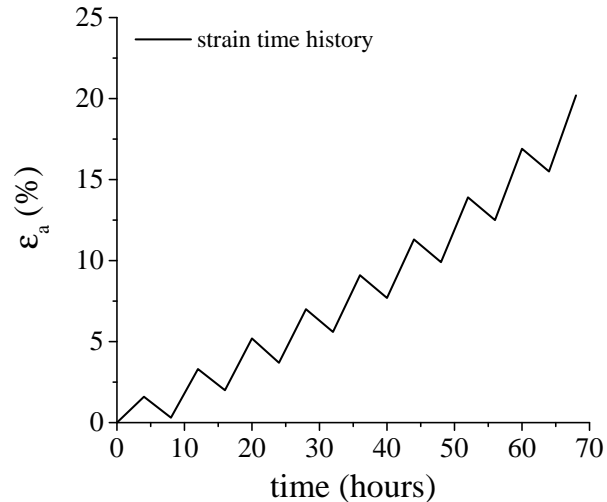


Figure 5.57. Time history of the imposed strain in a strain-controlled cyclic loading test on the BCF clay with $S_t = 5$ to 6

In the experiment, the specimen was first anisotropically reconsolidated from the residual stress to sufficiently high pressure ($p = 249$ and $q = 225$) to create a normally consolidated sample. Once this target stress was reached, samples were subjected to a drained creep period under a constant total stress, which was terminated when the measured creep axial strain rate reduced to $0.0025\%/hr$. During the period of the creep, there was a minor change of the effective stress, from ($p = 249$, $q = 225$) to ($p = 264$, $q = 229$), primarily due to the dissipation of the excess pore pressure generated during the reconsolidation. After the reconsolidation and creep, a prescribed cyclic strain path (Figure 5.57) was applied, which was a reproduction of the strain history experienced by a sample under a stress-controlled cyclic loading of $CSR=0.3$. The strain-controlled cyclic loading

is preferred for the investigation of cyclic degradation, as in stress-controlled cyclic tests, a sample will tend to collapse once material strength is less than the applied cyclic shear stress. In the simulation, a stress path from $(p = 21, q = 0)$ to $(p = 264, q = 229)$ is employed as a simplification of actual reconsolidation stress path. Then, the cyclic strain path shown in Figure 5.57 is reproduced in the simulation.

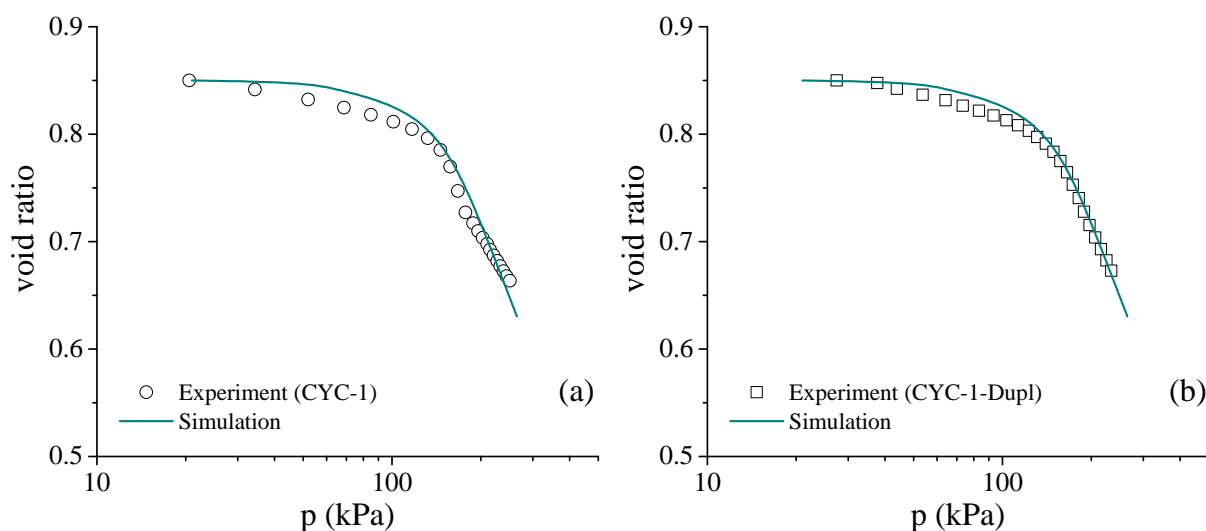


Figure 5.58. Comparison between the experimental observation and model simulation for the anisotropic consolidation on the BCF clay with $S_t = 5$ to 6: (a) CYC-1 test; (b) CYC-1-Dupl test

Figure 5.58 (a) shows the observed and computed BCF clay compression response in the reconsolidation stage. It can be seen that the simulation satisfactorily reproduces the experimental observations. However, the experimental data indicate that the tested sample experienced a rapid destructuration after yielding, which is followed by a stable compression, i.e., the slope of the compression curve is relatively constant. In contrast, the destructuration in the simulation is slower, and the compressibility at the end of the reconsolidation is higher than that in the experiment. To study the reason of the above

difference, Figure 5.58 (b) compares the same model simulation with the reconsolidation data of a duplicated test on a specimen that is obtained from the same tube as the previous sample. In this comparison, it is clear that the simulation well reproduces the behavior in the post-yield stage in the experiment. Therefore, the aforementioned discrepancy is more likely to be accidental instead of a systematic issue.

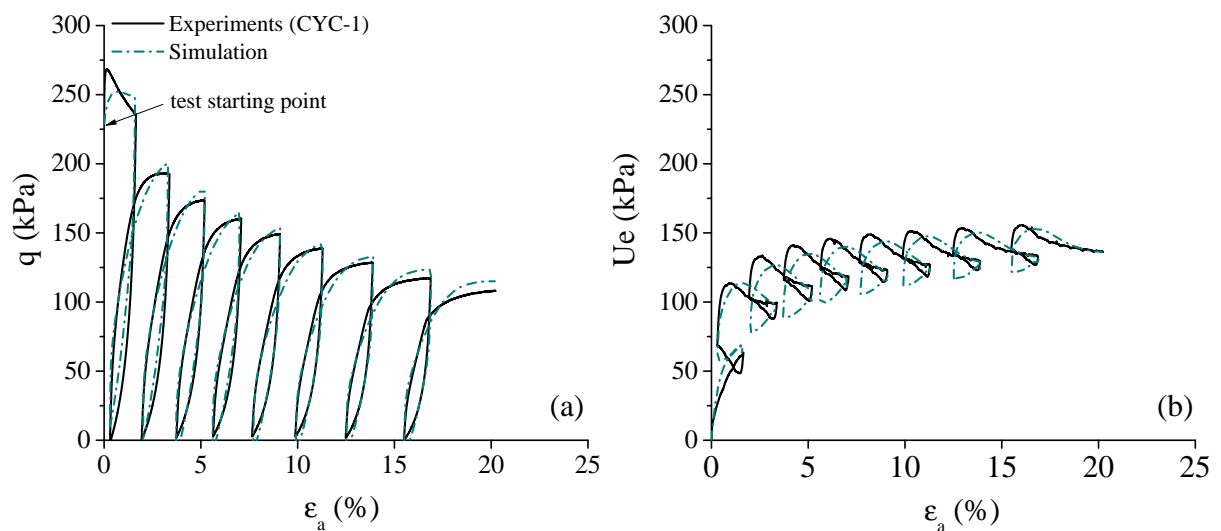


Figure 5.59. Comparison between the experimental observation and model simulation for a strain-controlled cyclic loading test on the BCF clay with $S_t = 5$ to 6: (a) stress-strain response; (b) strain-pore pressure response

Figure 5.59 shows the simulated and observed stress-strain-pore pressure response from the cyclic loading test. It can be seen that material strength significantly degrades during the cyclic loading, i.e., more than 50% of strength lost after eight loading cycles. This considerable strength loss is closely related to the high amount of strain accumulated in the cyclic loading (i.e., 20%). Note that the simulation reproduces this gradual reduction of material strength. A progressive decrease of material stiffness, which is reflected by the decreasing stress-strain curve slope, is observed in both the experiment and simulation.

Nevertheless, the degree of stiffness reduction is not remarkable. The comparison of pore pressure response in Figure 5.59(b) shows that the model both qualitatively and quantitatively reproduces the progressive excess pore pressure build up in cyclic loading. It is noted that the model simulation does not capture the peak strength value in the first cycle, but underestimates it by around 5%. This difference is probably due to the fact that the tested sample was subjected to drained creep before the cyclic loading, which may increase apparent preconsolidation stress and create secondary soil structure. All these changes can contribute to a slightly higher material strength. Since the proposed model is time-independent, the above factors are not represented in the simulated results.

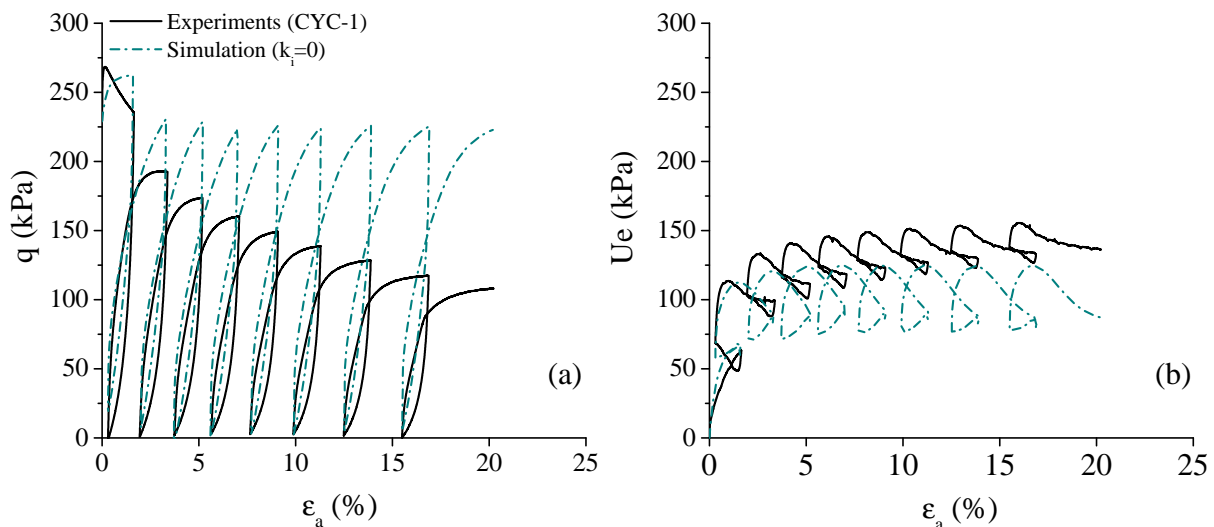


Figure 5.60. Comparison between the experimental observation and model simulation (no destructuration) for a strain-controlled cyclic loading on the BCF clay with $S_t = 5$ to 6: (a) stress-strain response; (b) strain-pore pressure response

To illustrate the role of the destructuration, Figure 5.60 shows the simulation of the same cyclic test but under the condition of $k_i = 0$, which implies the soil structure

degradation is deactivated. Compared with the experimental data, the simulation significantly underestimates the strength reduction in cyclic loading. The computed excess pore pressure stops accumulating after the first two cycles, which eventually leads to a lower magnitude of pore pressure build-up. The above observation signifies that ignoring the destructuration of natural clay can result in an unsafe assessment of the available material strength and excess pore pressure in cyclic loading, which leads to an unconservative evaluation of the stability of geotechnical facilities during and after cyclic loading.

5.5.9. Summary of Model Parameters for Different Structured Clays

Table 5.20 summarizes model parameters for the natural clays studied in the model verification. The minimum, maximum, and averaged values of parameters are also included. For most of the seven clays, the experimental data suitable to calibrate the Poisson's ratio ν are not available and consequently $\nu = 0.2$ is assumed. The model performance presented in the previous sections shows that $\nu = 0.2$ is a reasonable assumption when more accurate calibration is absent. It can be seen that the variation of parameter χ between different clays is limited, which indicates the possibility to make the parameter χ a constant in the model that is independent of clay type. Moreover, among all parameters, h_c and h_e have the largest variations. As discussed in section 4.4, to efficiently and more objectively calibrate these two parameters, parameters optimization techniques are recommended. Among the eight clays, cyclic experimental data are available only for the Grande Baleine clay, the Cloverdale clay and the BCF clay. For other five clays, the parameter w and c_d , which control the cyclic pore pressure and strains accumulation, respectively, take their default values (i.e., $w = 1$ and $c_d = 0$). So the variation of parameter

w and c_d between different soils cannot be evaluated in this work. Nevertheless, it can be seen that the default value $w = 1$ is a reasonable estimation for most of the available tests.

The parameters shown in Table 5.20 are calibrated based on the responses of a relatively wide range of natural clays. Consequently, from a model use point of view, the averaged value of parameters shown in Table 5.20 can serve as a first guess if the relevant experimental observations are not available. Furthermore, the range of each parameter shown in Table 5.20 can be treated as a guideline to check whether selected model parameters are reasonable.

Table 5.20. Summary of model parameters for different structured clays

Soil Name	κ	ν	λ	M_c	M_e/M_c	N_c	N_e/N_c	C	χ	h_c	h_e	w^*	c_d^*	k_i	A	r_c
Norrköping clay	0.047	0.2	0.35	1.6	0.88	1.15	0.96	10	1.73	25	25	1	0	16	0.9	0
Vallericca Clay	0.018	0.2	0.147	1.05	0.74	1.1	0.91	4	1.63	50	50	1	0	20	0.5	0.0
Bothkennar Clay	0.03	0.2	0.255	1.4	.74	1.3	0.77	10	1.74	500	500	1	0	10	0.4	0.17
Shanghai Clay	0.03	0.2	0.210	1.37	0.66	1.2	0.83	6	1.73	100	100	1	0	8	0.3	0.0
Wuzhou Clay	0.03	0.2	0.275	1.23	0.71	1.2	0.92	10	1.73	100	100	1	0	12	0.75	0.0
Grande Baleine Clay	0.007	0.2	0.136	1.49	0.67	1	1	12	1.73	200	550	1	-250	20	0.1	0.135
Cloverdale Clay	0.027	0.2	0.168	1.31	0.74	0.95	0.95	4	1.72	105	125	5	29	18	0	0
BCF Clay	0.022	0.24	0.186	1.27	0.72	1.22	0.66	8	1.98	30	25	2	-2	7	0.95	0
Minimum value	0.007	0.2	0.136	1.05	0.66	0.95	0.66	4	1.63	25	25	-	-	7	0	0
Maximum value	0.047	0.24	0.35	1.6	0.88	1.3	1	12	1.98	500	550	-	-	20	0.95	0.2
Averaged value	0.026	0.21	0.216	1.34	0.73	1.2	1	9	1.75	139	185	-	-	14	0.55	0.04

Note: * Minimum, maximum and averaged values are not provided, as the default values are used in most of cases.

5.6. Summary and Conclusions

This chapter presents the extension of the basic model presented in Chapter 4 to reproduce the effects of soil structure and its deterioration. In particular, the concept of structure surface and intrinsic surface are introduced, which govern the response of natural clay and its corresponding reconstituted state, respectively. A new internal variable S_b that represents the amount of soil structure and a destructuration law that quantifies the monotonic decrease of S_b under irrecoverable deformation are discussed. The proposed plastic potential surface in the extended model is a function of fabric anisotropy (internal variable α) and inter-particle bonds (internal variable p_t). The influences of these two aspects of soil structure on material plastic flow are explored based on the stress-dilatancy relation which is derived from the plastic potential surface. The appropriateness of this plastic potential surface to describe natural clay behavior is validated with experimental evidence. Finally, this chapter shows the validation of the extended model based on experimental data of eight natural clays. The main conclusions drawn from this chapter are:

- (1) The fabric anisotropy and inter-particle bonds can significantly affect plastic flow.

The change in fabric induced by the anisotropic loading tends to increase the plastic volume change. Moreover, when fabric anisotropy exists, after yielding the increase of isotropic stress in the absence of deviatoric stress can cause not only compression but also distortion, and purely compressive, non-distortional plastic deformation can occur for non-isotropic stress state. On the other hand, an increase in the inter-particle bonds exacerbates soil's plastic contraction and delays the occurrence of phase transformation as well as the plastic dilatancy. Moreover,

the influence of inter-particle bonds is dependent on confining stress, and the increase in confining stress level will weaken the effects of inter-particle bonds on the plastic flow. Careful examinations of stress-dilatancy relations derived from the proposed plastic potential with experimental evidence on structured soil prove the appropriateness of this plastic potential.

- (2) The versatility of the extended model has been validated with experimental observations on different natural clays that have a relatively wide range of index properties. The versatility, generality, and predictability of the model are emphasized by the fact that with a single set of parameters, the model can adequately represent material behavior under different stress histories, drainage conditions, and loading paths (i.e., compression v.s. shearing, monotonic v.s. cyclic). The model parameters can be determined based on conventional experiments in a relatively straightforward way. If one is only interested in the monotonic behavior of natural clay, compression tests (1D or isotropic), CK_0 TXC and CK_0 TXE tests on NC and OC samples are sufficient to define model parameters. If cyclic behavior is considered, then additional stress or strain controlled cyclic test is needed. The proposed analytical solutions provide reasonable estimations of the initial values of model internal variables.
- (3) Experimental data in cyclic loading tests on Grande Baleine clay and BCF clay show strength reduction of natural clay during cyclic loading is strongly correlated with the permanent strains developed. The model successfully captures this feature. Modeling of cyclic loading of BCF clay shows that ignoring de-structuration, in conditions where the cyclic loading results in significant plastic

strains, can lead to a significant underestimation of strength degradation and excess pore pressure build-up, which results in an unsafe assessment of the stability of geotechnical facilities in and after cyclic loadings.

CHAPTER 6

MODEL GENERALIZATION AND IMPLEMENTATION

6.1. Introduction

For the purpose of testing the proposed model with experimental observations and further using this model in the analysis of geotechnical boundary value problems, the model implementation is a necessary and important step. This chapter has been focused on the implementation of the proposed model and its associated stress integration strategy.

To facilitate the model implementation in 3D finite element codes, the generalization of the proposed model from triaxial space to multiaxial space is first introduced. The proposed model is implemented via an explicit stress integration method, namely Runge-Kutta-Fehlberg method. The specific stress integration algorithm is presented in this chapter.

Stress states in the laboratory tests are usually in triaxial condition. Also, constitutive model formulations in triaxial space are relatively simple and therefore easier to implement. To validate the proposed model with the experimental stress-strain response, the model is first implemented into a triaxial space constitutive driver in MATLAB, which can integrate stress-strain responses under mixed-control conditions (e.g., stress-controlled oedometer test). This driver will also provide benchmarks to validate further implementation of the model into 3D finite element code. The novelty of this driver is that it can handle constitutive models with an elastoplastic modulus that depends on strain rate. Detailed formulation of this driver is also presented in this chapter.

Lastly, model implementation into a general 3D finite element code, ABAQUS, is discussed, in which a single element test has been used to validate the implementation.

6.2. Model Generalization in Multiaxial Space

This section discusses the generalization of the bounding surface, plastic potential surface, plastic flow rule, internal variables hardening rule, plastic modulus as well as the projection center evolution rule. Benz (2007) has well documented the generalization of the small strain elasticity model. This will not be repeated herein. The only point worth noting is that the scalar-natured strain history variable $\bar{\gamma}_{hist}$ in the elasticity model is replaced by a tensor-natured variable $\boldsymbol{\varepsilon}_{hist}$ in multiaxial stress space. Besides, as the bounding surface and plastic potential surface in the proposed model are similar to the surfaces in SANICLAY model (Dafalias et al., 2006), the expressions of derivatives of surfaces in multiaxial space presented by Dafalias et al. (2006) are included in this work.

Model generalization is performed based on the following relations between tensor variables and their counterpart invariant scalars. First, deviatoric stress tensor \boldsymbol{s} is related to scalar q through:

$$[(3/2)\boldsymbol{s} : \boldsymbol{s}]^{1/2} = q \quad (6.1)$$

where bold symbol indicates tensor and the symbol $:$ implies the double dot production between two tensors, i.e., $\boldsymbol{A} : \boldsymbol{B} = A_{ij}B_{ij}$, with Einstein summation convention being applied. Deviatoric stress tensor is defined as:

$$\boldsymbol{s} = \boldsymbol{\sigma} - p\boldsymbol{I} \quad (6.2)$$

with \boldsymbol{I} being identity tensor. Along the same line, fabric tensor $\boldsymbol{\alpha}$ is introduced as the multiaxial counterpart of scalar α in the triaxial space formulations:

$$[(3/2)\boldsymbol{\alpha} : \boldsymbol{\alpha}]^{1/2} = \alpha \quad (6.3)$$

6.2.1. Structure Surface, Plastic Potential Surface and Plastic Flow Rule

In multiaxial space, the bounding surface (i.e., structure surface) is expressed as:

$$F_s = \frac{3}{2}(\bar{\mathbf{s}} - \bar{p}^* \boldsymbol{\alpha}) : (\bar{\mathbf{s}} - \bar{p}^* \boldsymbol{\alpha}) - (N^2 - \frac{3}{2} \boldsymbol{\alpha} : \boldsymbol{\alpha}) \bar{p}^* (p_{s0}^* - \bar{p}^*) \quad (6.4)$$

where $\bar{\mathbf{s}}$ is the image deviatoric stress tensor, given by:

$$\bar{\mathbf{s}} = \bar{\boldsymbol{\sigma}} - \bar{p} \mathbf{I} \quad (6.5)$$

Similar to equation 4.3, the image stress tensor is related to current stress tensor through a similarity ratio b and projection center tensor $\boldsymbol{\sigma}_c$:

$$\bar{\boldsymbol{\sigma}} = \boldsymbol{\sigma}_c + b(\boldsymbol{\sigma} - \boldsymbol{\sigma}_c) \quad (6.6)$$

In multiaxial space, the parameter N will be interpolated between N_c and N_e by means of the Lode angle $\bar{\theta}$ of deviatoric stress $\bar{\mathbf{s}} - \bar{p}^* \boldsymbol{\alpha}$. The definition of $\bar{\theta}$ and the shape of bounding surface are illustrated in Figure 6.1. The interpolation proposition by Argyris et al. (1974) is adopted in this work, which, with $c_N = N_e/N_c$, reads as:

$$N = \Theta(\bar{\theta}, c_N) N_c = \frac{2c_N}{(1 + c_N) - (1 - c_N) \cos 3\bar{\theta}} N_c \quad (6.7)$$

$$\cos 3\bar{\theta} = \sqrt{6} \text{tr} \bar{\mathbf{n}}^3; \quad \bar{\mathbf{n}} = \frac{\bar{\mathbf{s}} - \bar{p}^* \boldsymbol{\alpha}}{\|\bar{\mathbf{s}} - \bar{p}^* \boldsymbol{\alpha}\|}$$

The bracket ' $\|\dots\|$ ' denotes the Eulerian norm of a tensor, i.e., $\|\mathbf{A}\| = \sqrt{\mathbf{A} : \mathbf{A}}$. $\bar{\mathbf{n}}$ represents the unit tensor in deviatoric plane pointing from $\boldsymbol{\alpha}$ axis to the image stress point, as shown in Figure 6.1. The component form of $\bar{\mathbf{n}}^3$ is given as $\bar{n}_{ij} \bar{n}_{jk} \bar{n}_{kl}$, and $\text{tr}()$ represents the trace of a tensor.

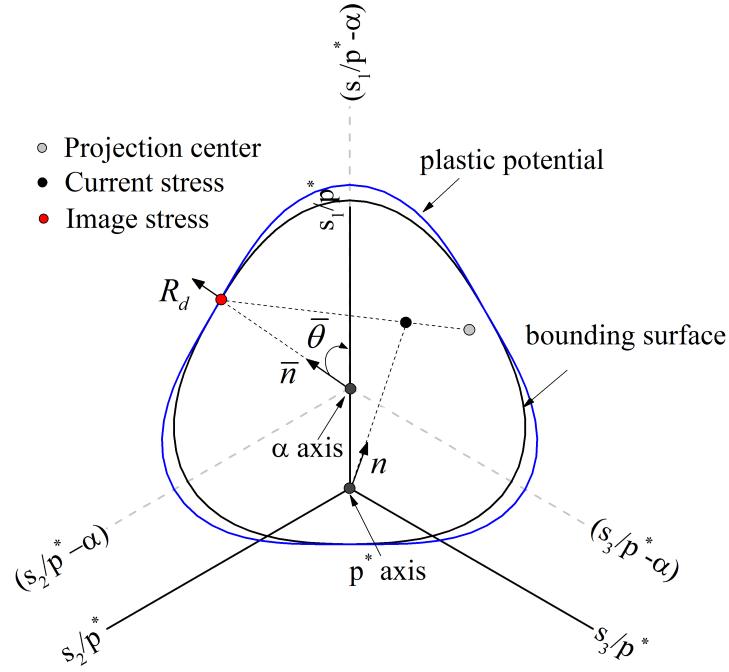


Figure 6.1. Schematic illustration of the dependence of parameters N , M and h on the Lode angle of $\bar{s} - \bar{p}^* \alpha$

Based on the bounding surface, the loading direction \mathbf{L} in multiaxial space is defined as:

$$\mathbf{L} = \frac{\partial F_s}{\partial \bar{\boldsymbol{\sigma}}} = \mathbf{L}_d + \frac{1}{3} L_v \mathbf{I} \quad (6.8)$$

with L_v and \mathbf{L}_d being given by:

$$\begin{aligned} L_v &= \text{tr} \left(\frac{\partial F_s}{\partial \bar{\boldsymbol{\sigma}}} \right) \\ &= \bar{p}^* (N^2 - \frac{3}{2} \bar{\mathbf{r}}^* : \bar{\mathbf{r}}^*) + 3 \left(\frac{\partial F_s}{\partial \theta} \right) \frac{\text{tr}(\bar{\mathbf{n}}^2 \alpha) - \text{tr} \bar{\mathbf{n}}^3 \text{tr}(\bar{\mathbf{n}} \alpha)}{\sqrt{3/2(1 - 6 \text{tr}^2 \bar{\mathbf{n}}^3)} \|\bar{s} - \bar{p}^* \alpha\|} \\ \mathbf{L}_d &= 3(\bar{s} - \bar{p}^* \alpha) + \sqrt{6} \left(\frac{\partial F_s}{\partial \theta} \right) \frac{(\text{tr} \bar{\mathbf{n}}^3) \bar{\mathbf{n}} - \bar{\mathbf{n}}^2}{\|\bar{s} - \bar{p}^* \alpha\| \sqrt{1 - 6 \text{tr}^2 \bar{\mathbf{n}}^3}} \end{aligned} \quad (6.9)$$

with $\bar{\mathbf{r}}^*$ being the image stress ratio in multiaxial space, i.e., $\bar{\mathbf{r}}^* = \bar{\mathbf{s}}/\bar{p}^*$ and

$$\frac{\partial F_s}{\partial \bar{\theta}} = 6N^2 \bar{p}^* (p_{s0}^* - \bar{p}^*) \left(\frac{1 - c_N}{2c_N} \right) \Theta(\bar{\theta}, c_N) \sin 3\bar{\theta} \quad (6.10)$$

The plastic potential surface in multiaxial space is expressed as:

$$g_s = \frac{3}{2} (\mathbf{s} - p^* \boldsymbol{\alpha}) : (\mathbf{s} - p^* \boldsymbol{\alpha}) - (M^2 - \frac{3}{2} \boldsymbol{\alpha} : \boldsymbol{\alpha}) p^* (p_a - p^*) \quad (6.11)$$

where parameter M also varies based on the same interpolation function in equation 6.7,

i.e.,

$$M = \Theta(\bar{\theta}, c_N) M_c = \frac{2c_M}{(1 + c_M) - (1 - c_M) \cos 3\bar{\theta}} M_c \quad (6.12)$$

with $c_M = M_e/M_c$.

The generalized plastic flow direction is given by:

$$\mathbf{R} = \mathbf{R}_d + \frac{1}{3} R_v \mathbf{I}; \quad (6.13)$$

\mathbf{R}_d , based on equation 4.8, is the deviatoric component of image stress flow direction, as shown in Figure 6.1:

$$\mathbf{R}_d = \frac{\partial g_s}{\partial \bar{\boldsymbol{\sigma}}} - \frac{1}{3} \text{tr} \left(\frac{\partial g_s}{\partial \bar{\boldsymbol{\sigma}}} \right) \mathbf{I} = 3(\bar{\mathbf{s}} - \bar{p}^* \boldsymbol{\alpha}) + \sqrt{6} \left(\frac{\partial g_s}{\partial \bar{\theta}} \right) \frac{(\text{tr} \bar{\mathbf{n}}^3) \bar{\mathbf{n}} - \bar{\mathbf{n}}^2}{\|\bar{\mathbf{s}} - \bar{p}^* \boldsymbol{\alpha}\| \sqrt{1 - 6 \text{tr}^2 \bar{\mathbf{n}}^3}} \quad (6.14)$$

where:

$$\frac{\partial g_s}{\partial \bar{\theta}} = 6M^2 \bar{p}^* (p_a - \bar{p}^*) \left(\frac{1 - c_M}{2c_M} \right) \Theta(\bar{\theta}, c_M) \sin 3\bar{\theta} \quad (6.15)$$

As discussed before, the volumetric component of plastic flow R_v combines the those from the current stress flow rule and image stress flow rule:

$$R_v = R_v^i g_i + R_v^c (1 - g_i) \quad (6.16)$$

And R_v^i in multiaxial space is given by:

$$R_v^i = tr\left(\frac{\partial g_s}{\partial \bar{\boldsymbol{\sigma}}}\right) = \bar{p}^* (M^2 - \frac{3}{2} \bar{\mathbf{r}}^* : \bar{\mathbf{r}}^*) + 3 \left(\frac{\partial g_s}{\partial \bar{\theta}}\right) \frac{tr(\bar{\mathbf{n}}^2 \boldsymbol{\alpha}) - tr \bar{\mathbf{n}}^3 tr(\bar{\mathbf{n}} \boldsymbol{\alpha})}{\sqrt{(3/2)(1 - 6tr^2 \bar{\mathbf{n}}^3)} \|\bar{\mathbf{s}} - \bar{p}^* \boldsymbol{\alpha}\|} \quad (6.17)$$

Similarly, R_v^c in multiaxial space can be expressed as:

$$R_v^c = p^* (M^2 - \frac{3}{2} s_l \mathbf{r}^* : \mathbf{r}^*) + 3b \left(\frac{\partial g_s}{\partial \bar{\theta}}\right) \frac{tr(\bar{\mathbf{n}}^2 \boldsymbol{\alpha}) - tr \bar{\mathbf{n}}^3 tr(\bar{\mathbf{n}} \boldsymbol{\alpha})}{\sqrt{(3/2)(1 - 6tr^2 \bar{\mathbf{n}}^3)} \|\bar{\mathbf{s}} - \bar{p}^* \boldsymbol{\alpha}\|} \quad (6.18)$$

with term $\partial g_s / \partial \bar{\theta}$ is rewritten as:

$$\frac{\partial g_s}{\partial \bar{\theta}} = 6M^2 p^* (p_a - p^*) \left(\frac{1 - c_M}{2c_M}\right) \Theta(\bar{\theta}, c_M) \sin 3\bar{\theta} \quad (6.19)$$

to reflect the nature of current stress dependence. The terms with “-” is due to the assumption that the value of M is solely determined by the location of image stress in deviatoric plane, even for the case that plastic flow direction is defined through current stress. Similarity ratio b is introduced as a result of $\partial \bar{\boldsymbol{\sigma}} / \partial \boldsymbol{\sigma}$ in the chain rule expansion $\partial \bar{\theta} / \partial \boldsymbol{\sigma} = (\partial \bar{\theta} / \partial \bar{\boldsymbol{\sigma}})(\partial \bar{\boldsymbol{\sigma}} / \partial \boldsymbol{\sigma})$.

In multiaxial space, the rule to define variable s_l is generalized as:

$$s_l = \begin{cases} 1 & \text{if } \mathbf{n}\bar{\mathbf{n}} \geq 0 \\ -1 & \text{if } \mathbf{n}\bar{\mathbf{n}} < 0 \end{cases} \quad (6.20)$$

As shown in Figure 6.1, \mathbf{n} is a unit tensor pointing from origin of deviatoric plane to current stress point.

6.2.2. Internal Variables Hardening Rules and Plastic Modulus

In multiaxial space, the isotropic hardening rule for internal variable p_0 is formed in the following way:

$$\dot{p}_0 = \langle \Lambda \rangle \bar{p}_0; \quad \bar{p}_0 = \left(\frac{1+e}{\lambda-\kappa} \right) p_0 R_v \quad (6.21)$$

The rotation hardening rule generalized by Dafalias et al. (2006) is adopted in this work:

$$\begin{aligned} \dot{\boldsymbol{\alpha}} &= \langle \Lambda \rangle \bar{\boldsymbol{\alpha}} \\ \bar{\boldsymbol{\alpha}} &= \sqrt{\frac{3}{2}} \left(\frac{1+e}{\lambda-\kappa} \right) C \left(\frac{\bar{p}^*}{p_{s0}^*} \right)^2 |R_v| \|(\bar{\mathbf{r}}^* - \chi \boldsymbol{\alpha})\| (\boldsymbol{\alpha}^b - \boldsymbol{\alpha}) \end{aligned} \quad (6.22)$$

where:

$$\boldsymbol{\alpha}^b = \sqrt{2/3} M \bar{\mathbf{n}}_x; \quad \bar{\mathbf{n}}_x = \frac{(\bar{\mathbf{r}}^* - \chi \boldsymbol{\alpha})}{\| \bar{\mathbf{r}}^* - \chi \boldsymbol{\alpha} \|} \quad (6.23)$$

The readers are referred to the work of Dafalias et al. (2006) for more details concerning above generalized rotation hardening law.

The destructuration law for internal variable S_b is generalized as:

$$\dot{S}_b = \langle \Lambda \rangle \bar{S}_b; \quad \bar{S}_b = -(k_i S_b) \sqrt{(1-A) R_v^2 + A(3/2 \mathbf{R}_d : \mathbf{R}_d)} \quad (6.24)$$

The hardening vector \mathbf{r} in equation 2.5 remains the same form as the one in triaxial space:

$$\mathbf{r} = [\bar{p}_0, \bar{\boldsymbol{\alpha}}, \bar{S}_b] \quad (6.25)$$

In multiaxial space, the plastic modulus takes the same form as in triaxial space:

$$K_p = \bar{K}_p + f(b) \quad (6.26)$$

Based on the consistency condition of the bounding surface, \bar{K}_p is given by:

$$\bar{K}_p = - \left(\frac{\partial F_s}{\partial p_{s0}^*} \bar{p}_{s0}^* + \frac{\partial F_s}{\partial \boldsymbol{\alpha}} : \bar{\boldsymbol{\alpha}} + r_c \frac{\partial F_s}{\partial \bar{p}^*} (p_0 \bar{S}_b + S_b \bar{p}_0) \right) \quad (6.27)$$

with

$$\frac{\partial F_s}{\partial \boldsymbol{\alpha}} = -3\bar{p}^* (\bar{\boldsymbol{s}} - p_{s0}^* \boldsymbol{\alpha}) \quad (6.28)$$

Function $f(b)$ remains the same:

$$f(b) = \frac{h(1+e)p_0^3}{\langle b/(b-1) - s \rangle} m_s \quad (6.29)$$

whereas the value of h in multiaxial space is assumed to be dependent on the location of image stress on deviatoric plane in the same way as M and N :

$$h = \Theta(\bar{\theta}, c_h) h_c = \frac{2c_h}{(1+c_h) - (1-c_h) \cos 3\bar{\theta}} h_c \quad (6.30)$$

with $c_h = h_e/h_c$.

6.2.3. Evolution Rule of Projection Center and Similarity Ratio b

To generalize the evolution rule of projection center, the variable X_d in equation 5.11 needs to be redefined in multiaxial space:

$$X_d = \frac{d_c}{d_d} \quad (6.31)$$

$$d_c = \|\mathbf{s}_c - p_c^* \boldsymbol{\alpha}\|; \quad d_d = \sqrt{\frac{2}{3} \left(N^2 - \frac{3}{2} \boldsymbol{\alpha} : \boldsymbol{\alpha} \right) p_c^* (p_{s0}^* - p_c^*)}$$

where

$$\mathbf{s}_c = \boldsymbol{\sigma}_c - p_c \mathbf{I} \quad (6.32)$$

and the value of N is determined by equation 6.7 with tensor $\bar{\mathbf{n}}$ being replaced by

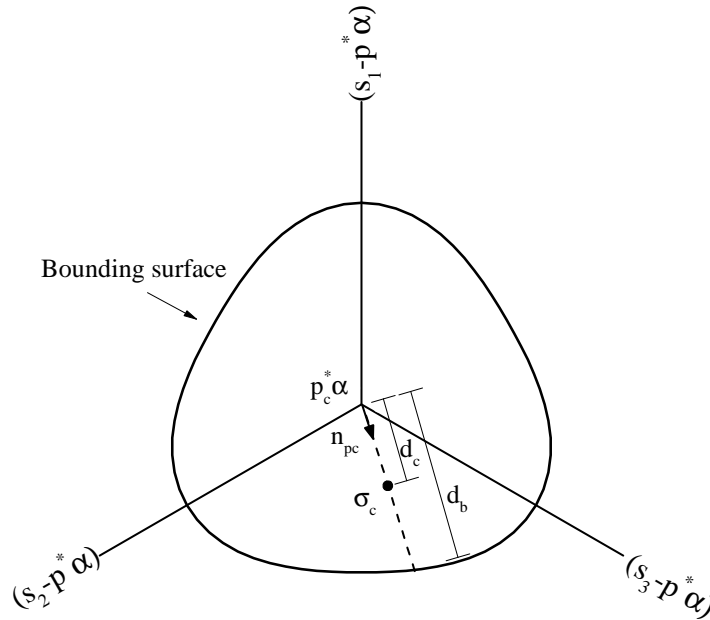


Figure 6.2. Schematic illustration of variables that define the position of projection center relative to the bounding surface in deviatoric plane

\mathbf{n}_{pc} , which will be discussed later. As illustrated in Figure 6.2, d_c and d_d denote the

distance between $\boldsymbol{\alpha}$ axis and projection center and bounding surface in deviatoric plane, respectively. And X_p maintains the same definition as triaxial space:

$$X_p = \frac{p_c^*}{p_{s0}^*} \quad (6.33)$$

In the multiaxial stress space, the projection center is a tensor, which has 6 independent components. As a result, to obtain a unique evolution rule for all components of projection center tensor, it is necessary to have a set of 6 linearly-independent equations. However, the linearization of equations of X_d and X_p can only provide two equations, which leaves the problem indeterminate.

To solve it, besides two scalar X_p , X_d , a new directional tensor \mathbf{n}_{pc} is introduced:

$$\mathbf{n}_{pc} = \frac{\mathbf{s}_c - p_c^* \boldsymbol{\alpha}}{\|\mathbf{s}_c - p_c^* \boldsymbol{\alpha}\|} \quad (6.34)$$

As shown in Figure 6.2, the tensor \mathbf{n}_{pc} indicates the direction pointing from the $\boldsymbol{\alpha}$ axis to the projection center $\boldsymbol{\sigma}_c$ in the deviatoric plane. As a result, tensor $\boldsymbol{\sigma}_c$ can be rewritten as:

$$\boldsymbol{\sigma}_c = \mathbf{s}_c + p_c \mathbf{I}; \quad \mathbf{s}_c = p_c^* \boldsymbol{\alpha} + d_c \mathbf{n}_{pc} \quad (6.35)$$

Suppose the tensor \mathbf{n}_{pc} remains constant between consecutive stress reversals, the evolution of the projection center is fully characterized by the change of scalars p_c^* , p_c and d_c as well as the changes of the internal variables:

$$\dot{\boldsymbol{\sigma}}_c = \dot{\mathbf{s}}_c + \dot{p}_c \mathbf{I} = \dot{p}_c^* \boldsymbol{\alpha} + p_c^* \dot{\boldsymbol{\alpha}} + \dot{d}_c \mathbf{n}_{pc} + \dot{p}_c \mathbf{I} \quad (6.36)$$

Following the approach in triaxial space, linearization of X_p and X_d leads to:

$$\begin{aligned} \dot{p}_c^* &= \frac{p_c^*}{p_{s0}^*} \dot{p}_{s0}^*; & \dot{p}_c &= \frac{p_c^*}{p_{s0}^*} \dot{p}_{s0}^* - \dot{p}_t \\ \dot{d}_c &= -d_c \left(\frac{3\boldsymbol{\alpha} : \dot{\boldsymbol{\alpha}}}{2N^2 - 3\boldsymbol{\alpha} : \boldsymbol{\alpha}} + \frac{(2p_c^* - p_{s0}^*)\dot{p}_c^*}{2p_c^*(p_{s0}^* - p_c^*)} - \frac{\dot{p}_{s0}^*}{2(p_{s0}^* - p_c^*)} \right) \end{aligned} \quad (6.37)$$

where

$$\dot{p}_{s0}^* = (1 + (1 + r_c)S_b)\dot{p}_0 + (1 + r_c)p_0\dot{S}_b; \quad \dot{p}_t = r_c(S_b\dot{p}_0 + p_0\dot{S}_b) \quad (6.38)$$

Finally, the rate form of the projection center evolution rule is obtained via substituting equation 6.37 into equation 6.36.

In terms of the similarity ratio b , its evolution rule has been generalized as:

$$\dot{b} = \frac{C_1}{C_2} \quad (6.39)$$

where:

$$\begin{aligned} C_1 &= -\frac{\partial F_s}{\partial \bar{\boldsymbol{\sigma}}} : (\dot{\boldsymbol{\sigma}}_c + b(\dot{\boldsymbol{\sigma}} - \dot{\boldsymbol{\sigma}}_c)) + \frac{\bar{K}_p}{K_p} \frac{\partial F_s}{\partial \bar{\boldsymbol{\sigma}}} : \dot{\boldsymbol{\sigma}}; \\ C_2 &= \frac{\partial F_s}{\partial \bar{\boldsymbol{\sigma}}} : (\boldsymbol{\sigma} - \boldsymbol{\sigma}_c) \end{aligned} \quad (6.40)$$

6.3. Stress Integration Algorithm

In general, the methods for implementing constitutive relations (i.e., stress point integration) are classified as either explicit or implicit schemes. In a fully implicit method, model components, like loading direction, plastic flow direction, and plastic modulus, are all evaluated at unknown states. Correspondingly, a system of local nonlinear equations must be solved iteratively. Besides, if a Newton scheme is used to solve the nonlinear equations, higher order derivatives of yield surface (or bounding surface) and plastic potential are required. As a payback, the implicit method is unconditionally stable, and

when used in classical elastoplasticity models, updated stress can be enforced on the yield surface to a specified tolerance. Furthermore, the Newton implicit stress integration usually provides an analytical expression for the consistent tangent modulus, which can lead to a quadratic rate of convergence in global Newton iterations and reduce the computation time (Simo and Hughes, 2006).

However, for more complex advanced models, the high order derivatives aforementioned sometimes lead to much tedious algebra. Also, high nonlinearity in advanced soil models may cause the divergence of local iterations in an implicit method (Jeremic, 2001). Such non-convergence tends to reduce the step size for global iteration and consequently weaken the benefits of implicit methods.

On the other hand, in explicit methods, model components are all evaluated at the known current states, which make it more straightforward to implement. Moreover, explicit methods do not require local iterations. Furthermore, combined with automatic substepping and error control, the accuracy and efficiency of explicit methods has been significantly enhanced (Sloan et al., 2001). Concerning the consistent tangent modulus for the purpose of quadratic convergence, a numerical perturbation technique can be employed to estimate it. Several comparisons regarding the performances of implicit and explicit methods tend to show the latter one is more robust and efficient (Potts and Ganendra, 1994; Tamagnini et al., 2000).

When explicit methods are used for classical elastoplasticity models, issues mainly arise from the requirement to find the intersection between an unknown stress increment path with the yield surface and the overshooting (i.e., the updated stress is outside the yield surface). For bounding surface models, it is not necessary to find the intersection

point, as the stress point will always be inside or on the bounding surface. For the latter issue, drift correction, or higher order explicit methods can be employed to provide satisfactory solutions (Sloan et al., 2001).

Based on the above considerations, an explicit stress integration method, namely Runge-Kutta-Fehlberg adaptive explicit integration, is selected for the implementation of the proposed model. This scheme is attractive since the error is controlled by specified tolerance. Moreover, the size of substepping is automatically extrapolated based on the difference between the second and third order Runge-Kutta approximation and a prescribed accuracy. This type of error control permits the varied substepping sizes (Sloan et al., 2001), which significantly improves computation efficiency. The stability and robustness of this method have been verified with several complex and advanced constitutive models (Tamagnini et al., 2000; Castellanza, 2002; Mašín, 2009).

The object of the stress integration is to update the stress states and a series of internal variables under a given amount of strain increment $\Delta\boldsymbol{\varepsilon}$ within a time period of Δt . In the proposed model, besides stress and internal variables, other state-dependent variables, including the projection center $\boldsymbol{\sigma}_c$, similarity ratio b as well as the strain history tensor $\boldsymbol{\varepsilon}_{hist}$ in elasticity model, also need to be appropriately updated.

As material rate effects are not considered in the proposed constitutive relations, for the purpose of stress integration, it is convenient to introduce a pseudo time, T , defined by:

$$T = (t - t_0)/\Delta t \quad (6.41)$$

where t_0 is the time at the beginning of loading increment, $t_0 + \Delta t$ is the time at the end of loading increment, and $0 \leq T \leq 1$. Since $dT/dt = 1/\Delta t$, application of chain rule will

transform the rate form of constitutive equations, e.g.,

$$\begin{aligned}\dot{\boldsymbol{\sigma}}_{trial} &= \mathbf{D}_e \dot{\boldsymbol{\varepsilon}} \\ \dot{\boldsymbol{\sigma}} &= \mathbf{D}_{ep} \dot{\boldsymbol{\varepsilon}}\end{aligned}\tag{6.42}$$

to forms as follow:

$$\begin{aligned}\Delta \boldsymbol{\sigma}_{trial} &= \int \frac{d\boldsymbol{\sigma}_{trial}}{dT} dT = \int \mathbf{D}_e \Delta \boldsymbol{\varepsilon} dT \\ \Delta \boldsymbol{\sigma} &= \int \frac{d\boldsymbol{\sigma}}{dT} dT = \int \mathbf{D}_{ep} \Delta \boldsymbol{\varepsilon} dT\end{aligned}\tag{6.43}$$

It is noteworthy that this transformation is under the assumption that strains vary “proportionally” (i.e., the ratio between the strain components remains constant) over given increment (Potts and Ganendra, 1994). Therefore, this transformation may introduce error into the computation if the aforementioned assumption is not valid.

It is also worth noting that both elasticity stiffness matrix \mathbf{D}_e and elasto-plasticity stiffness matrix \mathbf{D}_{ep} are dependent of the strain increment $\Delta \boldsymbol{\varepsilon}$, due to stiffness degradation mechanism introduced in the adopted elasticity model. In addition, as discussed before, such stiffness degradation is a function of finite strain increment instead of strain rate (Benz, 2007).

The increment form of constitutive equations exemplified by equation 6.43 is essentially a set of ordinary differential equations with respect to the pseudo time T , which can be numerically integrated via a substepping explicit integration. This method requires the strain increment $\Delta \boldsymbol{\varepsilon}$ to be further subdivided into a number of sub-strain increments, $\Delta \boldsymbol{\varepsilon}_k = \Delta \boldsymbol{\varepsilon} \Delta T_k$ and substep size ΔT_k satisfies the identity condition, i.e., $\sum_{k=1}^m \Delta T_k = 1$.

The complete stress integration algorithm is shown in Box 4.1. In step-1, a trial stress increment is obtained with one step Forward-Euler method, i.e., $\Delta T_k = 1$. If higher

accuracy is demanded, then substepping scheme described later can also be applied. The actual stress reversal criteria used in model implementation (i.e., equation 6.45) has been slightly modified compared with the one in equation 4.17. The reason is that elastic stress update, which follows a stress reversal, may bring updated stress outside the bounding surface, when stress before the update is close to the apex of the bounding surface and trial stress increment barely satisfies the criteria shown in equation 4.17. The modification, suggested by Sloan et al. (2001), provides a mechanism to allow aforementioned situation to be treated as elastoplasticity update determined by the specified tolerance and ensure the consistency condition of bounding surface is not violated. The directional tensor \mathbf{n}_{pc} will be updated after each stress reversal and remains the same before next stress reversal. Strain history tensor $\boldsymbol{\varepsilon}_{hist}$ will be updated according to the strain increment in each step according to the algorithm provided by Benz (2007), which will not be repeated.

After each elastoplasticity computation step, the consistency condition of the bounding surface in terms of the image stress will be checked. In other words, the updated image stress, which depends on the update of stress, projection center and similarity ratio, should be close enough to the bounding surface. This can be viewed as the counterpart of a stress drifting check from the yield surface in classical elastoplasticity models and provides an indication about the accuracy of stress integration. If the consistency criteria is not satisfied, the integration will be treated as inaccurate, and the information of corresponding stress points will be recorded. It is also worth mentioning that no correction of stress or other variables is attempted at current stage, and the strategy to correct image stress back to bounding surface will be part of future research work. Nevertheless, based on the author's experience, with employed Runge-Kutta-Fehlberg explicit

integration method, the stresses, internal variable and other state dependent variables are usually very accurate and seldom need to be corrected.

Box 4.1 Stress Integration Algorithm

Input: states at the end of the n th step ($\boldsymbol{\sigma}_n, \mathbf{q}_n, \boldsymbol{\sigma}_{c,n}, b_n, \boldsymbol{\varepsilon}_{hist,n}$) and strain increment for the $n+1$ step $\Delta\boldsymbol{\varepsilon}_{n+1}$;

Output: states at the end of the $n + 1$ th step ($\boldsymbol{\sigma}_{n+1}, \mathbf{q}_{n+1}, \boldsymbol{\sigma}_{c,n+1}, b_{n+1}, \boldsymbol{\varepsilon}_{hist,n+1}$)

Step-1: calculate the elastic stiffness matrix and trial stress increment;

$$\mathbf{D}_e = \mathbf{D}_e(\boldsymbol{\sigma}_n, \boldsymbol{\varepsilon}_{hist,n}, \Delta\boldsymbol{\varepsilon}_{n+1}); \quad \Delta\boldsymbol{\sigma}_{n+1}^{trial} = \mathbf{D}_e \Delta\boldsymbol{\varepsilon}_{n+1} \quad (6.44)$$

Step-2: calculate the normalized loading index;

$$L_n = \frac{\mathbf{L} \Delta\boldsymbol{\sigma}_{n+1}^{trial}}{\|\mathbf{L}\| \times \|\Delta\boldsymbol{\sigma}_{n+1}^{trial}\|} \quad (6.45)$$

with loading direction \mathbf{L} being evaluated at the state before update i.e.,

$$\mathbf{L} = \mathbf{L}(\boldsymbol{\sigma}_n, \mathbf{q}_n, \boldsymbol{\sigma}_{c,n}, b_n);$$

Step-3: decide loading or unloading (i.e., stress reversal);

$$\begin{cases} \text{stress reversal triggered, go to step-4} & \text{if } L_n < LTOL \\ \text{no stress reversal, go to step-5} & \text{if } L_n \geq LTOL \end{cases} \quad (6.46)$$

where $LTOL = 1e^{-6}$

Step-4: update projection center to current stress $\boldsymbol{\sigma}_n$, recalculate the variable b and tensor \mathbf{n}_{pc} for new projection center, freeze the internal variables, and update strain history tensor;

$$\begin{aligned} \boldsymbol{\sigma}_{c,n+1} &= \boldsymbol{\sigma}_n; & b_{n+1} &= b(\boldsymbol{\sigma}_{c,n+1}, \mathbf{q}_n); & \mathbf{n}_{pc,n+1} &= \mathbf{n}_{pc}(\boldsymbol{\sigma}_{c,n+1}, \mathbf{q}_n) \\ \boldsymbol{\sigma}_{n+1} &= \boldsymbol{\sigma}_n + \Delta\boldsymbol{\sigma}_{n+1}^{trial}; & \mathbf{q}_{n+1} &= \mathbf{q}_n; & \boldsymbol{\varepsilon}_{hist,n+1} &= \boldsymbol{\varepsilon}_{hist}(\boldsymbol{\varepsilon}_{hist,n}, \Delta\boldsymbol{\varepsilon}_{n+1}) \end{aligned} \quad (6.47)$$

This is the end of stress update for current step

Step-5: call Runge-Kutta-Fehlberg algorithm to do the elastoplasticity stress update:

$$(\boldsymbol{\sigma}_{n+1}, \mathbf{q}_{n+1}, \boldsymbol{\sigma}_{c,n+1}, b_{n+1}, \boldsymbol{\varepsilon}_{hist,n+1}) = \text{RKF}(\boldsymbol{\sigma}_n, \mathbf{q}_n, \boldsymbol{\sigma}_{c,n}, b_n, \boldsymbol{\varepsilon}_{hist,n}, \Delta\boldsymbol{\varepsilon}_{n+1}) \quad (6.48)$$

and check the bounding surface consistency after stress integration:

$$F_s = F_s(\bar{\boldsymbol{\sigma}}_{n+1}, q_{n+1}) \quad (6.49)$$

And:

$$\begin{cases} \text{consistency condition is fulfilled} & \text{if } |F_s|/|\|\bar{\boldsymbol{\sigma}}_{n+1}\|| \leq FTOL \\ \text{consistency condition is not fulfilled} & \text{if } |F_s|/|\|\bar{\boldsymbol{\sigma}}_{n+1}\|| > FTOL \end{cases} \quad (6.50)$$

where $\bar{\boldsymbol{\sigma}}_{n+1} = \boldsymbol{\sigma}_{c,n+1} + b_{n+1}(\boldsymbol{\sigma}_{n+1} - \boldsymbol{\sigma}_{c,n+1})$ and $FTOL = 1e^{-3}$

This is the end of stress update for current step

For strain increment $\Delta\boldsymbol{\varepsilon}_{n+1}$ not triggering a stress reversal, Runge-Kutta-Fehlberg explicit integration algorithm will be called to integrate the stress, internal variables and

other state-dependent variables. The detailed algorithm is presented in Box 4.2. In the initialization step, pseudo time T_k and iteration number N_{iter} are set to 0. In addition, the substepping size initially is set as its default value $\Delta T_k = 0.1$. For each strain sub-increment $\Delta \varepsilon^k$, second and third order accurate Runge-Kutta approximations are calculated based on the states at the end of previous substep (e.g., $\boldsymbol{\sigma}^{k-1}$ and \mathbf{q}^{k-1}). The differences between the above two approximations are used to quantify the integration error. Based on numerical tests and computation stability consideration, only stress, internal variables and similarity b are considered for the estimation of integration error. Since the magnitude order of various stress or internal variables are different, they are normalized and then put into a error (or residual) vector \mathbf{R}^k . The norm of such error vector is used as a scalar measurement of error. The value of this error scalar R^k and specific error tolerance $STOL$ are used to extrapolate strain sub-increment size for next substep via the extrapolation rule proposed by Sloan et al. (2001). The value 0.9 acts as a factor of safety, to prevent substepping size from failing to meet the chosen error tolerance $STOL$. A upper bound $1.1\Delta T_k$ and lower bound $0.1\Delta T_k$ are set up for accepted and rejected substeps, respectively. This helps reduce the number of failure substeps and increase the computation efficiency (Sloan et al., 2001). It is also worth mentioning that the strain history $\boldsymbol{\varepsilon}_{hist}$ will also be updated after each successful substep instead of merely after each step, which ensures the elasticity stiffness for next substep is appropriately degraded. This will be more important if larger strain sub-increments are involved in computations.

Box 4.2 Runge-Kutta-Fehlberg Adaptive Explicit Stress Integration

Algorithm

Input: states at the end of the n th step ($\boldsymbol{\sigma}_n, \mathbf{q}_n, \boldsymbol{\sigma}_{c,n}, b_n, \boldsymbol{\varepsilon}_{hist,n}$) and strain increment for the $(n + 1)$ th step $\Delta\boldsymbol{\varepsilon}_{n+1}$;

Output: states at the end of the $(n + 1)$ th step ($\boldsymbol{\sigma}_{n+1}, \mathbf{q}_{n+1}, \boldsymbol{\sigma}_{c,n+1}, b_{n+1}, \boldsymbol{\varepsilon}_{hist,n+1}$)

Step-1: Initialize the iteration control variables

$$k = 0; \quad T_k = 0; \quad \Delta T_k = 0.1; \quad N_{iter} = 0 \quad (6.51)$$

Step-2: While $T_k < 1$, perform steps 3-10; else go to step 11

Step-3: Compute the strain increment for k th substep

$$\Delta\boldsymbol{\varepsilon}^k = \Delta T_k \Delta\boldsymbol{\varepsilon}_{n+1} \quad (6.52)$$

and

$$N_{iter} = N_{iter} + 1 \quad (6.53)$$

reject substep stress integration if N_{iter} is larger than allowable maximum iteration number $N_{iter,max} = 1e^4$.

Step-4: Compute the stress increment, internal variable increment, projection center increment and variable b increment for $i=1,2,3$ based on their corresponding

rate form evolution rule and one step Forward-Euler method and

$$\begin{aligned}
\Delta \sigma_i^k &= D_{ep}(\sigma_{i-1}^k, \mathbf{q}_{i-1}^k, \sigma_{c,i-1}^k, b_{i-1}^k, \boldsymbol{\varepsilon}_{hist}^{k-1}, \Delta \boldsymbol{\varepsilon}^k) \Delta \boldsymbol{\varepsilon}^k \\
\Lambda &= \frac{L(\sigma_{i-1}^k, \mathbf{q}_{i-1}^k, \sigma_{c,i-1}^k, b_{i-1}^k) \Delta \sigma_i^k}{K_p(\sigma_{i-1}^k, \mathbf{q}_{i-1}^k, \sigma_{c,i-1}^k, b_{i-1}^k, \boldsymbol{\varepsilon}_{hist}^{k-1}, \Delta \boldsymbol{\varepsilon}^k)} \\
\Delta \mathbf{q}_i^k &= \Lambda \mathbf{r}(\sigma_{i-1}^k, \sigma_{c,i-1}^k, b_{i-1}^k) \\
\Delta \sigma_{c,i}^k &= \Delta \sigma_c(\mathbf{q}_{i-1}^k, \Delta \mathbf{q}_i^k) \\
\Delta b_i^k &= \Delta b(\sigma_{i-1}^k, \sigma_{c,i-1}^k, b_{i-1}^k, \Delta \sigma_{c,i}^k, \Delta \sigma_i^k)
\end{aligned} \tag{6.54}$$

where:

$$\begin{aligned}
\sigma_0^k &= \sigma^{k-1}; & \sigma_1^k &= \sigma^{k-1} + \frac{1}{2} \Delta \sigma_1^k; & \sigma_2^k &= \sigma^{k-1} - \Delta \sigma_1^k + 2 \Delta \sigma_2^k \\
\mathbf{q}_0^k &= \mathbf{q}^{k-1}; & \mathbf{q}_1^k &= \mathbf{q}^{k-1} + \frac{1}{2} \Delta \mathbf{q}_1^k; & \mathbf{q}_2^k &= \mathbf{q}^{k-1} - \Delta \mathbf{q}_1^k + 2 \Delta \mathbf{q}_2^k \\
\sigma_{c,0}^k &= \sigma_c^{k-1}; & \sigma_{c,1}^k &= \sigma_c^{k-1} + \frac{1}{2} \Delta \sigma_{c,1}^k; & \sigma_{c,2}^k &= \sigma_c^{k-1} - \Delta \sigma_{c,1}^k + 2 \Delta \sigma_{c,2}^k \\
b_0^k &= b^{k-1}; & b_1^k &= b^{k-1} + \frac{1}{2} \Delta b_1^k; & b_2^k &= b^{k-1} - \Delta b_1^k + 2 \Delta b_2^k;
\end{aligned} \tag{6.55}$$

Step-5: Compute the 2nd and 3rd order Runge-Kutta approximations

$$\begin{aligned}
\sigma_{2nd}^k &= \sigma^{k-1} + \Delta \sigma_2^k; & \sigma_{3rd}^k &= \sigma^{k-1} + \frac{1}{6} (\Delta \sigma_1^k + 4 \Delta \sigma_2^k + \Delta \sigma_3^k) \\
\mathbf{q}_{2nd}^k &= \mathbf{q}^{k-1} + \Delta \mathbf{q}_2^k; & \mathbf{q}_{3rd}^k &= \mathbf{q}^{k-1} + \frac{1}{6} (\Delta \mathbf{q}_1^k + 4 \Delta \mathbf{q}_2^k + \Delta \mathbf{q}_3^k) \\
\sigma_{c,2nd}^k &= \sigma_c^{k-1} + \Delta \sigma_{c,2}^k; & \sigma_{c,3rd}^k &= \sigma_c^{k-1} + \frac{1}{6} (\Delta \sigma_{c,1}^k + 4 \Delta \sigma_{c,2}^k + \Delta \sigma_{c,3}^k) \\
b_{2nd}^k &= b^{k-1} + \Delta b_2^k; & b_{3rd}^k &= b^{k-1} + \frac{1}{6} (\Delta b_1^k + 4 \Delta b_2^k + \Delta b_3^k)
\end{aligned} \tag{6.56}$$

Step-6: Estimate the error for k th substep

$$\mathbf{R}^k = \left[\frac{\Delta \boldsymbol{\sigma}^k}{\|\boldsymbol{\sigma}_{3rd}^k\|}, \frac{\Delta \mathbf{q}^k}{\|\mathbf{q}_{3rd}^k\|}, \frac{\Delta b^k}{|b_{3rd}^k|} \right] \quad (6.57)$$

where:

$$\begin{aligned} \Delta \boldsymbol{\sigma}^k &= \boldsymbol{\sigma}_{3rd}^k - \boldsymbol{\sigma}_{2nd}^k \\ \Delta \mathbf{q}^k &= \mathbf{q}_{3rd}^k - \mathbf{q}_{2nd}^k \\ \Delta b^k &= b_{3rd}^k - b_{2nd}^k \end{aligned} \quad (6.58)$$

and the scalar measurement of error

$$R^k = \|\mathbf{R}^k\| \quad (6.59)$$

Step-7: Estimate the size for $k + 1$ th substep

$$\Delta T_{k+1}^* = 0.9 \Delta T_k \left(\frac{STOL}{R^k} \right)^{(1/3)} \quad (6.60)$$

with $STOL = 1e^{-7}$

Step-8: Determine whether substep is acceptable or not:

$$\begin{cases} \text{substep accepted, go to step-9} & \text{if } R_k \leq STOL \\ \text{substep rejected, go to step-10} & \text{if } R_k > STOL \end{cases} \quad (6.61)$$

Step-9: Update stress, internal variables, projection center, similarity ratio and strain history

$$\boldsymbol{\sigma}^k = \boldsymbol{\sigma}_{3rd}^k; \quad \mathbf{q}^k = \mathbf{q}_{3rd}^k; \quad \boldsymbol{\sigma}_c^k = \boldsymbol{\sigma}_{c,3rd}^k; \quad b^k = b_{3rd}^k; \quad \boldsymbol{\varepsilon}_{hist}^k = \boldsymbol{\varepsilon}_{hist}(\boldsymbol{\varepsilon}_{hist}^{k-1}, \Delta \boldsymbol{\varepsilon}^k) \quad (6.62)$$

adjust the substep size for the $k + 1$ substep, and update pseudo time and substep number

$$\Delta T_{k+1} = \max(1.1\Delta T_k, \Delta T_{k+1}^*); \quad (6.63)$$

$$\Delta T_{k+1} = \min(1 - T_k, \Delta T_{k+1}) \quad (6.64)$$

$$T_k = T_k + \Delta T_k; \quad k = k + 1 \quad (6.65)$$

Step-10: Reduce the substep size

$$\Delta T_{k+1} = \min(0.1\Delta T_k, \Delta T_{k+1}^*) \quad (6.66)$$

and compare it with the allowable minimum substep size ΔT_{min} . If $\Delta T_{k+1} < \Delta T_{min}$, substep stress integration fails and the global step number for explicit integration should be increased so that the size of strain increment is reduced.

Step-11: Substep stress integration finishes, update stress, internal variables, projection center, similarity ratio and strain history for the $(n + 1)$ th step

$$\boldsymbol{\sigma}_{n+1} = \boldsymbol{\sigma}^k; \quad \mathbf{q}_{n+1} = \mathbf{q}^k; \quad \boldsymbol{\sigma}_{c,n+1} = \boldsymbol{\sigma}_c^k; \quad b_{n+1} = b^k; \quad \boldsymbol{\varepsilon}_{hist}^{n+1} = \boldsymbol{\varepsilon}_{hist}^k \quad (6.67)$$

6.4. Formulation of Triaxial Space Constitutive Driver

The formulation of the triaxial space constitutive driver are based on the linearized integration technique proposed by Bardet and Choucair (1991). The linearized constraints during a loading increment can be expressed as:

$$\mathbf{S}\Delta\boldsymbol{\sigma} + \mathbf{E}\Delta\boldsymbol{\varepsilon} = \Delta\mathbf{Y} \quad (6.68)$$

where $\Delta\boldsymbol{\sigma}$ and $\Delta\boldsymbol{\varepsilon}$ in triaxial space are expressed as the relevant invariants:

$$\Delta\boldsymbol{\sigma} = \begin{bmatrix} \Delta p \\ \Delta q \end{bmatrix}; \quad \Delta\boldsymbol{\varepsilon} = \begin{bmatrix} \Delta\varepsilon_v \\ \Delta\varepsilon_d \end{bmatrix} \quad (6.69)$$

and matrix \mathbf{S} and \mathbf{E} represent the linearized constraints on stress and strain increment, respectively. The first row of vector $\Delta\mathbf{Y}$ is always set to be zero, to enforce relations between components of stress or strains, while the second row represents the loading increment, which can be stress or strain. For instance, in a stress-controlled undrained triaxial compression test, the constraint is no volumetric deformation (i.e., $\varepsilon_v = 0$) and the driving variable is the growing shear stress (i.e., q stress). Therefore, equation 6.68 can be written as:

$$\begin{bmatrix} 0, 0 \\ 0, 1 \end{bmatrix} \begin{bmatrix} \Delta p \\ \Delta q \end{bmatrix} + \begin{bmatrix} 1, 0 \\ 0, 0 \end{bmatrix} \begin{bmatrix} \Delta\varepsilon_v \\ \Delta\varepsilon_d \end{bmatrix} = \begin{bmatrix} 0 \\ (q_1 - q_0)/N_l \end{bmatrix} \quad (6.70)$$

where $q_1 - q_0$ is the shear stress change in the test and the N_l is the number of loading steps in the test.

Under mixed-control conditions, both stress increment $\Delta\boldsymbol{\sigma}$ and strain increment $\Delta\boldsymbol{\varepsilon}$ are generally unknown. Considering the stress integration method discussed in the previous section, it is convenient to express $\Delta\boldsymbol{\sigma}$ as a function of $\Delta\boldsymbol{\varepsilon}$, i.e., $\Delta\boldsymbol{\sigma} = \mathbf{f}_c(\Delta\boldsymbol{\varepsilon})$. If $\Delta\boldsymbol{\varepsilon}$ for each step is small enough, $\Delta\boldsymbol{\sigma} = \mathbf{f}_c(\Delta\boldsymbol{\varepsilon})$ can be simplified as $\Delta\boldsymbol{\sigma} \approx \mathbf{D}\Delta\boldsymbol{\varepsilon}$ and depending on elasticity update or elasto-plasticity update, $\mathbf{D} = \mathbf{D}_e$ or $\mathbf{D} = \mathbf{D}_{ep}$. By further substituting this relation into equation 6.68, one can obtain:

$$\mathbf{M}\Delta\boldsymbol{\varepsilon} = \Delta\mathbf{Y} \quad (6.71)$$

with

$$\mathbf{M} = \mathbf{S}\mathbf{D} + \mathbf{E} \quad (6.72)$$

For constitutive models in which matrix \mathbf{D} is independent of strain increment $\Delta\boldsymbol{\varepsilon}$, the increment $\Delta\boldsymbol{\varepsilon}$ is uniquely determined, given the non-singularity of matrix \mathbf{M} (i.e., the determinant $\det(\mathbf{M})$ is not equal to 0). However, due to the adopted non-linear elasticity model, the matrix \mathbf{D} itself is a function of $\Delta\boldsymbol{\varepsilon}$, which make the equation 6.71 a set of nonlinear equations. Therefore, the Newton-Raphson method is used to solve these nonlinear equations. In addition, $\Delta\boldsymbol{\varepsilon}$ is not necessary to be very small, as substepping algorithm is used to solve $\Delta\boldsymbol{\sigma} = \mathbf{f}_c(\Delta\boldsymbol{\varepsilon})$.

First, equation 6.68 is rewritten as:

$$\mathbf{f}_r = \mathbf{S}\mathbf{f}_c(\Delta\boldsymbol{\varepsilon}) + \mathbf{E}\Delta\boldsymbol{\varepsilon} - \Delta\mathbf{Y} = \mathbf{0} \quad (6.73)$$

Then \mathbf{f}_r shall be expanded in a Taylor series about current strain increment $\Delta\boldsymbol{\varepsilon}_0$:

$$\mathbf{f}_r = \mathbf{f}_{r,0} + \left. \frac{\partial \mathbf{f}_r}{\partial \Delta\boldsymbol{\varepsilon}} \right|_{\Delta\boldsymbol{\varepsilon}_0} \delta\boldsymbol{\varepsilon} = \mathbf{0} \quad (6.74)$$

where $\mathbf{f}_{r,0}$ and $\left. \frac{\partial \mathbf{f}_r}{\partial \Delta\boldsymbol{\varepsilon}} \right|_{\Delta\boldsymbol{\varepsilon}_0}$ are the value of \mathbf{f}_r and Jacobian matrix that are evaluated at $\Delta\boldsymbol{\varepsilon}_0$, respectively. The strain increment correction $\delta\boldsymbol{\varepsilon}$ is given by solving above equation and the updated strain increment is obtained by:

$$\Delta\boldsymbol{\varepsilon} = \Delta\boldsymbol{\varepsilon}_0 + \delta\boldsymbol{\varepsilon} \quad (6.75)$$

This calculation is iteratively conducted until the value of \mathbf{f}_r reaches the specific tolerance:

$$\|\mathbf{f}_r\| \leq NTOL \quad (6.76)$$

where $NTOL$ is set as $1e^{-6}$ in this work. And corresponding stress and strain increment that fulfill loading increment are obtained.

To start the iteration, the first guess of strain increment is obtained by solving equation 6.68 under the assumption that material is purely elastic and no stiffness degradation is considered (i.e., $G = G_0$), which leads to a system of linear algebra equations. Considering the complexity in the derivation, a numerical perturbation is selected to obtain the Jacobian matrix $\partial\mathbf{f}_r/\partial\Delta\boldsymbol{\varepsilon}$. Forward difference method is used in the perturbation. Computation sequences and details of this mixed-control constitutive driver are summarized in Box 4.3.

Box 4.3 Mixed-Control Constitutive Driver Computation Sequences

Input: linearized constraint matrix \mathbf{S} and \mathbf{E} , loading variable \mathbf{Y} and the number of loading step N_l ;

Output: strain $\boldsymbol{\varepsilon}$ and stress $\boldsymbol{\sigma}$;

Step-1: Calculate the loading variable for each step

$$\Delta\mathbf{Y} = \mathbf{Y}/N_l \quad (6.77)$$

Step-2: Guess the strain increment $\Delta\boldsymbol{\varepsilon}_0$ by assuming material is elastic and solving

$$(\mathbf{SD} + \mathbf{E})\Delta\boldsymbol{\varepsilon}_0 = \Delta\mathbf{Y} \quad (6.78)$$

Step-3: Begin Newton-Raphson iteration to calculate strain increment that satisfies equation 6.73: While $\|\mathbf{f}_r\| > NTOL$, go to step 4-6; else go to step 7

Step-4: Approximate Jacobian matrix via numerical perturbation: for $j = 1$ to 2

$$\begin{aligned}\Delta\boldsymbol{\varepsilon}_n^* &= \Delta\boldsymbol{\varepsilon}_n \\ \Delta\boldsymbol{\varepsilon}_{n,j}^* &= \Delta\boldsymbol{\varepsilon}_{n,j}^* + \varepsilon_{pert} \\ \left(\frac{\partial \mathbf{f}_r}{\partial \Delta\boldsymbol{\varepsilon}}\right)_{ij} &= \frac{f_{r,i}(\Delta\boldsymbol{\varepsilon}_n^*) - f_{r,i}(\Delta\boldsymbol{\varepsilon}_n)}{\varepsilon_{pert}}\end{aligned}\quad (6.79)$$

where ε_{pert} is the strain perturbation amplitude, which is set as $1e^{-6}$ and i is the component of vector \mathbf{f}_r , i.e., $i = 1, 2$

Step-5: Calculate the strain increment correction and update strain increment

$$\begin{aligned}\delta\boldsymbol{\varepsilon}_{n+1} &= \left(\frac{\partial \mathbf{f}_r}{\partial \Delta\boldsymbol{\varepsilon}}\right)^{-1} \mathbf{f}_r(\Delta\boldsymbol{\varepsilon}_n) \\ \Delta\boldsymbol{\varepsilon}_{n+1} &= \Delta\boldsymbol{\varepsilon}_n + \delta\boldsymbol{\varepsilon}_{n+1}\end{aligned}\quad (6.80)$$

Step-6: Calculate new stress increment and updated \mathbf{f}_r :

$$\begin{aligned}\Delta\boldsymbol{\sigma}_{n+1} &= \mathbf{f}_c(\Delta\boldsymbol{\varepsilon}_{n+1}) \\ \mathbf{f}_{r,n+1} &= \mathbf{S}\Delta\boldsymbol{\sigma}_{n+1} + \mathbf{E}\Delta\boldsymbol{\varepsilon}_{n+1} - \Delta\mathbf{Y}\end{aligned}\quad (6.81)$$

Step-7: Accept the stress and strain increment, and internal variables as well as state dependent variables.

Step-8: Repeat step 3-7 until all the loading has been applied.

6.5. Model Implementation into UMAT Subroutine

The implementation of the proposed model into UMAT subroutine of ABAQUS is based on the UMAT file provided by the Soilmodels Projection (Gudehus et al., 2008; Miriano, 2011; Martinelli, 2012). While the same stress integration algorithm is employed in UMAT as shown in section 6.3, a slight modification has been made in terms of the criteria that determines when to relocate the projection center to the current stress.

Numerical tests after model implementation show that a very small amount of strain perturbation, which is of numerical origin, usually will trigger the stress reversal criteria and consequently relocation of projection center. However, this relocation of projection center should not happen based on the prescribed boundary conditions. Since the projection center plays a crucial role in various aspects of plasticity computation, this side effect decreases the stability of stress integration, increases the iteration number in global Newton iteration and sometimes even make the problem divergent.

As a solution, a new criteria for projection center relocation is superposed to the one described in equation 6.45:

$$\frac{\|\Delta\sigma_{trial}\|}{p_{s0}^*} \geq SRTOL \quad (6.82)$$

with $SRTOL = 1e^{-4}$. This implies that the magnitude of strain change should be large enough so that corresponding trial stress increment is sufficiently large compared with the size of bounding surface, before the projection center can be relocated. As a result, aforementioned strain perturbation can will only lead to the elastic stress update for current step and keep the projection center unchanged. Elastic stress update for current step is necessary, as the step that triggers stress reversal must correspond to a loss of

positive definition of plastic multiplier Λ . Nevertheless, the change of stress is expected to be very small due to the magnitude of strain increment.

To preserve the quadratic rate convergence of global Newton iteration in ABAQUS, the consistent tangent moduli is computed via similar numerical perturbation technique detailed in Box 4.3.

To validate the model implementation in UMAT of Abaqus, a single element test is conducted. Specifically, the stress-strain response from single element simulations is compared with the results from the constitutive driver, both of which are loaded under the same conditions.

Figure 6.3 shows the boundary conditions for the single element. The element type is CAX4, which is an axisymmetric element of four Gauss points at its four nodes. For undrained analysis, CAX4P element is used, whose four nodes have an additional freedom for pore pressure. As shown in Figure 6.3, this single element represents one-quarter of a vertical cross-section of a 2:1 cylindrical specimen. As a result, the vertical and horizontal displacement are restrained at the bottom and left boundaries of the element, respectively. Pressures are applied on the top and right boundaries to simulate the axial stress and lateral confining stress.

The model parameters used in the single element test is shown in Table 6.1. The loading programs in this validation and the corresponding initial conditions for simulations are summarized in Table 6.2

Table 6.1. Model parameters in the single element test of UMAT

λ	κ	M_c	M_e	N_c	N_e	C	χ	h_c	h_e	c_d	w	A_g	e_g	n_g	$\gamma_{0.7}$
0.08	0.02	1.2	0.9	1	1	16	1.56	30	30	0	1	180	2.64	0.635	5.00E-05

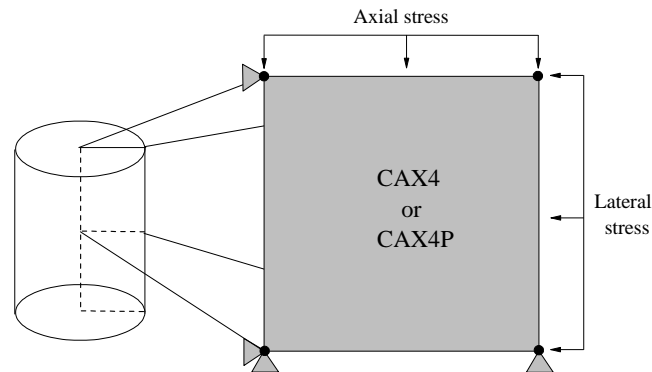


Figure 6.3. Single element and its boundary conditions for a triaxial sample

Table 6.2. Simulation cases in the single element test of UMAT

Case Num	Loading Path	p_0	α	S_b	p	q	void ratio
3	CAU TXC	40	0.3	1	80	27	0.75
5	CAU TXC	40	0.3	1	30	9	0.75
6	CAU TXE	40	0.3	1	80	27	0.75
8	CAU TXE	40	0.3	1	30	9	0.75
9	CAD TXC	40	0.3	1	80	27	0.75
11	CAD TXC	40	0.3	1	30	9	0.75
12	CAD TXE	40	0.3	1	80	27	0.75
14	CAD TXE	40	0.3	1	30	9	0.75
15	CAU TX-CYC	40	0.3	1	80	27	0.75

Figure 6.4 and 6.5 show the response of undrained and drained monotonic loading. Figure 6.6 displays the computed secant shear modulus G_{sec} degradation with the axial strain from the above simulations. Also, Figure 6.7 presents the simulated response in undrained cyclic loading. Results simulated by the single element in Abaqus and the constitutive driver are almost identical to each other, which suggests the model is correctly implemented in the UMAT of Abaqus.

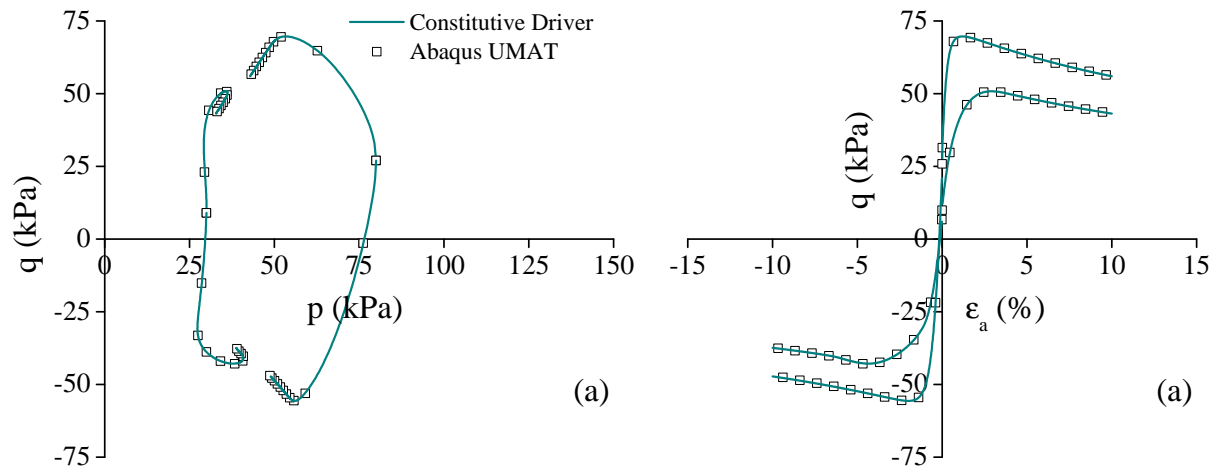


Figure 6.4. The comparison in undrained monotonic loading tests: (a) effective stress path; (b) stress-strain response

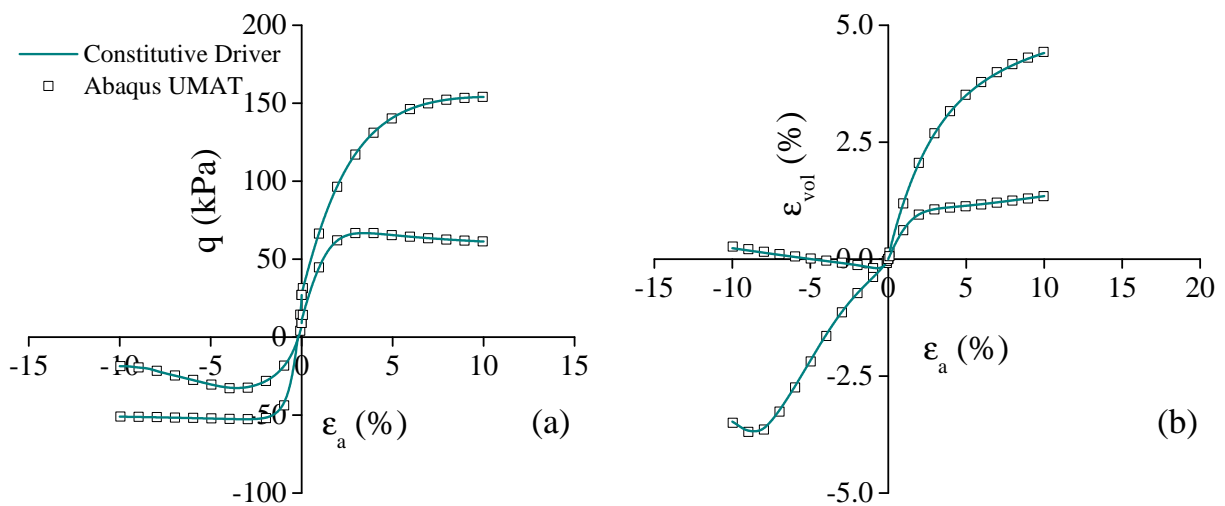


Figure 6.5. The comparison in drained monotonic loading tests: (a) stress-strain response; (b) volume change response

6.6. Summary and Conclusions

This chapter presents the generalization of the proposed model from triaxial space to multiaxial space, followed by the stress integration algorithm used in the model implementation, which is based on the Runge-Kutta-Fehlberg auto-stepping explicit method.

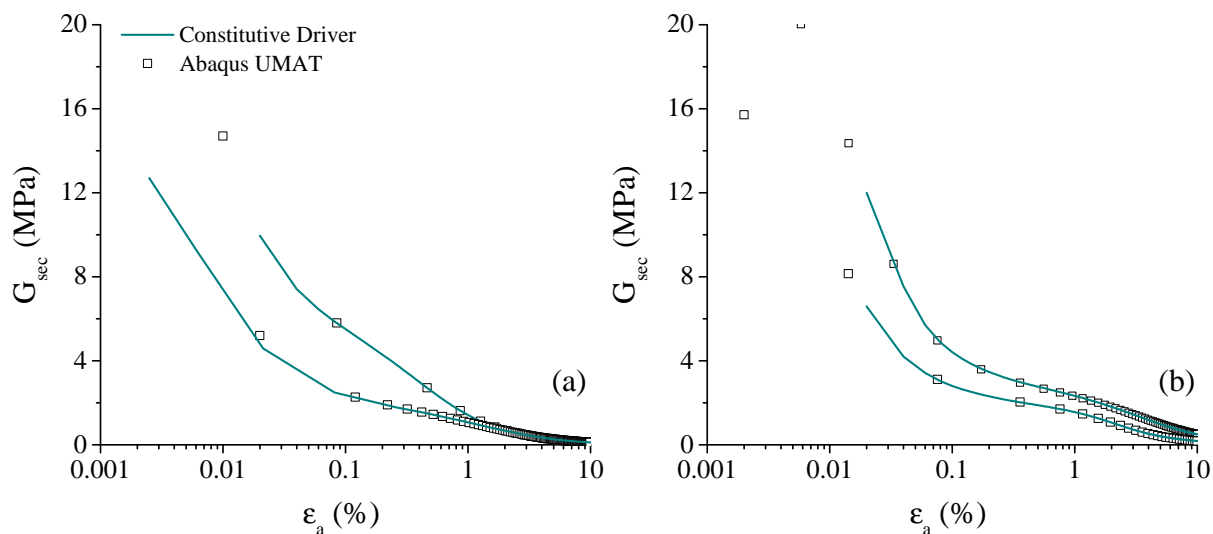


Figure 6.6. The comparison of small strain responses: (a) undrained compression tests; (b) drained compression tests

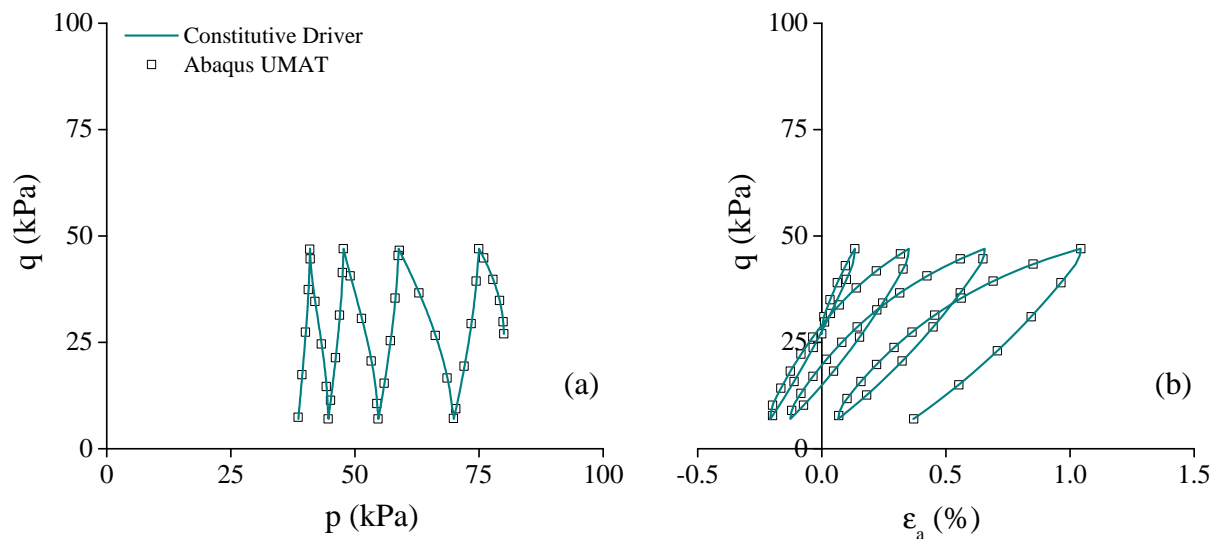


Figure 6.7. The comparison in undrained cyclic loading tests: (a) effective stress path; (b) stress-strain response

The proposed model is implemented into a triaxial space constitutive driver developed by this work aimed at integrating constitutive relations with elastoplastic modulus being dependent on strain rate. The formulation of this driver is presented in this chapter.

Lastly, Chapter 6 shows the implementation of the model into the finite element code Abaqus via its user-defined material subroutine (UMAT). The following main conclusions can be drawn from this chapter:

- (1) The Runge-Kutta-Fehlberg auto-stepping algorithm has been shown to be a stable and efficient integration method for the implementation of the proposed model into both the triaxial space constitutive driver and 3D finite element code.
- (2) The proposed constitutive driver provides a general and efficient method to integrate constitutive laws in triaxial space under various mixed-control conditions. Its capacity to handle constitutive models with an elastoplastic modulus that depends on strain rate enables it to serve as a platform to integrate other constitutive relations that have the same feature.
- (3) The single element test in Abaqus has proved the success of the model implementation in this 3D finite element code.

CHAPTER 7

SUMMARY AND CONCLUSIONS

7.1. Summary

The goal of this work is to develop a model which quantifies the strength degradation of natural clay during cyclic loading. This phenomenon is a key factor in the failure of clay slopes and retaining structures during earthquakes. A particular example studied in this work is the disastrous landslides in the city of Anchorage caused by the 1964 Alaska earthquake. The fundamental assumption made by this work is that the strength degradation is related to the deterioration of soil structure and effective stress changes when the natural clay is subjected to cyclic loading. To quantify such a strength loss, an effective stress based constitutive model is developed in two steps. First, a basic model is formulated to reproduce the responses of reconstituted clay during cyclic loading, i.e., the intrinsic cyclic behavior. Then, this basic model is extended to consider the effects of structure and its degradation as a function of plastic deformations. Both the basic model and the extended models have been verified with respect to the experimental observations.

Chapter 2 presents a literature review of various aspects related to the topic of this thesis. The studies about major landslides caused by the 1964 earthquake and the Bootlegger Cove Formation (BCF) that composes the failed slopes are reviewed. Observations from experimental tests on natural clay are summarized to illustrate the effects of soil structure on the mechanical behavior of natural clay. A review of clay behavior during undrained cyclic loading and post-cyclic shearing is presented to show the factors that affect strain accumulation during cyclic loading and post-cyclic shear strength. Lastly, Chapter 2 presents a review of bounding surface models aimed at simulating cyclically loaded clay and constitutive modeling strategies used to reproduce the effects of soil structure.

Chapter 3 presents a back analysis of an upper bound on the strength degradation of BCF clay needed to initiate failure of the Tunagain Height landslide during the 1964 earthquake. In-situ tests were conducted at Lynn Ary Park, Anchorage, which is adjacent to the Turnagain Heights landslide scarp. Chapter 3 presents the soil strength profile and stratigraphy at the Turnagain Heights area, which is generated based on the in-situ tests. The sensitivity of BCF clay is evaluated based on the same field investigations. Chapter 3 also discusses the correlation between the interpreted sensitivity and soil index properties and pore fluid chemical compositions. Lastly, this chapter presents the slope stability analysis of Turnagain Heights based on the strength parameters obtained from the in-situ tests, in which the stability condition before the 1964 earthquake and an upper bound on required strength reduction of BCF clay to trigger the slope failure are presented.

Chapter 4 presents the formulation of the basic model in triaxial space, which is developed within a bounding surface plasticity framework. Compared with other bounding surface plasticity models for cyclic clay behavior, three major enhancements are proposed, including the mixed plastic flow rule, a new form of plastic modulus to uniformly reproduce cyclic softening and shakedown, and the adoption of a small strain elasticity model. The results from a series of parametric studies are discussed, which elucidate the roles of new model components. The steps required to calibrate model parameters and estimate the initial values of the internal variables are presented. Finally, the basic model is validated with respect to experimental observations of two relatively unstructured types of clay: reconstituted Georgia kaolin and relatively insensitive BCF clay.

Chapter 5 extends the basic model presented in Chapter 4 to reproduce the effects of soil structure and its deterioration. In particular, the concept of structure surface and

intrinsic surface are introduced, which govern the response of natural clay and its corresponding reconstituted state, respectively. A new internal variable S_b that represents the amount of soil structure and a destructuration law that quantifies the monotonic decrease of S_b under irrecoverable deformation are discussed. The proposed plastic potential surface in the extended model is a function of fabric anisotropy (internal variable α) and inter-particle bonds (internal variable p_t). The influences of these two aspects of soil structure on material plastic flow are explored based on the stress-dilatancy relation which is derived from the plastic potential surface. The appropriateness of this plastic potential surface to describe natural clay behavior is validated with experimental evidence. Finally, this chapter shows the validation of the extended model based on experimental data of eight natural clays.

Chapter 6 presents the generalization of the proposed model from triaxial space to multi-axial space, followed by the stress integration algorithm used in the model implementation, which is based on the Runge-Kutta-Fehlberg auto-stepping explicit method. The proposed model is implemented into a triaxial space constitutive driver developed by this work aimed at integrating constitutive relations with elastoplastic modulus being dependent on strain rate. The formulation of this driver is presented in this chapter. Lastly, Chapter 6 shows the implementation of the model into the finite element code Abaqus via its user-defined material subroutine (UMAT).

7.2. Conclusions

From the in-situ tests at the Lynn Ary Park and the back analysis of Turnagain Heights landslide, the following main conclusions can be drawn:

- (1) The strength profile interpreted from FV and CPT tests suggests that BCF soil at the tested site (i.e., Lynn Ary Park) is overconsolidated at the top of the layer, and gradually becomes normally consolidated with depth. Also, this trend of stress history is supported by the classification of soil behavior type based on the normalized CPT data. BCF clay at this site can be divided into four sublayers based on their undrained strength variation: upper stiff clay, upper soft clay, lower soft clay and lower stiff clay.
- (2) The sensitivity of BCF clay interpreted from the in-situ tests at the Lynn Ary Park ranges from 2 to 10, with the majority of data falls between 2 and 6. This sensitivity, together with the liquidity index indicates that the BCF clay at the Lynn Ary Park is not very sensitive. Moreover, the sensitivity of the upper stiff clay and upper soft clay layers is noticeably larger than that of the lower soft clay and lower stiff clay layers.
- (3) A comparison between the pore fluid chemical composition concentration profile at the Lynn Ary Park and the variation of sensitivity suggests that the high sensitivity of the upper stiff clay and upper soft clay layers may be caused by the low concentration of total cation and the low percentage of the divalent cations.
- (4) The stability analysis based on the strength parameters interpreted from the in-situ tests shows that the Turnagain Heights slope was at a relatively safe condition before the 1964 earthquake (i.e., $FS=1.30 - 1.38$). Furthermore, stability analysis which decreases the strength of BCF clay reveals that 68% to 76% strength reduction for the upper stiff clay is needed to trigger slope failure under static condition, while a higher strength reduction is required for the upper soft clay

layer (80% to 88%). If a strength degradation uniformly occurs in both the above layers, a relatively lower reduction (37% to 43%) is sufficient to initiate the slope failure. These strength reductions represent an upper bound on the amount of degradation required to initiate failure during cyclic loading, and these results are compatible with the sensitivity interpreted from the in-situ tests implying that the degradation of BCF clays during the earthquake individually was sufficient to result in the landslide at Turnagain Heights.

- (5) The consideration of interbedded sand/silt lenses in the analysis tends to strengthen the stability of the slope slightly. And the study shows without significant reduction of the BCF clay strength, the liquefaction of such lenses during the earthquake is not able to trigger the landslide.
- (6) The current stability analyses provide an upper bound of the required strength reduction of BCF clay to initiate the landslide. Given that other unfavorable conditions (e.g., inertial forces in an earthquake) are not considered in this work, the actual strength loss is expected to be lower than the computed values. Furthermore, the above upper bound is obtained based on the assumption that the 1964 earthquake uniformly reduced the strength of clay throughout individual BCF layers. If inhomogeneous strength reduction occurred, the greater strength reduction than the analyses results might be required at local locations.

From the development and verification of the basic model aimed at reproducing intrinsic cyclic clay behavior, the following main conclusions can be drawn:

- (1) The verification with experimental observations shows that the proposed basic model is general, versatile and can reliably represent observed responses. With

a single set of parameters, the proposed basic model is capable of reproducing strain and pore pressure accumulation during cyclic loading with different shear stresses and various complex stress histories before cyclic loading.

- (2) The proposed mixed plastic flow rule incorporates characteristics of plastic flow direction defined by the current stress state into the existing image stress flow rule. The employment of this new flow rule successfully solves the undesirable early stop of pore pressure build-up inherent with the use of flow rule based on the image stress. Further, compared with the image stress flow rule, the proposed flow rule ensures that a correct trend of pore pressure build-up is reproduced. The new parameter w provides model users additional flexibility in controlling the amount of pore pressure build-up during undrained cyclic loading.
- (3) The proposed plastic modulus formulation enables the model to reproduce in a unified manner both cyclic softening and cyclic shakedown, which are observed in tests on the reconstituted Georgia kaolin and insensitive BCF clay, respectively.
- (4) When large plastic deformation develops and forms the majority of total deformation, ignoring small strain stiffness will not cause significant differences in computed responses. When cyclic strains are relatively small, incorporation of the small strain elasticity model will better simulate the cyclic stress-strain hysteresis loop, corresponding energy dissipation, and the recent stress history effects. Ignoring small strain stiffness under some circumstance can limit the amount of deformation accumulation and underestimate pore pressure build-up in cyclic loading, which may eventually lead to unsafe predictions if the number of cycles is large.

- (5) Experiments on relatively insensitive BCF clay show construction-induced stress changes significantly affect clay behavior during cyclic loading, including the amount and directional preference of strain accumulation. This feature is delicately reproduced by the proposed model. The proposed model also can satisfactorily capture the stress-strain-pore pressure responses observed in post-cyclic shearing on relatively insensitive BCF clay, which enables the model to be used in assessing the stability of geotechnical facilities after cyclic loading.

From the development and verification of the extended model aimed at capturing the structure degradation of natural clay during cyclic loading, the following main conclusions can be drawn:

- (1) The fabric anisotropy and inter-particle bonds can significantly affect plastic flow. The change in fabric induced by the anisotropic loading tends to increase the plastic volume change. Moreover, when fabric anisotropy exists, after yielding the increase of isotropic stress in the absence of deviatoric stress can cause not only compression but also distortion, and purely compressive, non-distortional plastic deformation can occur for non-isotropic stress state. On the other hand, an increase in the inter-particle bonds exacerbates soil's plastic contraction and delays the occurrence of phase transformation as well as the plastic dilatancy. Moreover, the influence of inter-particle bonds is dependent on confining stress, and the increase in confining stress level will weaken the effects of inter-particle bonds on the plastic flow. Careful examinations of stress-dilatancy relations derived from the proposed plastic potential with experimental evidence on structured soil prove the appropriateness of this plastic potential.

- (2) The versatility of the extended model has been validated with experimental observations on different natural clays that have a relatively wide range of index properties. The versatility, generality, and predictability of the model are emphasized by the fact that with a single set of parameters, the model can adequately represent material behavior under different stress histories, drainage conditions, and loading paths (i.e., compression v.s. shearing, monotonic v.s. cyclic). The model parameters can be determined based on conventional experiments in a relatively straightforward way. If one is only interested in the monotonic behavior of natural clay, compression tests (1D or isotropic), CK_0 TXC and CK_0 TXE tests on NC and OC samples are sufficient to define model parameters. If cyclic behavior is considered, then additional stress or strain controlled cyclic test is needed. The proposed analytical solutions provide reasonable estimations of the initial values of model internal variables.
- (3) Experimental data in cyclic loading tests on Grande Baleine clay and BCF clay show strength reduction of natural clay during cyclic loading is strongly correlated with the permanent strains developed. The model successfully captures this feature. Modeling of cyclic loading of BCF clay shows that ignoring de-structuration, in conditions where the cyclic loading results in significant plastic strains, can lead to a significant underestimation of strength degradation and excess pore pressure build-up, which results in an unsafe assessment of the stability of geotechnical facilities in and after cyclic loadings.

From the generalization of the proposed model to multiaxial space and its implementation, the following main conclusions can be drawn:

- (1) The Runge-Kutta-Fehlberg auto-stepping algorithm has been shown to be a stable and efficient integration method for the implementation of the proposed model into both the triaxial space constitutive driver and 3D finite element code.
- (2) The proposed constitutive driver provides a general and efficient method to integrate constitutive laws in triaxial space under various mixed-control conditions. Its capacity to handle constitutive models with an elastoplastic modulus that depends on strain rate enables it to serve as a platform to integrate other constitutive relations that have the same feature.
- (3) The single element test in Abaqus has proved the success of the model implementation in this 3D finite element code.

References

- L. W. Abramson, T. S. Lee, S. Sharma, and G. M. Boyce. *Slope Stability and Stabilization Methods*. John Wiley & Sons, 2002.
- M.A. Allman and J.H. Atkinson. Mechanical properties of reconstituted bothkennar soil. *Géotechnique*, 42(2):289–301, 1992.
- A. Amorosi. *Il Comportamento Meccanico di Una Argilla Naturale Consistente*. PhD thesis, University of Rome La Sapienza, 1996.
- A. Anandarajah and Y. F. Dafalias. Bounding surface plasticity. III: Application to anisotropic cohesive soils. *Journal of Engineering Mechanics*, 112(12):1292–1318, 1986.
- K. H. Andersen, W. F. Rosenbrand, S. F. Brown, and J. H. Pool. Cyclic and static laboratory tests on drammen clay. *Journal of the Geotechnical Engineering Division*, 106(5):499–529, 1980.
- K. I. Andrianopoulos, A. G. Papadimitriou, and G. D. Bouckovalas. Bounding surface plasticity model for the seismic liquefaction analysis of geostuctures. *Soil Dynamics and Earthquake Engineering*, 30(10):895–911, 2010.
- J. H. Argyris, G. Faust, J. Szimmat, E.P. Warnke, and K.J. Willam. Recent developments in the finite element analysis of prestressed concrete reactor vessels. *Nuclear Engineering and Design*, 28(1):42–75, 1974.
- A. S. Azzouz, A. M. Malek, and M. M. Baligh. Cyclic behavior of clays in undrained simple shear. *Journal of Geotechnical Engineering*, 115(5):637–657, 1989.

- A.S. Balasubramaniam and Z. Hwang. Yielding of weathered bangkok clay. *Soils and Foundations*, 20(2):1–15, 1980.
- P. K. Banerjee and N. B. Yousif. A plasticity model for the mechanical behaviour of anisotropically consolidated clay. *International Journal for Numerical and Analytical Methods in Geomechanics*, 10(5):521–541, 1986.
- J.P. Bardet and W. Choucair. A linearized integration technique for incremental constitutive equations. *International Journal for Numerical and Analytical Methods in Geomechanics*, 15(1):1–19, 1991.
- G. Belokas and M. Kavvadas. An anisotropic model for structured soils: Part i: theory. *Computers and Geotechnics*, 37(6):737–747, 2010.
- T. Benz. *Small-Strain Stiffness of Soils and its Numerical Consequences*. PhD thesis, 2007.
- T. Benz, P. A. Vermeer, and R. Schwab. A small-strain overlay model. *International Journal for Numerical and Analytical Methods in Geomechanics*, 33(1):25–44, 2009.
- L. Bjerrum. Geotechnical properties of norwegian marine clays. *Géotechnique*, 4(2):49–69, 1954.
- L. Bjerrum. Progressive failure in slopes of over-consolidated plastic clay and clay shales. *Journal of Soil Mechanics and Foundations Division*, 93(SM5):1–49, 1967.
- R. W. Boulanger and I. M. Idriss. Evaluating the potential for liquefaction or cyclic failure of silts and clays. Technical report, 2004.
- J. B. Burland. On the compressibility and shear strength of natural clays. *Géotechnique*, 40(3):329–378, 1990.

- G. Buscarnera and A. J. Whittle. Model prediction of static liquefaction: influence of the initial state on potential instabilities. *Journal of Geotechnical and Geoenvironmental Engineering*, 139(3):420–432, 2013.
- M. Calvello and R. J. Finno. Selecting parameters to optimize in model calibration by inverse analysis. *Computers and Geotechnics*, 31(5):410–424, 2004.
- R. Castellanza. *Weathering Effects on the Mechanical Behaviour of Bonded Geomaterials: An Experimental, Theoretical and Numerical Study*. PhD thesis, Politecnico di Milano, 2002.
- G. Castro and J. T. Christian. Shear strength of soils and cyclic loading. *Journal of Geotechnical Engineering Division*, 102(GT7):887–894, 1976.
- M. Cecconi and G. Viggiani. Structural features and mechanical behaviour of a pyroclastic weak rock. *International Journal for Numerical and Analytical Methods in Geomechanics*, 25(15):1525–1557, 2001.
- F. Cotecchia and R. J. Chandler. The influence of structure on the pre-failure behaviour of a natural clay. *Géotechnique*, 47(3):523–544, 1997.
- Y. F. Dafalias. A model for soil behavior under monotonic and cyclic loading conditions. In *Transactions, 5th International Conference on SMiRT*, volume K, West Berlin, Germany, 1979.
- Y. F. Dafalias. The concept and application of the bounding surface in plasticity theory. In *Physical Non-linearities in Structural Analysis, IUTAM Symposium*, pages 56–63. Springer, 1981.
- Y. F. Dafalias. An anisotropic critical state soil plasticity model. *Mechanics Research Communications*, 13(6):341–347, 1986a.

- Y. F. Dafalias. Bounding surface plasticity.I: Mathematical foundation and hypoplasticity. *Journal of Engineering Mechanics*, pages 966–987, 1986b.
- Y. F. Dafalias and L. R. Herrmann. A bounding surface formulation of soil plasticity. In G. N. Pande and O. C. Zienkiewicz, editors, *Soil Mechanics-Transient and Cyclic Loads*. John Wiley and Sons, 1982.
- Y. F. Dafalias and L. R. Herrmann. Bounding surface plasticity. II: Application to isotropic cohesive soils. *Journal of Engineering Mechanics*, 112(12):1263–1291, 1986.
- Y. F. Dafalias and M. T. Manzari. Simple plasticity sand model accounting for fabric change effects. *Journal of Engineering mechanics*, 130(6):622–634, 2004.
- Y. F. Dafalias, M. T. Manzari, and A. G. Papadimitriou. Saniclay: simple anisotropic clay plasticity model. *International Journal for Numerical and Analytical Methods in Geomechanics*, 30(12):1231–1257, 2006.
- E. Eberhardt, D. Stead, and J. S. Coggan. Numerical analysis of initiation and progressive failure in natural rock slope—the 1991 randa rockslide. *International Journal of Rock Mechanics and Mining Sciences*, 41(1):69–87, 2004.
- G. M. Elliott and E. T. Brown. Yield of a soft, high porosity rock. *Géotechnique*, 35(4): 413–423, 1985.
- J. A. Farrar, R. Torres, and L. G. Crutchfield. Cone penetrometer testing, scoggins dam, tualatin project, oregon. Technical report, Engineering Geology Group Bureau of Reclamation, Technical Services Center, Denver, Colorado, 2008.
- R. J. Finno and M. Calvello. Supported excavations: observational method and inverse modeling. *Journal of Geotechnical and Geoenvironmental Engineering*, 131(7):826–836, 2005.

- R. J. Finno and W. Cho. Recent stress-history effects on compressible chicago glacial clays. *Journal of Geotechnical and Geoenvironmental Engineering*, 137(3):197–207, 2010.
- R. J. Finno and T. Kim. Effects of stress path rotation angle on small strain responses. *Journal of Geotechnical and Geoenvironmental Engineering*, 138(4):526–534, 2012.
- R. J. Finno and D. G. Zapata-Medina. Effects of construction-induced stresses on dynamic soil parameters of bootlegger cove clays. *Journal of Geotechnical and Geoenvironmental Engineering*, 140(4):04013051–(1–12), 2013.
- Z. Gao and J. Zhao. Constitutive modeling of anisotropic sand behavior in monotonic and cyclic loading. *Journal of Engineering Mechanics*, page 04015017, 2015.
- A. Gens. *Stress–strain and strength of a low plasticity clay*. PhD thesis, Imperial College, London University, 1982.
- A. Gens and R. Nova. Conceptual bases for a constitutive model for bonded soils and weak rocks. *Geotechnical Engineering of Hard Soils-Soft Rocks*, 1(1):485–494, 1993.
- J. Graham, M. L. Noonan, and K. V. Lew. Yield states and stress-strain relationships in a natural plastic clay. *Canadian Geotechnical Journal*, 20(3):502–516, 1983.
- G. Gudehus, A. Amorosi, A. Gens, I. Herle, D. Kolymbas, D. Mašín, D. Wood, A. Niemunis, R. Nova, M. Pastor, et al. The soilmodels. info project. *International Journal for Numerical and Analytical Methods in Geomechanics*, 32(12):1571–1572, 2008.
- P. J. Haeussler and G. Plafker. Earthquakes in alaska. Technical Report USGS 95-624, 2004.
- W. R. Hansen. *Effects of the Earthquake of March 27, 1964, at Anchorage, Alaska*. US Government Printing Office, 1965.

- B. O. Hardin and V. P. Drnevich. Shear modulus and damping in soils: design equations and curves. *Journal of the Soil Mechanics and Foundations Division, ASCE*, 98(7): 667–692, 1972.
- D. W. Hight, A. Gens, and R. J. Jardine. Evaluation of geotechnical parameters from triaxial tests on offshore clay. In *Offshore Site Investigation*, pages 253–268. Springer, 1985.
- R. D. Holtz, D. Kovacs, W., and T. C. Sheahan. *An Introduction to Geotechnical Engineering*. Pearson, 2nd edition, 2010.
- S. Horpibulsuk, M. D. Liu, D. S. Liyanapathirana, and J. Suebsuk. Behaviour of cemented clay simulated via the theoretical framework of the structured cam clay model. *Computers and Geotechnics*, 37(1):1–9, 2010.
- Maosong Huang, Yanhua Liu, and Daichao Sheng. Simulation of yielding and stress–strain behavior of shanghai soft clay. *Computers and Geotechnics*, 38(3):341–353, 2011.
- B. Jeremic. Line search techniques for elasto-plastic finite element computations in geomechanics. *Communications in Numerical Methods in Engineering*, 17(2):115–126, 2001.
- J. Jiang and H. I. Ling. A framework of an anisotropic elastoplastic model for clays. *Mechanics Research Communications*, 37(4):394 – 398, 2010.
- J. Jiang, H. I. Ling, and V. N. Kaliakin. An associative and non-associative anisotropic bounding surface model for clay. *Journal of Applied Mechanics*, 79(3):031010(1–10), 2012.
- R. W. Jibson. Methods for assessing the stability of slopes during earthquakes a retrospective. *Engineering Geology*, 122(1):43–50, 2011.

- T. N. V. Karlstrom. Quaternary geology of the Kenai Lowland and glacial history of the Cook Inlet region, Alaska. Technical Report USGS-443, 1964.
- E. Kavazanjian, J. Wang, G. R. Martin, A. Shamsabadi, I. Lam, S. E. Dickenson, and C. J. Hung. LRFD seismic analysis and design of transportation geotechnical features and structural foundations reference manual. Technical Report FHWA-NHI-11-032, Washington DC, 2011.
- M. Kavvas and A. Amorosi. A constitutive model for structured soils. *Géotechnique*, 50(3):263–273, 2000.
- X. Kong, J. Liu, D. Zou, and H. Liu. Stress-dilatancy relationship of zipingpu gravel under cyclic loading in triaxial stress states. *International Journal of Geomechanics*, 16(4):04016001, 2016.
- F. H. Kulhawy and P. W. Mayne. Manual on estimating soil properties for foundation design. Technical report, Electric Power Research Inst., Palo Alto, CA (USA); Cornell Univ., Ithaca, NY (USA). Geotechnical Engineering Group, 1990.
- R. Lagioia and R. Nova. An experimental and theoretical study of the behaviour of a calcarenite in triaxial compression. *Géotechnique*, 45(4):633–648, 1995.
- R. Lagioia, A. M. Puzrin, and D. M. Potts. A new versatile expression for yield and plastic potential surfaces. *Computers and Geotechnics*, 19(3):171–191, 1996.
- G. Lefebvre. *Contribution à l'étude de la stabilité des pentes dans les argiles cimentées*. PhD thesis, Université Laval, 1970.
- G. Lefebvre, D. LeBoeuf, and B. Demers. Stability threshold for cyclic loading of saturated clay. *Canadian Geotechnical Journal*, 26(1):122–131, 1989.

- S. Leroueil and P. R. Vaughan. The general and congruent effects of structure in natural soils and weak rocks. *Géotechnique*, 40(3):467–488, 1990.
- S. Leroueil, F. Tavenas, F. Brucy, P. La Rochelle, and M. Roy. Behavior of destructured natural clays. *Journal of the Geotechnical Engineering Division*, 105(6):759–778, 1979.
- G. Lessard and J. K. Mitchell. The causes and effects of aging in quick clays. *Canadian Geotechnical Journal*, 22(3):335–346, 1985.
- P. I. Lewin. The influence of stress history on the plastic potential. In *Proceedings of the Symposium on the Role of Plasticity in Soil Mechanics*, 1973.
- T. Li and H. Meissner. Two-surface plasticity model for cyclic undrained behavior of clays. *Journal of Geotechnical and Geoenvironmental Engineering*, 128(7):613–626, 2002.
- R. Liang and F. Ma. Anisotropic plasticity model for undrained cyclic behavior of clays. i: Theory. *Journal of Geotechnical Engineering*, 118(2):229–245, 1992.
- M. D. Liu and J. P. Carter. Volumetric deformation of natural clays. *International Journal of Geomechanics*, 3(2):236–252, 2003.
- J. Locat and G. Lefebvre. The compressibility and sensitivity of an artificially sedimented clay soil: The grande-baleine marine clay, québec, canada. *Marine Georesources and Geotechnology*, 6(1):1–28, 1985.
- J. Lubliner. On loading, yield and quasi-yield hypersurfaces in plasticity theory. *International Journal of Solids and Structures*, 11(9):1011–1016, 1975.
- T. Lunne, P. K. Robertson, and J. J. M. Powell. *Cone Penetration Testing in Geotechnical Practice*. Blackie Academic/Routledge Publishing, 1997.
- M. Maccarini. *Laboratory Studies for a Weakly Bonded Artificial Soil*. PhD thesis, Imperial College London (University of London), 1987.

- G. Maier and T. Hueckel. Nonassociated and coupled flow rules of elastoplasticity for rock-like materials. In *International Journal of Rock Mechanics and Mining Sciences and Geomechanics Abstracts*, volume 16, pages 77–92. Elsevier, 1979.
- M. Martinelli. *Comportamento Dinamico di Fondazioni Su Pali in Sabbia*. PhD thesis, Sapienza Università di Roma, 2012.
- D. Mašín. 3D modeling of an natm tunnel in high k0 clay using two different constitutive models. *Journal of Geotechnical and Geoenvironmental Engineering*, 135(9):1326–1335, 2009.
- G. Masing. Eigenspannungen und verfestigung beim messing. In *Proceedings of the 2nd international congress of applied mechanics*, volume 100, pages 332–335, 1926.
- R. D. Miller and E. Dobrovlny. Surficial geology of anchorage and vicinity, alaska. Technical Report USGS Bulletin 1093, 1959.
- C. Miriano. *Modellazione Numerica Della Risposta sismica di Strutture di Sostegno Flessibili*. PhD thesis, Sapienza Università di Roma, 2011.
- J. K. Mitchell. *Fundamentals of Soil Behavior*. Wiley New York, 2 edition, 1993.
- J. K. Mitchell, W. N. Houston, and G. Yamane. The sensitivity and geotechnical properties of bootlegger cove clay. In *The Great Alaska Earthquake of 1964, Engineering*, pages 157–178. Committee on the Alaska Earthquake of the National Research Council, National Academy of Sciences, 1973.
- J. Moum, T. Løken, and J. K. Torrance. A geochemical investigation of the sensitivity of a normally consolidated clay from drammen, norway. *Géotechnique*, 21(4):329–340, 1971.

- Z. Mróz, V. A. Norris, and O. C. Zienkiewicz. An anisotropic hardening model for soils and its application to cyclic loading. *International Journal for Numerical and Analytical Methods in Geomechanics*, 2(3):203–221, 1978.
- Z. Mróz, V. A. Norris, and O. C. Zienkiewicz. An anisotropic, critical state model for soils subject to cyclic loading. *Géotechnique*, 31(4):451–469, 1981.
- V. Nadarajah. *Stress-Strain Properties of Lightly Overconsolidated Clays*. PhD thesis, University of Cambridge, 1973.
- H. W. Olsen. Sensitive strata in bootlegger cove formation. *Journal of Geotechnical Engineering*, 115(9):1239–1251, 1989.
- A. G. Papadimitriou and G. D. Bouckovalas. Plasticity model for sand under small and large cyclic strains: a multiaxial formulation. *Soil Dynamics and Earthquake Engineering*, 22(3):191–204, 2002.
- R. H. G. Parry and V. Nadarajah. A volumetric yield locus for lightly overconsolidated clay. *Géotechnique*, 23(3):450–453, 1973.
- M. Pastor, O. C. Zienkiewicz, and A. H. C. Chan. Generalized plasticity and the modelling of soil behaviour. *International Journal for Numerical and Analytical Methods in Geomechanics*, 14(3):151–190, 1990.
- R. B. Peck. Stability of natural slopes. *Journal of Soil Mechanics and Foundations Division*, 93(SM4):403–417, 1967.
- J. M. Pestana and A. J. Whittle. Formulation of a unified constitutive model for clays and sands. *International Journal for Numerical and Analytical Methods in Geomechanics*, 23(12):1215–1243, 1999.

- D. M. Potts and D. Ganendra. An evaluation of substepping and implicit stress point algorithms. *Computer Methods in Applied Mechanics and Engineering*, 119(3-4):341–354, 1994.
- S. Rampello, V. N. Georgiannou, and G. Viggiani. Strength and dilatancy of natural and reconstituted vallericca clay. In *Proceedings of International Symposium on the Geotechnical Engineering of Hard Soils–Soft Rocks*, volume 1, pages 761–768, Athens, 1993.
- P. K. Robertson. Soil classification using the cone penetration test. *Canadian Geotechnical Journal*, 27(1):151–158, 1990.
- P. K. Robertson. Interpretation of cone penetration tests—a unified approach. *Canadian Geotechnical Journal*, 46(11):1337–1355, 2009.
- Rocscience Inc. Slide version 6.036, 2015. URL <https://www.rocscience.com>.
- K. H. Roscoe, A. N. Schofield, and A. Thurairajah. Yielding of clays in states wetter than critical. *Géotechnique*, 13(3):211–240, 1963.
- M. Rouainia and M. D. Wood. A kinematic hardening constitutive model for natural clays with loss of structure. *Géotechnique*, 50(2):153–164, 2000.
- P. W. Rowe. The stress-dilatancy relation for static equilibrium of an assembly of particles in contact. In *Proceedings of the Royal Society of London A: Mathematical, Physical and Engineering Sciences*, volume 269, pages 500–527. The Royal Society, 1962.
- P. W. Rowe. Stress-dilatancy, earth pressures, and slopes. *Journal of the Soil Mechanics and Foundations Division*, 89(3):37–62, 1963.
- D.A. Sangrey, D.J. Henkel, and M.I. Esrig. The effective stress response of a saturated clay soil to repeated loading. *Canadian Geotechnical Journal*, 6(3):241–252, 1969.

- R. A. M. Schmidt. Pleistocene marine microfauna in the bootlegger cove clay, anchorage, alaska. *Science*, 141(3578):350–351, 1963.
- H. R. Schmoll, B. J. Szabo, M. Rubin, and E. Dobrovlny. Radiometric dating of marine shells from the bootlegger cove clay, anchorage area, alaska. *Geological Society of America Bulletin*, 83(4):1107–1114, 1972.
- F. Schnaid, P. D. M. Prietto, and N. C. Consoli. Characterization of cemented sand in triaxial compression. *Journal of Geotechnical and Geoenvironmental Engineering*, 127(10):857–868, 2001.
- A. Schofield and P. Wroth. *Critical State Soil Mechanics*. McGraw-Hill London, 1968.
- H. B. Seed and S. D. Wilson. The turnagain heights landslide, anchorage, alaska. *Journal of Soil Mechanics and Foundations Division*, 93(SM4):325–353, 1967.
- G. Seidalinov. *A Simple Anisotropic Bounding Surface Plasticity Model for Cyclic Response of Clays*. PhD thesis, University of British Columbia, 2012.
- G. Seidalinov and M. Taiebat. Bounding surface saniclay plasticity model for cyclic clay behavior. *International Journal for Numerical and Analytical Methods in Geomechanics*, 38(7):702–724, 2014.
- Shannon & Wilson Inc. Report on anchorage area soil studies, alaska. Technical report, Seattle, Washington, 1964.
- T. C. Sheahan. *An Experimental Study of the Time-Dependent Undrained Shear Behavior of Resedimented Clay Using Automated Stress Path Triaxial Equipment*. PhD thesis, Massachusetts Institute of Technology, 1991.
- W. Sheu. *Modeling of Stress-Strain-Strength Behavior of a Clay under Cyclic Loading*. PhD thesis, University of Colorado, 1985.

- J. C. Simo and T.J.R. Hughes. *Computational Inelasticity*, volume 7. Springer Science & Business Media, 2006.
- N. Sivasithamparam and M. Karstunen. An anisotropic bubble model for structured clays. In *4th International Workshop of Young Doctors in Geomechanics*, pages 43–47, 2012.
- S. W. Sloan, A. J. Abbo, and D. Sheng. Refined explicit integration of elastoplastic models with automatic error control. *Engineering Computations*, 18(1/2):121–194, 2001.
- P. J. Smith. Foraminifera from the bootlegger cove clay, Appendix J. In *Report on Anchorage Area Soil Studies, Alaska*. 1964.
- P. R. Smith, R. J. Jardine, and D. W. Hight. The yielding of bothkennar clay. *Géotechnique*, 42(2):257–274, 1992.
- J. Suebsuk, S. Horpibulsuk, and M. D. Liu. A critical state model for overconsolidated structured clays. *Computers and Geotechnics*, 38(5):648–658, 2011.
- H. U. Sverdrup, M. W. Johnson, R. H. Fleming, et al. *The Oceans: Their Physics, Chemistry, and General Biology*, volume 7. Prentice-Hall New York, 1942.
- M. Taiebat, Y. F. Dafalias, and R. Peek. A destructureation theory and its application to saniclay model. *International Journal for Numerical and Analytical Methods in Geomechanics*, 34(10):1009–1040, 2010.
- C. Tamagnini, G. Viggiani, R. Chambon, and J. Desrues. Evaluation of different strategies for the integration of hypoplastic constitutive equations: Application to the cloe model. *Mechanics of Cohesive-frictional Materials*, 5(4):263–289, 2000.
- F Tavenas and S Leroueil. Effects of stresses and time on yielding of clays. In *Proceedings of the 9th International Conference on Soil Mechanics and Foundation Engineering*, volume 1, pages 319–326, 1977.

- F. Tavenas and S. Leroueil. Discussion. In *Proc. 11th Int. Conf. on Soil Mech. Fdn Engng*, volume 5, pages 2693–2694, San Francisco, 1985.
- D. W. Taylor. *Fundamentals of Soil Mechanics*. John Wiley & Sons, Inc, 1948.
- G. R. Thiers and H. B. Seed. Cyclic stress-strain characteristics of clay. *Journal of Soil Mechanics and Foundations Division*, 1968.
- G. R. Thiers and H. B. Seed. Strength and stress-strain characteristics of clays subjected to seismic loading conditions. In *Vibration Effects of Earthquakes on Soils and Foundations*. ASTM International, 1969.
- R. G. Updike. Engineering geologic facies of the bootlegger cove formation. In *Anchorage, Alaska: Geological Society of America Abstracts with Programs*. 1982.
- R. G. Updike and H. W. Olsen. *Geologic and Geotechnical Conditions Adjacent to the Turnagain Heights Landslide, Anchorage, Alaska*. US Government Printing Office, 1988.
- R. G. Updike and C. A. Ulery. Engineering-geologic map of southwest anchorage, alaska. Technical report, 1986.
- U.S. Coast and Geodetic Survey. Preliminary report, Prince William Sound, Alaskan earthquakes march-april, 1964. Technical report, Washington, 1964.
- M. Vucetic. Cyclic threshold shear strains in soils. *Journal of Geotechnical Engineering*, 120(12):2208–2228, 1994.
- M. Vucetic and R. Dobry. Effect of soil plasticity on cyclic response. *Journal of Geotechnical Engineering*, 117(1):89–107, 1991.
- L. K. Walker and G. P. Raymond. Anisotropic consolidation of leda clay. *Canadian Geotechnical Journal*, 6(3):271–286, 1969.

- Z. Wang, Y. F. Dafalias, and C. Shen. Bounding surface hypoplasticity model for sand. *Journal of Engineering Mechanics*, 116(5):983–1001, 1990.
- B. Westerberg. *Lerors Mekaniska Egenskaper*. PhD thesis, Lulea University of Technology, Sweden, 1995.
- S. J. Wheeler, A. Ntnen, M. Karstunen, and M. Lojander. An anisotropic elastoplastic model for soft clays. *Canadian Geotechnical Journal*, 40(2):403–418, 2003.
- A. J. Whittle and M. Kavvasdas. Formulation of mite3 constitutive model for overconsolidated clays. *Journal of Geotechnical Engineering*, 120(1):173–198, 1994.
- D. M. Wood. *Soil Behaviour and Critical State Soil Mechanics*. Cambridge University Press, 1990.
- D. M. Wood. *Geotechnical Modelling*, volume 1. CRC Press, 2003.
- WSDOT. Geotechnical design manual. Technical report, Olympia, Washington, USA, 2006.
- K. Yasuhara. Postcyclic undrained strength for cohesive soils. *Journal of Geotechnical Engineering*, 120(11):1961–1979, 1994.
- K. Yasuhara, K. Hirao, and A. F. L. Hyde. Effects of cyclic loading on undrained strength and compressibility of clay. *Soils and Foundations*, 32(1):100–116, 1992. doi: 10.3208/sandf1972.32.100.
- Z. Yin, J. Yin, and H. Huang. Rate-dependent and long-term yield stress and strength of soft wenzhou marine clay: experiments and modeling. *Marine Georesources and Geotechnology*, 33(1):79–91, 2015.
- H. S. Yu. CASM: A unified state parameter model for clay and sand. *International Journal for Numerical and Analytical Methods in Geomechanics*, 22(8):621–653, 1998.

- H. S. Yu, C. Khong, and J. Wang. A unified plasticity model for cyclic behaviour of clay and sand. *Mechanics Research Communications*, 34(2):97–114, 2007a.
- H. S. Yu, S. M. Tan, and F. Schnaid. A critical state framework for modelling bonded geomaterials. *Geomechanics and Geoengineering*, 2(1):61–74, 2007b.
- D. G. Zapata-Medina. *Evaluation of Dynamic Soil Parameter Changes due to Construction-Induced Stresses*. PhD thesis, Northwestern University, 2012.
- D. G. Zapata-Medina, R. J. Finno, and C. A. Vega-Posada. Stress history and sampling disturbance effects on monotonic and cyclic responses of overconsolidated bootlegger cove clays. *Canadian Geotechnical Journal*, 51(6):599–609, 2014.
- M. Zergoun. *Effective stress response of clay to undrained cyclic loading*. PhD thesis, University of British Columbia, 1991.
- M. Zergoun and Y. P. Vaid. Effective stress response of clay to undrained cyclic loading. *Canadian Geotechnical Journal*, 31(5):714–727, 1994.
- O. C. Zienkiewicz, K. H. Leung, and M. Pastor. Simple model for transient soil loading in earthquake analysis. i. basic model and its application. *International Journal for Numerical and Analytical Methods in Geomechanics*, 9(5):453–476, 1985.
- M. Zytynski, M. F. Randolph, R. Nova, and C. P. Wroth. On modelling the unloading-reloading behaviour of soils. *International Journal for Numerical and Analytical Methods in Geomechanics*, 2(1):87–93, 1978.